

A NEW CONTINUUM DYNAMIC MODEL
FOR THE ANALYSIS OF EXTREMELY RAPID LANDSLIDE MOTION
ACROSS COMPLEX 3D TERRAIN

by

SCOTT MCDUGALL

B.A.Sc., University of Toronto, 1998

A THESIS SUBMITTED IN PARTIAL FULFILLMENT OF
THE REQUIREMENTS FOR THE DEGREE OF

DOCTOR OF PHILOSOPHY

in

THE FACULTY OF GRADUATE STUDIES

(Geological Engineering)

THE UNIVERSITY OF BRITISH COLUMBIA

August 2006

© Scott McDougall, 2006

ABSTRACT

Runout analysis, the prediction of landslide motion and its effects, is an essential component of landslide risk assessment. A new continuum dynamic model has been developed for the runout analysis of extremely rapid, flow-like landslides, including rock avalanches, debris avalanches, debris flows and flow slides. The new model, DAN3D, is a 3D extension of the existing 2D model DAN. It uses a meshless, Lagrangian numerical method adapted from Smoothed Particle Hydrodynamics to discretize and solve the depth-averaged equations of motion for an "equivalent fluid", a hypothetical material governed by simple rheological relationships. The required rheological parameters, rather than measured, are calibrated through back-analysis of real landslide case studies. The key capabilities of the model include: 1) the ability to simulate motion across complex 3D terrain without the need to input a pre-defined path direction or width and without introducing problems due to mesh distortion; 2) the ability to simulate strain-dependent, non-hydrostatic, anisotropic internal stresses due to 3D deformation of material with internal shear strength; 3) the ability to simulate mass and momentum transfer due to entrainment of path material; 4) the ability to simulate variations in rheology along the path and within the landslide; and 5) efficient and simple operation. The model outputs the simulated spatial distribution of hazard intensity parameters, including flow velocity and depth, which are required for delineating the potential impact area, estimating the vulnerability of elements within this area and designing protective measures. It has been tested using both analytical and experimental methods, and its general behaviour has been demonstrated using a series of simple parametric analyses. The model has also been applied at full-scale to the simulation of a wide variety of landslide types. These back-analyses form the basis for a more thorough calibration, but some useful patterns have already emerged. This experience has been applied in practice to landslide runout prediction, although so far only in a parametric way. With continued back-analysis of real cases and the development of a probabilistic approach to forward-analysis, true landslide runout prediction, including quantification of uncertainty, should eventually be possible using the new model.

TABLE OF CONTENTS

ABSTRACT	ii
TABLE OF CONTENTS	iii
LIST OF TABLES	viii
LIST OF FIGURES	ix
LIST OF SYMBOLS	xii
ACKNOWLEDGEMENTS	xiv
DEDICATION	xv
1 INTRODUCTION	1
1.1 Introduction	1
1.2 Purpose, scope and structure of this thesis	4
1.3 Runout analysis in the framework of landslide risk assessment	6
1.3.1 Estimating the spatial probability of impact	7
1.3.2 Estimating vulnerability	8
1.3.3 Designing protective measures	9
1.4 Continuum dynamic modelling as a runout analysis method	10
1.4.1 Empirical methods	11
1.4.2 Analytical methods	13
1.5 Discussion	16
1.6 Conclusion	17
2 OBJECTIVES FOR MODEL DEVELOPMENT	18
2.1 Introduction	18
2.2 Objective #1: the ability to simulate motion across complex 3D terrain	19
2.3 Objective #2: the ability to simulate the influence of internal strength	21
2.3.1 Rankine earth pressure theory	21
2.3.2 Strain-dependent internal stresses in landslides	25
2.4 Objective #3: the ability to simulate entrainment	28
2.4.1 Mechanisms of path material mobilization	29
2.4.2 Volume change	33
2.4.3 Momentum transfer	35
2.5 Objective #4: the ability to simulate variations in rheology	38
2.5.1 Variations along the path	38
2.5.2 Variations within the landslide	41
2.6 Objective #5: efficiency	42
2.7 Discussion	43
2.8 Conclusion	44

3 PREVIOUS WORK	45
3.1 Introduction	45
3.2 Model classification	45
3.2.1 2D vs. 3D.....	45
3.2.2 Eulerian vs. Lagrangian.....	46
3.3.3 Measurement vs. calibration.....	47
3.3 Existing continuum dynamic models	49
3.3.1 Extension of hydrodynamic methods.....	49
3.3.2 Incorporation of path-dependent rheology	50
3.3.3 Incorporation of earth pressure theory	51
3.3.4 Incorporation of entrainment capabilities.....	53
3.3.5 Towards a synthesis.....	54
3.4 Discussion	57
3.5 Conclusion.....	58
4 GOVERNING EQUATIONS	59
4.1 Introduction	59
4.2 Equivalent fluid concept.....	59
4.3 General conservation laws.....	61
4.4 Boundary conditions.....	64
4.4.1 Stress conditions.....	65
4.4.2 Kinematic conditions.....	65
4.5 Depth-averaging	66
4.5.1 Depth-averaging the mass balance equation	67
4.5.2 Depth-averaging the momentum balance equations	67
4.6 Further simplifications	71
4.6.1 Lagrangian reference frame.....	71
4.6.2 Shallow flow assumption	73
4.6.3 Stress state normalization.....	74
4.7 Basal shear resistance.....	76
4.7.1 Laminar	77
4.7.2 Turbulent	77
4.7.3 Plastic	78
4.7.4 Bingham	78
4.7.5 Frictional	78
4.7.6 Voellmy.....	80
4.8 Discussion	81
4.9 Conclusion.....	82
5 NUMERICAL SOLUTION METHOD	84
5.1 Introduction	84
5.2 Smoothed Particle Hydrodynamics	85
5.2.1 Background	85
5.2.2 Theory	86
5.3 SPH-based mass balance.....	88
5.3.1 Depth and depth gradient interpolation.....	88

5.3.2 Interpolating kernel	91
5.4 Strain interpolation	95
5.4.1 Incremental tangential strain state	95
5.4.2 Strain rosette method	96
5.4.3 Simplified strain rosette method	99
5.5 Stress update	100
5.5.1 Assumed orientation of principle axes	100
5.5.2 Internal yield criterion	101
5.5.3 Stress incrementation	104
5.6 Entrainment	106
5.6.1 Momentum transfer based on erosion velocity and growth rate	106
5.6.2 Mass transfer	109
5.7 Intensity parameter interpolation	111
5.8 Implementation	112
5.8.1 Initial conditions	114
5.8.2 Time stepping	115
5.9 Discussion	118
5.10 Conclusion	119
6 TESTS	120
6.1 Introduction	120
6.2 1D dam-break	120
6.2.1 Description	120
6.2.2 Methodology	121
6.2.3 Results and discussion	123
6.3 Slump test	125
6.3.1 Description	125
6.3.2 Methodology	125
6.3.3 Results and discussion	127
6.4 Parametric analyses	129
6.4.1 Description	129
6.4.2 Methodology	129
6.4.3 Results and discussion: # particles and particle smoothing	131
6.4.4 Results and discussion: internal friction	133
6.4.5 Results and discussion: internal stiffness	134
6.4.6 Results and discussion: velocity smoothing	136
6.4.7 Results and discussion: basal rheology	137
6.4.8 Results and discussion: entrainment	138
6.5 Channelization	155
6.5.1 Description	155
6.5.2 Methodology	155
6.5.3 Results and discussion	157
6.6 Chute experiments	158
6.6.1 Description	158
6.6.2 Methodology	158
6.6.3 Results and discussion	159

6.7 Deflection experiments.....	161
6.7.1 Description	161
6.7.2 Methodology	163
6.7.3 Results and discussion.....	163
6.8 Discussion	166
6.9 Conclusion.....	167
7 CASE STUDIES	169
7.1 Introduction	169
7.2 Frank.....	169
7.2.1 Description	169
7.2.2 Methodology	172
7.2.3 Results and discussion.....	173
7.3 Val Pola	175
7.3.1 Description	175
7.3.2 Methodology	176
7.3.3 Results and discussion.....	178
7.4 Cervinara	181
7.4.1 Description	181
7.4.2 Methodology	181
7.4.3 Results and discussion.....	183
7.5 Quindici	185
7.5.1 Description	185
7.5.2 Methodology	185
7.5.3 Results and discussion.....	186
7.6 Nomash River.....	188
7.6.1 Description	188
7.6.2 Methodology	189
7.6.3 Results and discussion.....	191
7.7 Zymoetz River	195
7.7.1 Description	195
7.7.2 Methodology	205
7.7.3 Results and discussion.....	207
7.8 McAuley Creek	212
7.8.1 Description	212
7.8.2 Methodology	214
7.8.3 Results and discussion.....	215
7.9 Kolka	217
7.9.1 Description	217
7.9.2 Methodology	219
7.9.3 Results and discussion.....	220
7.10 Other cases	225
7.11 Discussion	227
7.12 Conclusion.....	229

8 CONCLUSIONS	230
8.1 Introduction	230
8.2 Summary of work completed	230
8.3 Recommendations for future work.....	234
8.4 Discussion	237
8.5 Conclusion.....	237
REFERENCES.....	238

LIST OF TABLES

Table 1.1	Correlation coefficients for proposed volume-fahrböschung relationships	13
Table 6.1	Parameter values used in each parametric analysis	130
Table 6.2	Initial and final smoothing lengths corresponding to analyses (a) to (h)	133
Table 6.3	Limiting values of the stress coefficients in run (c)	134
Table 6.4	Configurations used in the deflected flow experiments	162
Table 6.5	Observed vs. predicted runup distances for Experiments 3, 5 and 7.....	166
Table 7.1	Parameter values used in each case study	228

LIST OF FIGURES

Figure 1.1	Screen capture from a runout analysis using DAN-W	3
Figure 1.2	Flooding of Lake Saniba, Russia caused by a landslide dam.....	8
Figure 1.3	Hazard intensity map for Cheekeye Fan, British Columbia.....	9
Figure 1.4	Hazard intensity modified by deflection berms, Cheekeye Fan.....	10
Figure 1.5	Schematic definition of the fahrböschung or angle of reach.....	12
Figure 1.6	The classical sliding block model.....	14
Figure 2.1	Branching and merging of debris avalanches/flows.....	20
Figure 2.2	Idealized loading conditions on soil adjacent to an embedded retaining wall	22
Figure 2.3	Schematic illustrations of idealized (a) active and (b) passive local failure	22
Figure 2.4	Mohr circles showing the two limiting stress conditions for the idealized loading shown in Figure 2.4	23
Figure 2.5	Theoretical range of horizontal earth pressure coefficients for a range of internal friction angles	25
Figure 2.6	Total stress state on an element of material within a landslide	27
Figure 2.7	Hypothetical Mohr circle representation of the 3D stress state shown in Figure 2.6.....	27
Figure 2.8	Schematic illustration showing entrainment of path material by both plowing at the margins and erosion/scour at the base	29
Figure 2.9	Aerial view of the 1965 Hope rock avalanche	30
Figure 2.10	Depth of bed instability predicted using Equations [2-4] and [2-5].....	32
Figure 2.11	The Tsing Shan debris flow.....	34
Figure 2.12	Energy grade line analysis of a single sliding block	35
Figure 2.13	Energy grade line analysis of two sliding blocks	37
Figure 2.14	Sliding block model demonstrating the influence of a change in basal material strength along the path	39
Figure 2.15	Aerial view of McAuley Creek rock avalanche	40
Figure 2.16	The distal end of a debris flow deposit near Prince Rupert, British Columbia ...	41
Figure 3.1	Eulerian vs. Lagrangian reference frames	47
Figure 4.1	Schematic illustration of the “equivalent fluid” approach.....	61
Figure 4.2	Generic orientation of the reference coordinate system	65
Figure 4.3	Orientation of the Lagrangian reference coordinate system used in DAN3D.....	72
Figure 4.4	Normalized total stress state on an element of material within a landslide.....	75
Figure 4.5	Relationships between frictional parameters.....	79
Figure 5.1	A physical interpretation of SPH.....	90
Figure 5.2	Comparison of different interpolating kernels.....	93
Figure 5.3	Plane strain measurement using strain gauge rosettes.....	96
Figure 5.4	Example of a DAN3D incremental tangential strain interpolation	98
Figure 5.5	Example of a DAN3D incremental tangential strain interpolation using the simplified method.....	100
Figure 5.6	Hypothetical Mohr circle representation of the normalized 3D stress state shown in Figure 4.4	102
Figure 5.7	Flowchart showing the main functions in DAN3D	113
Figure 5.8	Example of a DAN3D initial particle distribution	115

Figure 6.1	Analyses of the dam-break problem.....	124
Figure 6.2	Isometric view of initial geometry used in the slump test.....	126
Figure 6.3	Initial particle locations used in the slump test	126
Figure 6.4	Isometric view of interpolated initial geometry	127
Figure 6.5	Results of the slump test.....	128
Figure 6.6	Section through the final deposit.....	128
Figure 6.7	Initial configuration of the parametric analyses	131
Figure 6.8	Parametric analyses varying the number of particles and the particle smoothing coefficient	141
Figure 6.9	Parametric analyses varying the internal friction angle.....	145
Figure 6.10	Prevailing longitudinal and lateral stress states recorded at each time interval during run (c).....	147
Figure 6.11	Parametric analyses varying the dimensionless stiffness coefficient	148
Figure 6.12	Parametric analyses varying the velocity smoothing coefficient	150
Figure 6.13	Parametric analyses varying the basal rheology and its parameters.....	152
Figure 6.14	Parametric analyses neglecting centripetal acceleration and varying the entrainment growth rate.....	154
Figure 6.15	Erosion map corresponding to run (b) shown in Figure 6.14b.....	155
Figure 6.16	Initial configuration of the hypothetical particle channelization tests.....	156
Figure 6.17	Particle positions in channel at time $t = 30$ s.....	157
Figure 6.18	Initial configuration of the tests based on experiments presented by Gray et al. (1999) and Wieland et al. (1999).....	159
Figure 6.19	Simulation of the straight runout chute experiment presented by Gray et al. (1999).....	160
Figure 6.20	Photograph of the experimental apparatus	162
Figure 6.21	Calibrated simulation of Experiment 1.....	164
Figure 6.22	Comparisons of observed and predicted maximum runup distances	165
Figure 7.1	Oblique aerial view of the Frank Slide.....	170
Figure 7.2	Calibrated simulation of the Frank Slide.....	174
Figure 7.3	Oblique aerial view of the Val Pola landslide deposit.....	176
Figure 7.4	Calibrated simulation of the Val Pola landslide	179
Figure 7.5	Plot of the maximum simulated flow velocities recorded along the path	180
Figure 7.6	View of the source slope of the Cervinara landslide	182
Figure 7.7	Simulation of the Cervinara landslide	184
Figure 7.8	Two simulations of the Quindici landslide.....	187
Figure 7.9	View of the fan apex of the Quindici landslide.....	188
Figure 7.10	Oblique aerial views of the Nomash River rock slide –debris avalanche	189
Figure 7.11	Simulation of the Nomash River landslide.....	192
Figure 7.12	Comparison of simulated and measured trimlines	193
Figure 7.13	Erosion map corresponding to the simulation shown in Figure 7.11	193
Figure 7.14	View of the source slope of the Nomash River landslide.....	194
Figure 7.15	Simulation of the Nomash River landslide neglecting entrainment.....	195
Figure 7.16	Location of the June 8, 2002 Zymoetz River rock slide – debris flow.....	196
Figure 7.17	Aerial view of the Zymoetz River rock slide – debris flow	196
Figure 7.18	Plot of landslide volume vs. the tangent of the fahrböschung.....	197
Figure 7.19	Enlarged aerial view of the proximal part of the path	198

Figure 7.20	View from toe of source slope toward source area	200
Figure 7.21	Rock avalanche deposits on top of snow in the upper part of the cirque basin.	200
Figure 7.22	Oblique aerial view of the cirque basin	202
Figure 7.23	Enlarged aerial view of the distal part of the path.....	202
Figure 7.24	Oblique aerial view up the channel towards the source area.....	204
Figure 7.25	Oblique aerial view of the large fan created by the landslide	205
Figure 7.26	Calibrated simulation of the Zymoetz River landslide.....	208
Figure 7.27	Plot of the maximum simulated flow velocities recorded along the path	209
Figure 7.28	Simulated trimline and distribution of material after 600 s, superimposed on the aerial photograph	210
Figure 7.29	Aerial view of the McAuley Creek landslide	213
Figure 7.30	Simulation of the McAuley Creek landslide	216
Figure 7.31	View of the main deposit of the Kolka Glacier event	218
Figure 7.32	Calibrated simulation of the Kolka event.....	221
Figure 7.33	Matrix of maximum velocity plots	223
Figure 7.34	Comparison of arrival times along the path	224

LIST OF SYMBOLS

A	area
b	bed depth; maximum erosion depth; depth of instability
B	particle smoothing coefficient
c	constant shear strength
C	consequence; probability of loss given an occurrence
C	Chezy coefficient
C	velocity smoothing coefficient
D	stiffness coefficient
E	Young's elastic modulus
E_s	entrainment growth rate; displacement-dependent rate of material entrainment
E_t	erosion velocity; time-dependent rate of material entrainment at the base
f	Voellmy friction coefficient
f	value of a generic function
g	gravitational acceleration
\mathbf{g}	gravitational acceleration vector
h	flow depth
H	difference in elevation between crest of source and toe of deposit
i	central column/particle identification number
j	neighbouring column/particle identification number
k	stress coefficient ($k_x, k_y, k_{xy}, k_{xz}, k_{yx}, k_{yz}, k_{zx}$ and k_{zy})
k	node identification number
k_a	active earth pressure coefficient
k_p	passive earth pressure coefficient
ℓ	smoothing length
L	length of the horizontal projection of the streamline of motion
m	mass
n	Manning roughness coefficient
n	number of neighbouring particles within a local radius of influence
N	total number of particles
$P_{(L)}$	annual frequency of landslide occurrence
$P_{(LOL)}$	annual probability that a specific person will lose their life
$P_{(S:L)}$	spatial probability of impact given a landslide occurrence
$P_{(T:S)}$	temporal probability of impact given spatial impact
$R_{(prop)}$	risk to property; annual loss of property value
R	bed-normal radius of curvature of the path in the direction of motion
\mathbf{r}	position vector
r^2	correlation coefficient
r_u	pore pressure ratio; ratio of pore fluid pressure to total normal stress

s	distance
t	time
T	stress tensor
u	pore fluid pressure
v	velocity
\bar{v}	depth-averaged velocity
\mathbf{v}	velocity vector
V	volume
$V_{(D:T)}$	vulnerability; the probability of death given impact
$V_{(prop:T)}$	vulnerability; the degree of loss given impact, on an increasing scale of 0 to 1
W	interpolating kernel
α	inclination/angle of the bed from horizontal
α_d	deflection plane true dip angle
β	angle between original and corrected particle velocity vectors
δ	Dirac delta function
δ	deflection angle
Δ	increment operator
ϵ	normal strain
ϕ	dynamic basal friction angle
ϕ_b	bulk basal friction angle
ϕ_i	internal friction angle
γ	unit weight
γ	engineering shear strain
μ	dynamic viscosity
$\mu_{Bingham}$	Bingham viscosity
θ	angle in local $x - y$ plane counter-clockwise from positive x -axis
ρ	material density
σ	total normal stress
σ'	effective normal stress
σ'_h	effective horizontal normal stress
σ'_v	effective vertical normal stress
τ	shear stress
τ_f	shear strength
τ_{yield}	Bingham yield stress
ν	Poisson's ratio
ξ	Voellmy turbulence parameter
ζ	momentum correction coefficient
∇	gradient operator
\cdot	dot product
\otimes	tensor product

ACKNOWLEDGEMENTS

First, I have to thank my lovely wife and best friend, Samantha Ward, for her amazing support and patience. Thanks also to our families, who have been incredibly supportive of both of us and helped make this little adventure possible.

I am very grateful to have had the opportunity to work closely with Oldrich Hungr, who has been a fantastic advisor. His technical yet practical approach to complex subjects has been particularly influential, and I think that influence is quite obvious in this thesis. He also provided generous funding for a number of conference trips, including to exotic places like Brazil, Nepal and Saskatchewan. Thanks also to my thesis and examining committee members, Dave McClung, Roger Beckie, Garry Clarke, Roland Stull and Scott Dunbar for their encouragement and for all of the tough questions and stimulating discussions that led to many improvements. Special thanks to my external examiner, Barry Voight, for a thorough and truly constructive review.

I would also like to thank another great mentor, Erik Eberhardt, and my officemates, Jordan Severin, Lara Fletcher, Mike Scholz, Jonathan Mackin, Andrea Cade and Alex Strouth, for their input, friendship and general tolerance. Several other friends, colleagues and collaborators contributed to this work in a number of ways, including Steve Evans, Réjean Couture, Bob Gerath, Marina Pirulli, Claudio Scavia, Paola Revellino, Francesco Guadagno, Giovanni Crosta, Heike Willenburg, Suzanne Chalindar, Nikolai Hungr, Nichole Boulton, Marc-Andre Brideau, Doug Stead, Jim Schwab, Marten Geertsema, Kevin Turner, Rick Guthrie, Dana Ayotte, Olga Tutubalina, Sergey Chernomorets, Dmitry Petrakov and Valeriy Drobyshev. Their contributions are gratefully acknowledged.

Finally, this work was funded by the Natural Sciences and Engineering Research Council of Canada (NSERC). The Department of Earth and Ocean Sciences was instrumental in securing this and other funding, and also provided a terrific work environment. I would especially like to thank Alex Allen for all of her help over the past few years.

To Samantha

1 INTRODUCTION

1.1 Introduction

Flow-like landslides such as rock avalanches, debris avalanches, debris flows and flow slides travel at extremely rapid velocities and can impact large areas, often far from their source (cf., Hungr et al. 2001 for landslide classification). When the source of a potentially mobile landslide is identified, stabilization is not always a practical option and the consequences of failure must be considered. The extent of the potential impact area, the distribution of intensity (i.e., destructiveness) within it and the possibility of secondary effects, such as landslide-generated displacement waves, must all be estimated. The prediction of landslide motion and its effects is called runout analysis. As an essential component of landslide risk assessment, it can provide valuable guidance for land use planning decisions and the development of mitigation strategies, including the design of protective structures.

There is an increasing need for effective methods of performing landslide runout analysis, and this is the general motivation for this thesis. Worldwide, the annual cost of landslides, in terms of both life and economic losses, is rising, at least in part due to increasing exposure of people and property as development continues to push into marginally-stable land (Petley et al. 2005). These methods must be quantitative and as accurate, objective and accessible as possible. Quantification facilitates communication and rational decision making within a risk-based framework. Accuracy is required to minimize underestimation but also overestimation of risk, as decisions that are too conservative, particularly involving risk avoidance through land sterilization, can be extremely costly (e.g., Hungr 2004). Objectivity helps produce results that are repeatable and defensible, factors that promote widespread use and development of the methods in practice. In terms of accessibility, the methods must be made available to practitioners and should be as simple and as easy to understand as possible. Simplicity facilitates application of the methods as well as interpretation of the results, a step in the runout analysis process when subjective judgment plays an important role.

Continuum dynamic modelling of landslide motion has emerged as a method that may be able to satisfy all of these criteria. The spatial distribution of quantitative landslide hazard intensity parameters, such as flow velocity and depth (Hungr 1997), which are required to perform the calculations at each time step, can be easily output. Dynamic models can be developed into user-friendly software and experiences can be shared among users to aid in further development. Models with a minimal number of adjustable input parameters are simple and can be reasonably objective. Finally, dynamic modelling is potentially more accurate than traditional empirical methods because the unique geometry and mechanics of each case can be accounted for explicitly.

As a result, a large number of dynamic models have been proposed or are currently in development. Most are based on established hydrodynamic theory, with some landslide-specific modifications. The model proposed by Hungr (1995), DAN, simulates motion along a user-prescribed 2D path and includes several unique features to account for the most important characteristics of extremely rapid landslides, including the effects of internal strength, material entrainment and variations in rheology both within the slide mass and along the path (Figure 1.1). It is based on a highly efficient Lagrangian solution of the depth-averaged equations of motion for an "equivalent fluid" (Hungr 1995), a hypothetical material governed by simple internal and basal rheologies. The equivalent fluid represents an idealization of the actual landslide material, which in reality may be very complex and difficult to model.

DAN is a calibration-based model, which means that the appropriate rheological parameters must be constrained by trial-and-error back-analysis of previous real landslides. The trials are judged in terms of their ability to simulate the bulk characteristics of the prototype event, including the total travel distance, the distribution of deposits and the velocities estimated along the path. A large number of case studies have been analyzed and a valuable database of calibrated parameters has been created (e.g., Hungr and Evans 1996; Ayotte and Hungr 2000; Hungr et al. 2002; Revellino et al. 2004; Pirulli et al. 2004). For landslides of similar type and scale, the calibrated parameters are generally well-constrained, suggesting that accurate, first-order runout prediction is possible.

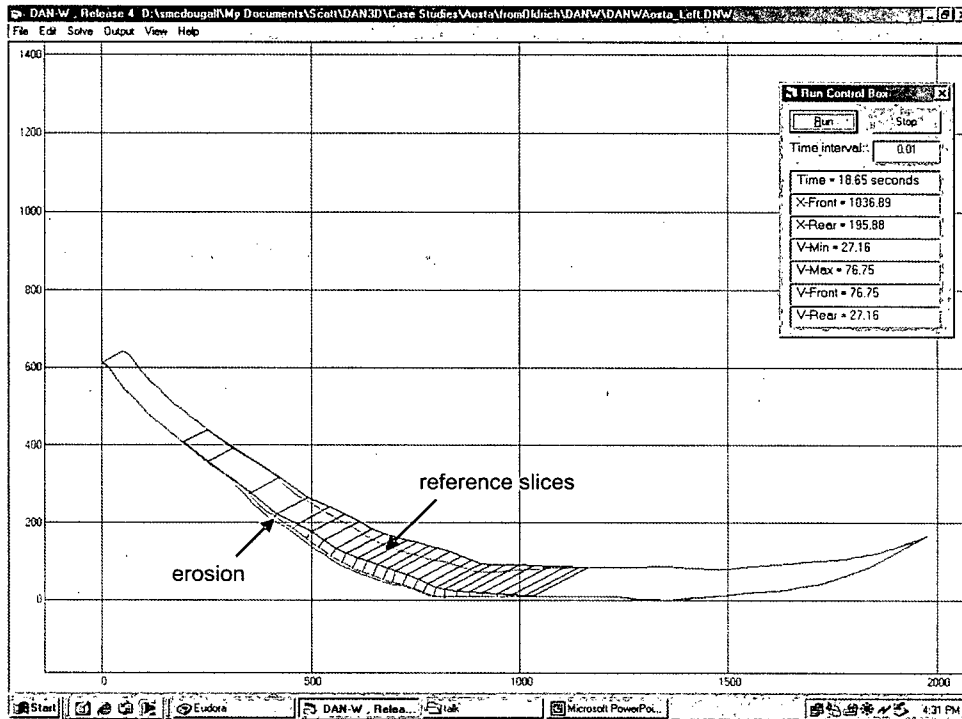


Figure 1.1. Screen capture from a runout analysis using DAN-W, the Windows-based commercial version of DAN. The depth-averaged momentum balance calculations are performed at each reference slice. Due to internal strength, the prevailing longitudinal strain at each reference slice (indicated by red for compression and black for extension) influences the magnitude of the local internal pressure gradient, which governs spreading. Mass balance, including the addition of material entrained from the path, is maintained between each pair of reference slices. Changes in rheology, in this example coinciding with entrainment, are indicated by different colours along the path.

However, DAN has three inherent limitations, which together comprise the specific motivation for this thesis. First, it requires the user to input the profile and width of the landslide path. This is not usually a problem during back-analysis, but the path direction and width can be very difficult to predict during forward-analysis, especially when the terrain is complex. Branching of a slide mass is particularly difficult to predict and to model. Second, it does not explicitly account for the energy losses that occur due to changes in direction and confinement along the path. Instead, these losses are accounted for implicitly with the calibrated resistance parameters, and so these parameters may only be valid for landslides involving similar path morphologies. Third, lateral variations in intensity are not accounted for, as the governing equations of motion apply uniformly across the width of the flow. This means that intensity may be inaccurately estimated at different locations across the path. For

example, the flow depths and velocities at the lateral margins are assumed to be the same as at the central streamline of the flow, when in fact they may be much lower. The use of width-averaged intensity values in the calculations can also influence the model results; rheological models that incorporate velocity and/or depth-dependence are particularly sensitive.

1.2 Purpose, scope and structure of this thesis

To address the limitations above, the focus of this thesis is the development of an extension of DAN for the simulation of landslide motion across 3D terrain. The overall objective is to create a new model that retains the key features of the original, but eliminates the need to input a pre-determined path direction and width, accounts explicitly for energy losses that are caused by complex topography and simulates a proper spatial distribution of landslide intensity. Several innovations are included in the new model to achieve this objective, the most obvious of which is the adaptation of a numerical method that was originally developed for the simulation of astrophysical phenomena. As such, while the new model is based conceptually on DAN, it is substantially original.

This thesis covers the background, theory, methodology and preliminary evaluation of the new model, DAN3D. The model described here is the latest version as of May 2006. Additional improvements, testing and calibration continue, but the many adjustments made during the course of development are not described in detail. I hope that this thesis can serve as a relatively concise reference for continued development of the model by others. The ultimate goal of this research, the creation of a substantial database of calibrated input parameters that can be used with DAN3D for prediction, is still far-off and will require much more work.

It should be noted that the dynamics of extremely rapid, flow-like landslides and snow avalanches are closely related. While this thesis is focused on landslide modelling, many concepts are derived from the snow avalanche literature and a distinction is not always

explicitly made. It may be possible to apply DAN3D to snow avalanche modelling, but this possibility is not investigated in this thesis.

The remainder of this chapter outlines the basic concepts of runout analysis in the framework of landslide risk assessment and the use of dynamic modelling as a tool for this purpose. Additional background information and basic theory are covered in Chapters 2 and 3; the objectives guiding the design of DAN3D, which are central to this thesis, are described in Chapter 2 and previous work is outlined in Chapter 3 in the context of these objectives. Chapters 4 and 5 comprise the detailed theory and methodology behind the model; the governing equations of motion are derived in Chapter 4 and the numerical method used to solve these equations is described in Chapter 5. Chapters 6 and 7 comprise a preliminary evaluation of the model; its performance is validated and its basic behaviour is demonstrated in Chapter 6 using a combination of analytical, laboratory and parametric tests and its ability to simulate real landslides is demonstrated in Chapter 7 using a series of back-analyses, which form the basis for a more thorough calibration. Finally, conclusions and recommendations for future work are presented in Chapter 8. Parts of each of these chapters have been published in the following papers:

McDougall, S. and Hungr, O. 2003. Objectives for the development of an integrated three-dimensional continuum model for the analysis of landslide runout. *In Proceedings of the 3rd International Conference on Debris-flow Hazards Mitigation: Mechanics, Prediction and Assessment, Davos. Edited by D. Rickenmann and C.L. Chen. Millpress, Rotterdam. pp. 481-490.*

McDougall, S. and Hungr, O. 2004. A universal model for 3-D runout analysis of landslides. *In Proceedings of the 9th International Symposium on Landslides, Rio de Janeiro. Edited by W.A. Lacerda, M. Ehrlich, S.A.B. Fontoura and A.S.F. Sayão. A.A. Balkema, London, pp. 1485-1488.*

McDougall, S. and Hungr, O. 2004. A model for the analysis of rapid landslide motion across three-dimensional terrain. *Canadian Geotechnical Journal*, 41: 1084-1097.

McDougall, S. and Hungr, O. 2005. Dynamic modelling for the design of debris flow deflection structures. *In Proceedings of the 58th Canadian Geotechnical Conference and 6th Joint CGS and IAHC-CNC Groundwater Specialty Conference, Saskatoon.*

McDougall, S. and Hungr, O. 2005. Dynamic modelling of entrainment in rapid landslides. *Canadian Geotechnical Journal*, 42: 1437-1448.

McDougall, S., Boulton, N., Hungr, O., Stead, D. and Schwab, J.M. 2006. The Zymoetz River landslide, British Columbia, Canada: description and dynamic analysis of a rock slide – debris flow. *Landslides* (in press). (with kind permission of Springer Science and Business Media)

Hungr, O., McDougall, S. and Bovis, M. 2005. Entrainment of material by debris flows. Chapter 7 *In Debris-flow Hazards and Related Phenomena. Edited by M. Jakob and O. Hungr.* Praxis-Springer Publishers, Heidelberg. pp. 135-158. (with kind permission of Springer Science and Business Media)

1.3 Runout analysis in the framework of landslide risk assessment

Although the basic framework of landslide risk assessment is widely understood and applied, a consensus on terminology and notation has not yet emerged. The method adopted in this section and throughout this thesis is based on Fell et al. (2005), with slight modifications to terminology and notation. Alternatives have been proposed by many others, including Wise et al. (2004). The purpose of this section is not to endorse an existing method nor propose a new method, but simply to place runout analysis in the context of more or less common landslide risk assessment practice.

Risk to property, $R_{(prop)}$, can be defined as the annual loss of property value and mathematically expressed as:

$$[1-1] \quad R_{(prop)} = P_{(L)} \times P_{(S:L)} \times P_{(T:S)} \times V_{(prop:T)} \times E$$

where $P_{(L)}$ is the annual frequency of landslide occurrence, $P_{(S:L)}$ is the probability of the landslide reaching a specific location (the spatial probability of impact given that a landslide occurs), $P_{(T:S)}$ is the probability that the element at risk is at the specified location at the time of the event (the temporal probability of impact given that the landslide reaches the specified location), $V_{(prop:T)}$ is the vulnerability of the element at risk to the landslide at the specified

location (the degree of loss given impact, on an increasing scale of 0 to 1) and E is the value of the element at risk.

Similarly, the annual probability that a specific person will lose their life, $P_{(LOL)}$, can be mathematically expressed as:

$$[1-2] \quad P_{(LOL)} = P_{(L)} \times P_{(S:L)} \times P_{(T:S)} \times V_{(D:T)}$$

where $V_{(D:T)}$ is the vulnerability of the person to the landslide at the specified location (the probability of death given impact).

Runout analysis provides information for estimating both the spatial probability of impact, $P_{(S:L)}$, and vulnerability, $V_{(prop:T)}$ and $V_{(D:T)}$, and is therefore an important component of risk analysis.

1.3.1 Estimating the spatial probability of impact

Runout analysis can be used to predict the extent of the area impacted directly by landslide debris. The most common question is: How far will the landslide travel? Equally important, however, is the potential lateral extent of impact.

Areas outside of the direct impact area can also be affected. Runout analysis can help to identify and characterize these secondary effects, such as flooding caused by landslide-generated displacement waves or landslide dam formation and outburst. For example, a landslide dam can cause flooding of property upstream of the direct impact area (Figure 1.2). Runout analysis can help to identify the potential for a landslide dam and may also be used to predict its depth, which can in turn be used to constrain the extent of upstream inundation. Similarly, landslides can sever transportation links and cut off access to resources that may be located far from the direct impact area. Runout analysis can help to identify existing infrastructure at risk and aid in route selection and design of new infrastructure.

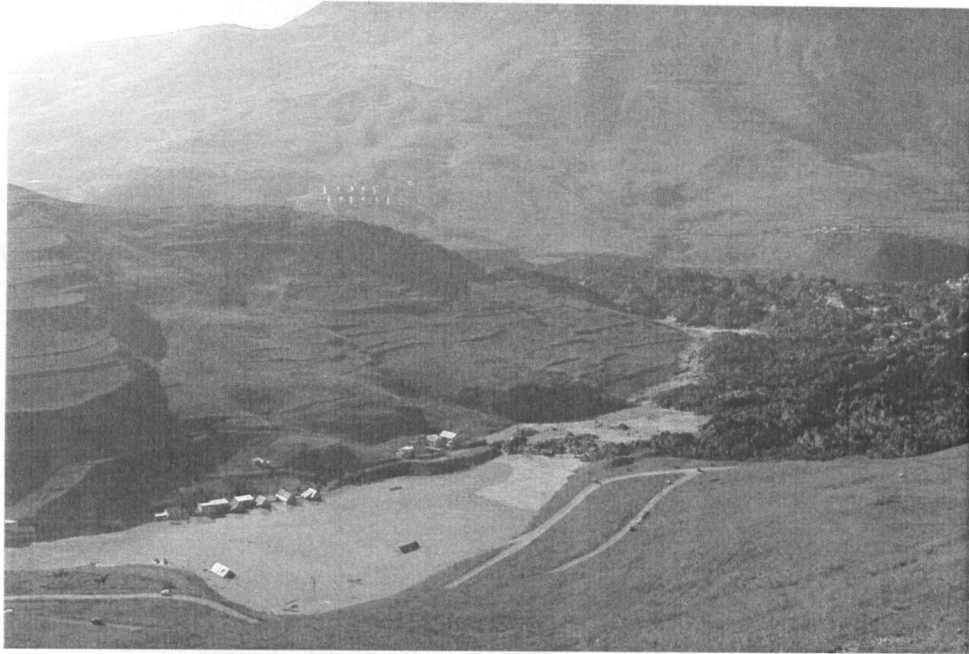


Figure 1.2. Flooding of Lake Saniba caused by a landslide dam in the Genaldon River valley, North Ossetia, Russia. (Photograph taken on September 22, 2002, two days after the event, courtesy of Mr. Igor Galushkin, Ministry of Natural Resources, North Ossetia, Russia)

1.3.2 Estimating vulnerability

The vulnerability of an element at risk is a function of both its robustness and the intensity, or destructiveness (Hungry 1997), of the landslide. For example, a concrete structure can be more robust than a comparable wooden structure, and therefore less vulnerable to a small debris flow. At the same time, both structures are relatively more vulnerable to a large debris flow, which has a relatively higher intensity.

As defined by Hungry (1997), intensity is a measure of the destructive potential of a landslide as a function of position and can be characterized by a number of spatially distributed parameters. The basic intensity parameters include flow velocity, flow density, flow depth, erosion depth and deposit depth. Runout analysis can be used to map the distribution of these parameters within the direct impact area (Figure 1.3). Additional parameters derived from the basic intensity parameters, such as discharge, impact pressure and kinetic energy, provide additional information for estimating vulnerability.

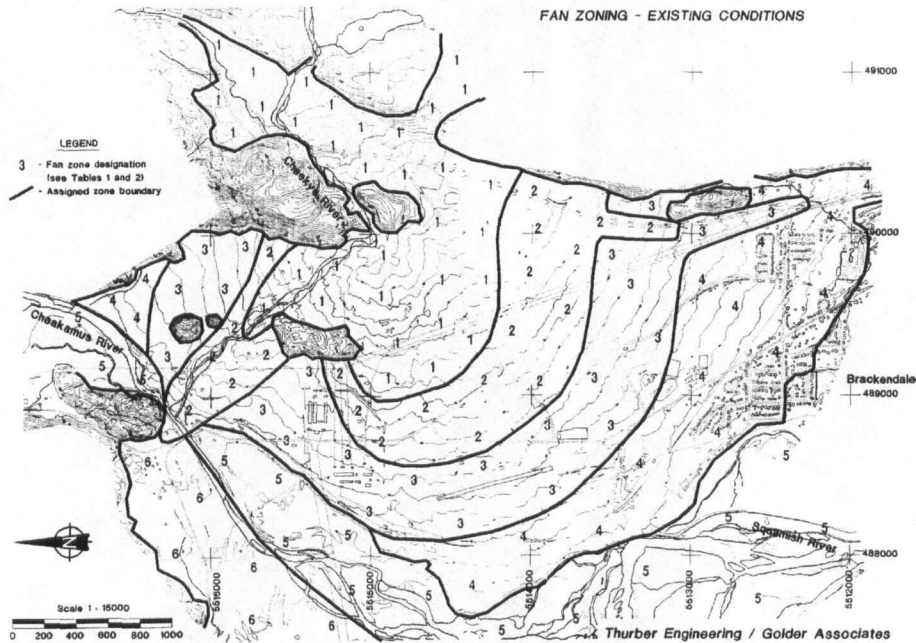


Figure 1.3. Hazard intensity map for Cheekeye Fan, British Columbia. The numbered fan zone designations refer to relative hazard intensity on a diminishing scale of 1 to 6, based on estimated flow velocities, flow depths and deposit depths at each location. (Image from Thurber Engineering Ltd. and Golder Associates Ltd. 1993)

1.3.3 Designing protective measures

Intensity parameters estimated by runout analysis are also useful for the design of protective measures, which can be used to mitigate/modify landslide risk. Protective measures include passive measures such as warning systems and active measures such as catch fences, check dams, debris storage basins and deflection structures. Runout analysis can be used to position these measures effectively and dimension them appropriately, and comparative analyses can be performed to help identify the most effective alternative.

For example, debris flow deflection structures are often used to confine flow to an established channel or divert it to a safer location and must be built high enough to prevent overtopping by extremely rapid debris flow surges. A number of runout analysis methods are available for estimating superelevation of flow through bends or against obstacles like

deflection berms, and these methods can be used to dimension such structures. At the same time, the effectiveness of possible alternative berm locations can be compared (Figure 1.4).

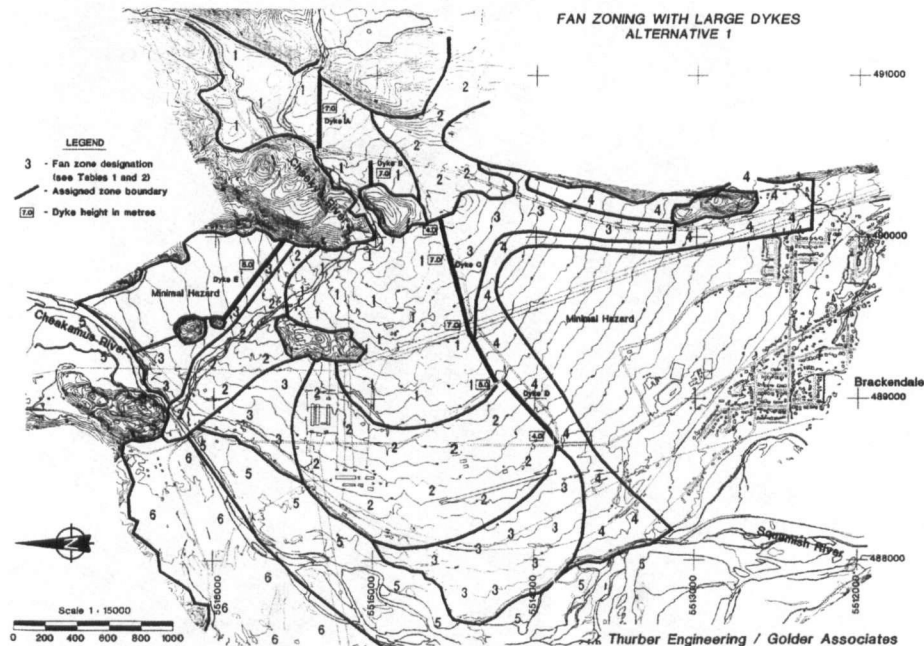


Figure 1.4. Hazard intensity modified by deflection berms, Cheekye Fan, British Columbia. The numbered fan zone designations refer to relative hazard intensity on a diminishing scale of 1 to 6, based on estimated flow velocities, flow depths and deposit depths at each location. Compare with Figure 1.3. (Image from Thurber Engineering Ltd. and Golder Associates Ltd. 1993)

1.4 Continuum dynamic modelling as a runout analysis method

Runout analysis can be both qualitative and quantitative. The simplest qualitative method is to estimate the potential direction of motion on a topographic map by following the direction of steepest descent from the source area and subjectively accounting for spreading, superelevation and possible avulsion in channel bends. The distal limit of motion and the distribution of intensity within the impact area can then be estimated based on experience and judgment. Quantitative runout analysis methods are less subjective and can be broadly classified as either empirical or analytical.

1.4.1 Empirical methods

Empirical methods are based on historical data trends, although the resulting statistical correlations are often justified by physical reasoning. The most common method is based on an apparent inverse relationship between landslide volume and fahrböschung, and several linear regression equations have been proposed (e.g., Scheidegger 1973; Li 1983; Corominas 1996). Introduced by Heim (1932), the fahrböschung, also known as the angle of reach, is the inclination of the line connecting the crest of the source with the toe of the deposit, as measured along the approximate streamline of motion (Figure 1.5). The fahrböschung is considered an index of the efficiency of energy dissipation, and so is inversely related to mobility. Similar correlations between volume and other simple mobility indices have been proposed (e.g., Hsu 1975; Hungr 1981; Davies 1982; Rickenmann 1999). Given an estimated source location, volume and path direction, these methods provide estimates of the distal limit of motion.

Methods based on volume balance between entrainment and deposition of material along the path, suitable for landslides that derive most of their volume by entrainment, such as debris flows, also provide estimates of the distal limit of motion (e.g., Cannon 1993; Fannin and Wise 2001). In addition, the distribution of flow, erosion and deposit depths can also be estimated. These methods require the input of more detailed path morphological parameters, but therefore account explicitly for site-specific conditions.

Similar to the volume-fahrböschung approach, statistical correlations between volume and deposit area have also been proposed (e.g., Li 1983; Iverson et al. 1998). These methods provide estimates of aerial, rather than distal, extent. Other correlations have been developed for estimating certain intensity parameters, including debris flow velocity and discharge (e.g., Rickenmann 1999). These methods only provide peak intensity estimates and no additional information regarding their spatial distribution.

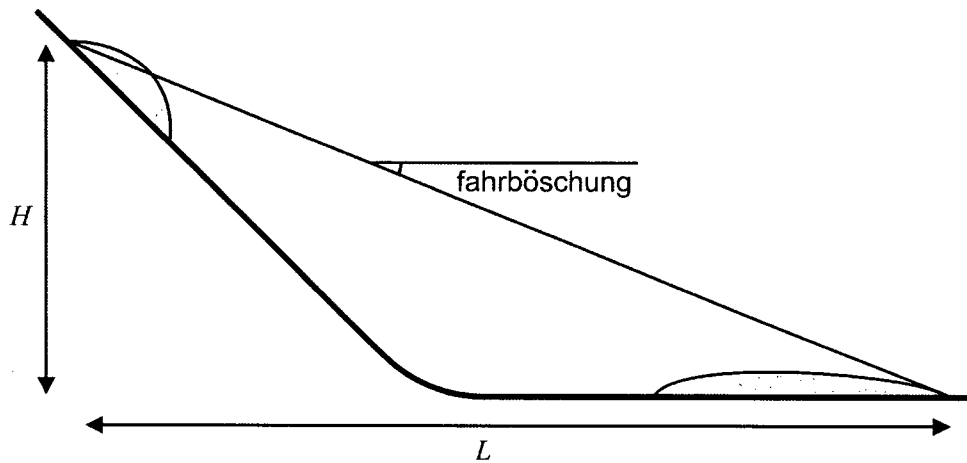


Figure 1.5. Schematic definition of the fahrböschung or angle of reach. H is the elevation difference between the crest of the source and the toe of the deposit and L is the length of the horizontal projection of the streamline connecting these two points.

Empirical methods are simple but are associated with a large amount of data scatter and are therefore difficult to apply in practice with a high degree of certainty. For example, Scheidegger (1973), Li (1983) and Corominas (1996) used linear regression to establish relationships between the base 10 logarithm of the landslide volume and the base 10 logarithm of the tangent of the fahrböschung. The correlation coefficients, r^2 , for some of these relationships are shown in Table 1.1 (for reference, a value of $r^2 \geq 0.95$ generally indicates a strong correlation). The sample stratification used by Corominas (1996), based on landslide type and path morphology, improved the strength of the correlations, but a significant amount of scatter remained. Similar sample stratification was proposed by Nicoletti and Sorriso-Valvo (1991).

One of the problems with sample stratification is that it divides an already small database into even smaller parts. Empirical/statistical models for snow avalanches are generally much better constrained because a much larger database of case histories is typically available. With improved record keeping and an expansion of the landslide case history database, the reliability of empirical landslide runout analysis methods may improve. Other empirical methods already developed for snow avalanches (e.g., Lied and Bakkehøi 1980; McClung and Mears 1991; McClung 2000) could also be investigated.

Reference	Proposed Relationship	r^2
Scheidegger (1973)	$\log_{10}(H/L) = -0.15666 \log_{10} V + 0.62419$	0.82
Li (1983)	$\log_{10}(H/L) = -0.1529 \log_{10} V + 0.6640$	0.7784
Corominas (1996) all landslides	$\log_{10}(H/L) = -0.085 \log_{10} V - 0.047$	0.625
Corominas (1996) rock falls	$\log_{10}(H/L) = -0.109 \log_{10} V + 0.210$	0.759
Corominas (1996) obstructed rock falls	$\log_{10}(H/L) = -0.091 \log_{10} V + 0.231$	0.834
Corominas (1996) unobstructed rock falls	$\log_{10}(H/L) = -0.119 \log_{10} V + 0.167$	0.924

Table 1.1. Correlation coefficients for some proposed volume-fahrböschung relationships (an example of weak correlation in empirical methods). H/L is the tangent of the fahrböschung (as shown in Figure 1.5) and V is the landslide volume. The proposed relationships and correlation coefficients are shown as originally published in the cited references, with no modifications to the number of significant figures.

1.4.2 Analytical methods

In contrast to empirical methods, analytical methods are based on mechanics and involve the solution of a governing system of equations of motion, either closed-form or numerically. Models that perform a time-wise numerical solution of the equations of motion and advance the location of the simulated landslide incrementally are known as dynamic models. The use of analytical methods is somewhat motivated by the limitations of purely empirical methods, as the unique geometry and materials involved in each case can be accounted for explicitly and a statistically-significant database of previous events is not necessarily required.

The simplest analytical model is the classical sliding block model (Figure 1.6), which is based on work-energy theory (e.g., Müller-Bernet in Heim 1932; Sassa 1988). Internal deformation and its associated energy dissipation are neglected and the landslide is treated as a lumped mass. At any point along the path, the sum of the potential energy, kinetic energy and net energy loss equals the initial potential energy. This energy balance can be visualized using the concept of energy grade lines, as shown in Figure 1.6.

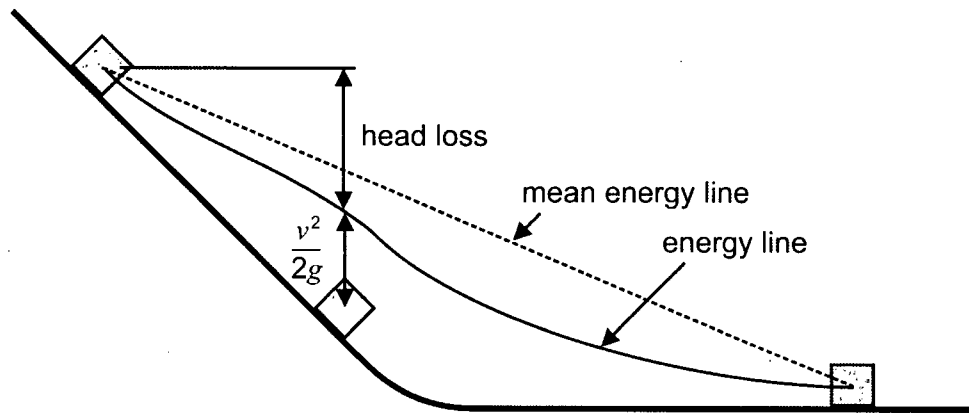


Figure 1.6. The classical sliding block model, based on work-energy theory. The concept of energy grade lines is useful for visualizing the energy balance. v is the velocity of the block, g is the vertical acceleration due to gravity and $v^2/2g$ is known as the velocity head, which is the kinetic energy of the block normalized by the product of its mass and g . The same normalization of net energy loss is known as head loss. Note that the positions of the energy lines are referenced to the centre of mass of the block and that the true energy line and mean energy line do not necessarily coincide.

Given the initial position of the centre of mass and a suitable relationship to approximate the energy losses, the position and velocity of the block can be determined at any given time. Depending on the complexity of the energy loss relationship, which may include basal resistance as well as additional influences, including momentum transfer to entrained material and momentum corrections due to abrupt slope changes (e.g., Perla et al. 1980), the model can be solved in closed-form or using a numerical method. The sliding block model has been used with various energy loss relationships by a number of workers to model both landslides and snow avalanches (e.g., Voellmy 1955; Salm 1966; Körner 1975; Pariseau 1980; Perla et al. 1980; McClellan and Kaiser 1984; McEwen and Malin 1989; Salm et al. 1990).

Strictly speaking, the sliding block model should only apply to the motion of the centre of mass of a rigid body, but in practice it is often applied to the motion of the leading edge of a deforming body, for example, to estimate runup height against an adverse slope (e.g., Mears 1981), or to back-calculate velocities based on observed runup heights (e.g., Costa 1991). More complex multi-block dynamic models have been developed to account explicitly for deformation during motion, including across 3D terrain (e.g., Kobayashi and Kagawa 1987).

Distinct element methods (Cundall and Strack 1979) have also been used to model mass movements in both 2D and 3D. Similar to multiple sliding block models, the distinct element method is a discontinuum method in which the main mass is modelled as an assemblage of discrete masses (distinct elements) that interact to simulate large-scale deformations. The distinct elements can be a variety of shapes and sizes and a variety of inter-particle and particle-bed contact relationships can be implemented, although this can require the input of certain parameters with limited physical basis. Cleary and Prakash (2004) demonstrated the potential of the method in landslide modelling, and some work has been done using the commercially-available Particle Flow Code (PFC) developed by HClasca (e.g., Calvetti et al. 2000; González et al. 2003; Pirulli et al. 2003). The method has been limited to the simulation of dry flows, but a recently-implemented fluid analysis feature in PFC may expand its applicability (cf., www.itascagc.com). Nevertheless, relatively long computing times remain a weakness (Gonzalez et al. 2003; Pirulli et al. 2003).

Much more attention has been given to the development of continuum methods, which forego the simulation of computationally-expensive small-scale interactions by concentrating on large-scale field effects. In their common depth-averaged form (cf., Chapter 4), continuum methods combine the simplicity and familiarity of sliding block models with a method to account for internal deformation that is based on established hydrodynamic theory. The same basal resistance and momentum transfer relationships that have been developed for sliding block models can be implemented in the depth-averaged continuum framework and, as in shallow water flow models, spreading is driven simply by internal stress gradients. At the same time, the relationships governing the internal stresses can be modified to account for the strength and saturation of the material using established earth pressure theory. But the method is not too complex; in its simplest form, a landslide continuum dynamic model can be governed by just two physically-based parameters: the basal and internal friction angles. A further advantage is that established continuum solution methods can be employed.

Closed-form and simple numerical continuum models have been developed for estimating debris flow runout onto fans (e.g., Takahashi and Yoshida 1979) and debris flow and snow avalanche superelevation around bends and runup against adverse slopes (e.g., Hungr et al.

1984; Hungr and McClung 1987; McClung and Mears 1995; McClung 2001). Advances in both theory and computational capacity have led to the development of a large number of continuum dynamic models, some of which, including DAN, are commercially-available. But despite this effort, the most important characteristics of extremely rapid landslide motion have not yet been captured by a single model (cf., Chapters 2 and 3).

The model proposed in this thesis is based on DAN because, despite its inherent limitations as a 2D model, it includes all of the basic features required to simulate these important characteristics, including methods to account for internal strength, material entrainment and rheology variations. It is also possible that the experience already gained using DAN, including the existing database of calibrated cases, can be transferred to the new model.

1.5 Discussion

Continuum dynamic modelling appears to have potential as a quantitative, accurate, objective and accessible method for analyzing extremely rapid landslides. The relatively large amount of attention focused on it suggests that it is widely viewed as the ultimate method, but this view ignores the relative strengths of the other approaches. Empirical/statistical methods may currently lack accuracy but are relatively easy to apply and, most importantly, are shaped by actual events. Simple analytical methods like the sliding block model may not be able to account for deformation but are also easy to apply and can provide spatial information, as well as a simple basis for a better understanding of the complex dynamics that are involved. Discontinuum methods may be relatively new and untested, but are already capable of fully 3D analysis, unlike depth-averaged continuum models, and are potentially better suited to the simulation of coarse-grained rock slides and rock avalanches, which may not strictly satisfy the continuum assumption. As a result, more than one method is likely to be useful in any given case and a multi-tool approach is recommended, which should always be supplemented by expert judgment. This thesis is not a quest for the ultimate method, just an effort to improve the state-of-the-art.

To do so, a semi-empirical approach has been adopted, in order to exploit the advantages of both empirical and analytical methods. This approach accounts for the unique geometrical and material characteristics of each case, but is shaped by the behaviour of previous events through model calibration. The micro-mechanics, which are considered intractable, are not directly considered and attention is instead focused on the large-scale characteristics of an event, which can be modelled using relatively simple rheological relationships. Still, the debate continues over whether to use the historical record to build dynamic models or simply to test them. From a purely scientific perspective, it may be a matter of what is physically correct (e.g., Iverson 2003), but from an engineering perspective, it is arguably more a matter of what works, and the utility of the semi-empirical approach has already been demonstrated using DAN and other similar models. The possibility that this approach could contribute to more informed decisions that can potentially reduce future life and property losses warrants further investigation. Besides, the two perspectives are not necessarily mutually exclusive, and work on both fronts could turn out to be mutually beneficial.

1.6 Conclusion

With continuing development of marginal areas and consequent increasing exposure of people and property to landslides, there is an increasing need for better methods of performing landslide runout analysis within the landslide risk assessment framework. Continuum dynamic modelling is one alternative that appears promising but still requires improvement. To address these needs, this thesis is focused on the development of a new continuum dynamic model that includes unique features to account for the most important characteristics of extremely rapid landslides. The objectives guiding these features are the subject of the next chapter.

2 OBJECTIVES FOR MODEL DEVELOPMENT

2.1 Introduction

Continuum dynamic models are based largely on the principles of hydrodynamics. However, while rock avalanches, debris flows, debris avalanches and flow slides all exhibit flow-like movement similar to that of fluids, landslide motion is fundamentally different from open channel water flow. Landslides travel across steep and irregular terrain, they contain earth materials that can resist internal strain, they can entrain substantial volumes of path material, their rheology can vary internally and change in the course of movement and their motion is highly unsteady and nonuniform.

Modifications to the basic shallow water equations and powerful computational methods are required in order to capture these unique characteristics. Specifically, a comprehensive model should have the following capabilities:

- 1) It should be able to simulate motion across complex 3D terrain without the need to input a pre-defined path direction or width. At the same time, it should be able to handle large displacements and deformations, including bifurcation.
- 2) It should be able to simulate strain-dependent, non-hydrostatic, anisotropic internal stresses due to 3D deformation of material with internal shear strength.
- 3) It should be able to simulate mass and momentum transfer due to entrainment of path material.
- 4) It should be able to simulate variations in rheology along the path and within the landslide.
- 5) It should be efficient and easy to use.

The first four criteria are strictly technical, as they are essential for the accurate simulation of real landslides. The last criterion is mainly practical. While it is possible to incorporate the four technical criteria into a complex model that runs on a supercomputer or for several days on a microcomputer, such a model would not be very useful in practice. The last criterion necessitates innovative approaches to satisfying the first four.

DAN3D has been designed specifically to satisfy all five criteria, which is unique among existing continuum dynamic models. Other models are reviewed in Chapter 3 in the context of these objectives. The purpose of this chapter is to describe these objectives in detail.

2.2 Objective #1: the ability to simulate motion across complex 3D terrain

Topography has a significant influence on landslide dynamics. It controls the orientation of the gravity driving stress, which dominates over the internal stresses on steep slopes. Sudden redirections due to abrupt changes in slope angle or orientation, even by minor surface irregularities, result in momentum and energy losses. Gradual slope changes also influence the dynamics, as centripetal acceleration due to local curvature of the path alters the total bed-normal stress, which in turn can affect both the internal stresses and the basal shear resistance.

Topography may or may not provide confinement. On unconfined slopes the path direction and width can be difficult to predict. A significant amount of spreading is possible and, in response to local topography, bifurcation (branching of the flow) can occur (Figure 2.1). Mergers are also possible.

Lateral spreading also dissipates energy, which can reduce the travel distance. In contrast, confinement typically decreases the slope angles at which landslides begin to deposit and increases their travel distance (Hung et al. 1984). However, sudden constrictions along the path can also cause momentum and energy losses. In confined reaches, lateral and transverse internal stresses can influence the flow depth, width and discharge. The shape of the channel bed cross-section plays an important role in the development of these stresses and, as in

fluvial hydraulics (e.g., Chow 1959), also controls the size of the basal surface area and therefore the magnitude of the basal resistance.



Figure 2.1. Branching and merging of debris avalanches/flows triggered by heavy rainfall in May 1998, Campania Region, Italy. (Photograph taken one day after the events, courtesy of Prof. Francesco M. Guadagno, University of Sannio, Benevento, Italy)

Momentum and energy losses can also occur in channel bends. At the same time, lateral and transverse internal stress changes caused by deformation can be significant and can contribute to superelevation or runup (Hungri 1995; McClung and Mears 1995; McClung 2001). Avulsion can occur when runup exceeds the height of the channel on the outside of a bend and bifurcation results when some of the flow remains in the channel. Although the path direction of a confined landslide is generally well-constrained, the locations of potential channel avulsions can be difficult to predict.

Whether confined or unconfined, landslides are sensitive to topography. In either case, they can travel extremely long distances and undergo large deformations. A model should be able to handle this behaviour without introducing numerical problems, for example, due to mesh distortion. In addition, it should be able to predict not only the distal limit of motion, but also the path direction and width and the spatial distribution of intensity parameters (cf., Chapter 1) within this area. Finally, simulation of an event should be based on a reasonably accurate representation of the actual topography.

2.3 Objective #2: the ability to simulate the influence of internal strength

Flow-like landslides (cf., Hungr et al. 2001) exhibit motion similar to fluids. In contrast to fluids, however, landslides are composed predominantly of earth materials that have internal shear strength. As a result, they can sustain internal shear stresses and resist internal strain. Complex 3D deformations may give rise to non-hydrostatic, anisotropic internal stresses that can have a significant influence on landslide dynamics. Sassa (1988) and Hutter and Savage (1988) were the first to incorporate this idea into their models, a major departure from the basic shallow water assumptions of hydrostatic, isotropic internal stresses. The concept is based on established Rankine earth pressure theory (e.g., Terzaghi and Peck 1967).

2.3.1 Rankine earth pressure theory

Rankine (1857) studied the limiting stress conditions for a vertical column of dry, cohesionless soil undergoing 1D horizontal strain (plane strain), an idealization of the loading conditions on soil adjacent to a retaining wall (Figures 2.2 and 2.3). Note that the distinction between dry and wet soil is important, as pore fluid pressures can significantly influence the stress conditions. The effective normal stress, σ' (the stress that is actually transmitted to the soil fabric), is the difference between the total normal stress, σ , and the pore fluid pressure, u . For cohesionless material, the shear strength, τ_f , is a function of σ' and the internal friction angle of the material, ϕ_i :

$$[2-1] \quad \tau_f = (\sigma - u) \tan \phi_i = \sigma' \tan \phi_i$$

The two idealized limiting stress conditions are illustrated by the Mohr circles in Figure 2.4. Since it is assumed that no shearing occurs in the horizontal and vertical planes, the effective horizontal and vertical normal stresses, σ_h' and σ_v' , are principal stresses.

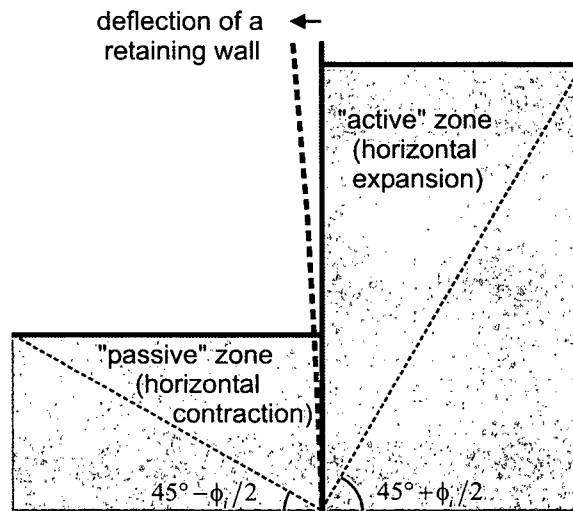


Figure 2.2. Idealized loading conditions on soil adjacent to an embedded retaining wall (wall friction is neglected and plane horizontal strain is assumed). The zones of horizontal expansion and contraction on either side of the wall are known as the active and passive zones, respectively. In each case, the dashed lines indicate the inclination of the local failure planes from horizontal.

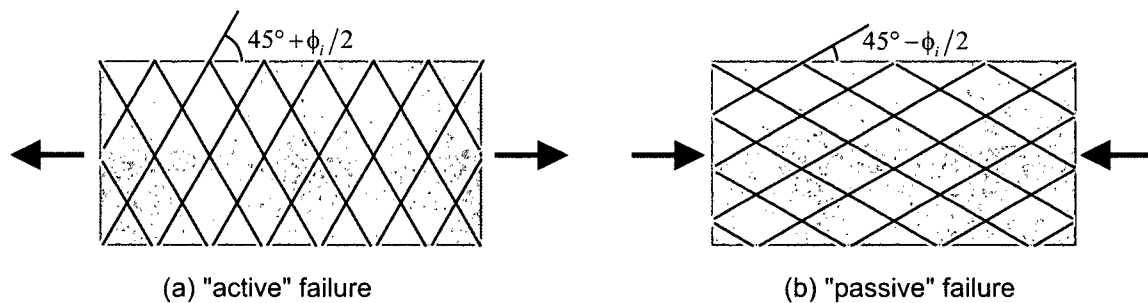


Figure 2.3. Schematic illustrations of idealized (a) active and (b) passive local failure. The arrows indicate the directions of the prevailing horizontal normal strain (not to be confused with the horizontal normal stress, which is always compressional).

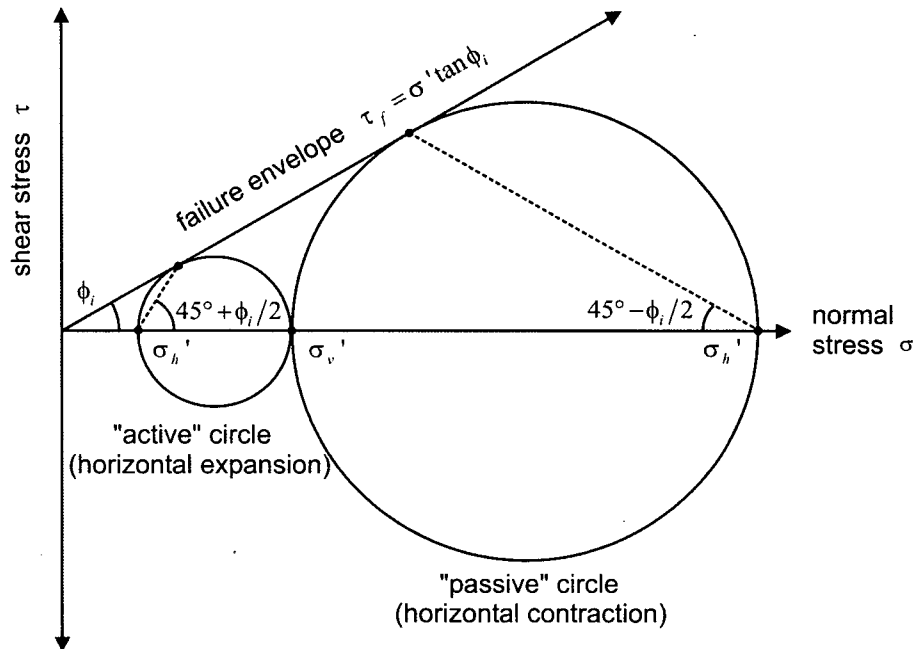


Figure 2.4. Mohr circles showing the two limiting stress conditions for the idealized loading shown in Figure 2.3. The limiting value of σ_h' is lower than σ_v' during horizontal expansion and higher than σ_v' during horizontal contraction. The dashed lines indicate the inclination of the local failure planes from horizontal.

The prevailing stress conditions are strain-dependent. During horizontal expansion, failure occurs on a set of planes inclined at $45^\circ + \phi_i/2$ from the horizontal. This is known as the “active” Rankine state and is illustrated by the small Mohr circle in Figure 2.4. In this state, the shear stresses that are mobilized on the failure planes act against gravity to resist expansion. The horizontal stress is lower than the vertical stress, and so the ratio σ_h'/σ_v' , which in this limiting condition is known as the active earth pressure coefficient, k_a , is less than one. From the geometry of the small Mohr circle in Figure 2.4:

$$[2-2] \quad k_a = \tan^2(45^\circ - \phi_i/2)$$

The response is different during horizontal contraction. Failure occurs on a set of planes inclined at a lower angle of $45^\circ - \phi_i/2$ from the horizontal. This is known as the “passive” Rankine state and is illustrated by the large Mohr circle in Figure 2.4. In this state, the shear stresses that are mobilized on the failure planes act with gravity to resist contraction. The horizontal stress is higher than the vertical stress, and so the ratio σ_h'/σ_v' , which in this limiting condition is known as the passive earth pressure coefficient, k_p , is greater than one. From the geometry of the large Mohr circle in Figure 2.4:

$$[2-3] \quad k_p = \tan^2 (45^\circ + \phi_i/2)$$

The value of the horizontal earth pressure coefficient can theoretically range between the two limiting values, k_a and k_p , depending on the prevailing horizontal strain. For example, in a dry sand with an internal friction angle of 30° , the horizontal earth pressure coefficient can theoretically range between about 0.33 and 3, a difference of almost one order of magnitude. The theoretical range for a range of internal friction angles is shown in Figure 2.5. At $\phi_i = 0^\circ$, the Mohr circles effectively collapse, and the active and passive earth pressure coefficients converge at 1. This represents the hydrostatic, isotropic conditions in a fluid, such as water, with no internal shear strength.

Rankine's theory has been validated through laboratory and field testing (e.g., Terzaghi and Peck 1967) and is widely applied in geotechnical practice. The basic implications are that lower than hydrostatic horizontal normal stresses are expected in granular soils undergoing horizontal expansion, whereas higher than hydrostatic horizontal normal stresses are expected in granular soils undergoing horizontal contraction. In effect, material that has internal shear strength can resist deformation, a characteristic that may have an important effect on landslide dynamics.

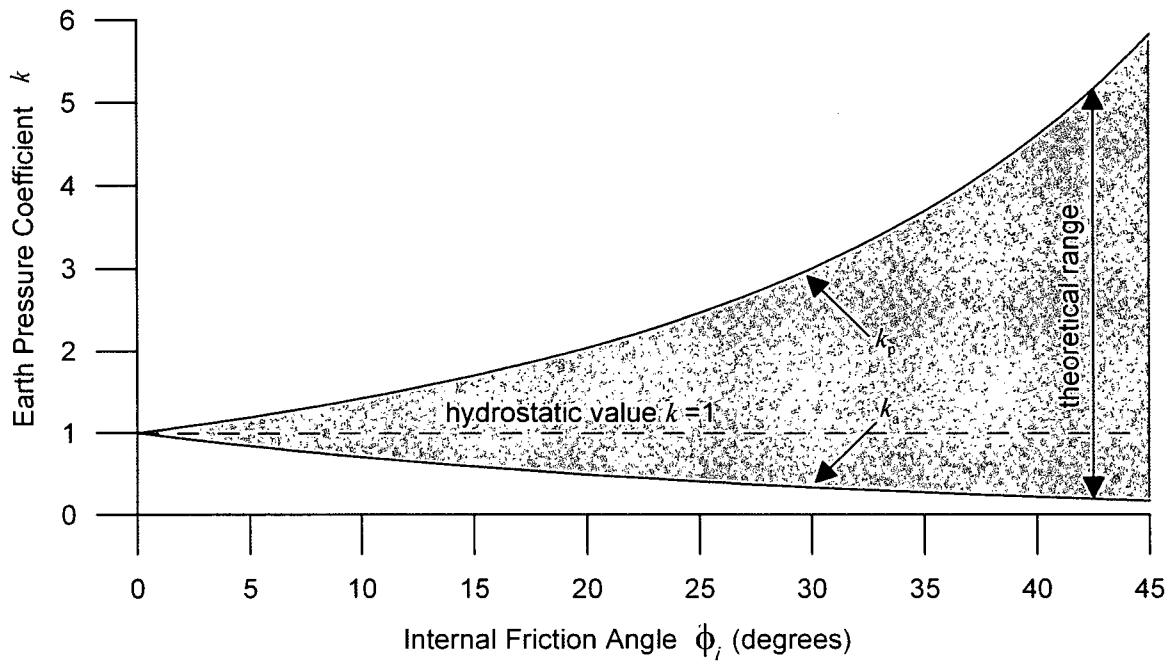


Figure 2.5. Theoretical range of horizontal earth pressure coefficients for a range of internal friction angles.

2.3.2 Strain-dependent internal stresses in landslides

The internal stresses in an extremely rapid landslide have never actually been measured, but strain-dependency can be inferred from the behaviour of experimental granular flows as well as real landslides. In particular, granular flows and landslides do not appear to spread out or contract as readily as fluids (Gray et al. 1999; Hungr 1995), a phenomenon that can be explained by the Rankine theory. In directions of flow divergence, the internal stresses may tend to an active state. The resulting sub-hydrostatic bed-parallel normal stresses translate into a decrease in the internal pressure gradients and therefore a decrease in the spreading forces. On the other hand, in directions of flow convergence, the internal stresses may tend to a passive state. The resulting super-hydrostatic bed-parallel normal stresses translate into an increase in the internal pressure gradients and therefore an increase in the spreading forces, which counteract contraction. There is also evidence that passive stresses developed during runup against an adverse slope may increase the runup distance (Hungr 1995).

However, the loading conditions within a landslide are much more complex than in Rankine's plane strain idealizations. Landslides travelling across complex 3D terrain can locally diverge or converge at varying rates in any direction. In fact, it is common for expansion in one direction to be accompanied by contraction in another. These anisotropic normal strains give rise to shear strains. Shear strains can also occur where there are sharp velocity gradients, such as near the base of a landslide or near the lateral margins of a strongly deflected or channelized flow. These shear strains are accompanied by shear stresses that are transmitted through the landslide. Additional isotropic dispersive stresses caused by fragmentation may also play a role (Davies et al. 1999; Davies and McSaveney 2002).

The complexity of the stress conditions within a landslide can be illustrated with analogy to Rankine's theory. The total stress state on an element of material within a landslide is shown in Figure 2.6. The right-handed, Cartesian reference coordinate system (x, y, z) can be arbitrarily-oriented, but for the purposes of this discussion it is useful to align z with the bed-normal direction, in which case σ_z is the total bed-normal stress, the shallow flow (cf., Chapter 4) analogue of σ_v in the simple Rankine analysis. Near the base of the flow, τ_{zx} and τ_{zy} are the basal shear stresses, which are transmitted through the landslide and therefore coupled with the other internal stresses. A corresponding hypothetical 3D stress state is illustrated by the three Mohr circles in Figure 2.7. Since shear stresses can be sustained in all three reference planes, the magnitudes and orientations of the principal stresses are not as straightforward to determine as in the simple Rankine analysis (they are, respectively, the eigenvalues and eigenvectors of the 3×3 stress tensor matrix) and probably change rapidly under continual and complex stress redistribution. But similar to the Rankine analysis, the bed-parallel normal stresses can be non-hydrostatic, and with multi-dimensional strain they can also be anisotropic.

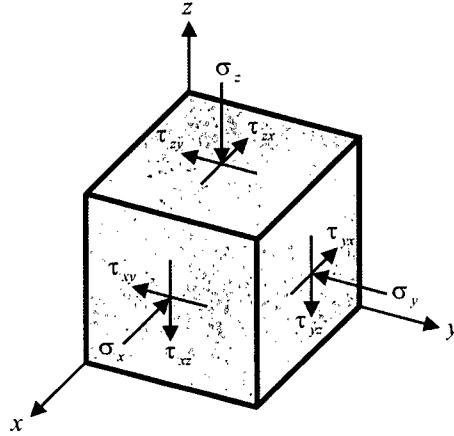


Figure 2.6. Total stress state on an element of material within a landslide. The stresses are considered positive as shown. If z is aligned with the bed-normal direction, then τ_{zx} and τ_{zy} are the basal shear stresses for an element near the base of the flow.

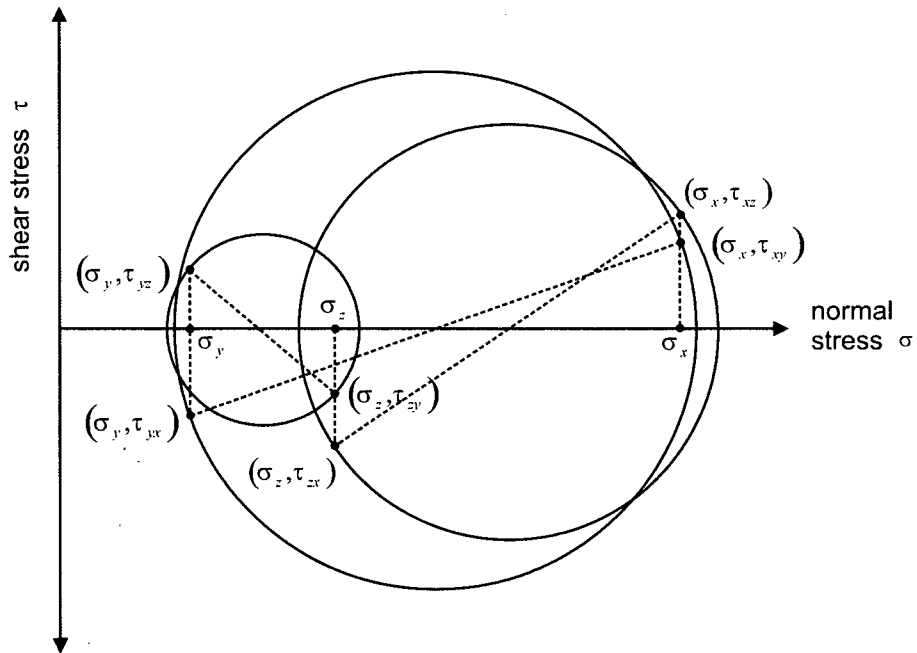


Figure 2.7. Hypothetical Mohr circle representation of the 3D stress state shown in Figure 2.6. Since shear stresses can be sustained in any of the reference planes, the stress state can be both non-hydrostatic and anisotropic, much more complex than in the simple Rankine analysis.

At the same time, the failure conditions are more difficult to define, and so no simple failure envelope can be superimposed on Figure 2.7. The internal strength of a landslide is spatially and temporally variable and not necessarily purely frictional. Even if this was the case, dynamic pore fluid pressures, which are themselves dependent on the highly dynamic loading conditions and the drainage characteristics of the material, would modify the local effective stress state and therefore the effective strength. Continual fragmentation and comminution (Sassa 2002) during motion would also change the frictional properties of the material as well as its pore pressure response. Additional causes and effects of variations in internal rheology are described in Section 2.5.

Nevertheless, the apparent effects of non-hydrostatic, anisotropic internal stresses on landslide motion should be accounted for somehow in continuum dynamic models. Active and passive style stresses should prevail in directions of diverging and converging flow, respectively. This means that models should be capable of tracking internal strains and incrementing the internal stresses accordingly. The extremely complex aspects of internal strength and associated internal stress redistribution may have to be approximated in some way. The estimated internal strain and stress states should satisfy strain and stress symmetry rules and be as independent of the chosen reference frame orientation as possible.

2.4 Objective #3: the ability to simulate entrainment

Landslide paths are typically covered by surficial deposits, sometimes several metres thick. These deposits, including colluvium, glacial till, residual soil, alluvium and organics, may be loose and have high water contents. Rapid loading by the weight and momentum of the moving landslide may cause failure and mobilization of these materials, which can have significantly different properties than the bulk of the landslide material. Entrainment of this material increases the volume, alters the composition and consequently may enhance the mobility of a landslide, which can significantly influence the size of its potential impact area. This can be an important characteristic of rapid landslides at any scale, including debris avalanches, debris flows, flow slides and rock avalanches. Dynamic models should be

capable of simulating both volume and rheology changes due to entrainment, which requires an understanding of actual entrainment mechanisms.

2.4.1 Mechanisms of path material mobilization

Rapid stress changes causing failure of path material can occur either at the margins or at the base of a rapid landslide (Figure 2.8). At the margins, landslides can plow into and displace path material. Plowing may be a dominant mechanism at the flow front when there is a rapid decrease in slope angle in the direction of motion, for example, at the base of a steep slope. The displaced material may not necessarily become entrained by the main landslide mass. During the Frank Slide, for example, laterally displaced alluvium caused most of the damage in the town itself (McConnell and Brock 1904; Cruden and Hungr 1986). Material displaced forward may similarly form a distinct flow front, or can be accreted to the main flow front or overtaken and entrained by the main mass. The typically fine-grained splash zones that surround the margins of many rock avalanche deposits (e.g., Buss and Heim 1981; Cruden and Hungr 1986; Voight and Sousa 1994; Abele 1997; Orwin et al. 2004) are often evidence of plowing. These zones can extend some distance from the main deposit, contain large fragments of the main debris and may be the source of distal mud or debris flows. An example is shown in Figure 2.9. As in snow avalanche dynamics (e.g., Gauer and Issler 2004), plowing is an important but complex mechanism that requires further research.

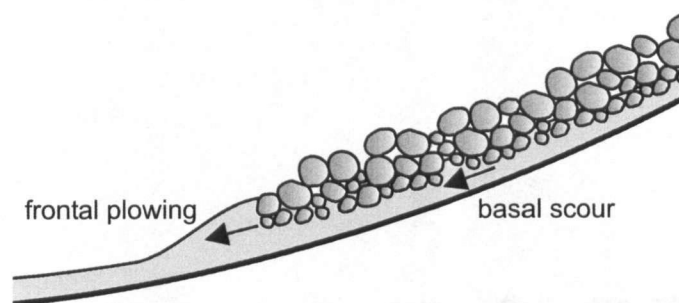


Figure 2.8. Schematic illustration showing entrainment of path material by both plowing at the margins and erosion/scour at the base.

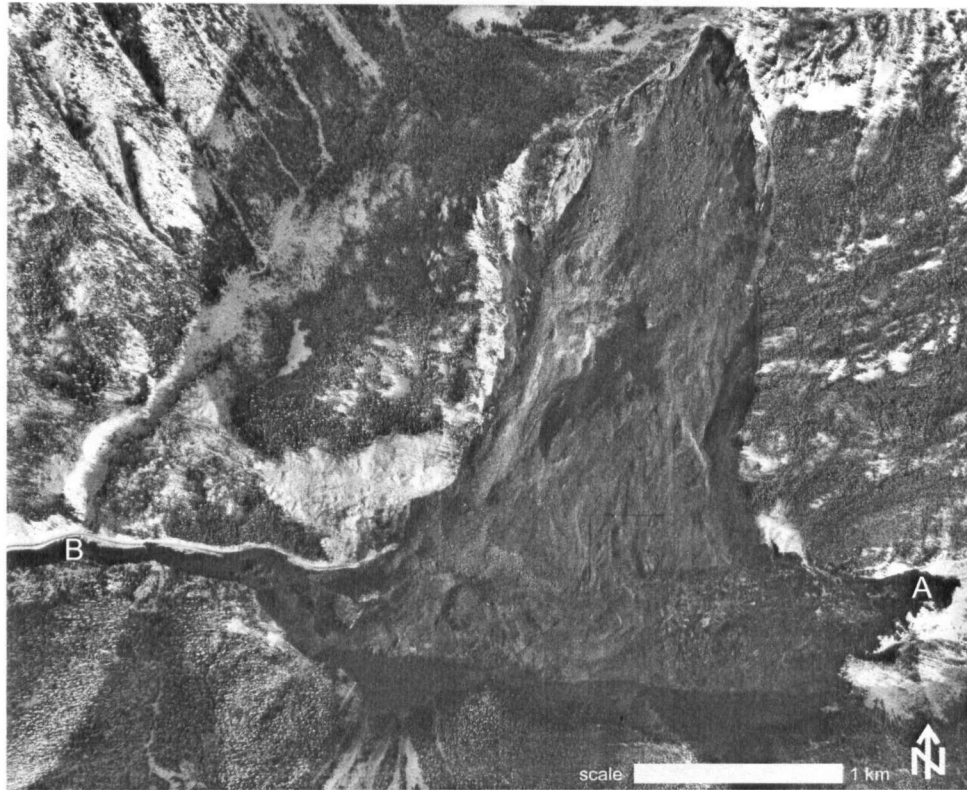


Figure 2.9. Aerial view of the 1965 Hope rock avalanche, British Columbia. The lighter areas in the centre of the landslide deposit are covered with large boulders. The darker areas on the left and right margins of the deposit represent liquefied, relatively fine-grained material displaced from the valley floor sediments (A). A mud flow tongue issued from the western margin and flowed for several kilometres along the Nicolum Creek valley (B). The dark, irregular band covering the southern margin of the deposit is a shadow. The image is approximately 4.5 km wide. (Aerial photograph BC5124-9. Copyright © 2005 Province of British Columbia. All rights reserved. Reprinted with permission of the Province of British Columbia.)

Bed destabilization at the base of a landslide is similar to bedload transport in fluvial hydraulics. Failure of bed material can be caused by the transmission of basal shear stress to the bed, isolated grain-bed interactions (i.e., impact and scour) and generation of excess pore water pressures due to rapid undrained loading, with possible liquefaction (Hutchinson and Bhandari 1971; Sassa 1985). As in fluvial bedload transport (Selby 1985), turbulence and lift may also play a role, especially in more dilute regions of a flow. Mobilized bed material may be entrained by the main mass or develop into or become entrained in a subsequent surge.

In analogy to bedload transport theory, Takahashi (1978) developed an equation to predict the maximum erosion depth in a saturated, granular, homogeneous bed subjected to drained loading at the base of a uniform debris flow. The depth of the bed was assumed to be unlimited, which is known as a “transport-limited” (Carson and Kirkby 1972) or “supply-unlimited” (Jakob 2005) condition. The following equation for estimating the maximum bed-normal erosion depth, b , or depth of instability, can be derived using infinite slope stability theory (e.g., Morgenstern and Sangrey 1978) and is equivalent to Takahashi’s (1978, Equation [22]):

$$[2-4] \quad b = h \left[\frac{\frac{\gamma_{(water)} - \gamma_{(debris)}}{\gamma_{(bed)}} \left(1 - \frac{\tan \alpha}{\tan \phi_{i(bed)}} \right)}{\left(1 - \frac{\tan \alpha}{\tan \phi_{i(bed)}} \right) - \frac{\gamma_{(water)}}{\gamma_{(bed)}}}} \right]$$

where h is the bed-normal flow depth, $\gamma_{(water)}$ is the unit weight of water, $\gamma_{(bed)}$ is the saturated unit weight of the bed material, $\gamma_{(debris)}$ is the bulk unit weight of the flow, α is the inclination of the bed from horizontal and $\phi_{i(bed)}$ is the internal friction angle of the bed material. The ratio $\tan \alpha / \tan \phi_{i(bed)}$ must be less than $1 - \gamma_{(water)} / \gamma_{(bed)}$ or the bed itself would be inherently unstable.

A similar equation with different implications can be derived by instead assuming that the bed is subjected to undrained loading, arguably a more appropriate assumption given the extremely rapid velocities of debris flow surges and the consequent short time available to dissipate the pore pressures that are generated in the bed:

$$[2-5] \quad b = h \left[\frac{\frac{\gamma_{(debris)} - \gamma_{(debris)}}{\gamma_{(bed)}} \left(1 - \frac{\tan \alpha}{\tan \phi_{i(bed)}} \right)}{\left(1 - \frac{\tan \alpha}{\tan \phi_{i(bed)}} \right) - \frac{\gamma_{(water)}}{\gamma_{(bed)}}}} \right]$$

The only difference between the two expressions is the first term in the numerator on the right side, but the results are significantly different (Figure 2.10). Assuming drained response, Equation [2-4] suggests that a certain amount of entrainment is possible for any value of $\gamma_{(debris)}$ less than $\gamma_{(water)} / (1 - \tan \alpha / \tan \phi_{i(bed)})$, with more dilute flows causing instability to greater depths. No entrainment would be predicted for fully-developed debris flows (i.e., when $\gamma_{(debris)} = \gamma_{(bed)}$). In contrast, assuming undrained response, the unstable depth increases with the bulk density of the flow and entrainment would be predicted for all values of $\gamma_{(debris)}$ and α , except when the bed is horizontal.

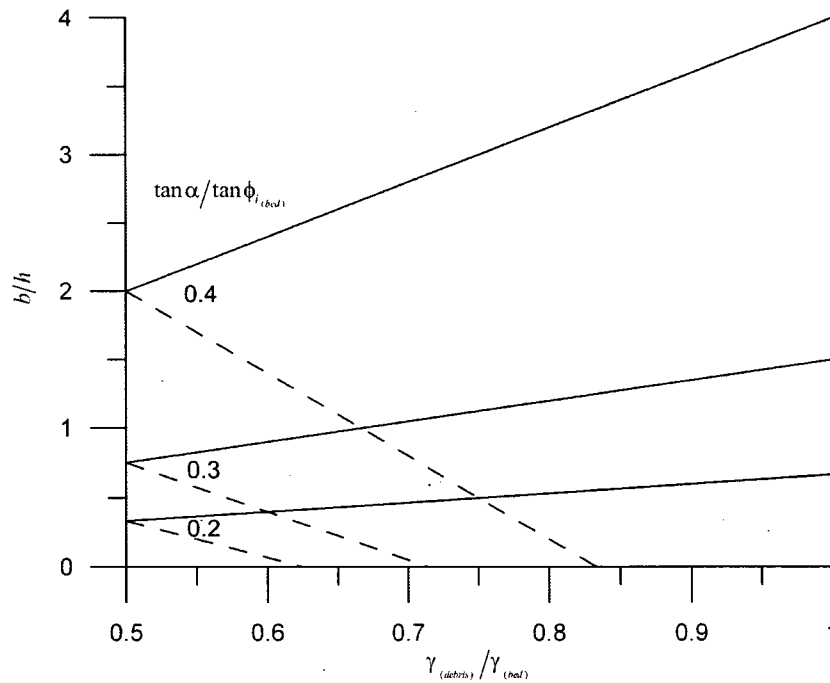


Figure 2.10. Depth of bed instability predicted using Equations [2-4] and [2-5] (dashed and solid lines, respectively). The ratio $\gamma_{(water)} / \gamma_{(bed)}$ is assumed to be 0.5.

Equations [2-4] and [2-5] are conceptually interesting but, besides highlighting the sensitivity of such an approach to the drainage assumptions, they are of limited practical value. In reality, landslide motion can be highly unsteady and nonuniform, and pore pressure distributions and the variation of bed material strength with depth can be very complex, making practical predictions of the maximum erosion depth in a supply-unlimited system

extremely difficult. In many cases, however, a firm substrate limits the depth of erosion and therefore limits the volume of path material available to be mobilized. This is known as a “weathering-limited” (Carson and Kirkby 1972) or “supply-limited” (Jakob 2005) condition. The depth to a non-erodible layer, such as bedrock, can be estimated in the field (Hungr et al. 1984; VanDine 1985).

Heterogeneity of the surficial material and complex stress conditions at the base of a landslide must also influence the *rate* of erosion (note that time-dependency does not enter into the stability calculations). Erosion may proceed progressively or failure may occur at depth, for example, at a weak interface with a different substrate. Some constitutive relationships for debris flow erosion rates have been proposed and tested using laboratory experiments (e.g., Takahashi 1991; Brufau et al. 2000; Egashira et al. 2001), but the validity of these equations under field conditions at full-scale has not yet been demonstrated.

Significant depletion by erosion may channelize trailing debris. Incision can also trigger bank failures that contribute additional material to a landslide or a subsequent surge. The volume of this material may be significant, but is difficult to quantify. Topography changes can be incorporated easily into numerical models, but the results are sensitive to assumptions about erosion rate and maximum erosion depth.

2.4.2 Volume change

Entrainment can significantly increase the volume of a landslide, which correlates with higher peak discharge (Rickenmann 1999) and larger potential inundation area (Li 1983; Iverson et al. 1998; Hungr 2002). The importance of volume changes due to entrainment depends on the size and type of a landslide, the availability and character of erodible path material and the efficiency of the entrainment mechanism. A simple index that quantifies volume change is the “entrainment ratio” (Hungr and Evans 2004a), defined as the ratio between the entrained volume and the initial landslide volume (accounting for expansion of the latter due to fragmentation of the initial failure). A large entrainment ratio suggests that volume change is a dominant factor.

Debris avalanches and debris flows, in particular, can derive most of their volume by entrainment. A well-documented example is the 1990 Tsing Shan debris flow in Hong Kong (King 1996), which initiated as a modest 400 m^3 failure but mobilized a total volume of approximately $20,000 \text{ m}^3$, corresponding to an entrainment ratio of about 50 (Figure 2.11). Revellino et al. (2004) reported similarly large relative volume changes for a number of recent events in the Campania region of southern Italy. Debris flow erosion depths up to 8 m and channel debris yield rates up to $300 \text{ m}^3/\text{m}$ have been reported worldwide (Li and Yuan 1983; Rickenmann et al. 2003). Clearly, volume change is a dominant characteristic of debris flows and debris avalanches and must be accounted for in numerical modelling of these types of landslides.



Figure 2.11. The Tsing Shan debris flow, which started as a relatively small slide of 400 m^3 but grew to a total volume of $20,000 \text{ m}^3$ through entrainment. (Photograph taken on September 14, 1990, courtesy of J. King, Geotechnical Engineering Office, Hong Kong)

However, entrainment can also be important at larger scales. For example, rock failures of moderate volume can still entrain relatively large volumes of material. Some recent events in British Columbia demonstrate the mobility of these types of landslides and the extensive damage that they can cause, often far from the source (Schwab et al. 2003; Boulton et al. 2006). Hungr and Evans (2004a) proposed the special term “rock slide - debris avalanche” to emphasize the role of entrainment in events in which the entrainment ratio exceeds 0.25.

2.4.3 Momentum transfer

Volume changes occur as mass is transferred from the bed to the landslide. Momentum transfer accompanies mass transfer, as the initially stationary path material is accelerated to the landslide velocity by a combination of solid collisions and fluid thrust. This process results in a velocity-dependent inertial resistance, which is additional to the basal shear resistance (e.g., Perla et al. 1980).

The effects of momentum transfer during entrainment can be illustrated using the simple sliding block model (cf., Chapter 1). Assuming purely frictional resistance and neglecting the influence of centripetal acceleration, which adds a velocity-dependent component to the frictional resistance in the curved transition zone, the inclination of the energy line for a single block is ϕ , the dynamic basal friction angle of the block (Figure 2.12). In this case, the actual energy line coincides with the mean energy line.

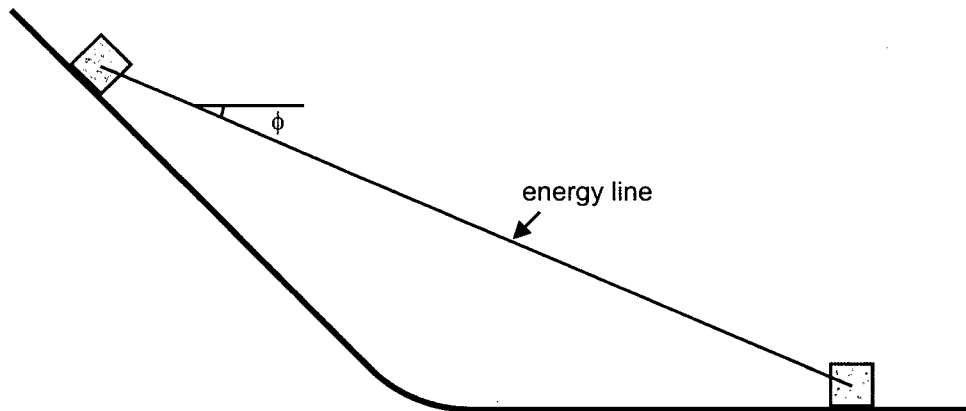


Figure 2.12. Energy grade line analysis of a single sliding block.

A different result is obtained if a second block is placed on the slope and “entrained” by the first block during its descent, by way of an inelastic collision. An inelastic collision is the sliding block analogue of entrainment in real landslides. In both cases, the entraining and the entrained material continue on at the same velocity and, while the momentum of the whole system is conserved (it is simply transferred from the entraining to the entrained material, with no net loss), some energy is dissipated. This scenario is illustrated in Figure 2.13. The velocity of block 1 immediately prior to the collision is v' and its momentum is m_1v' , where m_1 is its mass. Block 2 is stationary prior to the collision and therefore contributes no momentum to the two-block system. The total momentum of the system is conserved during the inelastic collision:

$$[2-6] \quad m_1v' = (m_1 + m_2)v$$

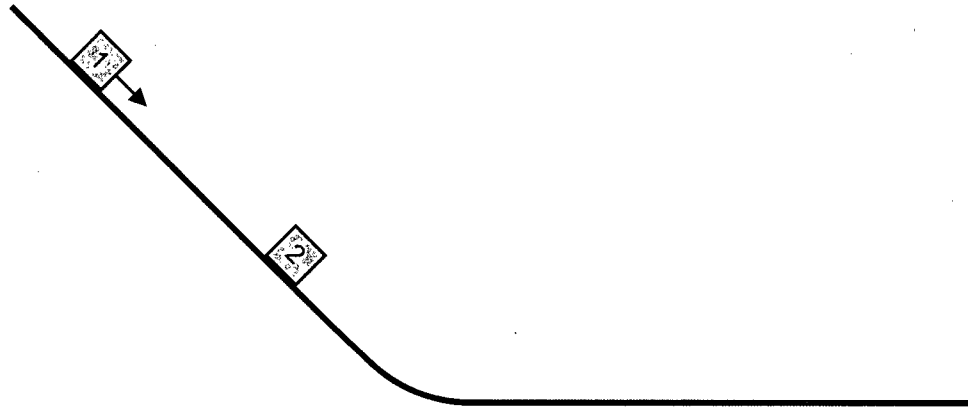
where m_2 is the mass of block 2 and v is the velocity of both blocks immediately after the collision. The energy dissipated during the collision is equal to the change in kinetic energy of the system:

$$[2-7] \quad \frac{1}{2}m_1(v')^2 - \frac{1}{2}(m_1 + m_2)v^2 = \frac{1}{2}\left(\frac{m_1m_2}{m_1 + m_2}\right)(v')^2$$

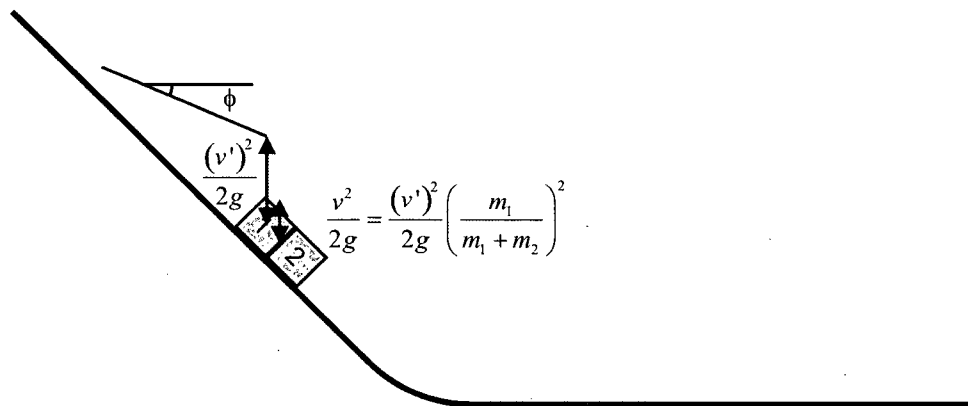
and the velocity head of the two-block system immediately after the collision is:

$$[2-8] \quad \frac{v^2}{2g} = \frac{(v')^2}{2g} \left(\frac{m_1}{m_1 + m_2}\right)^2$$

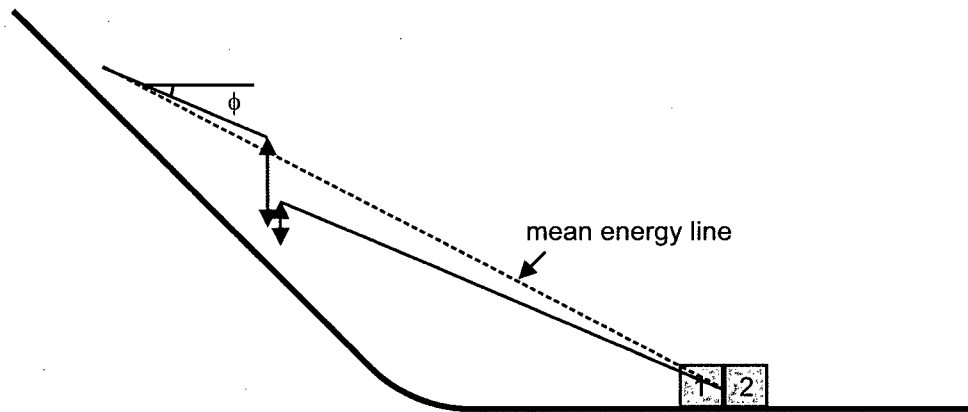
where g is the vertical acceleration due to gravity.



(a) initial conditions



(b) conditions at collision



(c) final conditions

Figure 2.13. Energy grade line analysis of two sliding blocks. Block 2 is “entrained” by block 1 during its descent (through an inelastic collision). (a) Block 1 is released while block 2 remains stationary. (b) Momentum is transferred from block 1 to block 2 during the collision. (c) The centre of mass of the two-block system does not travel as far as in the single block case (the slope of the mean energy line is steeper than ϕ).

The result is that the centre of mass of the two-block system does not travel as far as in the case of the single block. At the same time, the mean energy line is steeper than what might be expected by analyzing the joint centre of mass of the two blocks without accounting for their interaction because energy is dissipated during the collision. The same process occurs in real landslides. However, the momentum transfer and accompanying energy losses do not occur instantaneously but are spread out, sometimes over very long entrainment zones. As shown in Equation [2.7], these energy losses are proportional to the square of the flow velocity, and so can have a significant influence on the dynamics of extremely rapid landslides. When substantial entrainment occurs and/or when the velocity is high, the momentum transfer effect can account for a significant proportion of the total flow resistance.

Dynamic models should be able to account explicitly for this effect. An explicit approach (i.e., the separation of shear and entrainment related resistances) ensures compatibility between mass and momentum transfer. The use of bulk resistance relationships (e.g., Perla et al. 1980) is a common alternative, but cannot account for the isolated influence of distinct entrainment zones.

2.5 Objective #4: the ability to simulate variations in rheology

Landslides are composed of a variety of geological materials that can have very different characteristics, and their composition can vary in both space and time. Continuum dynamic models should be able to account for this variability, which can significantly influence the dynamics.

2.5.1 Variations along the path

Landslide mobility is related to the volume and character of the source material, but often more importantly to the extent, depth and character of the surficial material encountered along the path. As mentioned in the previous section, this material can strongly influence the shear resistance at the basal interface. Sassa (1988) was the first to explicitly incorporate this

idea into a continuum dynamic model. A reduction in the basal shear resistance can be caused by either a reduction in the actual basal shear strength due to interaction with weaker path material, or a reduction in the effective basal shear strength due to an increase in pore fluid pressure near the base (Figure 2.14). Increases in pore fluid pressure can be caused by both entrainment of additional water and rapid undrained loading of wet substrate (Hutchinson and Bandari 1971; Sassa 1985). In fact, liquefaction of basal material is the oldest explanation for the high mobility of rock avalanches (Buss and Heim 1881; Sassa 1988; Voight and Sousa 1994; Abele 1997; Hungr and Evans 2004a). A possible example of this effect is shown in Figure 2.15.

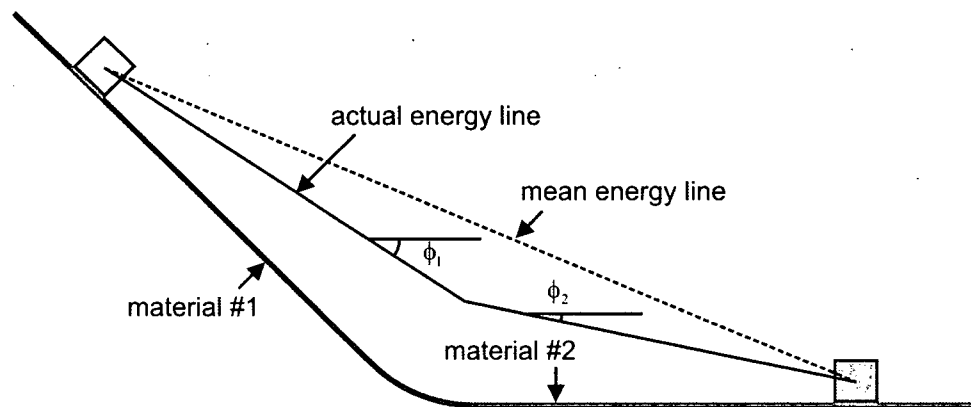


Figure 2.14. Sliding block model demonstrating the influence of a change in basal material strength along the path. In this example, purely frictional resistance is assumed and the influence of centripetal acceleration is neglected, resulting in a bilinear energy line. The velocities along the path are lower than would be predicted using the mean energy line.

The seasonal presence of snow/ice cover and meltwater can play an important role. If entrainment and subsequent mixing are substantial, they can also change the internal rheology of a landslide, which can influence its spreading behaviour. As mentioned previously, changes in basal and internal shear strength and pore pressure can also be caused by progressive fragmentation and comminution of grains during motion (Sassa 2002). With significant changes in composition and/or material properties, it is also possible for the rheological relationships themselves to change, for example, from velocity-independent to velocity-dependent. Dynamic models should therefore allow the selection of a variety of rheological relationships, as appropriate for the materials involved.



Figure 2.15. Oblique aerial view of the May/June 2002 McAuley Creek rock avalanche near Vernon, British Columbia. Most of the rock debris (about 7 Mm^3 total) deposited immediately below the source area (A), but about 1 Mm^3 continued another 1.6 km down the narrow valley (B). The mobility of this part of the landslide may have been enhanced by the presence of fine-grained, relatively weak and possibly saturated glaciolacustrine deposits in the path. (Photograph taken on August 26, 2002, courtesy of Dr. Réjean Couture, Geological Survey of Canada, Ottawa.)

Rheology changes along the path can be gradual or sudden, but in either case can significantly influence mobility. The most dramatic changes often coincide with the onset of substantial entrainment, which is why this influence is perhaps most obvious when the entrainment volume is comparable to the source volume, such as in rock slide – debris avalanches. In such cases, a reduction in resistance corresponding to entrainment can more than offset the momentum transfer effect. When a reduction in resistance occurs, constant rheology models tend to better reflect the later stages of motion and typically overestimate velocities and underestimate emplacement times (Sousa and Voight 1991; Voight and Sousa 1994). However, it is important to note that changes along the path do not always result in higher mobility. For example, a landslide that encounters coarse, dry talus or previous rock avalanche debris may actually experience an increase in resistance. A similar effect can

occur when a landslide enters a relatively densely-vegetated area. In any case, the possibility of changes along the path should always be considered, and so dynamic models should allow users to implement the appropriate changes.

2.5.2 Variations within the landslide

Spatial variations in rheology within a landslide are also an important consideration. Landslides can contain rigid, frictional, plastic and fluid components, as well as a significant volume of timber and other organic material (Figure 2.16). The strength, density, grain size, viscosity and pore pressure of these components may vary significantly over small domains. For example, coarse, dry rock debris can travel on a thin, liquefied basal layer. Similarly, liquefied quick clay can transport rafts of intact, desiccated clay. Heterogeneity can result from spatial variations in the composition of the source material as well as from entrainment, as mobilized path material may become isolated at different locations within the flow.



Figure 2.16. The distal end of a debris flow deposit near Prince Rupert, British Columbia (looking downstream). The relatively coarse-grained front contains several large trees, which may have encouraged deposition at this location.

In addition, internal sorting during motion can produce material and grain size segregation and may form important structures, such as boulder fronts (Pierson 1986), that can significantly influence the dynamics. Large-scale heterogeneity is a fundamental characteristic of debris flow behaviour (Iverson 1997; Hungr 2000), and this type of sorting can produce surges with peak discharges up to 40 times that of an extreme flood (VanDine 1985). Steep, coarse-grained margins can restrain more mobile, fluid interiors (Major and Iverson 1999), making the process of deposition extremely complicated, with successive surges pushing aside or overtaking decelerating flow fronts and increasing total travel distances (Iverson 1997).

The spatial distribution of different rheological zones within a moving mass is difficult to implement and introduces a complex set of input variables that can be difficult to constrain. However, the capability of dynamic models to simulate this kind of behaviour is a desirable option.

2.6 Objective #5: efficiency

Dynamic models should be able to satisfy the four technical objectives described above, which are essential for the accurate simulation of real landslides. At the same time, however, they must be efficient and user-friendly in order to be practical.

Computational efficiency facilitates rapid testing, back-analysis and prediction. While testing is typically done at the model design stage, when computing capabilities may be high and time constraints are not a major factor, back-analysis of previous landslides and forward-analysis of potential landslides are done in practice. Since most practitioners do not have access to a supercomputer and are typically under tight time constraints, practical dynamic models should be efficient enough to run on a microcomputer in a reasonable period of time. Some models require calibration of input parameters, which must be constrained by trial-and-error back-analysis. This requires the ability to perform multiple runs in as short a time as possible. However, even when calibration is not necessary, multiple predictive runs may be performed to study the sensitivity of the results to uncertain input parameters. A certain

amount of trial-and-error adjustment may also be required, in order to match model results to predictions based on other runout analysis methods and/or subjective judgment.

Models should therefore also be flexible enough to permit easy manipulation of input data and parameters. In addition, the input and output data formats should be as simple and as universal as possible, to facilitate communication of results and manipulation by GIS or other available mapping software. Models should also provide diagnostic output during run time, preferably in a visual format. Finally, the modelling methodology should be transparent and easy to understand, allowing practitioners to interpret the results and quickly identify model limitations and sources of potential error.

2.7 Discussion

It is important to incorporate all of the technical features together, as they are all interrelated to some degree. During entrainment, the momentum transfer effect and the basal shear stress comprise the total resistance. The rates of mass and momentum transfer, which are themselves coupled, may be influenced by the magnitude of the basal stresses. The basal stresses are transmitted through the landslide and therefore coupled to the other internal stresses. All of these stresses are influenced by complex 3D strain and governed by the strength, pore fluid and drainage characteristics of the materials, which may be highly variable and may include entrained material.

However, it is difficult to account for all of this complexity without sacrificing too much efficiency, and a high degree of uncertainty is associated with the large number of input variables that are required. At the same time, the actual mechanisms and processes that are involved, including those associated with entrainment, internal sorting, pore pressure response and stress redistribution, are presently poorly understood and require much more research. As a result, a simplified approach should be favoured at this stage, preferably one that can evolve with our understanding of landslide dynamics.

The “equivalent fluid” approach proposed by Hungr (1995) and implemented in DAN appears to be capable of accounting for such complexity within a sufficiently simple, efficient and flexible framework. All of the required technical features can be included and coupled accordingly, with appropriate, transparent assumptions and simplifications. The method also facilitates a modular approach to design, which allows updates to these features and potential new features to be “plugged in” in the future. The result should be an adaptive tool that can be used now, within the constraints of present knowledge.

2.8 Conclusion

Extremely rapid, flow-like landslides can be modelled within a hydrodynamics framework, but several important modifications are required. Specifically, continuum dynamic models should be able to account for the interdependent influences of 3D topography, internal strength, entrainment and spatial and/or temporal variations in rheology, while also being efficient enough for practical use. The capabilities of dynamic models have advanced incrementally in the past few decades, in parallel with increasing computational capabilities, to the point where all of these features can now be incorporated into a single model. The model proposed in this thesis is an extension of DAN, but is also based on a number of other existing models that have contributed to these advances. A review of these models is the subject of the next chapter.

3 PREVIOUS WORK

3.1 Introduction

Continuum dynamic modelling has emerged as a potentially powerful tool for landslide runout analysis. With resulting increased attention and coinciding advances in computational capabilities, a large number of models have been developed or are currently in development. Several of these models have included innovations that have significantly advanced both our ability to simulate real events and our fundamental understanding of rapid landslide processes. These models, including DAN (Hungri 1995), are the foundation for the model proposed in this thesis.

The purpose of this chapter is to present a critical review of existing continuum dynamic models. An emphasis is put on the most important innovations with time, specifically in the context of the essential capabilities described in Chapter 2. As such, a chronological order is attempted, although models that are closely related in this context are generally grouped together.

3.2 Model classification

There are potentially many ways to classify landslide continuum dynamic models, but three key distinctions are commonly made between: 1) models capable of simulating motion across 2D vs. 3D terrain; 2) models formulated in Eulerian vs. Lagrangian reference frames; and 3) models that require measurement vs. calibration of rheological parameters. These important differences are referred to throughout this thesis.

3.2.1 2D vs. 3D

Most continuum dynamic models make use of an approach known as depth-averaging, in which the governing mass and momentum balance equations are integrated with respect to the flow depth. Stresses are assumed to increase linearly with depth below the top surface of

the flow, which is assumed to be stress free, and shear stresses in the depth-wise direction are neglected. The latter simplification is based on the assumption that the depth varies gradually and is small relative to the length and width of the landslide. This is the classical shallow flow assumption of hydrodynamics (e.g., Chow 1959). The depth-averaging process is described in detail in Chapter 4.

Depth-averaging combined with the shallow flow assumption essentially eliminates one dimension, the depth-wise dimension, from the governing mass and momentum balances. This can lead to some confusion in terminology, as depth-averaged models that are capable of simulating motion across 3D terrain are often referred to as either 2D or depth-averaged 2D models. Similarly, models that simulate motion along a 2D path may be referred to as 1D or depth-averaged 1D. For the purposes of this thesis, however, 2D and 3D simply denote models that simulate motion across 2D and 3D terrain, respectively. Although it must be acknowledged that depth-averaged models are not strictly true 2D and 3D models, this terminology seems more intuitively representative of their capabilities.

3.2.2 Eulerian vs. Lagrangian

In continuum dynamics, the equations of motion can be formulated in one of two frames of reference: Eulerian or Lagrangian. An Eulerian reference frame is fixed in space, analogous to an observer standing still as a landslide passes. Models formulated in an Eulerian framework require the solution of a more complex form of the governing equations (cf., Chapter 4) using a dense, fixed computational grid, in which many elements may be located in void zones (Figure 3.1a). The Eulerian approach is the conventional method in computational fluid dynamics.

In contrast, a Lagrangian reference frame moves with the local velocity, analogous to an observer riding on top of a landslide. This method simplifies the governing equations (cf., Chapter 4) and does not sacrifice computational resources in void zones (Figure 3.1b). But because large deformations are typical of long-runout landslides, models that utilize a

traditional Lagrangian mesh, in which the computational elements are connected to each other, are susceptible to mesh distortion problems.

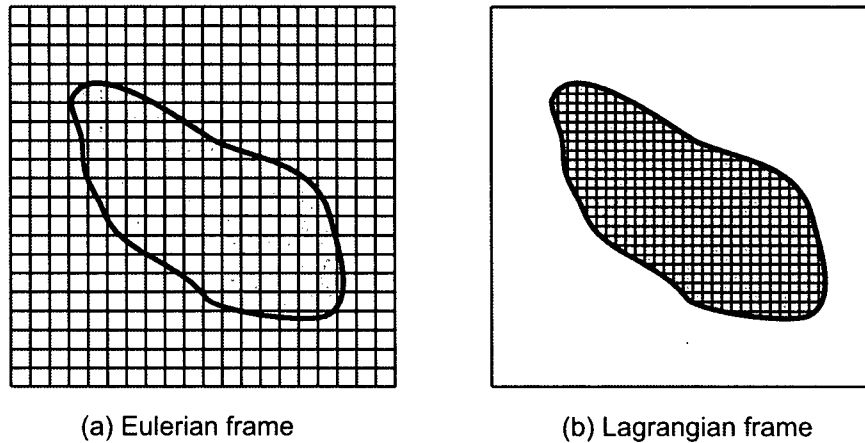


Figure 3.1. Eulerian vs. Lagrangian reference frames. An Eulerian reference frame is fixed in space (a), while a Lagrangian reference frame moves with the flow (b). With a comparable number of computational elements, the Lagrangian framework can provide higher resolution within the flow, but distortion of these elements can cause numerical problems.

3.2.3 Measurement vs. calibration

A less obvious distinction can be made between models that require the input of measured rheological parameters and models that must be calibrated by back-analysis. The difference between the two classes is not always clear because parameter measurement and parameter calibration are not necessarily characteristics of the models themselves (although the simplest models are only suitable for calibration-based analysis), but rather the modelling approach adopted by the model designers and users.

Parameter measurement is advocated by workers who believe that rapid landslide dynamics can be described by constitutive relationships that are functions of intrinsic material properties, that these relationships can be incorporated into dynamic models and that the required material properties can be measured using independent methods. Measurement-based models are typically tested using established analytical solutions and back-analyses of

controlled experiments before being applied to the analysis of real cases. This could be considered the traditional scientific approach to dynamic analysis.

In contrast, in the calibration-based approach, rheological parameters are constrained by systematic adjustment during trial-and-error back-analysis of full-scale prototype events. Simulation is typically achieved by matching the simulated travel distance, velocities and extent and depth of the deposit to those of the prototype. Calibration-based models may utilize the same physically-justifiable constitutive relationships as measurement-based models and should similarly be tested using analytical solutions and controlled experiments before being calibrated to specific classes of field problems.

Critics of the calibration-based approach argue that model calibration, especially without controlled testing, is equivalent to tuning or curve-fitting (i.e., successful simulation can be achieved by arbitrary adjustments of the right type and number of variables), and that model adaptability can therefore be mistaken for model accuracy (Iverson 2003). Parameter selection for the purposes of prediction can also be difficult because, while simulation of a single event can be performed quite efficiently, back-analysis of a significant number of similar prototype events is required for the calibrated parameters to be physically and/or statistically-justifiable. Accurate data for several suitable events can be hard to acquire and the calibration process can be time-consuming.

On the other hand, given the extreme complexity of landslide dynamics, the measurement-based approach could be considered idealistic. Although it is scientifically appealing to be able to measure the input parameters independently, no standard tests are available to measure, for example, the properties of coarse rock avalanche debris travelling at extremely rapid velocities. Such properties, even if measurable, may change significantly during the course of motion, along with the rheology itself, and may be significantly scale-dependent. True measurement-based models must be able to account for any evolution in behaviour without the need for user-imposed changes and without using constitutive laws that include ad hoc assumptions. These requirements are extremely challenging.

Again, the only real difference between measurement-based and calibration-based models is the prescribed method of constraining the required rheological parameters. Nevertheless, although there appears to be significant common ground between the two approaches, convergence into a single accepted methodology may not occur for some time, if ever, and the distinction is therefore important to maintain.

3.3 Existing continuum dynamic models

As described in Chapter 1, continuum dynamic models evolved from established lumped mass and hydrodynamic methods. Subsequent innovations have included various methods to account for internal strength, entrainment and rheology variations.

3.3.1 Extension of hydrodynamic methods

The earliest continuum dynamic models for landslides and snow avalanches were essentially dam-break or flood routing models with modified basal rheologies. Lang et al. (1979) modified an existing 2D Eulerian hydrodynamic model to include frictional resistance in addition to classical kinematic viscosity. The frictional component in the model (AVALNCH) was increased at low speeds to simulate the “fast-stops” that had been observed during snow avalanche deposition. Appropriate values for the resistance parameters were investigated by back-analyses of actual events (Lang and Martinelli 1979).

Dent and Lang (1980) modified another 2D Eulerian hydrodynamic model, based on the Simplified Marker-and-Cell numerical method, to include various combinations of frictional, viscous and turbulent resistances and a series of large-scale experiments were back-analyzed. Dent and Lang (1983) modified the same model to include a biviscous resistance, similar to the Bingham rheology (e.g., Johnson 1970), and back-analyzed the same series of experiments. The model (BVSMAC) has also been used to back-analyze full-scale rock and debris avalanches (Trunk et al. 1986; Sousa and Voight 1991; Voight and Sousa 1994). Sousa and Voight (1991) and Voight and Sousa (1994) used progressively-decreasing resistance parameters to simulate changes along the path.

The Bingham rheology has been implemented by other workers. Jeyapalan (1981) and Jeyapalan et al. (1983a) presented a 2D Eulerian model (TFLOW) based on the Bingham rheology, which was used to back-analyze mine waste flow slides (Jeyapalan 1981; Jeyapalan et al. 1983b). Schamber and MacArthur (1985) and MacArthur and Schamber (1986) developed 2D and 3D Eulerian models for routing mud flows, also based on the Bingham rheology, for the United States Army Corps of Engineers Hydrologic Engineering Centre. Liu and Mei (1989) used a 3D Eulerian model to demonstrate the spreading of a Bingham fluid on an inclined plane.

O'Brien et al. (1993) presented a 3D Eulerian model for routing floods, mud flows and debris flows using a generalized quadratic rheology, which is capable of accounting for various combinations of plastic/frictional, viscous and turbulent/dispersive resistances. The model (FLO-2D) was tested against an established hydrodynamic model and was demonstrated using a full-scale mudflow case study. FLO-2D is notable because it is currently the only commercially-available 3D model and it has been used extensively in practice (e.g., Hübl and Steinwendtner 2001; O'Brien 2003; García et al. 2004).

Laigle and Coussot (1997) presented a 2D Eulerian model for mud flows based on the Herschel-Bulkley rheology (e.g., Coussot 1994). The input parameters were measured independently using standard rheometric techniques. A sensitivity analysis was performed and the model was tested using laboratory flume experiments.

3.3.2 Incorporation of path-dependent rheology

With noted exceptions (i.e., Lang et al. 1979; Sousa and Voight 1991; Voight and Sousa 1994), the aforementioned models used constant bulk rheological parameters and neglected the influence of internal strength. Sassa (1988) presented a 3D Eulerian model that included a method to account explicitly for changes in resistance along the path using a frictional resistance model. Instead of using a constant friction angle for the duration of motion, Sassa (1988) used a spatially-variable effective basal friction angle, which accounts for the influence of pore water pressure implicitly. He argued that the basal resistance is governed

by the properties of the bed material, which can fail under rapid loading (Hutchinson and Bhandari 1971; Sassa 1985), and proposed that the effective basal friction angle at different locations could be measured using high speed ring shear tests on samples taken from the path.

3.3.3 Incorporation of earth pressure theory

Sassa (1988) also recognized that flowing earth materials do not spread out at the same rate as fluids because of their ability to sustain non-hydrostatic internal stresses. Adopting an established soil mechanics technique (cf., Chapter 2), he normalized the internal horizontal normal stresses by the total vertical normal stress using pressure coefficients (depth-averaging was performed in the vertical direction). He suggested that the stress coefficients could range between 0 and 1 (representing solid and fluid extremes, respectively) and used a value based on Jaky's (1944) equation for the static, or "at rest" (Terzaghi 1920), earth pressure coefficient, which he assumed to be valid during motion and horizontally-isotropic. The model was demonstrated using a hypothetical experiment and a back-analysis of a real rock avalanche.

Hutter and Savage (1988) presented a 2D model for the simulation of dry granular flows that incorporated a more advanced method to account for internal strength. A detailed description of the model was presented by Savage and Hutter (1989). Significantly, they recognized that the internal stresses in a deforming granular mass are strain-dependent and coupled with the basal shear strength. They assumed that both the internal and basal rheologies were frictional but could be governed by distinct friction angles. Using classical Rankine earth pressure theory, they suggested that the internal stresses in a deforming granular mass tend to either active or passive states as the material diverges or converges, respectively (cf., Chapter 2). In contrast to Sassa's (1988) assumptions, this implied that the internal stresses could be greater than hydrostatic in directions of converging motion. They used only the theoretical limiting values for the stress coefficients in their model, independent of spreading rate or magnitude, an approach that assumes instantaneous stress response and therefore implies infinite stiffness of the granular mass. In contrast to previous models, in which the

conventional Eulerian approach was always adopted, Savage and Hutter (1989) experimented with both Eulerian and Lagrangian models and concluded that the Lagrangian approach was simpler, more efficient and more reliable. The model was tested against the results of laboratory flume experiments, conducted by Huber (1980), involving the motion of dry gravel down a confined chute.

The so-called Savage-Hutter theory has been the basis for a large body of work. Savage and Hutter (1991) modified their original model to account for centripetal acceleration due to curvature of the path, which influences the magnitudes of the internal and basal stresses. They used the same Lagrangian numerical method and tested the model using their own series of laboratory flume experiments, similar to Huber's (1980), involving dry plastic beads. The best simulations were achieved by incorporating velocity-dependent resistance into the model, which they justified on the basis of tests on glass beads that were presented by Stadler (1986). Hutter and Koch (1991) and Greve and Hutter (1993) compared model results to additional confined chute experiments involving the motion of various materials through both concave and convex path segments. Velocity-dependent resistance was not implemented in these tests and differences between measured and calibrated basal friction angles were observed.

Hutter et al. (1993) extended the Savage-Hutter theory for the simulation of 3D motion down an inclined plane. To maintain compatibility of the multi-dimensional internal stresses, they assumed that the stresses in the downslope direction dominate, consistent with the original Savage and Hutter (1989) model. Instantaneous stress response was still assumed and, in contrast to Sassa's (1988) 3D model, anisotropic stress states were possible. A series of sensitivity analyses were performed using analytical and numerical solutions of simplified forms of the proposed system of governing equations. Agreement between the model results and a corresponding series of laboratory experiments (not presented) was reportedly poor. As a result, Greve et al. (1994) and Koch et al. (1994) developed an improved 3D extension of the Savage-Hutter theory, which they solved using a Lagrangian finite difference scheme that employed a triangular mesh. The improved numerical model produced qualitatively better simulations of the previous laboratory experiments. The model was also tested using

additional laboratory experiments involving the motion of various dry granular materials down a plane, through an unconfined concave transition zone and onto a flat surface.

Gray et al. (1999) extended the Savage-Hutter theory further for the simulation of motion across irregular 3D terrain. The assumption of stress dominance in the general downslope direction, as measured in a global reference coordinate system, was maintained and a similar Lagrangian method was employed. The model was tested using partially confined chute experiments involving deposition on a flat surface. Additional tests with various materials were presented by Wieland et al. (1999). Tai and Gray (1998) proposed a modification to the model to account for gradual transitions between limiting stress states, which reduced artificial shocks and instabilities that were caused by the original numerical method. Various alternative shock-capturing methods, including Eulerian schemes, have been investigated by Gray et al. (2003), Wang et al. (2004) and Chiou et al. (2005). Pudasaini and Hutter (2003) and Pudasaini et al. (2005) proposed additional modifications to permit the simulation of motion down highly irregular channels.

3.3.4 Incorporation of entrainment capabilities

Entrainment capabilities within a continuum framework were introduced by Takahashi (1991), who developed 2D and 3D Eulerian models for simulating debris flows in which the solid-fluid mixture was modelled as a dilatant fluid (Bagnold 1954). The internal stresses were assumed to be hydrostatic and isotropic. Mass and momentum transfer due to erosion and deposition of material were accounted for explicitly using semi-empirical relationships for erosion and deposition rates. Simulation results were compared with laboratory experiments and observations of real debris flow deposits.

An alternative to Takahashi's (1991) erosion/deposition rate formulas was proposed by Egashira and Ashida (1997) and implemented in the 2D models of Brufau et al. (2000) and Egashira et al. (2001). In both cases, numerical results were compared with laboratory experiments. Brufau et al. (2000) separated the mass balances of the solid and fluid constituents in order to simulate spatial and temporal variations in flow density. This two-

phase model was extended to 3D by Ghilardi et al. (2001) and was used to back-analyze two real debris flows.

3.3.5 Towards a synthesis

Hungr (1995) presented a 2D Lagrangian model (DAN) that synthesized much of the earlier work by including features to account for internal strength, entrainment and rheology variations. He formalized the concept of “equivalent fluid”, used tacitly by previous workers, by modelling the landslide as a hypothetical material governed by simple internal and basal rheological laws. As in the Savage-Hutter theory, the bulk of the material was assumed to be frictional and therefore capable of sustaining strain-dependent internal stresses that could range between active and passive states. The influence of internal stiffness was accounted for by incrementing the stresses in proportion to the magnitude of the prevailing strain, the same concept proposed later by Tai and Gray (1998). Compatibility of the internal and basal stresses was neglected in the original model, but the Savage-Hutter coupled stress approach has since been implemented. Instead of imposing a single basal rheological law, as in previous models, Hungr (1995) included a selection of rheologies, which could be assigned to different zones within the landslide and/or different segments along the path. The user could also specify the depth of erodible path material in each segment, and mass and momentum transfer during entrainment were accounted for explicitly. The model was tested using previous laboratory experiments, including Huber’s (1980) sand flume experiments and Jeyapalan’s (1981) oil flume experiments, compared with results using other models (BVSMAC and TFLOW) and used to back-analyze several cases of mine waste flow slides. DAN has since been used by many workers to back-analyze a variety of landslides (e.g., Hungr and Evans 1996; Hungr et al. 1998; Ayotte and Hungr 2000; Jakob et al. 2000; Evans et al. 2001; Pirulli et al. 2003; Hürlimann et al. 2003; Revellino et al. 2004). It has also been used to demonstrate conceptual theories on the dynamics of rapid landslides, such as the influence of longitudinal sorting on the surging behaviour of debris flows (Hungr 2000) and the influence of entrainment on landslide mobility (Hungr and Evans 2004a).

A 3D extension of DAN, based on a Lagrangian finite element method, was proposed by Chen and Lee (2000). Internal stiffness and compatibility of the multi-dimensional internal stresses were neglected. Instead, instantaneous stress response was implemented in orthogonal, but otherwise arbitrarily-oriented, horizontal directions (depth-averaging was performed in the vertical direction). Entrainment capabilities were not incorporated. The model was tested using Huber's (1980) flume experiments and the frictional basal rheology was implemented to back-analyze two real landslides. Bingham and Voellmy rheologies were implemented in subsequent back-analyses (Chen and Lee 2002; Chen and Lee 2003; Crosta et al. 2004).

Iverson (1997) challenged the use of bulk rheological relationships in the dynamic modelling of debris flows, whose dynamics are strongly influenced by the interaction of relatively distinct solid and fluid components. He proposed a generalization of the Savage-Hutter theory, based on grain-fluid mixture theory, to account for viscous pore fluid effects explicitly, and incorporated the theory into a 2D Lagrangian model. The original Savage-Hutter assumptions of coupled internal and basal stresses and instantaneous stress response to deformation were retained. Iverson (1997) imposed a longitudinal pore pressure distribution, based on experimental evidence, and used the model to simulate a large-scale flume experiment. Viscous effects were neglected in the simulations and the required frictional input parameters were based on independently measured static values. Significant differences between the measured and simulated travel distance and travel time were observed, which were attributed to multiple surges that developed in the experiment but were not modelled.

Iverson and Denlinger (2001) and Denlinger and Iverson (2001) presented a 3D extension of the theory, which they implemented in a conventional Eulerian framework. The theory was demonstrated using analytical solutions of simplified forms of the governing equations and the numerical model was tested using both small-scale and large-scale flume experiments. A kinematic criterion was used to identify relatively high resistance zones near frictional flow margins, allowing the spatial distribution of pore pressure to evolve automatically throughout each simulation. The internal stress distribution computed in the model was dependent on

the orientation of the local reference frame, which was itself arbitrarily-oriented. Partially as a result, Denlinger and Iverson (2004) presented a revised 3D model for dry flows based on a unique Eulerian-Lagrangian hybrid numerical method. The governing equations were solved in an Eulerian framework, similar to the previous model, while a Lagrangian finite element method was simultaneously used to track deformations and redistribute the internal stresses accordingly. The model was demonstrated using hypothetical experiments and tested using analytical solutions of the dam-break problem. Iverson et al. (2004) presented additional experimental tests involving the motion of granular materials across an irregular surface.

Mangeney-Castelnau et al. (2003) presented a 3D model for simulating dry granular flows using a kinetic scheme. The model (SHWCIN) was based largely on the Savage-Hutter theory but used the three parameter velocity and depth-dependent basal resistance relationship proposed by Pouliquen (1999), which was also implemented in the 3D model used by Heinrich et al. (2001) and Voight et al. (2002). A hydrostatic, isotropic internal stress state was assumed. The model was tested using analytical solutions of the dam-break problem derived by Mangeney et al. (2000) and laboratory flume experiments presented by Pouliquen (1999). Pirulli (2005) proposed modifications to SHWCIN to combat observed mesh-dependency problems, permit simulation of motion across irregular 3D terrain, incorporate the influence of internal strength and allow the selection of more than one possible basal resistance relationship. The modified model (RASH3D) employed an unstructured finite volume mesh and Iverson and Denlinger's (2001) frame-dependent method to account for non-hydrostatic internal stresses. The model was tested using laboratory flume experiments involving strongly deflected flow of plastic beads (performed at the University of British Columbia and presented in Chapter 6 of this thesis) and was used to back-analyze two historic rock avalanches.

Pitman et al. (2003a) presented a 3D Eulerian model based on the Savage-Hutter theory for dry granular flows. The model (TITAN2D) was designed to provide high resolution using a parallel, adaptive mesh numerical method, which runs on distributed memory supercomputers. Iverson and Denlinger's (2001) frame-dependent method was employed to account for non-hydrostatic internal stress states. The model was demonstrated using

examples involving both simple and complex topography, and additional comparisons with laboratory experiments were presented by Patra et al. (2005). Entrainment capabilities, based on an empirical erosion rate, were incorporated by Pitman et al. (2003b) and demonstrated with a back-analysis of a historic rock avalanche, which was presented in more detail by Sheridan et al. (2005).

Entrainment capabilities have also been incorporated into snow avalanche models. Entrainment of a finite depth of snow cover by plowing at the flow front was included in the 3D Lagrangian model (SAMOS) presented by Sailer et al. (2002). Sovilla and Bartelt (2002) used a 2D Eulerian model to investigate plowing at the front as well as erosion at the base of dense snow avalanches, and their simulations were compared with field mass balance measurements. Entrainment of snow cover was also enabled in simulations presented by Turnbull and Bartelt (2003) using a 2D Eulerian model. Naim et al. (2003) presented a 3D Eulerian model that accounted for erosion and deposition explicitly using kinematic criteria similar to the semi-empirical erosion/deposition rate formulas proposed by Takahashi (1991) and Egashira and Ashida (1997).

Alternative solution methods have also been explored. Sampl (1993) used the Eulerian-Lagrangian hybrid Particle-in-Cell method to solve the 3D Savage-Hutter equations and model the dense flow component of snow avalanches. Lagrangian Smoothed Particle Hydrodynamics has been applied to the simulation of pyroclastic flows (Nagasawa and Kuwahara 1993) and dam-breaks (Cleary and Prakash 2004) in true 3D. Bursik et al. (2003) coupled the numerical methods of Cellular Automata and Smoothed Particle Hydrodynamics in a depth-averaged form to model erosion and consequent surface evolution by debris floods in 3D. The model was demonstrated using hypothetical experiments and was used to simulate actual gully formation and debris flood events.

3.4 Discussion

Clearly, the four technical objectives described in Chapter 2 have been addressed in previous work, which suggests that there is no need to “reinvent the wheel”. Methods to account for

landslide-specific features have been established and may only require refinement as they are incorporated into new models. This has been the recent trend, with attention shifting away from the development of innovative methods to account for real landslide behaviour and towards the development of more accurate methods to solve established governing equations. Still, no model has ever satisfied all four of the technical objectives of Chapter 2 at the same time. All of these features need to be integrated together and incorporated directly into the governing equations, which raises an important question: Are more accurate solution methods really a priority at this stage, if the equations themselves are not yet accurate?

Furthermore, the need for efficiency has typically been overlooked. For example, Pitman et al. (2003b) addressed the technical requirements by including features to account for both internal strength and entrainment in their 3D model and suggesting that rheology variations could be incorporated in the future. But a supercomputer, which would not be accessible to most prospective users, is required to run the model. Sheridan and Patra (2005) acknowledged that this is a significant challenge, especially when it comes to making models available to practitioners in resource-poor countries. Again, efficiency is a key requirement that can strongly influence the design of the technical features and should be integrated from the start.

3.5 Conclusion

A number of continuum dynamic models have been proposed in the past few decades and, in the process, both the theory and methodology of landslide modelling have been advanced. Models have progressed from simple extensions of established hydrodynamic models to more complex models with important landslide-specific features. However, there is still room for improvement, as the most important capabilities have not yet been incorporated into a single model. These features must be integrated together, beginning with the formulation of the governing equations, and this approach has been adopted in the development of DAN3D. A detailed derivation of the governing equations used in DAN3D is presented in the next chapter.

4 GOVERNING EQUATIONS

4.1 Introduction

Landslide-specific features have been included in previous continuum dynamic models, but the most important capabilities have never been incorporated together in the same model. Aspects of each of the five key objectives for model development that were outlined in Chapter 2 (3D terrain; internal strength; mass and momentum transfer due to entrainment; rheology variations along the path and within the landslide; efficiency) must be incorporated directly into the governing equations of motion, irrespective of the subsequent numerical solution method.

The purpose of this chapter is to present a detailed derivation of the equations used by DAN3D, with all of the assumptions and approximations stated explicitly. The underlying method is based on the concept of “equivalent fluid”, as formalized by Hungr (1995).

4.2 Equivalent fluid concept

Landslides are complex phenomena that are much more difficult to simulate than fluids. As described in Chapter 2, the standard hydrodynamic assumptions of hydrostatic, isotropic internal stresses and material homogeneity do not apply. At the same time, the different materials that can be involved, including rigid, frictional, plastic and fluid components, may have non-Newtonian rheologies that are strongly influenced by complex interactions during highly unsteady and nonuniform motion across steep and irregular terrain.

Given such complexity, any single material constitutive relationship may only be valid within a narrow domain of space and time. As a result, the traditional scientific approach to analysis, formulating a constitutive law on the basis of fundamental principles and/or laboratory tests and incorporating it into a boundary or initial value problem, appears very difficult to apply. Advocates for such a measurement-based approach, including Iverson

(1997) and Denlinger and Iverson (2001), have demonstrated some success, but so far only in the simulation of controlled experiments.

Like DAN (Hungr 1995), DAN3D uses a simpler semi-empirical approach based on the concept of “equivalent fluid” (Figure 4.1), defined by Hungr (1995) and used tacitly by a number of other workers (e.g., Sousa and Voight 1991; O’Brien et al. 1993; Rickenmann and Koch 1997). The heterogeneous and complex landslide material is modelled as a hypothetical material, which is governed by simple internal and basal rheological relationships that may be different from each other. The internal rheology is assumed to be frictional (“equivalent *fluid*” is therefore somewhat of a misnomer) and is governed by one parameter, the internal friction angle, ϕ_i (cf., Chapter 2). In contrast, a single basal rheology is not imposed. Instead, the basal rheological model and its associated parameters, generally only one or two, are selected based on an empirical calibration procedure, in which actual landslides of a given type are subjected to trial-and-error back-analysis. The results are judged in terms of their ability to reproduce the bulk external behaviour of a prototype event, including the travel distance and duration and the spatial distribution of velocities and flow/deposit depths (wherever comparable estimates are available). The calibrated parameters are considered apparent, rather than actual, material properties.

Extensive back-analysis is required to build a significant database of input parameters that can be used for prediction. However, this approach reduces reliance on laboratory-derived material properties and constitutive relationships that may be difficult to obtain and may not be valid at full-scale. At the same time, it facilitates direct comparison of established rheological models (several alternative relationships can be implemented) and accommodates new rheological models that may be proposed in the future.

The premise of the equivalent fluid approach is perhaps summarized best by Voight and Pariseau (1979), who wrote, “Any model that allows the slide mass to move from its place of origin to its resting place in the time limits that bound the slide motion is likely to be consistent with the principal observable fact – that of the slide occurrence itself.” In the same sense, continuum dynamic models that can accurately simulate/predict the extent and

duration of a landslide and the distribution of intensity within the impact area, regardless of the underlying micro-mechanics, should be considered useful. For the practical purposes of landslide risk assessment, this is the only information that is relevant (cf., Chapter 1).

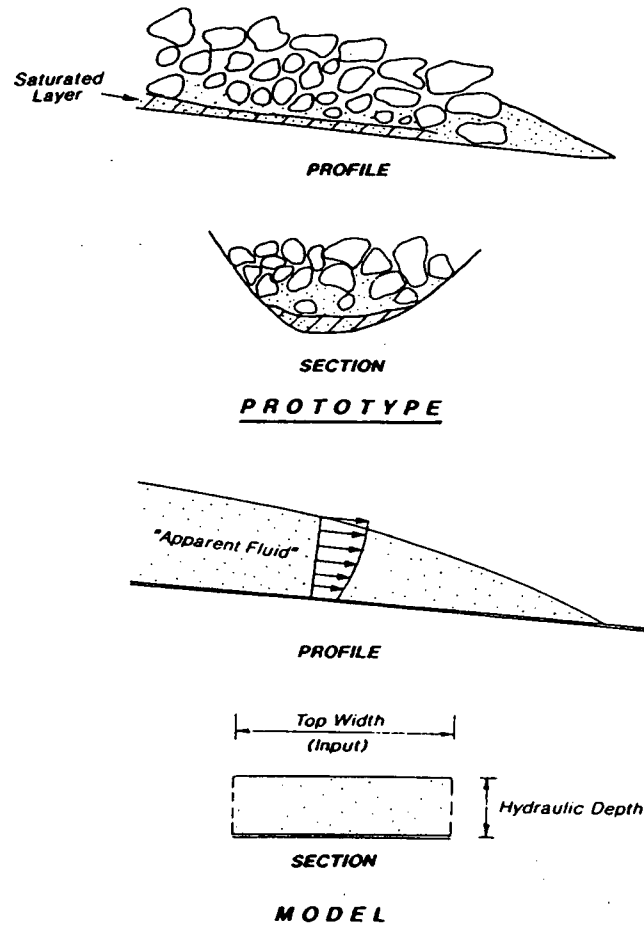


Figure 4.1. Schematic illustration of the “equivalent fluid” approach, after Hungr (1995). The complex landslide material is modelled as a hypothetical material governed by simple internal and basal rheologies. (Image from Hungr 1995)

4.3 General conservation laws

The continuum approach is based on the assumption that the landslide material can be modelled as a continuum (the so-called continuum assumption), which is considered valid if the particle size of the material is small relative to the dimensions, particularly the depth, of

the landslide. In reality, this is not always the case. For example, rock slides and rock avalanches can involve relatively large, intact and rigid blocks of material, particularly during the initial stages of motion, when the slide mass may be largely coherent. Progressive fragmentation can reduce the mean particle size during the course of motion, but significantly large fragments and voids can still remain. In such cases, internal stresses may be highly localized and dominated by discrete particle interactions. Similar behaviour may influence clay flow slides that transport relatively large rafts of coherent material. Results of continuum simulations of these types of landslides should therefore be viewed with some skepticism and interpreted accordingly.

But in many cases, especially those involving relatively fine-grained material and/or interstitial fluid, the continuum assumption is appropriate and the laws of continuum mechanics can be applied. In a continuum, numerous discrete interactions on a relatively small scale produce continuous internal stress fields, and gradients within these stress fields govern internal deformation. Modelling stress fields, rather than the discrete interactions that produce them, can be much more computationally-efficient.

The derivation that follows is similar to rigorous derivations presented by previous workers (e.g., Savage and Hutter 1989; Gray et al. 1999), but the resulting system of governing equations is unique. The derivation proceeds from an Eulerian frame of reference (cf., Chapter 3).

The following mass and momentum balance laws govern the mechanics of a continuum:

$$[4-1] \quad \frac{\partial \rho}{\partial t} + \nabla \cdot \rho \mathbf{v} = 0$$

$$[4-2] \quad \frac{\partial (\rho \mathbf{v})}{\partial t} + \nabla \cdot \rho \mathbf{v} \otimes \mathbf{v} = -\nabla \cdot \mathbf{T} + \rho \mathbf{g}$$

where ρ is the material bulk density, t is time, \mathbf{v} is the velocity vector, \mathbf{T} is the stress tensor, \mathbf{g} is the gravitational acceleration vector, ∇ is the gradient operator, \cdot denotes the dot product and \otimes denotes the tensor product.

Assuming that the material density is spatially and temporally constant (i.e., incompressible) Equations [4-1] and [4-2] simplify to:

$$[4-3] \quad \nabla \cdot \mathbf{v} = 0$$

$$[4-4] \quad \rho \left(\frac{\partial \mathbf{v}}{\partial t} + \nabla \cdot \mathbf{v} \otimes \mathbf{v} \right) = -\nabla \cdot \mathbf{T} + \rho \mathbf{g}$$

Spatial and temporal density variations occur in reality, but are neglected here for two reasons. First, in extremely rapid landslides, shear strain and associated dilation and contraction are likely to be concentrated near the base, with a more or less uniform density profile above (Savage and Hutter 1989; Savage and Hutter 1991). Second, density variations have been incorporated previously into dynamic models (Brufau et al. 2000) but reportedly did not produce appreciably different results, probably because density variations are small in comparison with changes in the other dynamic variables (Denlinger and Iverson 2004). The assumption of constant density also applies to entrained material, as described in the next section.

The total stress state on an element of material in an arbitrarily-oriented, right-handed Cartesian coordinate system (x, y, z) was shown in Figure 2.6 in Chapter 2. The associated stress tensor is:

$$[4-5] \quad \mathbf{T} = \begin{bmatrix} \sigma_x & \tau_{xy} & \tau_{xz} \\ \tau_{yx} & \sigma_y & \tau_{yz} \\ \tau_{zx} & \tau_{zy} & \sigma_z \end{bmatrix}$$

where the symbols σ and τ denote total normal and shear stresses, respectively, consistent with traditional soil mechanics practice. Expanding Equations [4-3] and [4-4] gives the following system of mass and x , y and z direction momentum balance equations, respectively:

$$[4-6] \quad \frac{\partial v_x}{\partial x} + \frac{\partial v_y}{\partial y} + \frac{\partial v_z}{\partial z} = 0$$

$$[4-7] \quad \rho \left(\frac{\partial v_x}{\partial t} + \frac{\partial (v_x^2)}{\partial x} + \frac{\partial (v_x v_y)}{\partial y} + \frac{\partial (v_x v_z)}{\partial z} \right) = - \left(\frac{\partial \sigma_x}{\partial x} + \frac{\partial \tau_{yx}}{\partial y} + \frac{\partial \tau_{zx}}{\partial z} \right) + \rho g_x$$

$$[4-8] \quad \rho \left(\frac{\partial v_y}{\partial t} + \frac{\partial (v_y v_x)}{\partial x} + \frac{\partial (v_y^2)}{\partial y} + \frac{\partial (v_y v_z)}{\partial z} \right) = - \left(\frac{\partial \tau_{xy}}{\partial x} + \frac{\partial \sigma_y}{\partial y} + \frac{\partial \tau_{zy}}{\partial z} \right) + \rho g_y$$

$$[4-9] \quad \rho \left(\frac{\partial v_z}{\partial t} + \frac{\partial (v_z v_x)}{\partial x} + \frac{\partial (v_z v_y)}{\partial y} + \frac{\partial (v_z^2)}{\partial z} \right) = - \left(\frac{\partial \tau_{xz}}{\partial x} + \frac{\partial \tau_{yz}}{\partial y} + \frac{\partial \sigma_z}{\partial z} \right) + \rho g_z$$

Equations [4-6] to [4-9] are the most general form of the incompressible continuum mass and momentum balance equations.

4.4 Boundary conditions

Extremely rapid landslides are generally well-bounded by the landslide-atmosphere interface at the top and the landslide-bed interface at the base. The stress state and kinematic conditions at these two interfaces comprise the boundary conditions. It is useful to orient the reference coordinate system so that the depth of the flow, h , and the depth of the bed, b , are measured in the z direction, with $z=0$ corresponding to the bottom of the bed (Figure 4.2). For the moment, this direction can still be somewhat arbitrary and does not necessarily have

to correspond with either the vertical or bed-normal directions (the directions in which subsequent depth-averaging is typically performed).

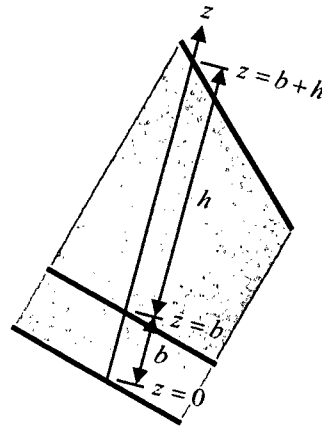


Figure 4.2. Generic orientation of the reference coordinate system. A more specific orientation is employed in DAN3D (cf., Figure 4.3).

4.4.1 Stress conditions

The top surface is assumed to be stress free (relative to the atmospheric pressure). The bed-normal stress at the base balances the bed-normal component of the total weight of material above, including the influence of centripetal acceleration due to bed curvature. The basal shear stress can depend on many factors, including the composition of the material near the base and its strength and drainage characteristics. A description of alternative constitutive relationships for the basal shear strength, consistent with the equivalent fluid approach, is deferred to Section 4.7 in order to keep this derivation as general as possible.

4.4.2 Kinematic conditions

It is assumed that material does not enter or leave the landslide at the free surface. This approach neglects entrainment of material from bank failures that may occur as the landslide passes and also neglects possible ejection of material from the free surface. The kinematic boundary condition at the free surface is then:

$$[4-10] \quad \frac{\partial(b+h)}{\partial t} + v_{x(z=b+h)} \frac{\partial(b+h)}{\partial x} + v_{y(z=b+h)} \frac{\partial(b+h)}{\partial y} - v_{z(z=b+h)} = 0$$

It is assumed that material may only enter the landslide at the bed, due to scour of material in the path. Although plowing is technically a free surface phenomenon, which occurs at the flow front, it is treated here mathematically as a component of basal erosion. Consistent with the previous assumption of constant density, it is assumed that the bulk density of the entrained material is the same as that of the landslide. This assumption is valid, for example, for debris avalanches that initiate in the same surficial deposits that are encountered along the path. It is also a reasonable assumption for rock avalanches that entrain saturated material. It must be acknowledged, however, that some common path materials, including ice and snow, can have bulk densities significantly different from those of an overriding landslide, which limits the validity of the constant density assumption in certain cases. The time-dependent rate at which bed material enters the landslide, E_t , is also known as the “erosion velocity” (Takahashi 1991). The erosion velocity is considered to be positive during erosion, consistent with Takahashi’s (1991) definition. The kinematic boundary condition at the bed is:

$$[4-11] \quad \frac{\partial b}{\partial t} + v_{x(z=b)} \frac{\partial b}{\partial x} + v_{y(z=b)} \frac{\partial b}{\partial y} - v_{z(z=b)} = -E_t$$

4.5 Depth-averaging

It would be computationally-expensive to perform a numerical solution of the full system of governing equations presented in Section 4.3. Integrating these equations between the bed and the free surface, imposing the boundary conditions, substituting appropriate depth-averaged values and making appropriate assumptions based on scaling arguments produces a much more useful system of equations. The classical St. Venant shallow water equations are based on the same depth-averaging procedure.

Two important manipulations are used frequently during the depth-averaging process. The first is Leibniz's rule for interchanging the order of differentiation and integration (e.g.,

$$\int_{z=b}^{z=b+h} \frac{\partial v_x}{\partial x} dz = \frac{\partial}{\partial x} \int_{z=b}^{z=b+h} v_x dz - v_{x(z=b+h)} \frac{\partial(b+h)}{\partial x} + v_{x(z=b)} \frac{\partial b}{\partial x}).$$

The second defines a depth-averaged value of a function as the depth-wise integral of the function divided by the depth (e.g.,

$$\bar{v}_x = \frac{1}{h} \int_{z=b}^{z=b+h} v_x dz, \text{ where the overbar denotes a depth-averaged value).}$$

4.5.1 Depth-averaging the mass balance equation

Integrating Equation [4-6] in the z direction from $z = b$ to $z = b + h$:

$$\begin{aligned} \int_{z=b}^{z=b+h} \left(\frac{\partial v_x}{\partial x} + \frac{\partial v_y}{\partial y} + \frac{\partial v_z}{\partial z} \right) dz &= 0 \\ &= \frac{\partial(\bar{v}_x h)}{\partial x} + \frac{\partial(\bar{v}_y h)}{\partial y} \\ &\quad - \left(v_{x(z=b+h)} \frac{\partial(b+h)}{\partial x} + v_{y(z=b+h)} \frac{\partial(b+h)}{\partial y} - v_{z(z=b+h)} \right) \\ &\quad + \left(v_{x(z=b)} \frac{\partial b}{\partial x} + v_{y(z=b)} \frac{\partial b}{\partial y} - v_{z(z=b)} \right) \end{aligned} \quad [4-12]$$

Substituting the kinematic boundary conditions from Equations [4-10] and [4-11] into Equation [4-12], the depth-averaged mass balance equation is:

$$[4-13] \quad \frac{\partial h}{\partial t} + \frac{\partial(\bar{v}_x h)}{\partial x} + \frac{\partial(\bar{v}_y h)}{\partial y} = E_t$$

4.5.2 Depth-averaging the momentum balance equations

The depth-averaging process is described here in the x direction only, but identical manipulations apply in the y and z directions. Integrating first the left side of Equation [4-

7] in the z direction from $z = b$ to $z = b + h$:

$$\begin{aligned}
 & \int_{z=b}^{z=b+h} \left(\rho \left(\frac{\partial v_x}{\partial t} + \frac{\partial (v_x^2)}{\partial x} + \frac{\partial (v_x v_y)}{\partial y} + \frac{\partial (v_x v_z)}{\partial z} \right) \right) dz \\
 [4-14] \quad & = \rho \left(\begin{aligned} & \frac{\partial (\overline{v_x h})}{\partial t} + \frac{\partial (\overline{v_x^2 h})}{\partial x} + \frac{\partial (\overline{v_x v_y h})}{\partial y} \\ & - v_{x(z=b+h)} \left(\frac{\partial (b+h)}{\partial t} + v_{x(z=b+h)} \frac{\partial (b+h)}{\partial x} + v_{y(z=b+h)} \frac{\partial (b+h)}{\partial y} - v_{z(z=b+h)} \right) \\ & + v_{x(z=b)} \left(\frac{\partial b}{\partial t} + v_{x(z=b)} \frac{\partial b}{\partial x} + v_{y(z=b)} \frac{\partial b}{\partial y} - v_{z(z=b)} \right) \end{aligned} \right)
 \end{aligned}$$

Substituting the kinematic boundary conditions from Equations [4-10] and [4-11] into Equation [4-14]:

$$\begin{aligned}
 & \int_{z=b}^{z=b+h} \left(\rho \left(\frac{\partial v_x}{\partial t} + \frac{\partial (v_x^2)}{\partial x} + \frac{\partial (v_x v_y)}{\partial y} + \frac{\partial (v_x v_z)}{\partial z} \right) \right) dz \\
 [4-15] \quad & = \rho \left(\frac{\partial (\overline{v_x h})}{\partial t} + \frac{\partial (\overline{v_x^2 h})}{\partial x} + \frac{\partial (\overline{v_x v_y h})}{\partial y} - v_{x(z=b)} E_t \right)
 \end{aligned}$$

where $E_t \geq 0$ (a negative value of E_t signifies deposition). This constraint must be imposed explicitly on the momentum balance equations because the process of deposition is external to the chosen reference frame. Material that leaves simply removes its own share of the momentum, without influencing the momentum of the material that remains within the reference frame (Hungry 1995). A negative erosion velocity in the momentum balance equations would imply, erroneously, that the process is internal to the flow and would produce a thrust in the direction of motion similar to that of a rocket (cf., Cannon and Savage 1988; Hungry 1990; Cannon and Savage 1990; Erlichson 1991).

Because the depth-wise velocity profile may be nonuniform, resulting in differential advection of momentum, momentum corrections must be applied to relate $\overline{v_x^2}$ to $\overline{v_x}^2$ and $\overline{v_x v_y}$ to $\overline{v_x} \overline{v_y}$, which allows the derivation to proceed with a further separation of terms (e.g., $\overline{v_x^2} = \zeta \overline{v_x}^2$, where ζ is a momentum correction coefficient). When the velocity in the y direction is zero, for example, a value of $\zeta = 1.2$ applies if the depth-wise velocity profile is parabolic (i.e., no basal sliding) and a value of $\zeta = 1$ applies if the depth-wise velocity profile is uniform (i.e., full basal sliding) (Savage and Hutter 1989). Since rapid landslides typically exhibit some degree of basal sliding, the required momentum correction is typically small and it is therefore commonly assumed that $\overline{v_x^2} = \overline{v_x}^2$ and $\overline{v_x v_y} = \overline{v_x} \overline{v_y}$. Substituting these relationships into Equation [4-15], expanding the partial derivatives and collecting terms:

$$\begin{aligned}
 [4-16] \quad & \int_{z=b}^{z=b+h} \left(\rho \left(\frac{\partial v_x}{\partial t} + \frac{\partial (v_x^2)}{\partial x} + \frac{\partial (v_x v_y)}{\partial y} + \frac{\partial (v_x v_z)}{\partial z} \right) \right) dz \\
 & = \rho \left(\overline{v_x} \left(\frac{\partial h}{\partial t} + \frac{\partial (\overline{v_x} h)}{\partial x} + \frac{\partial (\overline{v_y} h)}{\partial y} \right) + h \left(\frac{\partial \overline{v_x}}{\partial t} + \overline{v_x} \frac{\partial \overline{v_x}}{\partial x} + \overline{v_y} \frac{\partial \overline{v_x}}{\partial y} \right) - v_{x(z=b)} E_t \right)
 \end{aligned}$$

Substituting the depth-averaged mass balance Equation [4-13] into Equation [4-16]:

$$\begin{aligned}
 [4-17] \quad & \int_{z=b}^{z=b+h} \left(\rho \left(\frac{\partial v_x}{\partial t} + \frac{\partial (v_x^2)}{\partial x} + \frac{\partial (v_x v_y)}{\partial y} + \frac{\partial (v_x v_z)}{\partial z} \right) \right) dz \\
 & = \rho \left(h \left(\frac{\partial \overline{v_x}}{\partial t} + \overline{v_x} \frac{\partial \overline{v_x}}{\partial x} + \overline{v_y} \frac{\partial \overline{v_x}}{\partial y} \right) + (\overline{v_x} - v_{x(z=b)}) E_t \right)
 \end{aligned}$$

Now, integrating the right side of Equation [4-7] in the z direction from $z = b$ to $z = b + h$:

$$\begin{aligned}
& \int_{z=b}^{z=b+h} \left(- \left(\frac{\partial \sigma_x}{\partial x} + \frac{\partial \tau_{yx}}{\partial y} + \frac{\partial \tau_{zx}}{\partial z} \right) + \rho g_x \right) dz \\
[4-18] \quad & = - \left(\frac{\partial(\overline{\sigma_x h})}{\partial x} + \frac{\partial(\overline{\tau_{yx} h})}{\partial y} \right. \\
& \quad \left. - \left(\sigma_{x(z=b+h)} \frac{\partial(b+h)}{\partial x} + \tau_{yx(z=b+h)} \frac{\partial(b+h)}{\partial y} - \tau_{zx(z=b+h)} \right) \right. \\
& \quad \left. + \left(\sigma_{x(z=b)} \frac{\partial b}{\partial x} + \tau_{yx(z=b)} \frac{\partial b}{\partial y} - \tau_{zx(z=b)} \right) \right) + \rho h g_x
\end{aligned}$$

Substituting the stress free boundary condition at the top into Equation [4-18]:

$$\begin{aligned}
& \int_{z=b}^{z=b+h} \left(- \left(\frac{\partial \sigma_x}{\partial x} + \frac{\partial \tau_{yx}}{\partial y} + \frac{\partial \tau_{zx}}{\partial z} \right) + \rho g_x \right) dz \\
[4-19] \quad & = - \left(\frac{\partial(\overline{\sigma_x h})}{\partial x} + \frac{\partial(\overline{\tau_{yx} h})}{\partial y} + \left(\sigma_{x(z=b)} \frac{\partial b}{\partial x} + \tau_{yx(z=b)} \frac{\partial b}{\partial y} - \tau_{zx(z=b)} \right) \right) + \rho h g_x
\end{aligned}$$

As mentioned, the same series of manipulations can be performed in the y and z directions. The resulting depth-averaged momentum balance equations in the x , y and z directions are, respectively:

$$\begin{aligned}
& \rho \left(h \left(\frac{\partial \overline{v_x}}{\partial t} + \overline{v_x} \frac{\partial \overline{v_x}}{\partial x} + \overline{v_y} \frac{\partial \overline{v_x}}{\partial y} \right) + (\overline{v_x} - v_{x(z=b)}) E_t \right) \\
[4-20] \quad & = - \left(\frac{\partial(\overline{\sigma_x h})}{\partial x} + \frac{\partial(\overline{\tau_{yx} h})}{\partial y} + \left(\sigma_{x(z=b)} \frac{\partial b}{\partial x} + \tau_{yx(z=b)} \frac{\partial b}{\partial y} - \tau_{zx(z=b)} \right) \right) + \rho h g_x
\end{aligned}$$

$$\begin{aligned}
& \rho \left(h \left(\frac{\partial \overline{v_y}}{\partial t} + \overline{v_x} \frac{\partial \overline{v_y}}{\partial x} + \overline{v_y} \frac{\partial \overline{v_y}}{\partial y} \right) + (\overline{v_y} - v_{y(z=b)}) E_t \right) \\
[4-21] \quad & = - \left(\frac{\partial(\overline{\tau_{xy} h})}{\partial x} + \frac{\partial(\overline{\sigma_y h})}{\partial y} + \left(\tau_{xy(z=b)} \frac{\partial b}{\partial x} + \sigma_{y(z=b)} \frac{\partial b}{\partial y} - \tau_{zy(z=b)} \right) \right) + \rho h g_y
\end{aligned}$$

$$\begin{aligned}
[4-22] \quad & \rho \left(h \left(\frac{\partial \bar{v}_z}{\partial t} + \bar{v}_x \frac{\partial \bar{v}_z}{\partial x} + \bar{v}_y \frac{\partial \bar{v}_z}{\partial y} \right) + (\bar{v}_z - v_{z(z=b)}) E_t \right) \\
& = - \left(\frac{\partial (\bar{\tau}_{xz} h)}{\partial x} + \frac{\partial (\bar{\tau}_{yz} h)}{\partial y} + \left(\tau_{xz(z=b)} \frac{\partial b}{\partial x} + \tau_{yz(z=b)} \frac{\partial b}{\partial y} - \sigma_{z(z=b)} \right) \right) + \rho h g_z
\end{aligned}$$

Equations [4-13], [4-20], [4-21] and [4-22] are the most general form of the Eulerian, depth-averaged governing equations.

4.6 Further simplifications

4.6.1 Lagrangian reference frame

A number of additional manipulations can be performed to simplify this system. First, the equations can be recast in their Lagrangian form by substituting Lagrangian derivatives for their Eulerian counterparts (e.g., $\frac{Dh}{Dt} = \left(\frac{\partial h}{\partial t} + \bar{v}_x \frac{\partial h}{\partial x} + \bar{v}_y \frac{\partial h}{\partial y} \right)$, where the left side is the Lagrangian form and the right side is the Eulerian form). Lagrangian derivatives are taken with respect to a reference frame that moves with the material and are therefore also known as material, substantive, advective or convective derivatives. Expanding the partial derivatives in the mass balance Equation [4-13], collecting terms and substituting the Lagrangian derivative of h for its corresponding Eulerian derivative gives the following Lagrangian form of the depth-averaged mass balance equation:

$$[4-23] \quad \frac{Dh}{Dt} + h \left(\frac{\partial (\bar{v}_x)}{\partial x} + \frac{\partial (\bar{v}_y)}{\partial y} \right) = E_t$$

Second, several terms cancel out of the momentum balance equations with an appropriate reorientation of the reference coordinate system. In DAN3D, the z direction is aligned with the local bed-normal direction (Figure 4.3) and the x direction is aligned with the local

direction of motion, which eliminates spatial derivatives of b as well as y and z direction components of velocity.

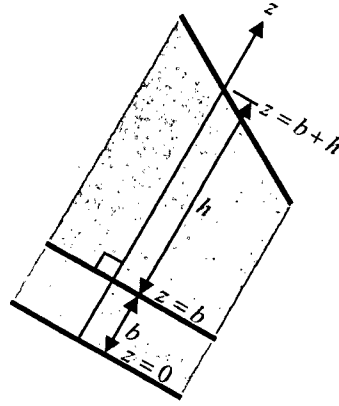


Figure 4.3. Orientation of the Lagrangian reference coordinate system used in DAN3D. The z direction is aligned with the local bed-normal direction (the x direction, not shown, is aligned with the local direction of motion).

Substituting the Lagrangian derivatives of v_x , v_y and v_z for their corresponding Eulerian counterparts and reorienting the local reference coordinate system, the Lagrangian forms of the depth-averaged momentum balance equations in the x , y and z directions are, respectively:

$$[4-24] \quad \rho \left(h \frac{D\bar{v}_x}{Dt} + (\bar{v}_x - v_{x(z=b)}) E_t \right) = -\frac{\partial(\bar{\sigma}_x h)}{\partial x} - \frac{\partial(\bar{\tau}_{yx} h)}{\partial y} + \tau_{zx(z=b)} + \rho h g_x$$

$$[4-25] \quad \rho h \frac{D\bar{v}_y}{Dt} = -\frac{\partial(\bar{\tau}_{xy} h)}{\partial x} - \frac{\partial(\bar{\sigma}_y h)}{\partial y} + \rho h g_y$$

$$[4-26] \quad \rho h \frac{D\bar{v}_z}{Dt} = -\frac{\partial(\bar{\tau}_{xz} h)}{\partial x} - \frac{\partial(\bar{\tau}_{yz} h)}{\partial y} + \sigma_{z(z=b)} + \rho h g_z$$

A Lagrangian approach has been adopted for the following three reasons: 1) as shown above, the convective acceleration terms are eliminated from the momentum balance equations, which facilitates subsequent numerical integration and improves efficiency; 2) higher resolution is possible because available computational resources can be concentrated within the simulated slide mass, where they are needed (cf., Chapter 3); and 3) DAN3D becomes a logical extension of DAN, which was also formulated in the Lagrangian framework.

4.6.2 Shallow flow assumption

Further simplifications can be made using the following scaling argument, which is well-established (cf., Savage and Hutter 1989; Gray et al. 1999). Assuming that the depth varies gradually and is small relative to the length and width of the landslide, the terms containing shear stress derivatives of τ_{xz} and τ_{yz} in Equation [4-26] are correspondingly small relative to the total bed-normal stress at the base, $\sigma_{z(z=h)}$, and can therefore be neglected. This is the classical shallow flow assumption (e.g., Chow 1959).

When the flow is in contact with the bed, the bed-normal curvature of the flow is equal to the bed-normal curvature of the path. It follows that, unless the material is airborne, the Lagrangian derivative of v_z is equal to the centripetal acceleration due to bed-normal curvature of the path in the direction of motion:

$$[4-27] \quad \frac{D\overline{v_z}}{Dt} = \frac{\overline{v_x}^2}{R}$$

where R is the bed-normal radius of curvature of the path in the direction of motion, which is considered to be positive for concave curvature. The z direction component of gravity is:

$$[4-28] \quad g_z = -g \cos \alpha$$

where g is the acceleration due to gravity and α is the inclination of the bed from horizontal. Substituting Equations [4-27] and [4-28] into Equation [4-26], neglecting the relatively small shear stress derivatives and rearranging terms produces the following expression for the total bed-normal stress at the base:

$$[4-29] \quad \sigma_{z(z=b)} = \rho h \left(g \cos \alpha + \frac{v_x^2}{R} \right)$$

Note that the value of $\sigma_{z(z=b)}$ becomes negative when $\frac{v_x^2}{R} > g \cos \alpha$, which implies that the material becomes airborne. Although ballistic/freefall conditions commonly occur in extremely rapid landslides, they are not accounted for explicitly in DAN3D (or in any other existing continuum dynamic model). As a result, net energy losses associated with impact after freefall must be implicitly accounted for in the basal shear strength term. A method to account for such effects explicitly could possibly be implemented in a future version of the model.

4.6.3 Stress state normalization

Further simplifications are possible with the use of classical soil mechanics techniques. Assuming that all stresses increase linearly with depth below the free surface, and consistent with the Rankine earth pressure theory described in Chapter 2, it is useful to normalize the stress state with respect to the total bed-normal stress using stress coefficients, denoted by k (e.g., $\sigma_x = k_x \sigma_z$). The use of stress coefficients facilitates a function that allows the internal stress distribution to develop in compatibility with strain as the landslide deforms. This function is described in detail in the next chapter. Note that the normalization in this case is performed on total stresses, whereas the Rankine normalization described in Chapter 2 was performed on effective stresses. With reference to Figure 2.6 in Chapter 2, the normalized total stress state on an element of material within a landslide is shown in Figure 4.4. Substituting the appropriate terms into Equations [4-24] and [4-25]:

$$[4-30] \quad \rho \left(h \frac{D\bar{v}_x}{Dt} + (\bar{v}_x - v_{x(z=h)}) E_t \right) = -\frac{\partial(k_x \bar{\sigma}_z h)}{\partial x} - \frac{\partial(k_{yx} \bar{\sigma}_z h)}{\partial y} + \tau_{zx(z=h)} + \rho h g_x$$

$$[4-31] \quad \rho h \frac{D\bar{v}_y}{Dt} = -\frac{\partial(k_{xy} \bar{\sigma}_z h)}{\partial x} - \frac{\partial(k_y \bar{\sigma}_z h)}{\partial y} + \rho h g_y$$

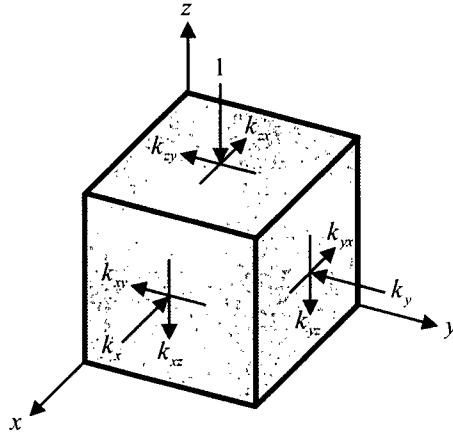


Figure 4.4. Normalized total stress state on an element of material within a landslide. The normalization is with respect to the total bed-normal stress (e.g., $k_x = \sigma_x / \sigma_z$). The stress coefficients are considered positive as shown. Compare with Figure 2.6 in Chapter 2.

Finally, it is assumed that spatial variations in the normalized stress state (e.g., $\frac{\partial k_x}{\partial x}$) are relatively small and can therefore be neglected (Gray et al. 1999). Expanding the partial derivatives in Equations [4-30] and [4-31], neglecting terms containing derivatives of stress coefficients and rearranging terms, the Lagrangian forms of the depth-averaged momentum balance equations in the x and y directions are, respectively:

$$[4-32] \quad \rho h \frac{D\bar{v}_x}{Dt} = \rho h g_x - k_x \sigma_{z(z=h)} \frac{\partial h}{\partial x} - k_{yx} \sigma_{z(z=h)} \frac{\partial h}{\partial y} + \tau_{zx(z=h)} - \rho (\bar{v}_x - v_{x(z=h)}) E_t$$

$$[4-33] \quad \rho h \frac{D\bar{v}_y}{Dt} = \rho h g_y - k_y \sigma_{z(z=h)} \frac{\partial h}{\partial y} - k_{xy} \sigma_{z(z=h)} \frac{\partial h}{\partial x}$$

The terms on the left side of Equations [4-32] and [4-33] represent local depth-averaged accelerations of a moving reference column of material (multiplied by the mass of the column per unit basal area). The first three terms on the right side represent depth-averaged gravity, normal and transverse shear stresses, respectively. Additional terms appear in the x direction momentum balance equation due to the assumed orientation of the reference coordinate system. The fourth term on the right side of Equation [4-32] represents the basal shear stress, which is described in more detail in the next section. The fifth term represents momentum flux due to entrainment of path material. Note again that $E_i \geq 0$.

Equations [4-23], [4-29], [4-32] and [4-33] are the fundamental system of depth-averaged, Lagrangian mass and momentum balance equations used in DAN3D. Additional simplifications due to assumptions specific to the numerical solution method are described in Chapter 5.

4.7 Basal shear resistance

The basal shear stress, $\tau_{zx(z=h)}$, opposes motion and, due to the chosen reference coordinate system orientation, is always negative. Consistent with the concept of equivalent fluid, $\tau_{zx(z=h)}$ is governed by a basal rheology that may be different from the internal rheology. To allow the simulation of different types of rapid landslides involving different geological materials, a variety of basal rheological relationships can be implemented in DAN3D, including laminar, turbulent, plastic, Bingham, frictional and Voellmy rheologies. The user can change the basal rheology along the path or within the slide mass, in accordance with Objective #4 in Chapter 2.

4.7.1 Laminar

Laminar flow is characteristically smooth and streamlined and is exhibited by Newtonian fluids (in which shear stresses are linearly proportional to shear rate) at relatively low Reynolds numbers (the ratio of inertial to viscous stresses). Laminar basal shear resistance is proportional to the depth-averaged flow velocity and inversely proportional to the flow depth. In the DAN3D coordinate system:

$$[4-34] \tau_{zx(z=h)} = -\frac{3\mu\bar{v}_x}{h}$$

where μ is the dynamic viscosity. Note that, in the equivalent fluid framework, the landslide material does not have to be strictly Newtonian for the laminar resistance relationship to be applied.

4.7.2 Turbulent

At relatively higher ratios of inertial to viscous stresses, flow may transition to a turbulent regime, which is characterized by intense mixing. Turbulent basal shear resistance is proportional to the square of the depth-averaged flow velocity and can be calculated using the Manning equation:

$$[4-35] \tau_{zx(z=h)} = -\frac{\rho g n^2 \bar{v}_x^2}{h^{\frac{1}{3}}}$$

where n is the Manning roughness coefficient. A common alternative to Equation [4-35] is the Chézy equation:

$$[4-36] \tau_{zx(z=h)} = -\frac{\rho g \bar{v}_x^2}{C^2}$$

where C is the Chézy coefficient, which is related to Manning's n by $C = h^{1/6}/n$. Again, turbulent resistance does not necessarily apply only to Newtonian fluids within the equivalent fluid framework.

4.7.3 Plastic

Plastic behaviour occurs when the basal shear strength is constant:

$$[4-37] \tau_{zx(z=h)} = -c$$

where c represents a constant shear strength, such as the undrained shear strength of clay.

4.7.4 Bingham

The Bingham resistance model combines plastic and viscous behaviour. A so-called Bingham fluid behaves as a rigid material below a threshold yield strength, but as a viscous material above. The following cubic equation must be solved to determine the basal shear resistance:

$$[4-38] \tau_{zx(z=h)}^3 + 3 \left(\frac{\tau_{yield}}{2} + \frac{\mu_{Bingham} \bar{V}_x}{h} \right) \tau_{zx(z=h)}^2 - \frac{\tau_{yield}^3}{2} = 0$$

where τ_{yield} is the Bingham yield stress and $\mu_{Bingham}$ is the Bingham viscosity.

4.7.5 Frictional

Frictional behaviour was introduced in Chapter 2 and is often exhibited by granular materials. Frictional basal resistance is proportional to the effective bed-normal stress at the

base, σ'_z , which is the difference between the total bed-normal stress at the base, σ_z , and the pore fluid pressure at the base, u :

$$[4-39] \quad \tau_{zx(z=h)} = -(\sigma_z - u)_{(z=h)} \tan \phi = -\sigma'_z{}_{(z=h)} \tan \phi$$

where ϕ is the dynamic basal friction angle. Pore fluid pressure can be related to the total bed-normal stress using the pore pressure ratio, $r_u = u/\sigma_z$, in which case:

$$[4-40] \quad \tau_{zx(z=h)} = -\sigma_z{}_{(z=h)} (1 - r_u)_{(z=h)} \tan \phi$$

Equation [4-40] can be simplified to include only one independent variable, a bulk basal friction angle, ϕ_b , where $\tan \phi_b = (1 - r_u) \tan \phi$:

$$[4-41] \quad \tau_{zx(z=h)} = -\sigma_z{}_{(z=h)} \tan \phi_b$$

Use of a constant pore pressure ratio or bulk basal friction angle assumes loading response that is intermediate between purely drained and undrained responses. The relationships between the various frictional parameters are shown in Figure 4.5.

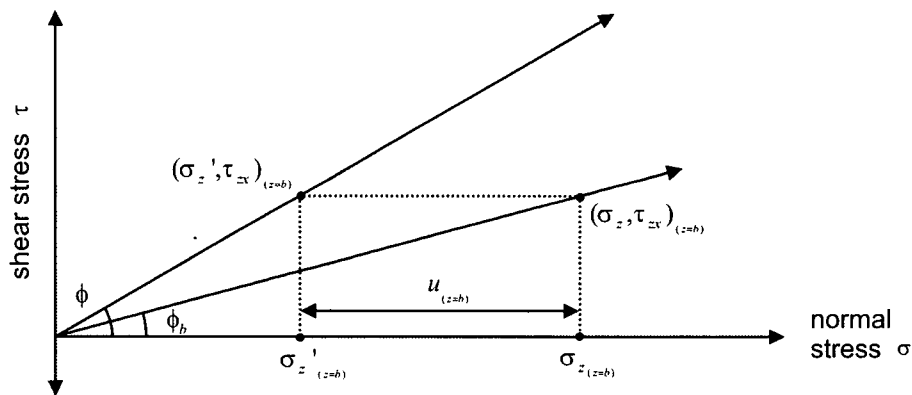


Figure 4.5. Relationships between frictional parameters in Equations [4-39] to [4-41].

4.7.6 Voellmy

The Voellmy resistance model combines frictional and turbulent behaviour:

$$[4-42] \quad \tau_{zx(z=h)} = - \left(\sigma_{z(z=h)} f + \frac{\rho g v_x^{-2}}{\xi} \right)$$

where f is the friction coefficient and ξ is the so-called turbulence parameter. The first term on the right side accounts for any frictional component of resistance and has the same form as Equation [4-41] (f is analogous to $\tan \phi_b$). The second term was originally introduced by Voellmy (1955) to account for the velocity-dependent influence of air drag on snow avalanches and has the same form as Equation [4-36] (ξ is analogous to the square of the Chézy coefficient). In the context of landslide dynamics and the equivalent fluid approach, the second term is not included to account for either air drag or turbulence alone, but rather to empirically account for all possible sources of velocity-dependent resistance (additional to the effects of path curvature and momentum transfer during entrainment, which are accounted for explicitly in DAN3D).

Although the Voellmy rheology should be viewed in this empirical sense, some physical justification for its application to saturated granular flows may have been provided by Bagnold (1954), who showed that both the effective normal stress and the shear stress in a dense dispersion of grains in fluid, rapidly sheared at constant volume, are proportional to the square of the shear strain rate. While this is still frictional behaviour, Voellmy's frictional term, defined only in terms of total stress, is unable to account for it. In effect, the turbulence-style term provides a correction that mimics the influence of velocity-dependent pore pressure and effective stress changes. In any case, the Voellmy rheology has been used successfully by many researchers to model various types of mass movements, including snow avalanches, rock avalanches, flow slides, debris avalanches and debris flows (e.g., Perla et al. 1980; Körner 1976; Hungr et al. 2002; Revellino et al. 2004; Rickenmann and Koch 1997).

4.8 Discussion

Equations [4-23], [4-29], [4-32] and [4-33], when combined with one of Equations [4-34] to [4-42], produce a flexible system that incorporates all five of the essential features that were described in Chapter 2. The effects of 3D terrain, including centripetal acceleration due to path curvature, are handled using a depth-averaged multi-dimensional approach. The resulting equations account for the possibility of non-hydrostatic, anisotropic internal stresses using a method based on classical Rankine earth pressure theory. Mass and momentum transfer due to entrainment are incorporated using the established concept of erosion velocity. An open basal rheological kernel permits the simulation of a variety of landslide types and allows users to implement rheology changes. Finally, the use of a Lagrangian reference frame with a suitable orientation simplifies the governing equations and minimizes the number of calculations required to solve them.

The system represents a 3D extension of the equivalent fluid approach first formalized by Hungr (1995), and the original DAN equations now form a special case. Neglecting transverse shear stresses and lateral (y direction) bed and free surface gradients, the depth-averaged momentum balance reduces to a single equation in the x direction, which is equivalent to the governing equation used by Hungr (1995):

$$[4-43] \quad \rho h \frac{D\bar{v}_x}{Dt} = \rho h g \sin \alpha - k_x \sigma_{z(z=h)} \frac{\partial h}{\partial x} + \tau_{zx(z=h)} - \rho \bar{v}_x E_t$$

where α is considered to be negative for an adverse slope and entrained bed material is assumed to be initially stationary (i.e., $v_{x(z=h)} = 0$).

The classical shallow water equations form another special case. Assuming hydrostatic, isotropic internal stress conditions appropriate for water (i.e., $k_x = k_y = 1$ and $k_{xy} = k_{yx} = 0$) and neglecting entrainment, the x and y direction momentum balance equations reduce to, respectively:

$$[4-44] \quad \rho h \frac{D\bar{v}_x}{Dt} = \rho h g_x - \sigma_{z(z=h)} \frac{\partial h}{\partial x} + \tau_{zx(z=h)}$$

$$[4-45] \quad \rho h \frac{D\bar{v}_y}{Dt} = \rho h g_y - \sigma_{z(z=h)} \frac{\partial h}{\partial y}$$

Flow is steady and uniform when $\frac{D\bar{v}_x}{Dt} = \frac{D\bar{v}_y}{Dt} = 0$, $R = \infty$ and $\frac{\partial h}{\partial x} = \frac{\partial h}{\partial y} = 0$, in which case:

$$[4-46] \quad \tau_{zx(z=h)} = -\rho h g \sin \alpha$$

The classical sliding block model is another special case. Assuming $\frac{\partial h}{\partial x} = \frac{\partial h}{\partial y} = 0$, the x and y direction momentum balance equations reduce to, respectively:

$$[4-47] \quad \rho h \frac{D\bar{v}_x}{Dt} = \rho h g_x + \tau_{zx(z=h)} - \rho (\bar{v}_x - v_{x(z=h)}) E_t$$

$$[4-48] \quad \rho h \frac{D\bar{v}_y}{Dt} = \rho h g_y$$

where ρh represents the mass of the block per unit basal area.

As in the most general case, in both the shallow water and sliding block cases a number of different scenarios can be analyzed using the available alternative basal resistance relationships.

4.9 Conclusion

The system of governing equations used in DAN3D has been derived from first principles using a straightforward series of explicit and justifiable assumptions and approximations.

Aspects of each of the five objectives for model development have been incorporated. The generality of the system, in accordance with the equivalent fluid approach, makes it applicable in a wide variety of situations. This flexibility facilitates the simulation of real landslides, but an equally flexible and efficient solution method is also required. The numerical method used in DAN3D is described in the next chapter.

5 NUMERICAL SOLUTION METHOD

5.1 Introduction

Continuum simulation is possible using a suitable discretization and numerical solution of the depth-averaged governing equations presented in Chapter 4 (Equations [4-23], [4-29], [4-32] and [4-33] plus one of [4-34] to [4-42]). The typical Lagrangian procedure involves discretization of the equations by applying them to a number of reference columns, which are distributed throughout the simulated slide mass and advected with the flow. The instantaneous local acceleration at each reference column location is determined by time-wise numerical integration of the momentum balance equations. Within a short time step, the local flow velocities are updated and the columns are advanced to new positions accordingly.

Estimates of the instantaneous values of the local independent variables, including the depth-averaged flow velocity, depth, depth gradient, stress coefficients, bed inclination angle, bed-normal radius of curvature of the path in the direction of motion and applicable entrainment and rheological parameters, are required to perform the momentum balance calculations. The depth and depth gradient estimates must satisfy mass balance requirements. In accordance with Objective #5 in Chapter 2, the methods used to estimate all of these values and perform the calculations should be as efficient as possible.

The purpose of this chapter is to describe the numerical method used in DAN3D, which represents a unique adaptation of a meshless Lagrangian method known as Smoothed Particle Hydrodynamics. Supplementary methods have been developed for estimating internal strain, redistributing internal stresses and accounting for mass changes due to entrainment. The resulting model runs on a microcomputer.

5.2 Smoothed Particle Hydrodynamics

5.2.1 Background

Traditional Lagrangian finite difference and finite element methods have been applied to the discretization approach described above (e.g., Gray et al. 1999; Chen and Lee 2000). Both methods require a mesh, which connects the computational elements, to perform the mass balance calculation (mass balance is maintained within the cells of the mesh). Problems with mesh tangling or distortion may limit the ability of these methods to handle large deformations due to spreading and/or splitting of the slide mass (Wieland et al. 1999). Adaptive meshing techniques can be incorporated, but at the expense of efficiency and continuity of information at the moving calculation points. The latter is an important limitation in landslide modelling, as the complex local stress conditions need to be carried forward in each time step.

Meshless particle methods (not to be confused with distinct element methods) provide an alternative and have been applied to many problems in computational fluid dynamics (e.g., Johnson 1996). In lieu of a mesh, mass balance is determined from the spatial distribution of a number of moving reference masses (known as particles). As described in Chapter 3, the Simplified Marker-and-Cell (Harlow and Welch 1965; Amsden and Harlow 1970) and Particle-in-Cell (Evans and Harlow 1957; Harlow 1957) methods have been applied specifically to landslide and snow avalanche modelling, respectively (e.g., Dent and Lang 1980; Sampl 1993). These methods require interpolation of data back and forth between the particles and a fixed grid, where the Eulerian momentum balance calculations are performed. Smoothed Particle Hydrodynamics (SPH) is a related but fully-Lagrangian method in which all of the calculations are performed directly at the particle-centred locations, eliminating the need for a fixed grid and the diffusion that can result from back and forth interpolation.

SPH was originally developed for the simulation of stellar evolution and other compressible astrophysical phenomena (e.g., Lucy 1977; Gingold and Monaghan 1977). Its development was motivated by the need for a flexible and efficient numerical method that could handle the

large distortions and complex dynamics inherent to such phenomena, similar to the objectives guiding the design of DAN3D. Comprehensive reviews of SPH were presented by Benz (1989) and Monaghan (1992). The full 3D SPH algorithm has been applied to the simulation of pyroclastic flows (Nagasawa and Kuwahara 1993) and dam-breaks (Cleary and Prakash 2004), but more efficient depth-averaged adaptations have been presented by Wang and Shen (1999) and Bursik et al. (2003), the latter specifically in the context of landslide modelling.

5.2.2 Theory

SPH is based on the following concept from interpolation theory: the value of any function, f , at any location, \mathbf{r} , can be interpolated from its known values at locations \mathbf{r}' throughout the domain of interest:

$$[5-1] \quad f(\mathbf{r}) = \int f(\mathbf{r}')W(\mathbf{r}-\mathbf{r}',\ell) d\mathbf{r}'$$

where \mathbf{r} and \mathbf{r}' are position vectors, W is an interpolating kernel and ℓ is a smoothing length, which is a measure of the radius of influence of the kernel. The kernel has dimensions of L^{-1} , L^{-2} and L^{-3} in 1D, 2D and 3D, respectively, and integrates to unity across the infinite domain in each case:

$$[5-2] \quad \int W(\mathbf{r}-\mathbf{r}',\ell) d\mathbf{r}' = 1$$

The kernel approaches the form of a Dirac delta function, δ , as the smoothing length approaches zero:

$$[5-3] \quad \lim_{\ell \rightarrow 0} W(\mathbf{r}-\mathbf{r}',\ell) d\mathbf{r}' = \delta(\mathbf{r}-\mathbf{r}')$$

In the simplest sense, Equation [5-1] represents a weighted averaging procedure, in which the weighting is based on proximity, $r - r'$, according to the interpolating kernel. A number of kernels are possible, but most place higher weighting on closer values.

In numerical work, the value of a function is not known across the entire domain, but rather at a finite number of discrete locations. The fundamental premise of SPH is the discretization of Equation [5-1] into a usable form. The total mass is divided among a finite number of reference masses that are advected with the flow (known as smooth particles) and the integral interpolant in Equation [5-1] is approximated by the following summation interpolant:

$$[5-4] \quad f(r_i) = \sum_{j=1}^N \frac{m_j}{\rho(r_j)} f(r_j) W(r_i - r_j, \ell)$$

where N is the total number of particles, r_i is the position of particle i , r_j is the position of particle j , m_j is the mass of particle j and $\rho(r_j)$ is the flow density at r_j . Particle i is included in the N particles used in the summation. Significantly, the derivatives of the interpolant can be obtained by ordinary differentiation of the interpolating kernel. For example, the gradient of the function can be approximated by:

$$[5-5] \quad \nabla f(r_i) = \sum_{j=1}^N \frac{m_j}{\rho(r_j)} f(r_j) \nabla W(r_i - r_j, \ell)$$

The ratio $\frac{m_j}{\rho(r_j)}$ represents the volume occupied by particle j and its inverse, $\frac{\rho(r_j)}{m_j}$, represents the local number of particles per unit volume, or the volumetric particle number density. When the flow density is spatially and temporally constant, as assumed in the derivation presented in Chapter 4, the density of particle j , ρ_j , equals the local flow density, $\rho(r_j)$, and Equation [5-4] simplifies to:

$$[5-6] \quad f(\mathbf{r}_i) = \sum_{j=1}^N V_j f(\mathbf{r}_j) W(\mathbf{r}_i - \mathbf{r}_j, \ell)$$

where V_j is the volume of particle j . Equation [5-6] is the most general form of the SPH summation interpolant for 3D, incompressible flow. Equations [5-4] to [5-6] can be adapted for depth-averaged applications by using an areal, rather than volumetric, definition of the particle number density. For compressible flows the areal particle number density is

$$\frac{\rho(\mathbf{r}_j)}{m_j} h(\mathbf{r}_j) \text{ and for incompressible flows it is } \frac{h_j}{V_j}, \text{ in which case the depth-averaged form of}$$

Equation [5-6] is:

$$[5-7] \quad f(\mathbf{r}_i) = \sum_{j=1}^N \frac{V_j}{h(\mathbf{r}_j)} f(\mathbf{r}_j) W(\mathbf{r}_i - \mathbf{r}_j, \ell)$$

Note that a 1D or 2D interpolating kernel that satisfies Equations [5-2] and [5-3] must be used in this framework.

5.3 SPH-based mass balance

The main advantage of SPH is its ability to satisfy continuity implicitly, while other Lagrangian methods require some form of mesh within which to calculate the mass balance. In SPH, the required distribution of mass can be interpolated from the known distribution of the reference masses (the smooth particles) at any given time.

5.3.1 Depth and depth gradient interpolation

The procedure for estimating the landslide depth and depth gradient at each reference column location is as follows. The total volume of the landslide is divided among N particles. Each particle has a finite volume, which may only increase due to entrainment, and remains centred at the base of one of the moving reference columns (a method of distributing the

particles, given an initial distribution of material, is described in Section 5.9). As such, the column and corresponding particle positions on the sliding surface are identical, and it is therefore convenient to use the following abbreviated form of Equation [5-7]:

$$[5-8] \quad f_i = \sum_{j=1}^N \frac{V_j}{h_j} f_j W_{ij}$$

where subscripts i and j denote values corresponding to the interchangeable column/particle positions on the sliding surface. The flow depth, h_i , at each column/particle location can be approximated using Equation [5-8] by substituting the flow depth, h , for the generic function, f :

$$[5-9] \quad h_i = \sum_{j=1}^N V_j W_{ij}$$

Note that the flow depth is eliminated from the right side of the equation; only the known particle volumes and positions are required to perform the calculation. Again, particle i is included in the N particles used in the summation. Because only nearby particles contribute significantly to the summation, the efficiency of the method can be dramatically improved by limiting the summation to an appropriate radius of influence:

$$[5-10] \quad h_i = \sum_{j=1}^n V_j W_{ij}$$

where $j = 1$ to n are particles located within a local radius of influence, which depends on the chosen kernel and its smoothing length. In this context, the kernel determines how the volume of each particle is distributed about its centre. For example, using a Gaussian kernel, the volume of each particle is normally distributed about its centre and the particles can therefore be visualized as bell-shaped objects. According to Equation [5-10], the flow depth

anywhere can be determined simply by superposition of the bell-shaped particles. A simple physical interpretation of Equation [5-10] is presented in Figure 5.1.

As shown in Equation [5-5], the gradient of the summation interpolant can be obtained by ordinary differentiation of the interpolating kernel. As a result, the local depth gradient can be approximated by:

$$[5-11] \quad \nabla h_i = \sum_{j=1}^n V_j \nabla W_{ij}$$

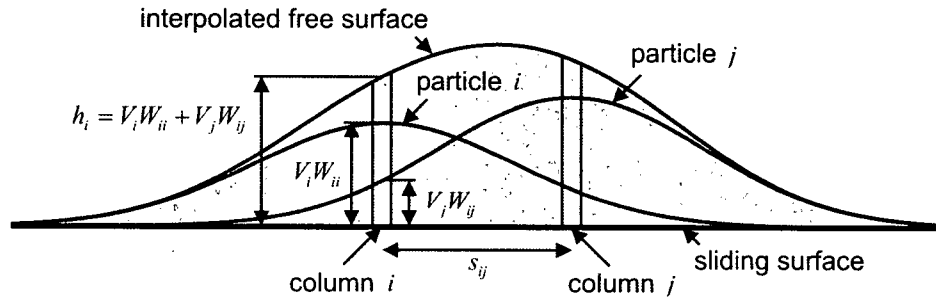


Figure 5.1. A physical interpretation of SPH in a depth-averaged framework. When the interpolating kernel is Gaussian, the particles can be visualized as bell-shaped objects. The total depth and depth gradient at any location are determined by superposition of the particles.

The depth and depth gradient interpolations in Equations [5-10] and [5-11] are essentially the same as those used by Wang and Shen (1999) in their SPH-based simulation of the classical 1D dam-break problem. In DAN3D, however, they are applied to interpolation across a potentially irregular 3D surface. The position of j with respect to i is defined by the local Cartesian coordinate system $(x, y, z)_i$, which is oriented as described in Chapter 4. The z axis intersects the column/particle-centred position on the sliding surface and is zeroed at the bottom of the bed (i.e., the base of the column is located at $z = b$), the z direction is aligned with the local bed-normal direction and the x direction is aligned with the local direction of motion. The distance between i and j is approximated by the straight-line distance s_{ij} :

$$[5-12] \quad s_{ij} = \sqrt{x_{ij}^2 + y_{ij}^2 + z_{ij}^2}$$

where x_{ij} , y_{ij} and z_{ij} are the distances between i and j with respect to the local coordinate axes. Curvature of the local sliding surface introduces some error, which is minimal as long as the flow depth is less than the radius of curvature of the surface, or in other words as long as the shallowness assumption is valid (cf., Chapter 4). The x and y components of Equation [5-11] are approximated by, respectively:

$$[5-13] \quad \left(\frac{\partial h}{\partial x} \right)_i = \sum_{j=1}^n V_j \left| \frac{\partial W}{\partial s} \right|_{ij} \frac{x_{ij}}{\sqrt{x_{ij}^2 + y_{ij}^2}}$$

$$[5-14] \quad \left(\frac{\partial h}{\partial y} \right)_i = \sum_{j=1}^n V_j \left| \frac{\partial W}{\partial s} \right|_{ij} \frac{y_{ij}}{\sqrt{x_{ij}^2 + y_{ij}^2}}$$

5.3.2 Interpolating kernel

A number of interpolating kernels that satisfy the criteria in Equations [5-2] and [5-3] can be used. However, as recommended by Monaghan (1992), a Gaussian kernel has been used almost exclusively in DAN3D. In 2D form (appropriate for a depth-averaged model for 3D terrain):

$$[5-15] \quad W_{ij \text{ (Gaussian)}} = \frac{1}{\pi \ell^2} e^{-\left(\frac{s_{ij}}{\ell}\right)^2}$$

$$[5-16] \quad \left| \frac{\partial W}{\partial s} \right|_{ij \text{ (Gaussian)}} = \frac{2s_{ij}}{\pi \ell^4} e^{-\left(\frac{s_{ij}}{\ell}\right)^2}$$

where the smoothing length at any given time is assumed to be the same everywhere. The Gaussian kernel and kernel gradient are asymptotic to zero at an infinite distance, but in

practice they are negligible at distances greater than about 3ℓ , so only the n particles within this radius need to be included in the summations. Because the kernel never actually reaches zero, a cutoff depth representing the margin of the flow must be specified by the user. Other kernels have explicit cutoffs. Kernels based on linear, quadratic and cubic functions, in which W and ∇W are zero if $\frac{s_{ij}}{\ell} > 2$, have also been implemented as options in DAN3D.

In 2D form they are, respectively:

$$[5-17] \quad W_{ij(\text{linear})} = \frac{1}{\pi \ell^2} \left(\frac{3}{8} \right) \left(2 - \frac{s_{ij}}{\ell} \right) \quad \text{if } \frac{s_{ij}}{\ell} < 2$$

$$[5-18] \quad \left| \frac{\partial W}{\partial s} \right|_{ij(\text{linear})} = \frac{1}{\pi \ell^3} \left(\frac{3}{8} \right) \quad \text{if } \frac{s_{ij}}{\ell} < 2$$

$$[5-19] \quad W_{ij(\text{quadratic})} = \frac{1}{\pi \ell^2} \left(\frac{3}{2} \right) \left(1 - \frac{s_{ij}}{\ell} + \frac{1}{4} \left(\frac{s_{ij}}{\ell} \right)^2 \right) \quad \text{if } \frac{s_{ij}}{\ell} < 2$$

$$[5-20] \quad \left| \frac{\partial W}{\partial s} \right|_{ij(\text{quadratic})} = \frac{1}{\pi \ell^3} \left(\frac{3}{2} \right) \left(1 - \frac{1}{2} \left(\frac{s_{ij}}{\ell} \right) \right) \quad \text{if } \frac{s_{ij}}{\ell} < 2$$

$$[5-21] \quad W_{ij(\text{cubic})} = \begin{cases} \frac{1}{\pi \ell^2} \left(\frac{5}{14} \right) \left(2 - \frac{s_{ij}}{\ell} \right)^3 & \text{if } 1 \leq \frac{s_{ij}}{\ell} < 2 \\ \frac{1}{\pi \ell^2} \left(\frac{10}{7} \right) \left(1 - \frac{3}{2} \left(\frac{s_{ij}}{\ell} \right)^2 + \frac{3}{4} \left(\frac{s_{ij}}{\ell} \right)^3 \right) & \text{if } \frac{s_{ij}}{\ell} < 1 \end{cases}$$

$$[5-22] \quad \left| \frac{\partial W}{\partial s} \right|_{ij(\text{cubic})} = \begin{cases} \frac{1}{\pi \ell^3} \left(\frac{15}{14} \right) \left(2 - \frac{s_{ij}}{\ell} \right)^2 & \text{if } 1 \leq \frac{s_{ij}}{\ell} < 2 \\ \frac{1}{\pi \ell^3} \left(\frac{30}{7} \right) \left(\frac{s_{ij}}{\ell} - \frac{3}{4} \left(\frac{s_{ij}}{\ell} \right)^2 \right) & \text{if } \frac{s_{ij}}{\ell} < 1 \end{cases}$$

The four alternative interpolating kernels are compared in Figure 5.2. The linear and quadratic kernels are not strictly smooth, as the resulting interpolated free surface contains peaks at each particle location. With the cone-shaped linear kernel, neighbouring particles “push” each other apart with the same force at any distance within two smoothing lengths of one another, which causes instabilities. The Gaussian and cubic kernels are very similar. In fact, with appropriate different smoothing lengths (i.e., when $\ell_{(cubic)} \cong \sqrt{10/7} \ell_{(Gaussian)}$) they are virtually identical. As a result, like other SPH-based models (e.g., Monaghan 1992), DAN3D is not very sensitive to the choice between them. Marginal efficiency can be gained with the cubic kernel, but because it is a well-known function with a simple physical interpretation (Monaghan 1992), the Gaussian kernel has been used for all of the analyses presented in this thesis.

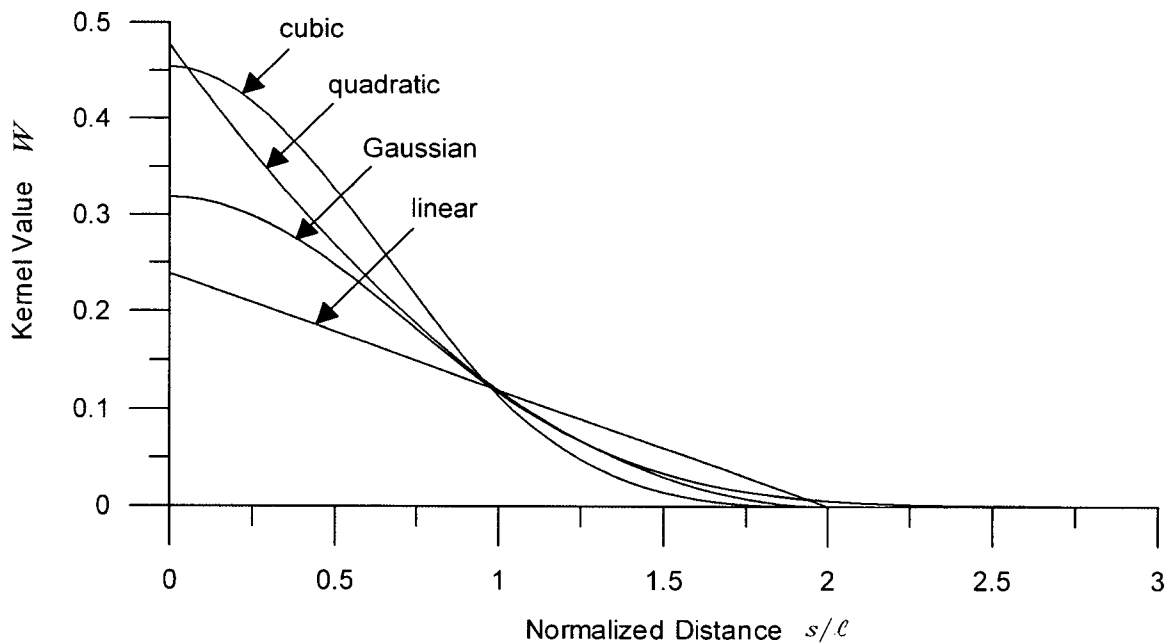


Figure 5.2. Comparison of different interpolating kernels that can be implemented in DAN3D. Physically, an interpolating kernel represents a cross-section of a single particle with unit volume. The Gaussian and cubic kernels form similar bell-shaped particles that produce smooth free surfaces.

To maintain resolution during large deformations (i.e., to have a relatively constant number of neighbouring particles within the radius of influence), DAN3D uses an adaptive smoothing length, analogous to an adaptive finite element mesh:

$$[5-23] \quad \ell = \frac{B}{\sqrt{\frac{\sum_{j=1}^N h_j}{V_j} \frac{1}{N}}}$$

where B is a dimensionless particle smoothing coefficient, which influences the smoothness

of the interpolated flow depth. The term $\frac{\sum_{j=1}^N h_j}{V_j} \frac{1}{N}$ is the average areal particle number density, which means that the number of particles within a radius of one smoothing length of each particle is, on average, equal to πB^2 . For example, a value of $B = 4$ gives each particle, on average, about 50 neighbours within a radius of one smoothing length. The sensitivity of the model to the value of B is investigated in Chapter 6.

This method of adaptive smoothing was recommended by Monaghan (1985) and has been used for all of the analyses presented in this thesis. But because the smoothing length is the same for all of the particles (i.e., spatially-constant), some resolution is sacrificed in regions with local particle number densities that deviate strongly from the overall average. This can occur near the flow margins, within channelized reaches of the path or within secondary flows that become separated from the main mass. A spatially-variable smoothing length is an alternative and can be implemented by limiting the summation in Equation [5-23] to a suitable radius of influence. Preliminary testing of this alternative has suggested that, while resolution can be improved, the ability of the model to handle highly channelized cases may be simultaneously sacrificed. This is because relatively higher local smoothing lengths result in channelized sections of the path, where each particle has a reduced number of neighbours in the lateral direction. The increased smoothing results in weaker inter-particle forces, which are then dominated by gravitational forces that eventually cause the particles to line up in the downstream direction. A directional spatially-variable smoothing method is a possible

solution to this problem. However, sensitivity analyses have suggested that both of these issues (resolution and particle alignment during channelization) can be resolved simply with the use of more particles (cf., Chapter 6). Because the capabilities of personal computers continue to improve, this solution may be the easiest to implement in future versions of the model.

5.4 Strain interpolation

5.4.1 Incremental tangential strain state

As described in Chapter 2, stresses in earth materials are strain-dependent, and strain within a 3D deforming landslide mass may be extremely complex. Similar to the stress tensor in Equation [4-5], the 3D strain tensor is:

$$[5-24] \quad \boldsymbol{\varepsilon} = \begin{bmatrix} \varepsilon_x & \frac{\gamma_{xy}}{2} & \frac{\gamma_{xz}}{2} \\ \frac{\gamma_{yx}}{2} & \varepsilon_y & \frac{\gamma_{yz}}{2} \\ \frac{\gamma_{zx}}{2} & \frac{\gamma_{zy}}{2} & \varepsilon_z \end{bmatrix}$$

where ε and γ denote normal and engineering shear strains, respectively. In the framework of a depth-averaged model, estimates of strain tangential to the bed are required in order to determine the tangential stresses using the Rankine theory. Plane strain in the tangential $x-y$ plane is assumed. As described in Section 5.5, the updated tangential stresses are coupled with the updated bed-normal and basal shear stresses to obtain the updated 3D stress state. The incremental tangential strain tensor is:

$$[5-25] \quad \Delta\boldsymbol{\varepsilon} = \begin{bmatrix} \Delta\varepsilon_x & \frac{\Delta\gamma_{xy}}{2} \\ \frac{\Delta\gamma_{yx}}{2} & \Delta\varepsilon_y \end{bmatrix}$$

5.4.2 Strain rosette method

The particle-tracking nature of the SPH method provides a framework for approximating the incremental tangential strain state at each reference column location. Tangential flow deformation can be approximated from relative particle motion; converging particles indicate flow compression while diverging particles indicate flow extension. DAN3D uses an approach analogous to strain measurement in flat plates using strain gauge rosettes (Figure 5.3).

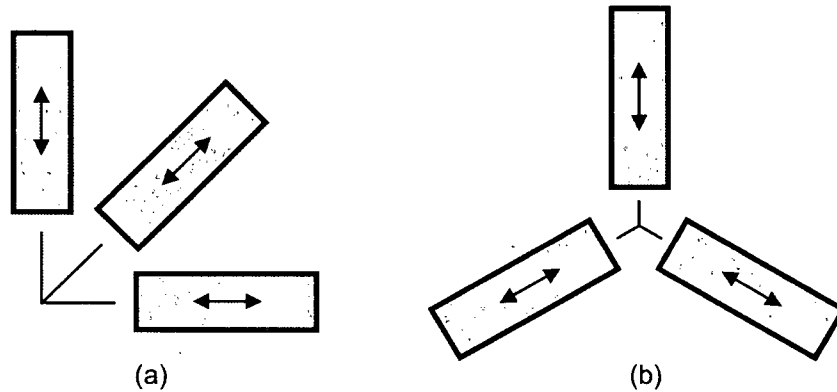


Figure 5.3. Plane strain measurement using strain gauge rosettes, a common technique in structural and mechanical engineering. The complete plane strain state (e.g., in a flat metal plate) can be determined using only three directional strain measurements. The directions can be arbitrary, as long as they are different, but typical rosette configurations are shown: (a) rectangular and (b) delta.

Neglecting the influence of reorientation of the local reference frame during the small time interval, the incremental tangential strain between two particles can be approximated by:

$$[5-26] \quad \Delta \epsilon_{ij} = \frac{s_{ij}' - s_{ij}}{s_{ij}'}$$

where the old separation distance is primed. Convergence of particles produces a positive strain. The relative direction to the neighbouring particle can be approximated by:

$$[5-27] \quad \theta_{ij} = \tan^{-1} \left(\frac{y_{ij}}{x_{ij}} \right)$$

where θ_{ij} is an angle in the local $x-y$ plane, measured counter-clockwise from the positive x -axis.

Using conventional strain compatibility theory, the particle-centred incremental tangential strain state in Equation [5-25] can be represented by the function:

$$[5-28] \quad \Delta\varepsilon(\theta)_i = \left(\frac{\Delta\varepsilon_x + \Delta\varepsilon_y}{2} \right)_i + \left(\frac{\Delta\varepsilon_x - \Delta\varepsilon_y}{2} \right)_i \cos 2\theta + \left(\frac{\Delta\gamma_{xy}}{2} \right)_i \sin 2\theta$$

where $\Delta\varepsilon(\theta)$ is the incremental tangential strain in the direction θ , θ is a parametric angle in the local $x-y$ plane, measured counter-clockwise from the positive x -axis, $\Delta\varepsilon_x$ is the incremental strain in the x -direction, $\Delta\varepsilon_y$ is the incremental strain in the y -direction and $\Delta\gamma_{xy}$ is the incremental transverse engineering shear strain. Equation [5-28] has the form of an equation of a plane, with $\cos 2\theta$ and $\sin 2\theta$ being the independent variables.

The procedure for interpolating the tangential strain state is as follows. At each time step and at each particle, values of $\Delta\varepsilon_{ij}$ and θ_{ij} corresponding to each neighbouring particle within a distance of one smoothing length are calculated. Substituting these values into Equation [5-28] produces a system of equations with three unknowns ($\Delta\varepsilon_x$, $\Delta\varepsilon_y$ and $\Delta\gamma_{xy}$). Analogous to the three gauge rosette method shown in Figure 5.3, when exactly three neighbouring particles are present there are three equations and the system is determined. With less than three neighbours the system is indeterminate and the influence of strain must be neglected; when two or three particles are isolated together the deformations are extremely limited, making this assumption reasonable, and when a single particle is isolated the flow depth gradient is zero and the local strain and stress states become irrelevant (cf., governing Equations [4-32] and [4-33]). With more than three neighbours, which is much more typical

when a smoothing coefficient close to $B = 4$ is used, the system is redundant and a least squares approximation is used to fit a plane to the data points, providing estimates of $\Delta\epsilon_x$, $\Delta\epsilon_y$ and $\Delta\gamma_{xy}$. A sample interpolation from a DAN3D simulation is shown in Figure 5.4.

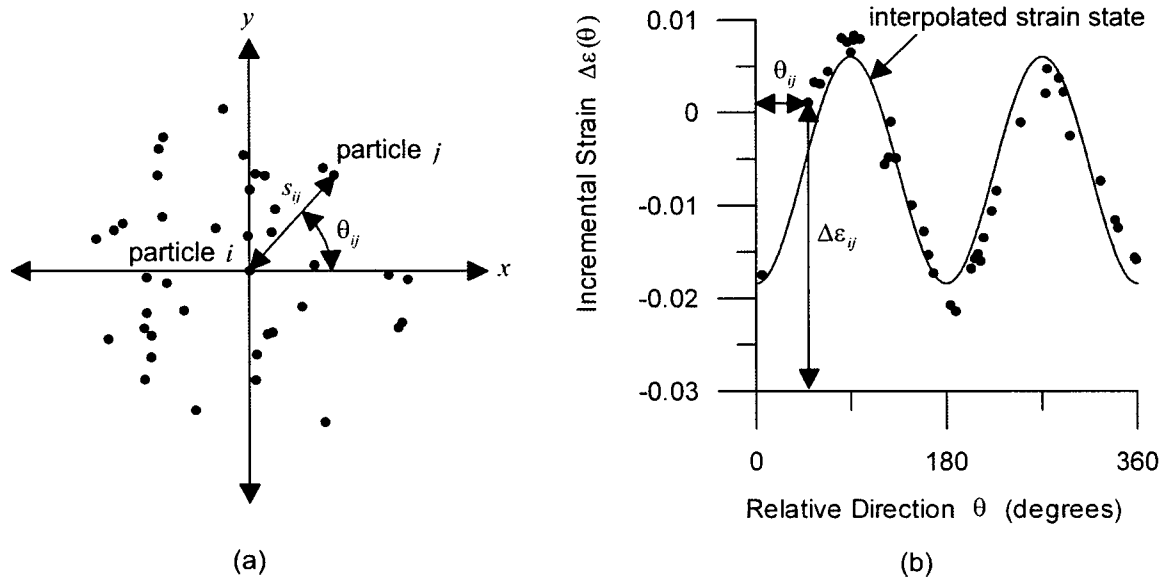


Figure 5.4. Example of a DAN3D incremental tangential strain interpolation. (a) The relative positions of neighbouring particles are updated at each time step. (b) $\Delta\epsilon_{ij}$ (Equation [5-26]) and θ_{ij} (Equation [5-27]) are calculated for each neighbouring particle, and a least squares fit of Equation [5-28] provides an estimate of the column/particle-centred strain state.

This strain interpolation method requires no assumptions regarding the orientation of the principal incremental tangential strains. Denlinger and Iverson's (2004) model is the only other existing continuum dynamic model with this capability. The interpolated strain state can then be used to increment the internal stress state accordingly, but this step is not straightforward, as the process of stress redistribution following yielding within a rapidly deforming landslide is extremely complex and poorly understood. Denlinger and Iverson (2004) proposed an iterative method for redistributing the stresses at each time step to satisfy a plastic yield criterion. A similar iterative method was originally implemented in DAN3D, but such an approach uses ad hoc assumptions regarding stress redistribution while sacrificing considerable computational efficiency.

5.4.3 Simplified strain rosette method

The transparency and efficiency of the strain interpolation and resulting stress redistribution can be improved significantly by explicitly assuming a suitable orientation of the principal incremental tangential strains. To help determine a reasonable assumption, the interpolated strains associated with randomly selected particles were tracked during a series of DAN3D runs in which the stress state was assumed to be hydrostatic. These tests showed that the direction of maximum straining typically corresponds very closely with the direction of motion, implying predominantly streamlined flow. Exceptions occurred, but did not persist for long, when there were very abrupt changes in direction that caused strong oblique shocks. The strain interpolation shown in Figure 5.4, taken from one of these tests, is a good example of this behaviour. The maximum and minimum points on the curve, which represent the interpolated principal incremental strains, correspond with directions at approximately 90° increments from the direction of motion.

As a result, a simplified approach has been adopted. Assuming that $\Delta\varepsilon_x$ (in the direction of motion) and $\Delta\varepsilon_y$ approximate the principal incremental tangential strains (i.e., assuming $\Delta\gamma_{xy} = 0$), Equation [5-28] becomes:

$$[5-29] \quad \Delta\varepsilon(\theta)_i = \left(\frac{\Delta\varepsilon_x + \Delta\varepsilon_y}{2} \right)_i + \left(\frac{\Delta\varepsilon_x - \Delta\varepsilon_y}{2} \right)_i \cos 2\theta$$

This approach is analogous to strain measurement using a two gauge rosette, in which the gauges are aligned with the assumed directions of the principal strains. Equation [5-29] has the form of an equation of a straight line. Similar to the two gauge rosette method, when exactly two neighbouring particles are present there are two equations and the system is determined. With less than two neighbours the system is indeterminate and the influence of strain must be neglected. With more than two neighbours, the system is redundant and a much more efficient two-parameter least squares approximation is used to fit a line to the data points, providing estimates of $\Delta\varepsilon_x$ and $\Delta\varepsilon_y$. An example is shown in Figure 5.5.

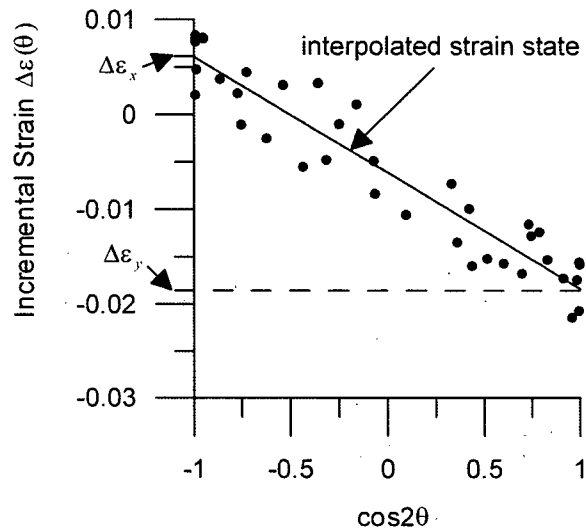


Figure 5.5. Example of a DAN3D incremental tangential strain interpolation using the simplified method. Similar to the rigorous method shown in Figure 5.4 (and using the same data), the relative positions of neighbouring particles are updated at each time step and $\Delta\epsilon_{ij}$ and θ_{ij} are calculated for each neighbouring particle. However, a least squares fit of linear Equation [5-29], rather than planar Equation [5-28], provides an estimate of the column/particle-centred strain state.

Trial comparative runs using typical slide geometries have indicated that this simplified method produces results comparable to the rigorous method. Similar assumptions regarding the orientation of the principal strains have been made by other workers, as described in the next section. Note that the use of this simplified method does not preclude the implementation of the more rigorous method in the future, when justifiable assumptions about stress redistribution can be made and computational efficiency is not such a significant constraint.

5.5 Stress update

5.5.1 Assumed orientation of principal axes

Referring to Figure 2.6 in Chapter 2, with the assumption of $\Delta\gamma_{xy} = 0$ and again neglecting the influence of reorientation of the local reference frame during the small time interval,

shear stresses τ_{xy} and τ_{yx} equal zero and σ_y (the cross-stream normal stress) is therefore one of the 3D principal stresses.

It is useful to compare this assumption with those used by other workers. Gray et al. (1999) used a similar approach, but instead assumed that the principal axes correspond with the mean downslope direction, as measured in a reference system. When the mean downslope direction equals the actual downslope direction and the direction of motion is exactly downslope, these two assumptions are identical. In contrast, Chen and Lee (2000) assumed that the principal axes are aligned with a global coordinate system, which makes the results dependent on the choice of global coordinate orientation. Similarly, Iverson and Denlinger (2001) assumed that the principal axes are oriented at a fixed angle from arbitrarily-oriented local coordinate axes. Again, in DAN3D the principal axes are aligned with the direction of motion. This is by no means an exact assumption, especially in the case of strongly curving flow or flow around obstacles, but one that appears the most intuitive of those above. As mentioned in the previous section, the only other known alternative is to make assumptions about complex 3D stress redistribution, similar to Denlinger and Iverson (2004), at the expense of model transparency and efficiency.

With the assumption that the transverse shear stresses equal zero, the governing x and y direction momentum balance Equations [4-32] and [4-33] become, respectively:

$$[5-30] \quad \rho h \frac{D\bar{v}_x}{Dt} = \rho h g_x - k_x \sigma_{z(z=h)} \frac{\partial h}{\partial x} + \tau_{zx(z=h)} - \rho (\bar{v}_x - v_{x(z=h)}) E_t$$

$$[5-31] \quad \rho h \frac{D\bar{v}_y}{Dt} = \rho h g_y - k_y \sigma_{z(z=h)} \frac{\partial h}{\partial y}$$

5.5.2 Internal yield criterion

In accordance with the equivalent fluid concept (cf., Chapter 4) and the assumptions of other workers, a frictional model, distinct from the basal rheology, has been adopted to simulate

the internal rheology of the slide mass. The yield criterion is governed by a single parameter, the internal friction angle, ϕ_i . Similar to the bulk basal friction angle, ϕ_b (Equation [4-41]), the influence of pore fluid pressure can be accounted for implicitly with ϕ_i . A hypothetical Mohr circle representation of the normalized 3D stress state is shown in Figure 5.6.

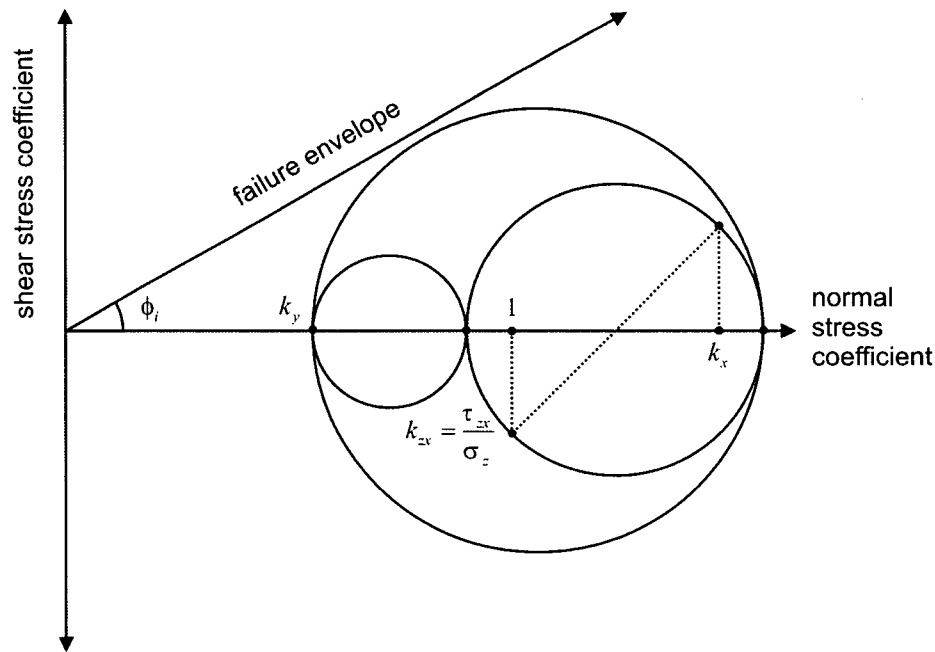


Figure 5.6. Hypothetical Mohr circle representation of the normalized 3D stress state shown in Figure 4.4 in Chapter 4. Since the transverse shear stress coefficients, k_{xy} and k_{yx} , are assumed to be zero, k_y is a principal stress coefficient.

As in the Rankine theory (cf., Chapter 2), the stress coefficients are limited by the yield criterion. The minimum and maximum limiting values correspond with the active and passive stress states, respectively. Similar to the approach used by Gray et al. (1999), and consistent with the assumption that downstream deformations dominate, the x -direction is given priority. This assumption is also made implicitly in DAN (Hungar 1995) and other 2D models that neglect the influence of lateral strain. As long as $\left| \frac{\tau_{zx}}{\sigma_z} \right| \leq \tan \phi_i$ (Iverson 1997), after Savage and Hutter (1989):

$$[5-32] \quad k_{x(\min/\max)} = 2 \left(\frac{1 \pm \sqrt{1 - \cos^2 \phi_i \left(1 + \left(\frac{\tau_{zx}}{\sigma_z} \right)^2 \right)}}{\cos^2 \phi_i} \right) - 1$$

The limiting k_y values are then a function of the prevailing value of k_x :

$$[5-33] \quad k_{y(\min)} = \left(\left(\frac{k_x + 1}{2} \right) + \sqrt{\left(\frac{k_x - 1}{2} \right)^2 + \left(\frac{\tau_{zx}}{\sigma_z} \right)^2} \right) \left(\frac{1 - \sin \phi_i}{1 + \sin \phi_i} \right)$$

$$[5-34] \quad k_{y(\max)} = \left(\left(\frac{k_x + 1}{2} \right) - \sqrt{\left(\frac{k_x - 1}{2} \right)^2 + \left(\frac{\tau_{zx}}{\sigma_z} \right)^2} \right) \left(\frac{1 + \sin \phi_i}{1 - \sin \phi_i} \right)$$

On the other hand, when $\left| \frac{\tau_{zx}}{\sigma_z} \right| > \tan \phi_i$:

$$[5-35] \quad k_{x(\min/\max)} = \frac{1 + \sin^2 \phi_i}{\cos^2 \phi_i}$$

$$[5-36] \quad k_{y(\min)} = \frac{1}{1 + \sin \phi_i}$$

$$[5-37] \quad k_{y(\max)} = \frac{1}{1 - \sin \phi_i}$$

Note that a value of $\phi_i = 0^\circ$ produces the liquefaction condition of $k_x = k_y = 1$ and can therefore be used to simulate fluid flow.

5.5.3 Stress incrementation

Assuming elastic-plastic behaviour with a constant value of ϕ_i , the stress response to deformation is implemented as follows. Initially, stress coefficients k_x and k_y are set to 1 (the tangential normal stresses are assumed to be hydrostatic and isotropic). Use of the classical “at rest” earth pressure coefficient (Terzaghi 1920; Jaky 1944), which is less than 1, may seem more appropriate from a theoretical standpoint, but does not have a significant influence on the model results, as the stress conditions change rapidly following initial deformation. At each time step, the change in the local stress state is calculated based on:

$$[5-38] \quad \begin{Bmatrix} \Delta\sigma_x \\ \Delta\sigma_y \end{Bmatrix} = \Delta\sigma_z \begin{Bmatrix} k_x' \\ k_y' \end{Bmatrix} + \frac{E}{(1+\nu)(1-2\nu)} \begin{bmatrix} 1-\nu & \nu \\ \nu & 1-\nu \end{bmatrix} \begin{Bmatrix} \Delta\epsilon_x \\ \Delta\epsilon_y \end{Bmatrix}$$

where old values are primed, E is the Young's elastic modulus and ν is the Poisson's ratio. The first term on the right side of Equation [5-38] represents the incremental change in tangential stress due to a change in the total bed-normal stress. The second term is an expression of Hooke's Law and represents the incremental change in tangential stress due to tangential strain, as estimated using the method described in Section 5.4. The matrix in this term is the stiffness matrix for an elastic, isotropic material in plane strain. It must be acknowledged that the assumption of linear elastic response is a major simplification. In reality, the stress-strain relationship within a rapidly deforming landslide may be extremely complex (e.g., non-linear; highly dependent on pore pressure response; spatially, temporally and cyclically variable). Furthermore, assuming for simplicity that the x and y direction responses are de-coupled (i.e., that the Poisson's ratio is zero), Equation [5-38] simplifies to:

$$[5-39] \quad \begin{Bmatrix} \Delta\sigma_x \\ \Delta\sigma_y \end{Bmatrix} = \Delta\sigma_z \begin{Bmatrix} k_x' \\ k_y' \end{Bmatrix} + E \begin{Bmatrix} \Delta\epsilon_x \\ \Delta\epsilon_y \end{Bmatrix}$$

Technically, such de-coupling is inconsistent with the assumption of incompressibility, but it does not have a significant influence on the model results. Expanding Equation [5-39] and substituting appropriate stress coefficients:

$$[5-40] \quad \begin{Bmatrix} k_x \sigma_z - k_x' \sigma_z' \\ k_y \sigma_z - k_y' \sigma_z' \end{Bmatrix} = \begin{Bmatrix} k_x' \sigma_z - k_x' \sigma_z' \\ k_y' \sigma_z - k_y' \sigma_z' \end{Bmatrix} + E \begin{Bmatrix} \Delta \epsilon_x \\ \Delta \epsilon_y \end{Bmatrix}$$

Dividing Equation [5-40] by the updated total bed-normal stress, σ_z , and rearranging terms produces the following equation for the updated tangential stress coefficients:

$$[5-41] \quad \begin{Bmatrix} k_x \\ k_y \end{Bmatrix} = \begin{Bmatrix} k_x' \\ k_y' \end{Bmatrix} + \frac{E}{\sigma_z} \begin{Bmatrix} \Delta \epsilon_x \\ \Delta \epsilon_y \end{Bmatrix}$$

In order to satisfy the assumption that all of the internal stresses increase linearly with depth from zero at the free surface (cf., Chapter 4), the normalized elastic modulus, E/σ_z , is assumed to be constant:

$$[5-42] \quad \begin{Bmatrix} k_x \\ k_y \end{Bmatrix} = \begin{Bmatrix} k_x' \\ k_y' \end{Bmatrix} + D \begin{Bmatrix} \Delta \epsilon_x \\ \Delta \epsilon_y \end{Bmatrix}$$

where D is a dimensionless stiffness coefficient, which is assumed to be spatially and temporally constant. This assumption is consistent with the observation that the stiffness of cohesionless material increases with increasing confining pressure. Stiffness is also assumed to be independent of strain. The current default value in DAN3D is $D = 200$ for both compression and extension. This is within the range of dimensionless stiffness coefficients estimated by Hungr (1995), which were based on measured values of stiffness of granular soil behind retaining walls during active and passive deformation (Terzaghi and Peck 1967). The sensitivity of the model to the value of D is investigated in Chapter 6. The results show that DAN3D is not very sensitive to the specified value of D , as Hungr (1995) also found with DAN, but it is possible that the incremental approach can aid numerical stability. Stress

response occurs over several time steps, smoothing anomalous strain interpolations and preventing numerical oscillation between active and passive stress states (Tai and Gray 1998). As described in Chapter 3, with the exception of Denlinger and Iverson (2004), other existing models assume instantaneous stress response, equivalent to using an infinite D value. The apparent insensitivity of models to the assumed stress-strain relationship suggests that deformation is so large and occurs so fast in extremely rapid landslides that the stress response assumptions may be virtually immaterial.

5.6 Entrainment

5.6.1 Momentum transfer based on erosion velocity and growth rate

As described in Chapter 4, a momentum flux term due to entrainment of path material appears in the x direction momentum balance Equation [5-30]. Assuming, as in DAN (Hungri (1995), that the entrained material is initially stationary (i.e., $v_{x(z=b)} = 0$), Equation [5-30] becomes:

$$[5-43] \quad \rho h \frac{D\bar{v}_x}{Dt} = \rho h g_x - k_x \sigma_{z(z=b)} \frac{\partial h}{\partial x} + \tau_{zx(z=b)} - \rho \bar{v}_x E_t$$

The momentum flux term (the last term on the right side of Equation [5-43]) arises because momentum must be transferred, by solid collisions, fluid thrust and friction, from the landslide to the path material in order to accelerate it (in this case from rest) to the reference frame velocity, \bar{v}_x . As mentioned in Chapter 2, this process results in a velocity-dependent inertial resistance, which is additional to the basal shear resistance (Perla et al. 1980). An alternative to this explicit formulation is to account for the momentum transfer effect implicitly during calibration of a bulk basal rheology. However, separating the terms is useful because it facilitates independent analysis of shear and entrainment related resistances, permits simulation of cases involving isolated entrainment zones that can be independently quantified and ensures compatibility between momentum and mass balances.

Entrained material is assumed to have the same constant bulk density as the overriding landslide, which is approximately valid in most practical cases (cf., Chapter 4). Spatial and temporal variations in density can be handled by the SPH-based discretization method, which was originally developed for the simulation of compressible flows, but the necessary modifications have not been incorporated into DAN3D.

Some of the most challenging assumptions concern the availability of erodible material and the rate at which it is entrained by the landslide. DAN3D requires that maximum erosion depths be estimated independently, for example, using surficial geological maps, aerial photographs or field surveys, and input at nodal locations on a fixed reference grid. Finite or infinite values can be used to simulate supply-limited or supply-unlimited conditions, respectively (cf., Chapter 2). Entrainment occurs when a particle is centred within a fixed grid cell containing erodible material.

As the flow velocity increases, the bed erosion velocity, E_t , can have an important influence on the momentum balance Equation [5-43]. As described in Chapters 2 and 3, limited effort has been directed at understanding actual entrainment mechanisms and constraining erosion rates, and so it appears that an empirical approach must be adopted at this time. Takahashi (1991) and Hungr (1995) used different approaches to ensure that the predicted maximum erosion depth at a point is reached only after the entire landslide passes. In DAN (Hungr 1995), the erosion rate increases in proportion to the flow depth, resulting in a depth-proportional distribution of entrained material and natural exponential growth of the landslide with displacement. Although largely empirical, the method has a physical basis, as the changes in stress conditions leading to failure within the path material can be related to changes in the total bed-normal stress and therefore the flow depth.

DAN3D uses a similar empirical approach based on a user-prescribed parameter, E_s , which represents the bed-normal depth eroded per unit flow depth and unit displacement or, equivalently, the displacement-dependent natural exponential growth rate (with dimensions L^{-1}). Note the difference between the erosion velocity, E_t , a time-dependent erosion rate

(with subscript t) and the growth rate, E_s , a displacement-dependent erosion rate (with subscript s). A constant growth rate is independent of flow velocity. For example, a value of $E_s = 0.01 \text{ m}^{-1}$ produces a 1% increase in local flow volume per metre travelled, irrespective of flow velocity. The assumption of natural exponential growth with displacement is used for its simplicity and may eventually serve as a baseline for more complex entrainment modelling, including the development of constitutive relationships for growth rates that are based on actual entrainment mechanisms. Similar to the open basal rheological kernel used in DAN3D, the user could potentially select an appropriate entrainment relationship from a menu of proposed models. Such models could incorporate dependence on other factors, including flow velocity, slope angle, path curvature, surface roughness or the strength and drainage characteristics of local path material. In the meantime, different values of E_s can be assigned to distinct entrainment zones to empirically account for such factors.

The erosion velocity and the growth rate are related by:

$$[5-44] \quad E_t = E_s h \overline{v_x}$$

The x direction momentum balance Equation [5-43] then becomes:

$$[5-45] \quad \rho h \frac{D\overline{v_x}}{Dt} = \rho h g_x - k_x \sigma_{z(z=h)} \frac{\partial h}{\partial x} + \tau_{zx(z=h)} - \rho h E_s \overline{v_x}^2$$

The momentum flux term in Equation [5-45], and therefore the inertial resistance produced by entrainment, is then a function of the flow depth and the square of the flow velocity. This velocity-squared term has the potential to dominate the resistance at high flow velocities. However, the momentum transfer effect may be countered by a coinciding reduction in the effective basal shear strength caused by undrained loading or the incorporation of additional water and/or weak path material (cf., Chapter 2). DAN3D allows the user to modify the basal rheology at the onset of entrainment to simulate this effect. Note that E_s is

automatically set to zero if the grid cell in which the particle is located does not contain any entrainable material (including the condition when available material has been depleted by preceding flow).

5.6.2 Mass transfer

SPH provides a simple framework for handling mass transfer between the landslide and an erodible bed. The basal area independently covered by particle i , A_i , can be approximated by (Wang and Shen 1999):

$$[5-46] \quad A_i = \frac{V_i}{h_i}$$

The volume of each particle, and therefore the total volume of the landslide, may increase in a time step due to entrainment. Following from Equation [5-44], the volume of material entrained by particle i , ΔV_i , which travels a distance, Δs_i , in a time step is:

$$[5-47] \quad \Delta V_i = E_s h_i A_i \Delta s_i$$

Substituting Equation [5-46] into Equation [5-47] produces the following incremental form of the natural exponential growth equation:

$$[5-48] \quad \Delta V_i = E_s V_i \Delta s_i$$

As path material is added to each particle it is simultaneously removed from the local fixed reference grid using the following relationship, based on Equation [5-10]:

$$[5-49] \quad \Delta b_k = - \sum_{j=1}^n \Delta V_j W_{kj}$$

where Δb_k is the change in bed depth at node k and $j=1$ to n are nearby particles. Equation [5-49] ensures mass balance between the landslide and the bed. As an option, DAN3D can account for the resulting changes in bed elevation, which may cause self-channelization that can influence the lateral spreading of open slope landslides such as debris avalanches. Entrainment proceeds within a fixed grid cell until the available material is exhausted or the entire landslide passes.

One of the limitations of this simple approach is the use of an additional user-specified parameter, E_s , which must be adjusted by trial-and-error in order to obtain a reasonable distribution of entrained material. For example, using an average growth rate, $\overline{E_s}$, for a specific entrainment zone produces results similar to Takahashi et al. (1992) and Hungr (1995), in which the entrainable material is distributed throughout the entire length of a passing landslide. A useful preliminary estimate of the average growth rate for a specific entrainment zone can be obtained from the following natural exponential growth equation:

$$[5-50] \quad V_f = V_0 \exp(\overline{E_s} \overline{S})$$

where V_f is the estimated total volume of the landslide exiting the zone, V_0 is the estimated total volume of the landslide entering the zone and \overline{S} is the approximate average path length of the zone. Rearranging Equation [5-50] gives:

$$[5-51] \quad \overline{E_s} = \frac{\ln(V_f/V_0)}{\overline{S}}$$

Under supply-limited conditions, V_f can be approximated by summing V_0 and the total volume of entrainable material in the entrainment zone, assuming an appropriate path width. In such a case, using a value of E_s higher than the estimated average growth rate would distribute more of the available material toward the flow front, which could be used to simulate plowing. Alternatively, a relatively higher rate could be assigned to the margins.

5.7 Intensity parameter interpolation

SPH provides a framework for estimating the value of intensity parameters anywhere within the domain of interest, which is required for landslide hazard mapping (cf., Chapter 1). Each particle carries information about the local flow properties, including depth and velocity, as it is advected with the flow. This information can be output directly, for use in scatter-type plots that show the flow properties at each particle location. At the same time, variations of Equation [5-8] can be used to interpolate any of these properties from the moving particles back to the fixed reference grid for output in the form of intensity contour maps or 3D surfaces. This eliminates the need to post-process the particle-centred properties using other software. For example, similar to Equation [5-10], the flow/deposit depth at each grid node can be interpolated using:

$$[5-52] \quad h_k = \sum_{j=1}^n V_j W_{kj}$$

where $j = 1$ to n are nearby particles. The following variation of Equation [5-8], which eliminates edge effects near the flow margins, is useful for estimating the value of other flow properties at each grid node:

$$[5-53] \quad f_k = \frac{1}{h_k} \sum_{j=1}^n V_j f_j W_{kj}$$

For example, the flow velocity at each node can be interpolated using:

$$[5-54] \quad \mathbf{v}_k = \frac{1}{h_k} \sum_{j=1}^n V_j \mathbf{v}_j W_{kj}$$

where \mathbf{v}_k and \mathbf{v}_j are velocity vectors in the global coordinate system. Equation [5-53] represents a simple weighted average, in which the influence of a single particle is weighted according to its relative contribution to the local flow depth.

The landslide depths and velocities calculated using Equations [5-52] and [5-54] can be output at user-specified intervals. Over the course of a simulation, the program also stores maximum recorded values of these parameters at each grid node. The maximum recorded flow depth data is useful for generating a map of the simulated landslide trimline, which delineates the direct impact area. As described in Chapter 1, additional intensity parameters, such as discharge, impact pressure and kinetic energy, can be derived using the depth and velocity data. DAN3D can be configured to perform these calculations automatically and output the results.

5.8 Implementation

The model has been coded in C++ and runs on an IBM compatible personal computer. The program reads spatial data in the form of user-created grid files, which contain the following data at nodal locations on a global fixed grid: 1) the bed elevation; 2) the landslide source depth (the distance between the original ground surface and the rupture surface, measured in the vertical direction and increased as appropriate to account for dilation/bulking of the failed mass); and 3) the depth of the erodible bed (measured in the bed-normal direction). The user inputs the required rheological and control parameters, such as the time step interval. A variety of data files can be output at user-prescribed intervals and processed by a 3D surface-modelling program, such as Surfer (Golden Software Inc.) or a suitable GIS package. The final output takes the form of hazard intensity contour maps (cf., Chapter 1) and static or animated isometric views.

The duration of each simulation depends on the number of particles used, the size of the global reference grid, the length of the time step interval, the frequency of output required and the nature of the landslide in question. For a typical simulation using 4000 particles, a 2 GHz computer processes approximately one time step per second. A flowchart summarizing the main program functions is shown in Figure 5.7 (for proprietary reasons, the actual program code cannot be published in this thesis).

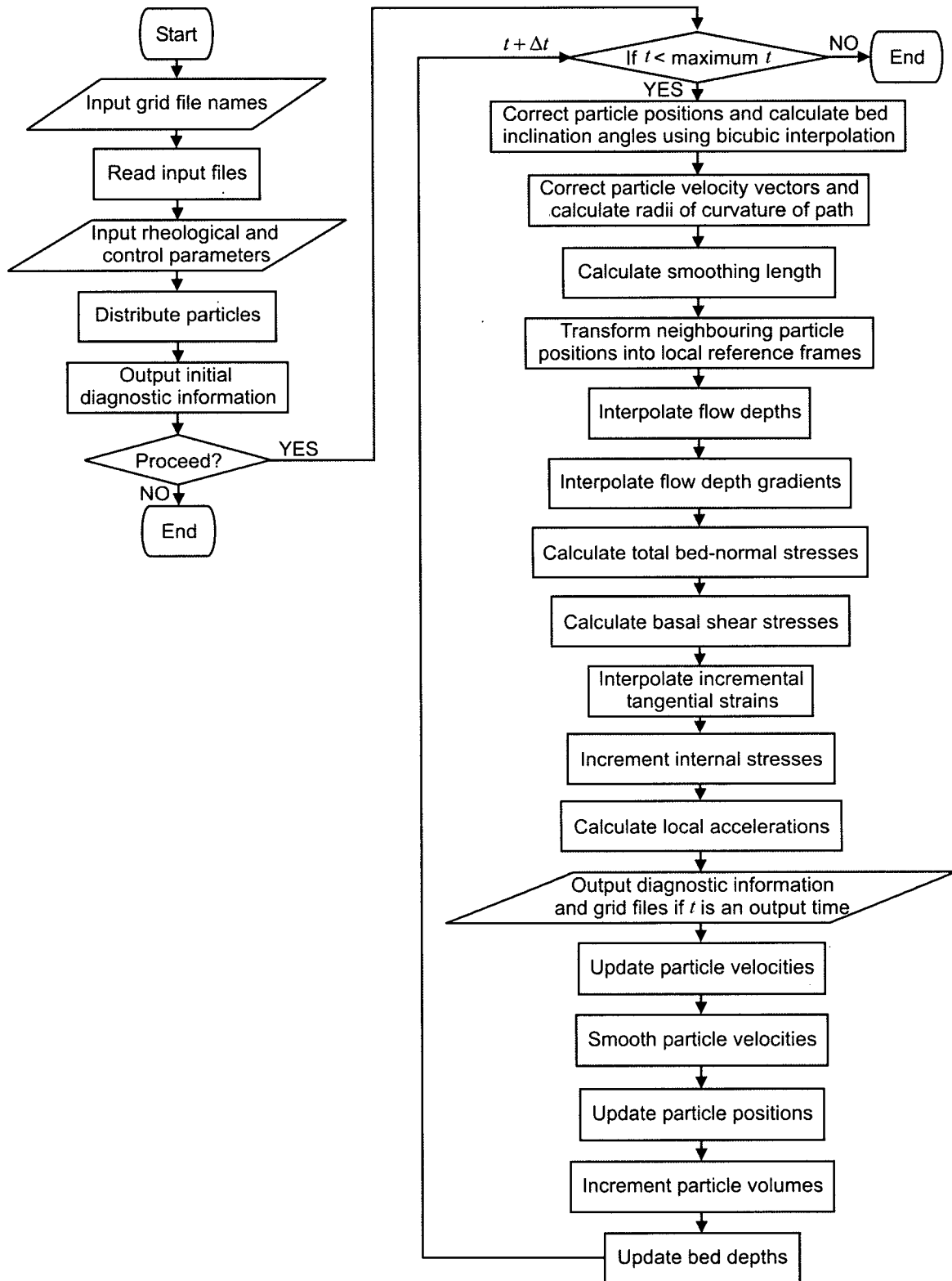


Figure 5.7. Flowchart showing the main functions in DAN3D. The column on the right represents the loop that is performed during each time step.

5.8.1 Initial conditions

From the source depth data, the program calculates the area covered by the source landslide and the initial volume of slide material contained in each cell of the global reference grid (using the trapezoidal rule). The total initial landslide volume is divided evenly among N particles. The initial average particle density is estimated and Equation [5-23] is used to calculate the initial particle smoothing length. Two different particle distribution methods can then be used, depending on whether the source landslide depths are irregular or uniform.

When the initial depths are irregular, the particles are systematically placed in the source area, one at a time, according to the following procedure: 1) the program searches the reference grid for the cell requiring the largest volume of material (to match the input data); 2) a particle is placed at a random location within this cell; 3) Equation [5-52] is used to update the required nodal depths within the radius of influence of the particle, and 4) the required cell volumes are updated. The procedure is repeated until all of the particles have been placed. This process is analogous to filling a number of bins (the reference grid cells) with equal buckets of material (the particles) until each bin contains the correct amount of material. The particles are smooth and therefore typically influence more than one grid cell in their neighbourhood, or analogously, the buckets of material can spill into neighbouring bins. This method is capable of reproducing complex landslide configurations and does not require a matrix inversion. The random placement of the particles within each cell prevents particle stacking and alignment. The input depths can typically be reproduced with an error of less than a few percent, which tends to be slightly larger near the landslide margins, where the smooth particles have a tapering effect. An example is shown in Figure 5.8.

When the initial depth is uniform, the following alternative particle distribution method can be used. Rather than being placed randomly within each cell, the particles are placed evenly on an orthogonal grid. The spacing of the grid is a multiple of the fixed global grid spacing and is adjusted by the program to maximize the number of particles used in the simulation (up to the limiting value). This method is capable of reproducing a specified uniform initial depth with negligible uniform errors, except near the margins.

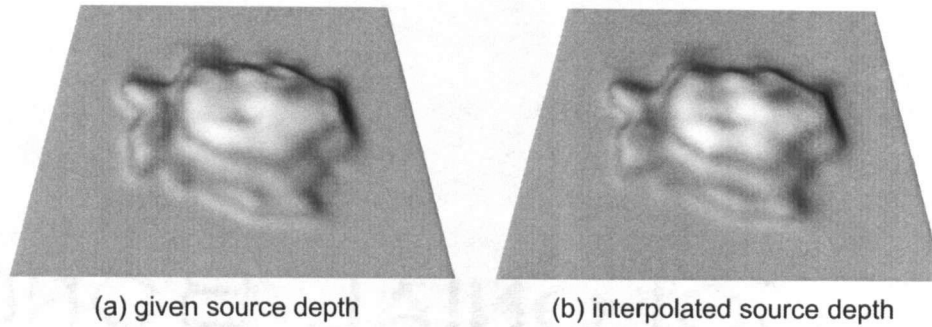


Figure 5.8. Example of a DAN3D initial particle distribution for a very irregular source comparing (a) the given source depth with (b) the interpolated source depth following distribution of the particles (the images are isometric views of 3D surface plots). In this case, the source area is approximately 1 km x 1 km and the maximum depth is about 185 m. The maximum discrepancy between (a) and (b) is 10 m. 4000 particles were used with a particle smoothing coefficient of $B = 5$.

5.8.2 Time stepping

With the additional assumptions introduced in this chapter, Equations [5-45] and [5-31] are the x and y direction momentum balance equations used in DAN3D. Numerical integration of these equations determines how the particles move in each time step. Again, the x direction is aligned with the local direction of motion, but when a particle is stationary this direction is undefined. In such a case, a predictor step, in which the local x -axis is arbitrarily oriented, is used to predict the direction of potential motion (based on the vector sum of local driving stresses) and the local axes are re-oriented accordingly.

At the start of a time step, each particle occupies a new position determined in the previous time step. Due to the irregular 3D topography, the updated position of the particle may be temporary because it does not necessarily correspond with the new local sliding surface. Given its temporary global coordinates, the new position of the particle on the 3D sliding surface is approximated using a bicubic interpolation, which ensures smoothness of both elevation and slope values across the global reference grid (Press et al. 2002). For gradual bed curvature and a reasonably small time step, this correction is small. The particle velocity vector is then re-oriented so that it lies in the new local tangent plane.

This correction also provides information for approximating the local bed-normal radius of curvature of the path in the direction of motion:

$$[5-55] \quad R_i = \frac{\Delta s_i}{\beta_i}$$

where Δs_i is the distance travelled by the particle during the time step and β_i is the angle between the original and corrected velocity vectors.

Following this correction, each particle occupies a position on the 3D sliding surface and is centred at a reference column. The particle smoothing length is calculated using Equation [5-23] (using flow depth values from the previous time step) and the positions of neighbouring particles are transformed into the local coordinate system $(x, y, z)_i$. The updated local flow depth is calculated using Equation [5-10] and the local depth gradient is calculated using Equations [5-13] and [5-14]. The local total bed-normal stress is calculated using Equation [4-29] and the local basal shear resistance is calculated using one of Equations [4-34] to [4-42], as governed by the specified local basal rheology and its associated parameters. The incremental tangential strain state is approximated using the simplified interpolation method described in Section 5.4 and the local stress coefficients are incremented using Equation [5-42]. If the updated stress state breaches the failure envelope, the stress coefficients are corrected accordingly using Equations [5-32] to [5-37]. The momentum balance Equations [5-45] and [5-31] are then used to solve for the instantaneous local acceleration, $\frac{D\bar{v}_x}{Dt}$ and $\frac{D\bar{v}_y}{Dt}$, of the particle and its associated reference column.

Assuming constant local acceleration during a short time step, Δt , the column/particle velocity is updated by a forward difference approximation:

$$[5-56] \quad \begin{Bmatrix} \overline{v_x} \\ \overline{v_y} \end{Bmatrix}_i = \begin{Bmatrix} \overline{v_x}' \\ \overline{v_y}' \end{Bmatrix}_i + \Delta t \begin{Bmatrix} \frac{D\overline{v_x}}{Dt} \\ \frac{D\overline{v_y}}{Dt} \end{Bmatrix}_i$$

where velocities at the beginning of the time step are primed. The user-prescribed time step interval must be short enough to ensure stability, which is achieved empirically by running a few simulations and systematically decreasing Δt until no significant difference is observed in the model results.

To minimize so-called “particle penetration” (Monaghan 1989), which tends to occur near strong shocks (cf., Chapter 6), especially in the absence of real or numerical viscosity, a velocity smoothing option is available in DAN3D. The following correction can be applied to the updated column/particle velocities (based on the “XSPH variant” proposed by Monaghan 1989):

$$[5-57] \quad \overline{\mathbf{v}}_i = \overline{\mathbf{v}}_i + C\Delta\overline{\mathbf{v}}_i$$

where $\overline{\mathbf{v}}_i$ is the velocity vector in the global coordinate system (and the vector on the right side is derived from Equation [5-56]), C is a user-specified velocity smoothing coefficient and $\Delta\overline{\mathbf{v}}_i$ is the following velocity correction:

$$[5-58] \quad \Delta\overline{\mathbf{v}}_i = \sum_{j=1}^n \frac{V_j}{\left(\frac{h_i + h_j}{2}\right)} (\overline{\mathbf{v}}_j - \overline{\mathbf{v}}_i) W_{ij}$$

Equation [5-58] is simply a variation of Equation [5-8] that ensures conservation of linear momentum. Essentially, use of Equation [5-57] means that the particles move with a velocity that is closer to the average velocity in their neighbourhood (Monaghan 1992), and the magnitude of the velocity smoothing coefficient determines how much the velocities of

neighbouring particles influence the central particle. The sensitivity of the model to C is investigated in Chapter 6. Velocity smoothing introduces some numerical diffusion, which appears to smooth out strong shocks, increase stability and reduce the tendency for particles to line up in the downstream direction in channelized reaches of the path. But too much smoothing can impose unrealistically streamlined and coherent behaviour.

Following velocity smoothing, the particle is advanced along the local tangent plane to its temporary position by a central difference approximation:

$$[5-59] \quad \begin{Bmatrix} \Delta x \\ \Delta y \end{Bmatrix}_i = \frac{\Delta t}{2} \begin{Bmatrix} \overline{v_x} + \overline{v_x}' \\ \overline{v_y} + \overline{v_y}' \end{Bmatrix}_i$$

The particle volume is updated using Equation [5-48] and the bed depth at neighbouring grid nodes is updated using Equation [5-49]. If the bed elevation change option is enabled, the bed elevation is correspondingly updated.

When all of the particle positions are updated, the model proceeds to the next time step.

5.9 Discussion

The numerical method described in this chapter includes a number of innovations that were driven by the objectives outlined in Chapter 2. Smoothed Particle Hydrodynamics, which was originally developed for the simulation of compressible flow in 3D, has been adapted for incompressible, depth-averaged flow across an irregular 3D surface. The method is fully-Lagrangian, which means that the relatively simple momentum balance equations derived in Chapter 4 can be solved efficiently. At the same time, mass balance is satisfied without the need for a mesh. A unique interpolation method based on strain gauge rosette theory permits strain estimation within this meshless framework, and because the method provides strain magnitude, rather than simply direction, the internal stresses can be incremented in proportion. This incremental approach has a physical basis but may also improve numerical

stability. The updated internal stresses are limited by a frictional yield criterion, which allows for non-hydrostatic, anisotropic conditions, and are coupled to the basal shear stress, which remains a generic function within the equivalent fluid framework. Bicubic interpolation of surface elevations and slopes ensures smoothness of these values across the global reference grid and permits the estimation of local path curvature and resulting centripetal acceleration, which can strongly influence the internal and basal stresses.

In addition, a simple entrainment algorithm has been incorporated. The rates of mass and momentum transfer are controlled by a single parameter, the natural exponential growth rate, which has a physical significance and is related in a simple way to the established concept of erosion velocity. The availability of entrainable material is controlled by a spatially-variable bed depth, which permits the simulation of supply-limited conditions. Rheology changes associated with entrainment can also be implemented.

Finally, the SPH-based method can produce hazard intensity maps without requiring separate post-processing of data. This capability eliminates the need for supplementary software and improves the overall efficiency of the runout analysis process.

All of these features have been designed to be modular and as simple as possible, which should facilitate future modifications and allow the model to evolve with increasing understanding of extremely rapid landslides.

5.10 Conclusion

An original numerical method has been developed to solve the system of governing equations that were derived in Chapter 4. Together, the governing equations and the solution method satisfy all of the objectives that were outlined in Chapter 2, making DAN3D unique among existing landslide continuum dynamic models. With these capabilities, the model can be used to analyze a wide variety of landslide types at any scale, and the model output is suitable for direct use in landslide risk assessment. But before it can be used in practice, its accuracy must be validated using controlled tests. Model testing is the subject of the next chapter.

6 TESTS

6.1 Introduction

The DAN3D system of governing equations and corresponding numerical solution method were introduced in the previous two chapters. The program incorporates all of the essential features described in Chapter 2, but its ability to accurately solve the governing equations and its applicability to real cases must still be verified. Testing allows a somewhat clearer distinction to be made between model adaptability and model accuracy (e.g., Iverson 2003). This is particularly important within a calibration-based framework such as the equivalent fluid approach, in which arbitrary adjustment of resistance parameters can often produce good-looking results.

However, analytical solutions of the complete system of equations are not possible, and so only the most basic form of DAN3D (i.e., excluding the influences of irregular terrain, internal strength and material entrainment) can be tested this way. The full algorithm can only be evaluated (not strictly tested) by comparison with controlled experiments. At the same time, hypothetical experiments and parametric analyses can provide valuable insight into basic model behaviour and sensitivity.

The purpose of this chapter is to validate and evaluate DAN3D by comparison with both analytical and experimental results. A series of parametric analyses are included to demonstrate the influences of the various control and rheological parameters. The ability of the model to provide accurate first-order runout predictions is also demonstrated.

6.2 1D dam-break

6.2.1 Description

The 1D dam-break problem provides a basic test for the computational algorithm presented in Chapter 5. It has been used previously by Hungr (1995), Wang and Shen (1999),

Mangeney et al. (2000) and Denlinger and Iverson (2004) to validate other dynamic models. Stoker (1957) presented an analytical solution to the classical 1D dam-break problem, which involves zero bed slope, zero internal friction (i.e., hydrostatic internal stresses) and zero basal resistance. Mangeney et al. (2000) generalized the classical dam-break solution to account for bed slope and basal friction. In the general case, at time t after failure the bed-normal flow depth, h , at horizontal location X between the crest of the flow at

$$X = \left(-t\sqrt{gh_0} \cos \alpha + \frac{t^2}{2}(g \sin \alpha - g \cos \alpha \tan \phi_b) \right) \cos \alpha \quad \text{and} \quad \text{the flow front at}$$

$$X = \left(2t\sqrt{gh_0} \cos \alpha + \frac{t^2}{2}(g \sin \alpha - g \cos \alpha \tan \phi_b) \right) \cos \alpha \quad \text{is (after Mangeney et al. 2000):}$$

$$[6-1] \quad h(X) = \frac{1}{9g} \left(\frac{X}{t \cos \alpha} - 2\sqrt{gh_0} \cos \alpha - \frac{t}{2}(g \sin \alpha - g \cos \alpha \tan \phi_b) \right)^2$$

where $X = 0$ is the location of the dam-break, g is the vertical acceleration due to gravity, h_0 is the initial bed-normal depth behind the dam, α is the angle of the bed from horizontal and ϕ_b is the bulk basal friction angle (Equation [4-41]). The general solution converges on the classical solution when α and ϕ_b are both equal to zero, in which case the bed-normal flow depth between the crest of the flow at $X = -t\sqrt{gh_0}$ and the flow front at $X = 2t\sqrt{gh_0}$ is (after Stoker 1957):

$$[6-2] \quad h(X) = \frac{1}{9g} \left(\frac{X}{t} - 2\sqrt{gh_0} \right)^2$$

6.2.2 Methodology

DAN3D can be converted for depth-averaged simulation of motion along a 2D path by neglecting lateral (local y direction) bed and free surface gradients and using a 1D interpolating kernel, W , that satisfies the conditions of Equations [5-2] and [5-3]. The

following 1D Gaussian kernel was used in the simulations presented in this section (similar to Equation [5-15]):

$$[6-3] \quad W = \frac{1}{\sqrt{\pi\ell}} e^{-\left(\frac{s}{\ell}\right)^2}$$

where ℓ is the smoothing length and s is the distance along the path from the point of interest. The adaptive smoothing length was calculated using (similar to Equation [5-23]):

$$[6-4] \quad \ell = \frac{BN}{\sum_{i=1}^N \frac{h_i}{V_i}}$$

where B is a dimensionless particle smoothing coefficient. In 1D, particle volumes, V , are

specified per unit width of flow. As described in Chapter 5, the term $\frac{\sum_{j=1}^N \frac{h_j}{V_j}}{N}$ is the average areal particle number density. In 1D, this means that the number of particles within a distance of one smoothing length of each particle is, on average, equal to $2B$.

A frictional basal rheology (Equation [4-41]) was implemented and the following three cases were considered: a) the classical problem with $\alpha = 0^\circ$ and $\phi_b = 0^\circ$; b) the general problem with $\alpha = 30^\circ$ and $\phi_b = 20^\circ$; and c) the general problem with $\alpha = 30^\circ$ and $\phi_b = 10^\circ$. The hydrostatic internal stress conditions were accounted for in the model by setting the internal friction angle, ϕ_i , to zero. The following control parameters were used in each case: $N = 4000$ particles, particle smoothing coefficient $B = 10$ and velocity smoothing coefficient $C = 0$ (i.e., velocity smoothing was neglected).

The initial conditions were simulated by placing the particles on the sliding surface at equal intervals between horizontal locations $X = -2000 \cos \alpha$ m and $X = 0$ m. Each particle was assigned a volume per unit width of 5 m^3 , producing an initial bed-normal depth of 10 m.

6.2.3 Results and discussion

The simulated bed-normal depths at each particle location are shown with the corresponding analytical solutions at 10 s intervals in Figure 6.1. The numerical and analytical predictions for all three configurations are comparable at most locations, with two notable exceptions. First, the model did not reproduce the asymptotic profile of the analytical solution near the flow front, because depths at particle locations could only be resolved to a minimum of $h_i = V_i / \sqrt{\pi} \ell$. For example, in Figure 6.1a the smoothing length at $t = 30$ s was approximately 5.3 m, and the flow depth at the lead particle, which had separated from the others, was therefore approximately 0.53 m; theoretically, it should have been lower. This issue was slightly exaggerated in these examples because the value of the smoothing length was influenced considerably by the large number of particles that remained closely spaced behind the crest, strongly skewing the smoothing length towards a lower value. The 100x vertical exaggeration in the figures also exaggerates this discrepancy. However, it should be noted that the asymptotic profile predicted by the analytical solution is unrealistic, as a bore would be expected to develop at the flow front in a real fluid (Chow 1959) or a geological material.

Second, the analytical solution predicted a sharp change in the profile at the crest (a singularity), which the model smoothed. Increasing the number of particles used in the simulation or employing a spatially-variable smoothing length, as in Wang and Shen (1999), would increase the resolution and improve the results. As mentioned in Chapter 5, these improvements are ongoing, but at present the number of particles is limited to 4000 and a satisfactorily robust spatially-variable smoothing method has not yet been developed.

In spite of these limitations, the generally good correspondence between the simulated and analytical results demonstrates the ability of the basic algorithm to accurately solve the governing mass and momentum balance equations. No calibration was required; the input parameters for both the numerical and analytical methods were identical.

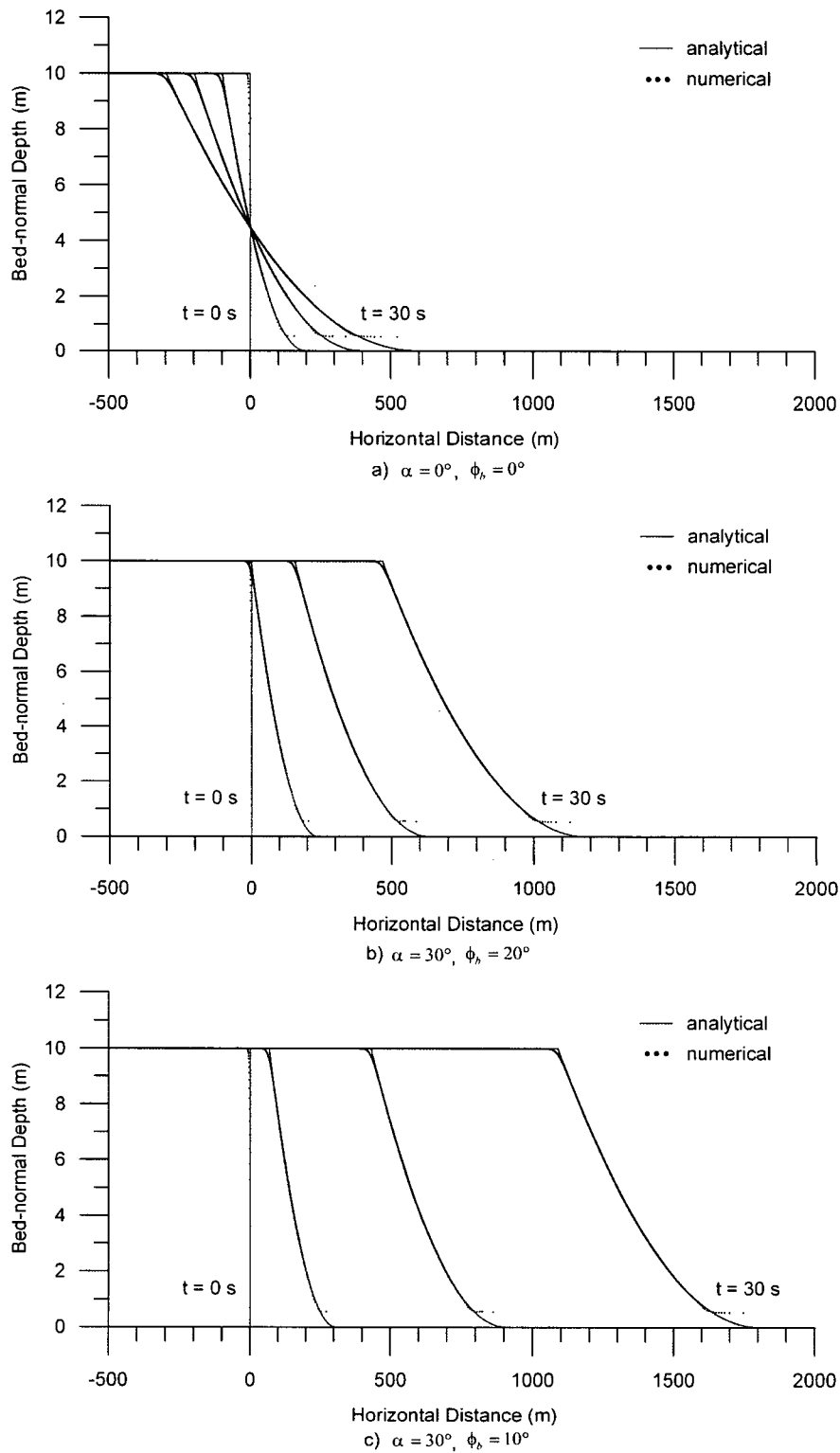


Figure 6.1. Analyses of the dam-break problem. (a) The classical problem with $\alpha = 0^\circ$ and $\phi_b = 0^\circ$. (b) The general problem with $\alpha = 30^\circ$ and $\phi_b = 20^\circ$. (c) The general problem with $\alpha = 30^\circ$ and $\phi_b = 10^\circ$. The flow depth profiles are shown at 10 s intervals.

6.3 Slump test

6.3.1 Description

The collapse of a cylindrical column of material, a 2D analogue of the dam-break problem, provides a simple test of grid-dependency (Denlinger and Iverson 2004). The results should be symmetrical regardless of the specified orientation of both the global and local reference systems. A similar test was used by Denlinger and Iverson (2004) to validate their dynamic model.

6.3.2 Methodology

The full DAN3D algorithm was used in this test and in every other example that follows in this thesis. The initial radius and height of the cylindrical column were set to 0.354 m and 0.5 m, respectively, similar to the initial conditions used by Denlinger and Iverson (2004). The initial geometry is shown in Figure 6.2. To simulate the behaviour of a typical dry sand, a frictional basal rheology (Equation [4-41]) with a bulk basal friction angle of $\phi_b = 30^\circ$ was implemented and the internal friction angle was set to $\phi_i = 35^\circ$. The following control parameters were used: particle smoothing coefficient $B = 6$, velocity smoothing coefficient $C = 0$ and stiffness coefficient $D = 200$. Denlinger and Iverson (2004) did not report their input material properties, making it difficult to compare the two results quantitatively.

The initial conditions were simulated by spacing the particles evenly using the uniform particle distribution method described in Chapter 5. $N = 3917$ particles, each representing a volume of approximately 50 mL, were placed within the specified column radius of 0.354 m at an orthogonal spacing of 0.01 m, as shown in Figure 6.3. The initial distribution was perfectly symmetrical about the global X and Y axes. The resulting interpolated initial geometry is shown in Figure 6.4. In comparison with Figure 6.2, inaccuracies due to smoothing are evident near the margins; in practical cases this effect is insignificant.

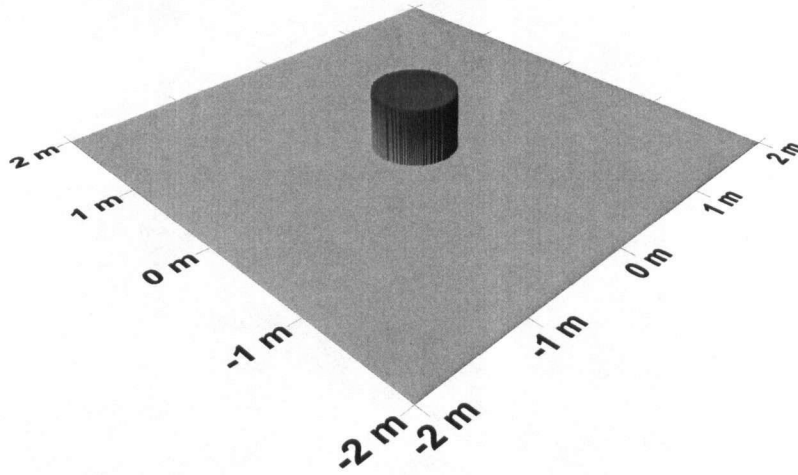


Figure 6.2. Isometric view of initial geometry used in the slump test. The cylindrical column of material was 0.5 m high with a radius of 0.354 m.

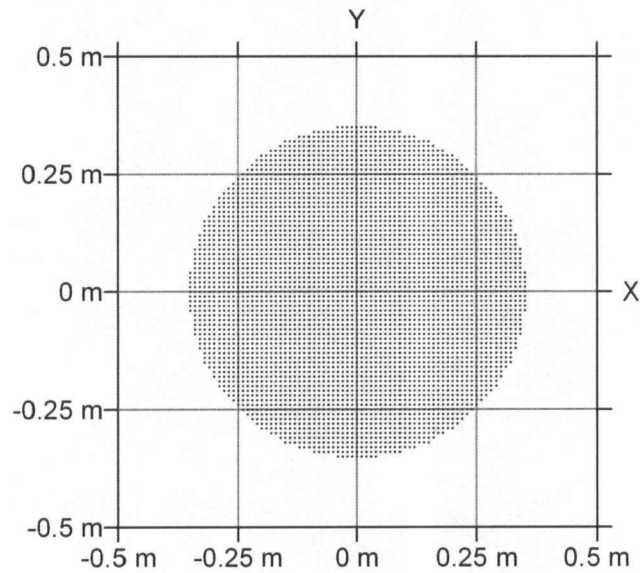


Figure 6.3. Initial particle locations used in the slump test. The particles represent equal volumes of material and are spaced evenly at 0.01 m centres within a radius of 0.354 m from the origin.

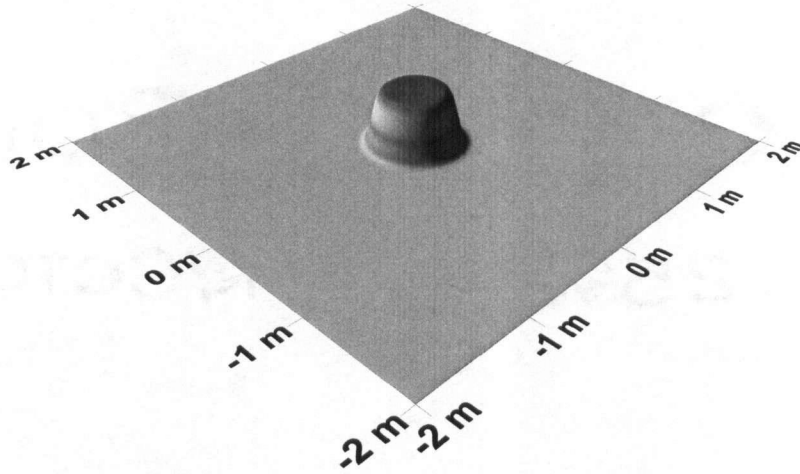


Figure 6.4. Isometric view of interpolated initial geometry using the initial particle distribution shown in Figure 6.3. Due to smoothing, the model could not reproduce the steep margin evident in Figure 6.2.

6.3.3 Results and discussion

The results are shown in Figure 6.5. As in the 1D dam-break simulations, the same failure to produce a perfectly asymptotic margin occurred because the depths at particle locations could only be resolved to a minimum of $h_i = V_i / \pi \ell^2$. Again, a spatially-variable smoothing method is a possible solution to this problem that remains to be tested. The problem appears to be minor in Figure 6.6, which is a true-scale section through the final deposit.

The final distribution of material was perfectly symmetrical about the global X and Y axes, but not perfectly radially-symmetric (although the contour lines appear to be nearly circular). These results can be attributed to the grid-dependent initial particle distribution, which displayed the same asymmetry. However, it is important to note that the solution method did not introduce any other types of grid-dependency. For real landslides, which can travel large distances from their source and undergo significant deformations, the grid-dependency of the initial particle distribution probably has a negligible influence. When the source depths are irregular and the particles are initially placed at random locations within the grid cells, the more common particle distribution method in practical cases, such grid-dependency is not an issue.

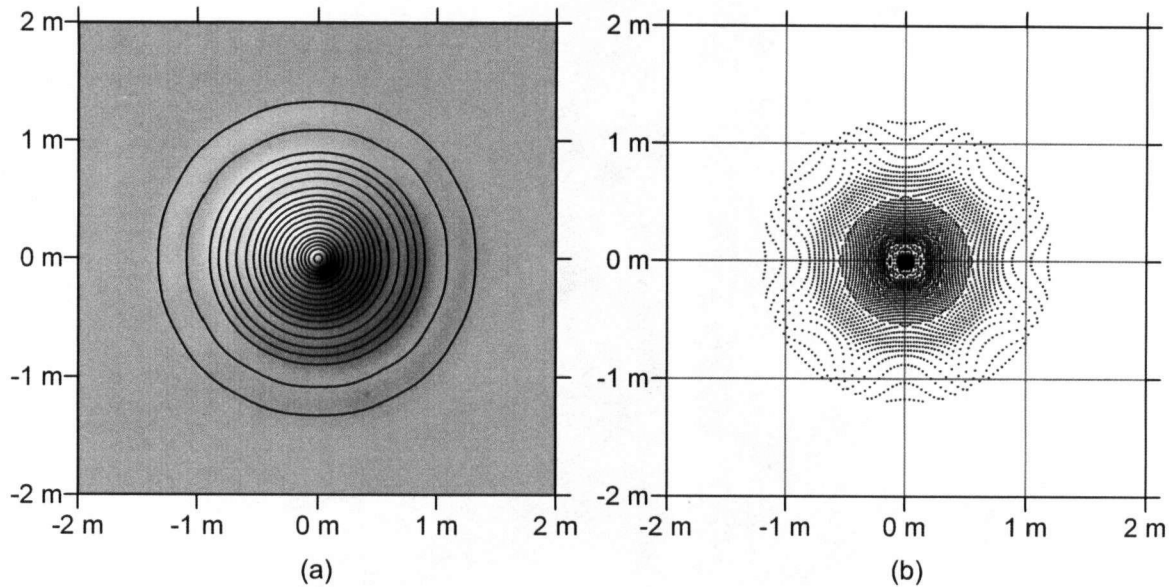


Figure 6.5. Results of the slump test. (a) Final distribution of material (a contour map is superimposed on a shaded relief image of the deposit). (b) Final particle locations. Similar to the initial conditions, the results are symmetrical about the global X and Y axes.



Figure 6.6. Section through the final deposit (at true scale), taken along the global X axis. Similar to the 1D dam-break results, the margin is not perfectly asymptotic to the sliding surface.

The assumed orientation of the principal internal stresses (cf., Chapter 5) did not have an effect in this case, as radial deformation satisfies the assumption that the principal axes correspond with the direction of motion. The influence of this assumption in more general cases has not yet been evaluated in detail, although, as mentioned in Chapter 5, trial comparative runs have suggested that it is minor. This should be a subject of future work, when the more rigorous strain interpolation method can be coupled to an appropriate stress redistribution algorithm.

6.4 Parametric analyses

6.4.1 Description

The model is influenced by a number of parameters, including both control and rheological parameters. The control parameters include the number of particles, N , the particle smoothing coefficient, B , the velocity smoothing coefficient, C , and the stiffness coefficient, D . The rheological parameters include the internal friction angle, ϕ_i , the basal rheological parameters (which depend on the selected basal rheology) and, if applicable, the entrainment growth rate, E_s . The comparative analyses presented in this section demonstrate the general behaviour of the model and its sensitivity to these parameters.

6.4.2 Methodology

The sliding surface and source geometry were the same in each case in order to facilitate comparison. The simulations involved the motion of a hypothetical material across a simple 3D surface comprising a 45° incline and a horizontal plane, which were joined by a curved transition zone. The bed-normal source depths, h_0 (in metres), were defined by:

$$[6-5] \quad h_0 = 0.15(1 - (s_0 / 0.3)^2)$$

where ($0 \text{ m} \leq s_0 \leq 0.3 \text{ m}$) and s_0 is the distance from the centre of the source area, located at global coordinates ($X = 0, Y = 0$). The resulting source volume was approximately 21.2 litres. Six different sets of analyses were performed, comprising 26 in total. The parameter values used in each analysis are listed in Table 6.1 and the initial conditions are detailed in Figure 6.7.

Parameters Varied	Results in Section/ Figure	Run	N	B	C	D	ϕ_i ($^\circ$)	ϕ_b ($^\circ$)	f	ξ (m/s^2)	E_s (m^{-1})
N and B	6.4.3/ 6.8	(a)	4000	3	0	n/a	0	25	n/a	n/a	0
		(b)	2000	3	0	n/a	0	25	n/a	n/a	0
		(c)	4000	4	0	n/a	0	25	n/a	n/a	0
		(d)	2000	4	0	n/a	0	25	n/a	n/a	0
		(e)	4000	5	0	n/a	0	25	n/a	n/a	0
		(f)	2000	5	0	n/a	0	25	n/a	n/a	0
		(g)	4000	6	0	n/a	0	25	n/a	n/a	0
		(h)	2000	6	0	n/a	0	25	n/a	n/a	0
ϕ_i	6.4.4/ 6.9, 6.10	(a)	4000	6	0	200	25	25	n/a	n/a	0
		(b)	4000	6	0	200	30	25	n/a	n/a	0
		(c)	4000	6	0	200	35	25	n/a	n/a	0
		(d)	4000	6	0	200	40	25	n/a	n/a	0
D	6.4.5/ 6.11	(a)	4000	6	0	25	35	25	n/a	n/a	0
		(b)	4000	6	0	50	35	25	n/a	n/a	0
		(c)	4000	6	0	100	35	25	n/a	n/a	0
		(d)	4000	6	0	10000	35	25	n/a	n/a	0
C	6.4.6/ 6.12	(a)	4000	6	0.005	200	35	25	n/a	n/a	0
		(b)	4000	6	0.01	200	35	25	n/a	n/a	0
		(c)	4000	6	0.015	200	35	25	n/a	n/a	0
		(d)	4000	6	0.02	200	35	25	n/a	n/a	0
ϕ_b , f and ξ	6.4.7/ 6.13	(a)	4000	6	0	200	35	20	n/a	n/a	0
		(b)	4000	6	0	200	35	30	n/a	n/a	0
		(c)	4000	6	0	200	35	n/a	0.1	500	0
		(d)	4000	6	0	200	35	n/a	0.2	1000	0
E_s	6.4.8/ 6.14	(a)	4000	6	0	200	35	25	n/a	n/a	0
		(b)	4000	6	0	200	35	25	n/a	n/a	2.22

Table 6.1. Parameter values used in each parametric analysis. N is the number of particles, B is the particle smoothing coefficient, C is the velocity smoothing coefficient, D is the stiffness coefficient, ϕ_i is the internal friction angle, ϕ_b is the bulk basal friction angle (for frictional basal resistance), f is the basal friction coefficient (for Voellmy basal resistance), ξ is the turbulence parameter (for Voellmy basal resistance) and E_s is the entrainment growth rate within a specified entrainment zone.

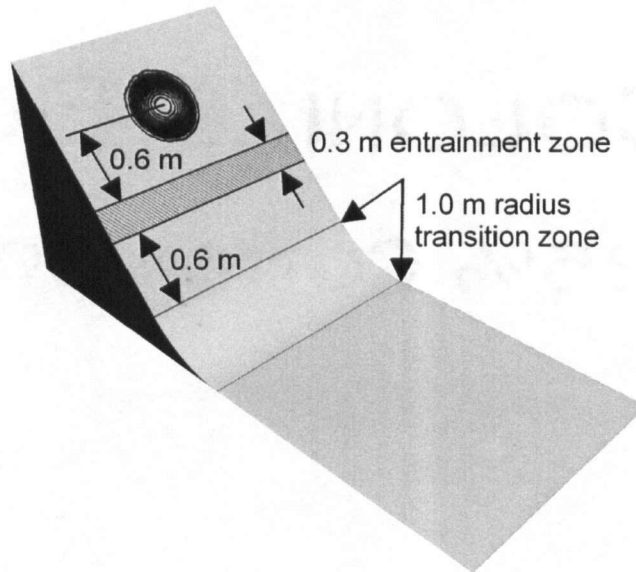


Figure 6.7. Initial configuration of the parametric analyses. The starting plane was inclined at 45° and connected to the horizontal plane by a 1 m radius smooth transition zone. The source depths (Equation [6-5]) are shown at 1 cm intervals.

6.4.3 Results and discussion: number of particles and particle smoothing

As described in Chapter 5, continuum simulation is achieved through discretization of the governing equations, but a sufficiently large number of computational elements (particles) are required to capture the behaviour at every important location within the slide mass. At the lower limit, using only one particle, the model can only simulate the motion of the centre of mass, without accounting for internal deformation. Increasing the number of particles increases the resolution of the continuum method. The present upper limit is $N = 4000$, based on the speed and memory limitations of current personal computers. All of the analyses presented in this thesis were performed using either 4000 or 2000 particles (2000 was a previous upper limit).

Interpolation plays a key role in this numerical method and the particle smoothing coefficient, B , which governs the interpolation distances and therefore the degree of smoothing, is expected to have a strong influence. As shown in Equation [5-23], its influence is in turn affected by the number of particles. This series of analyses demonstrates the related influences of control parameters N and B . The parameter values used in each

analysis are shown in Table 6.1. A frictional basal rheology (Equation [4-41]) was implemented and hydrostatic conditions were imposed (i.e., $\phi_i = 0^\circ$).

The results are shown as depth contour maps in Figure 6.8 (parts (a) to (h) correspond with the respective cases listed in Table 6.1). With lower values of B , the interpolated depths were irregular (the contour lines appear wavy), and these irregularities appeared to propagate to subsequent time steps. As the particle smoothing coefficient increased, the smoothness of the depth interpolation at each time step also increased, resulting in a more stable and symmetrical simulation. But it appears to be possible to produce too much smoothing with a sufficiently high smoothing coefficient, an effect that was evident in run (h), which exhibited too much tapering at the margins. Decreased lateral spreading was also exhibited as the smoothing coefficient increased, a result of lower interpolated depth gradients. At the extreme, sufficiently high smoothing would produce negligible depth gradients and therefore negligible particle interactions, resulting in zero spreading. A high smoothing coefficient can also cause inefficiency, as the number of particles included in the necessary summations increases exponentially with the value of B .

The key is to optimize B to produce sufficiently smooth depth interpolations while maximizing efficiency, but the results in Figure 6.8 suggest that the optimum value changes with the value of N . In this particular series of analyses, the optimum values appeared to be about $B = 4$ for $N = 2000$ (Figure 6.8d) and $B = 6$ for $N = 4000$ (Figure 6.8g). These two simulations produced very similar, reasonably smooth and stable results. The initial and final smoothing lengths (Equation [5-23]) for each simulation are listed in Table 6.2. The similarities between the smoothing lengths in simulations (d) and (g) are notable. It is possible that the ideal amount of smoothing is related to the smoothing length, irrespective of the number of particles. However, each case is unique and no general relationship can be drawn from these results. At present, it is therefore recommended that the particle smoothing coefficient, B , be adjusted by the user until the initial depth interpolation appears smooth, but still corresponds with the given geometry (probably in the range of $B = 4$ to 6). At the least, this approach limits instabilities that may compound as a result of irregularities introduced by the numerical method at startup.

Run	N	B	$\ell_{initial}$ (m)	ℓ_{final} (m)
(a)	4000	3	0.022	0.038
(b)	2000	3	0.031	0.052
(c)	4000	4	0.029	0.049
(d)	2000	4	0.041	0.067
(e)	4000	5	0.036	0.061
(f)	2000	5	0.052	0.081
(g)	4000	6	0.044	0.071
(h)	2000	6	0.062	0.093

Table 6.2. Initial and final smoothing lengths corresponding to analyses (a) to (h) presented in Section 6.4.3 and Figure 6.8.

6.4.4 Results and discussion: internal friction

As described in Chapter 2, the internal strength of landslide material has an important mitigating influence on spreading; because of it, landslides do not spread out or contract as readily as fluids. This series of analyses demonstrates the influence of the internal friction angle, ϕ_i , which governs the limiting internal stress states in DAN3D (cf., Chapter 5). The parameter values used in each analysis are shown in Table 6.1. A frictional basal rheology (Equation [4-41]) was implemented. Note that run (g) in Section 6.4.3 and Figure 6.8 is considered part of this series, as the same set of parameter values were used, but with $\phi_i = 0^\circ$ to simulate hydrostatic conditions.

The results are shown as depth contour maps in Figure 6.9 (parts (a) to (d) correspond with the respective cases listed in Table 6.1). A higher value of ϕ_i resulted in slower initial spreading, as the internal stresses initially tended to the active state in both the longitudinal and lateral directions. However, longitudinal convergence during motion through the concave transition zone resulted in the development of passive stresses in the longitudinal direction, which increased the longitudinal spreading forces in this segment of the path. The result was a longer deposit (the final position of the flow front increased, while the final

position of the tail decreased). The final location of the centre of mass did not change very much, although it did increase slightly as ϕ_i increased, due mainly to the degree of lateral spreading. In this case, the tendency to active lateral stress states along most of the path resulted in less lateral spreading with higher values of ϕ_i . Less lateral spreading in turn resulted in less energy dissipation, which allowed the centre of mass to travel farther (cf., Chapter 2).

The prevailing stress states recorded at each time interval during run (c) are shown in Figure 6.10. The limiting values of the stress coefficients in this case are shown in Table 6.3. Simultaneous longitudinal contraction and lateral expansion through the concave transition zone resulted in anisotropic conditions (i.e., simultaneous longitudinal passive stresses and lateral active stresses). Note that passive longitudinal stress conditions near the flow front did not necessarily persist through the entire runout zone. Run (c) represents the “base case” for the rest of the analyses presented in this section, which all used $\phi_i = 35^\circ$.

$k_{x(\min/\max)}$	$k_{y(\min/\max)}$
$k_{x(\max)} = 3.26$	$k_{y(\max)} = 3.35$
	$k_{y(\min)} = 0.91$
$k_{x(\min)} = 0.71$	$k_{y(\max)} = 1.34$
	$k_{y(\min)} = 0.36$

Table 6.3. Limiting values of the stress coefficients in run (c), in which $\phi_b = 25^\circ$ and $\phi_i = 35^\circ$ (cf., Equations [5-32] to [5-34] in Chapter 5).

6.4.5 Results and discussion: internal stiffness

As described in Chapter 5, the dimensionless stiffness coefficient, D , controls the strain-dependent rate of the transition between active and passive internal stress states. At one extreme, a value of $D=0$ produces hydrostatic conditions, as the stresses cannot change from their initial values, which are assumed to be hydrostatic in DAN3D. At the other

extreme, an infinite value of D produces instantaneous stress response, with no intermediate states possible between the active and passive limits.

In the original DAN model (Hungry 1995), the value of the stiffness coefficient was based on values measured in granular soil behind retaining walls (after Terzaghi and Peck 1967). Different values were used depending on whether the deformation was contractional or expansional: $D = (k_p - k_a) / 0.05$ in contraction and $D = (k_p - k_a) / 0.025$ in expansion, where k_p and k_a were user-specified values of the passive and active earth pressure coefficients, respectively. For the limiting stress coefficients that applied in this series of simulations (Table 6.3), the appropriate value of D should therefore fall within the range of about 25 to 100. A value of $D = 10000$, representing the approximate equivalent of infinite stiffness, commonly assumed by other workers (cf., Chapter 2), was also tested for comparison. The parameter values used in each analysis are shown in Table 6.1. A frictional basal rheology (Equation [4-41]) was implemented. Note that run (g) in Section 6.4.3 and Figure 6.8 and run (c) in Section 6.4.4 and Figure 6.9 are considered part of this series, as they represent comparable simulations using $D = 0$ and $D = 200$, respectively.

The results are shown as depth contour maps in Figure 6.11 (parts (a) to (d) correspond with the respective cases listed in Table 6.1). A higher stiffness coefficient produced a longer deposit, due to the relatively faster transition between the active longitudinal stress state on the inclined plane and the passive state through the concave transition zone. The faster transition increased the duration of the passive state, which gave the flow front a longer “push” that caused it to travel slightly farther. The otherwise minor differences between these simulations suggest that the use of different stiffness values in contraction or expansion would not make a significant difference and is probably not necessary.

Somewhat surprisingly, the use of a pseudo-infinite stiffness coefficient did not appear to introduce numerical instability in this case (cf., Chapter 5). On the contrary, run (d) appeared to produce even more orderly and symmetrical results than the other analyses. This may have been in part due to the very simple geometry, which caused only a couple of cycles

between active and passive states. The process of stress transition may play a more important role over more complex topography. But it is also possible that infinite stiffness actually improves stability by ensuring an immediate reduction in tangential stresses during expansion and an immediate increase in tangential stresses during contraction, which is an extremely responsive form of damping. On the other hand, infinite stiffness does not allow for the possibility of stress states intermediate between active and passive, which could possibly develop during pseudo-steady-state motion in long, uniform reaches of a landslide path. Unfortunately, a general conclusion on this issue cannot be drawn from this series of results alone. A default value of $D = 200$ is therefore recommended, pending further work.

6.4.6 Results and discussion: velocity smoothing

As described in Chapter 5, velocity smoothing, which introduces some numerical diffusion, is an option that smoothes out strong shocks by reducing so-called particle penetration (Monaghan 1989). It may also increase numerical stability and improve the behaviour of the model in channelized reaches of the path by reducing the tendency for particles to line up in the downstream direction. This series of analyses demonstrates the influence of the velocity smoothing coefficient, C , which governs the degree of velocity smoothing in DAN3D (cf., Equation [5-57] in Chapter 5). The parameter values used in each analysis are shown in Table 6.1. A frictional basal rheology (Equation [4-41]) was implemented. Note that run (c) in Section 6.4.4 and Figure 6.9 is considered part of this series.

The results are shown as depth contour maps in Figure 6.12 (parts (a) to (d) correspond with the respective cases listed in Table 6.1). An increase in the velocity smoothing coefficient tended to reduce the amount of initial spreading, as particles near the margins became increasingly influenced by the conditions further within the flow. This behaviour could potentially be exploited to simulate initial cohesion in real landslides, including rock slides in the early stages of fragmentation. Velocity smoothing also smoothed out the shock, or hydraulic jump (e.g., Chow 1959), that formed near the tail of the flow during deposition; the tail of the deposit was not as steep and did not travel as far with increased smoothing, since particles could not penetrate as easily into the material that had deposited ahead.

It appears that it is possible for this form of numerical damping to produce too much smoothing. For example, in run (d) the material may have exhibited too much cohesiveness, considering that the friction angles used in this case were appropriate for dry sand with no cohesion. Although a universal value of C cannot be recommended based on these results, a value up to about $C = 0.01$ is probably appropriate.

It should be noted that the final location of the centre of mass was not affected significantly. A very slight decrease with increasing velocity smoothing (about 1 mm horizontally for each 0.005 increment of C) can be attributed to the shock smoothing as well as a corresponding decrease in energy dissipation due to decreased lateral spreading. But otherwise, linear momentum was completely conserved.

6.4.7 Results and discussion: basal rheology

Modifications to the basal rheology and its parameters can have a dominant influence on the results, a characteristic that is demonstrated in this series of analyses. In the first two analyses, the frictional rheology (Equation [4-41]) was used to simulate a range of granular flow behaviour between approximately saturated and dry conditions. In the last two analyses, the Voellmy rheology (Equation [4-42]) was used with friction coefficients and turbulence parameters within a range of common calibrated values (e.g., Hungr and Evans 1996). The parameter values used in each analysis are shown in Table 6.1. As described in Chapter 4, a number of basal rheologies have been implemented in DAN3D, but the frictional and Voellmy rheologies have been used exclusively in the examples presented in this thesis.

The results are shown as depth contour maps in Figure 6.13 (parts (a) to (d) correspond with the respective cases listed in Table 6.1). With the frictional basal rheology, an increase in the bulk basal friction angle reduced both spreading and translation of the slide mass, resulting in a deeper deposit. With $\phi_b = 30^\circ$ the deposit did not travel far beyond the toe of the source slope, while with $\phi_b = 20^\circ$ it spread out relatively thinly and covered a larger area. In both

analyses, as in all of the previous frictional analyses presented in this section, the final location of the centre of mass was in the proximal part of the deposit.

Significantly different behaviour resulted with use of the Voellmy basal rheology. While the frictional components of resistance in runs (c) and (d) were less than those in runs (a) and (b) (friction coefficients 0.1 and 0.2 are equivalent to bulk basal friction angles of about 5.7° and 11.3° , respectively), the added velocity-dependent resistance mitigated spreading and downslope acceleration during the early stages of motion. This added resistance had a relatively higher influence near the flow margins, as the turbulence term in Equation [4-42] dominates when the flow depths are low (infinite resistance results when the flow depth is zero, which occurs directly at the margins). Gray and Tai (1998) recognized the existence of this singularity and proposed an alternative to the Voellmy model to permit motion of the margins. In DAN3D, the interpolated flow depths at particle locations are always non-zero, but this effect can still be significant at very low flow depths. In this case, it allowed the deeper part of the flow to attain relatively higher velocities on the source slope, which created a steep flow front followed by a tapered tail, similar to the classic profile of a debris flow surge, and allowed the centre of mass to travel farther into the distal part of the deposit, in contrast to the frictional examples. The relatively lower frictional resistance then allowed the material to spread out thinly over a large area.

The dominant influence of the turbulence term is evident when comparing cases (c) and (d). Even though a smaller friction coefficient was used in case (c), the mass did not travel as far because the lower turbulence parameter significantly reduced its momentum. Note the inverse relationship between the turbulence parameter and resistance, and that the Voellmy model converges on the frictional model when the turbulence parameter is infinite.

6.4.8 Results and discussion: entrainment

As described in Chapter 2, mass and momentum transfer during entrainment of path material can have an important influence on landslide dynamics. On one hand, the volume of the landslide increases, which can result in increased flow and deposit depths as well as

increased impact and deposit areas. On the other hand, momentum transfer contributes resistance, which can have an effect on the degree of spreading and translation. This series of simulations demonstrates the effects of mass and momentum transfer during entrainment.

For comparison, two cases were considered: one involving no entrainment and the other involving entrainment that doubled the volume over a short distance of 0.3 m (Figure 6.7) using a growth rate of $E_s = 2.22 \text{ m}^{-1}$. In this example, centripetal acceleration was neglected. It would have otherwise contributed a velocity-squared component to the internal and basal stresses in the concave transition zone, making it more difficult to highlight the differences between the two cases. The parameter values used in each analysis are shown in Table 6.1. A frictional basal rheology (Equation [4-41]) was implemented.

The results are shown as depth contour maps in Figure 6.14. It is useful to compare these results with the idealized sliding block model described in Chapter 2 (both the single and multi-block cases). Recall that in the case of the single sliding block, the inclination of the energy line would equal the dynamic basal friction angle if centripetal acceleration was neglected. Analogously, in run (a) the inclination of the line connecting the initial and final positions of the centre of mass should have been slightly less than ϕ_b (slightly less because of energy dissipation during lateral spreading). However, the centre of mass travelled horizontally approximately 1.5% further than expected. This discrepancy can be attributed to the inability of the model to handle the strong shock (hydraulic jump) that formed near the tail in the latter stages of deposition (e.g., Wieland et al. 1999). Trailing particles penetrated the deposit without losing the correct amount of energy at the jump. This problem, which was observed in every analysis presented in this section, did not affect the model in the more important (from a risk assessment point of view) distal runout zone, where the transition from supercritical to subcritical flow during deposition (the mechanism for a hydraulic jump) was not as abrupt. As mentioned in Section 6.4.6, velocity smoothing appears to help by smoothing out the shock and reducing particle penetration.

Analogous to the multi-block case, in run (b) the centre of mass did not travel as far due to the additional resistance caused by momentum transfer in the entrainment zone. At the same

time, the increase in volume resulted in more spreading that produced a larger deposit area (by approximately 30%), but with a thicker average depth (by approximately 55%). As described in Chapter 3, the momentum transfer effect has been neglected (at least in an explicit form) by many workers and is perhaps one reason why the Voellmy rheology, which contains a similar velocity-dependent term, has been used successfully to simulate landslides involving substantial entrainment. Such an implicit approach can be used (e.g., Perla et al. 1980), but it cannot account for isolated entrainment. Furthermore, the results shown here suggest that the accompanying increase in volume also has an important influence and should be accounted for explicitly.

Figure 6.15 shows the final bed-normal erosion depths within the entrainment zone. Erosion extended beyond the boundaries of the simulated entrainment zone as a result of the smoothing imposed by Equation [5-49] (if the interpolating kernel, W , is wider than the fixed grid cell width, a particle can reach beyond its own cell and remove material from adjacent cells). This effect is minor at larger scales and, in any case, real entrainment zone boundaries are difficult to accurately delineate. Mass balance was satisfied in the simulation, as the volume of material removed from the path, approximately 21.2 litres, was equal to the volume entrained by the landslide.

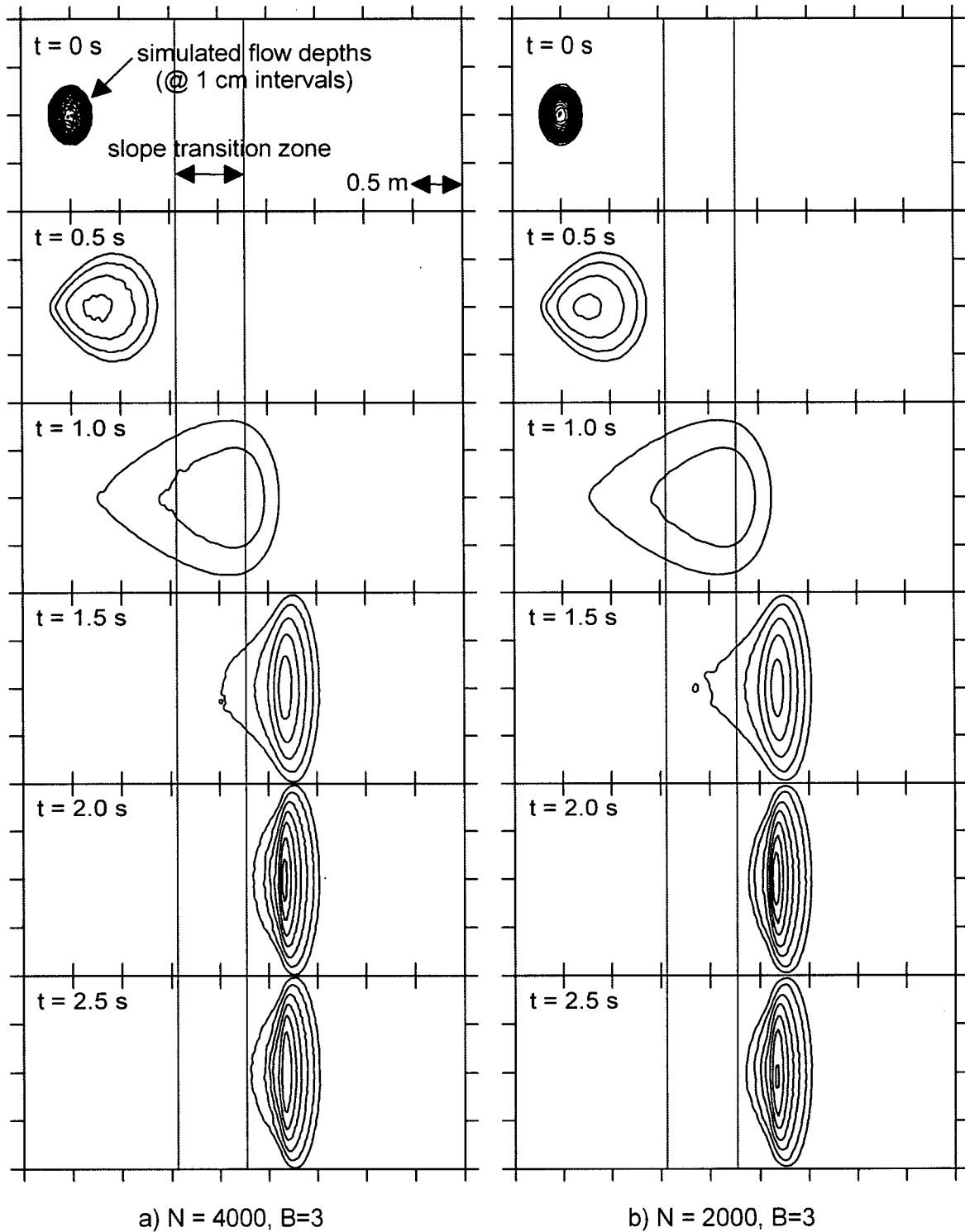


Figure 6.8. Parametric analyses varying the number of particles and the particle smoothing coefficient. (a) $N = 4000$ and $B = 3$. (b) $N = 2000$ and $B = 3$. The results are discussed in Section 6.4.3.

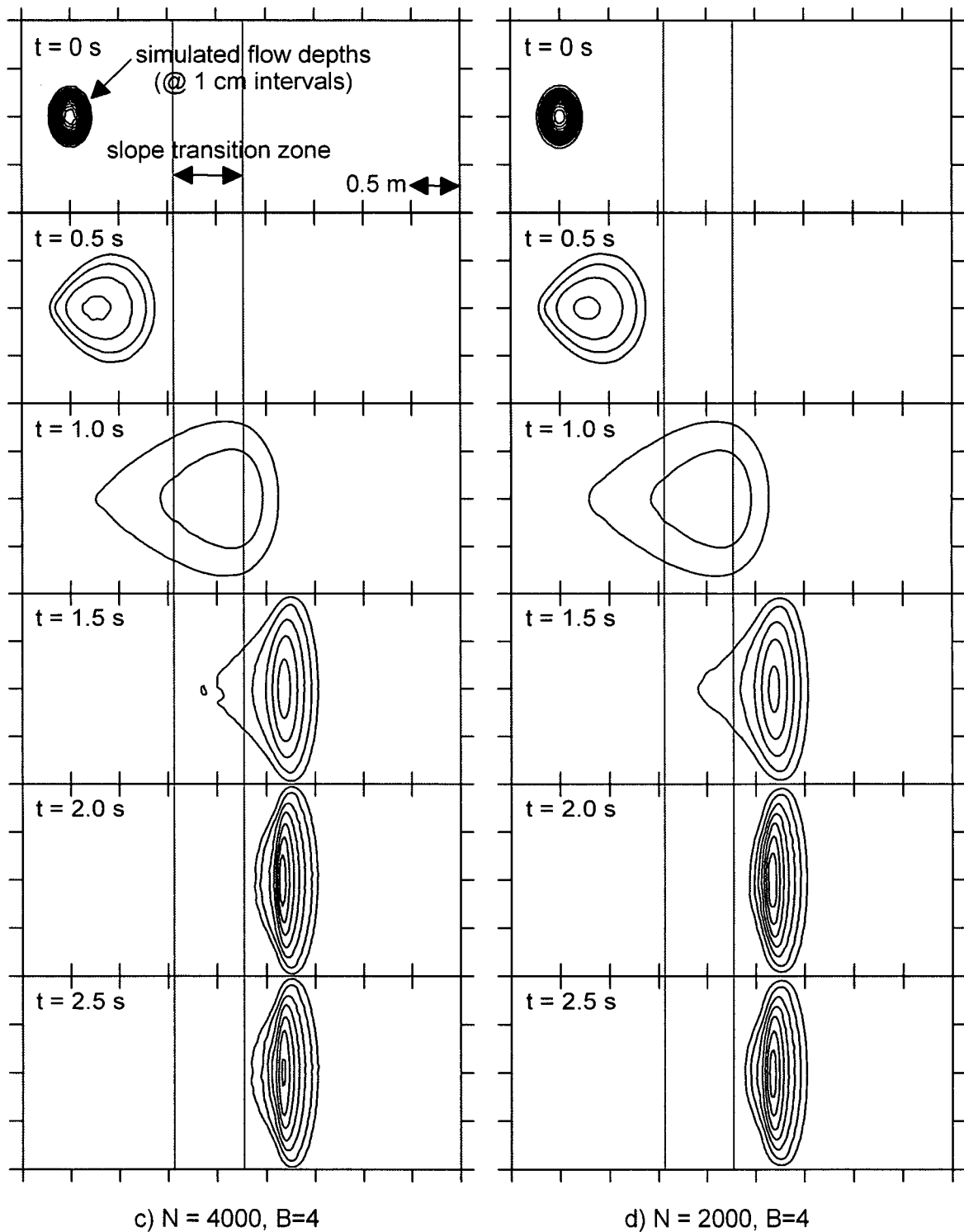


Figure 6.8 (continued). Parametric analyses varying the number of particles and the particle smoothing coefficient. (c) $N = 4000$ and $B = 4$. (d) $N = 2000$ and $B = 4$. The results are discussed in Section 6.4.3.

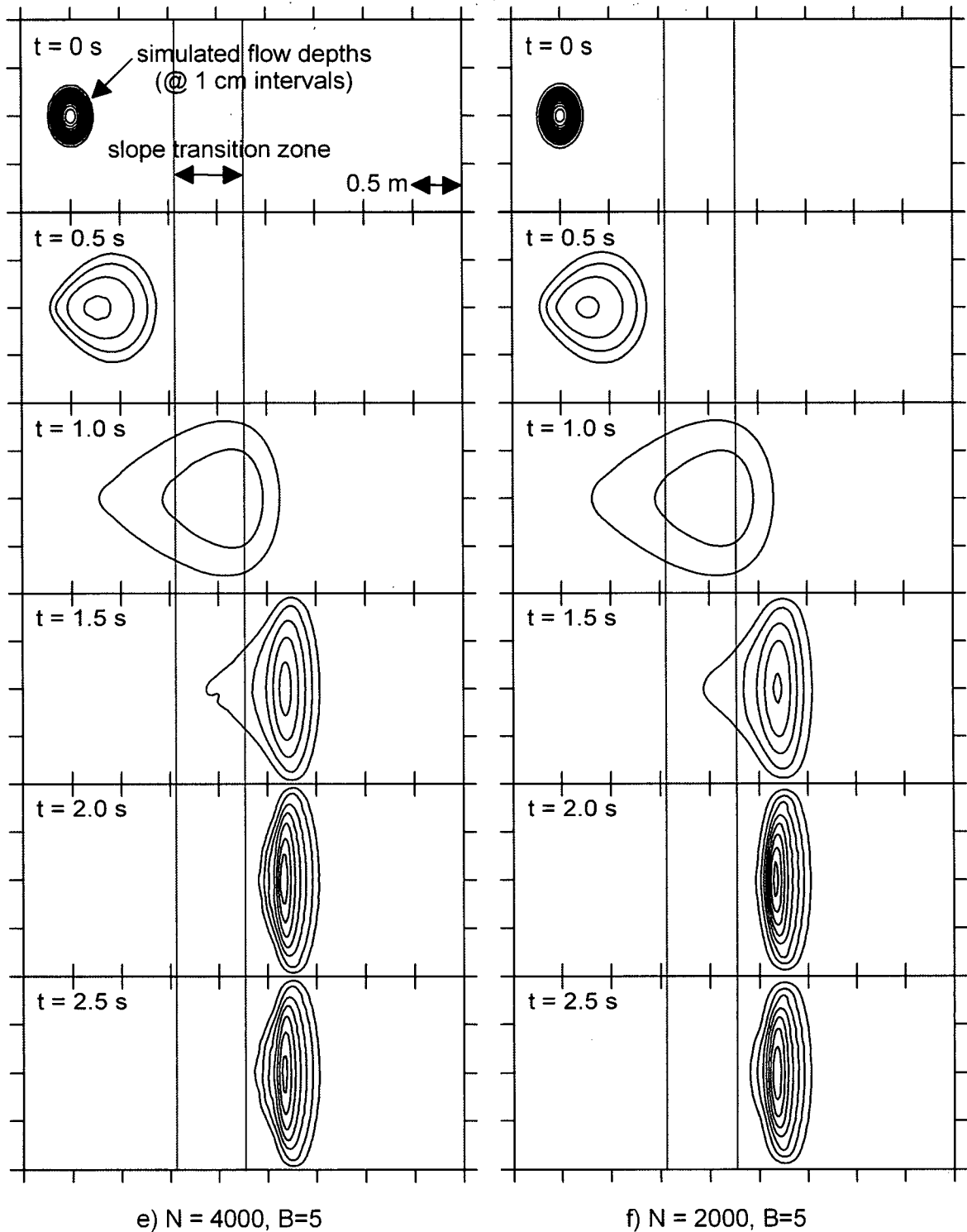


Figure 6.8 (continued). Parametric analyses varying the number of particles and the particle smoothing coefficient. (e) $N = 4000$ and $B = 5$. (f) $N = 2000$ and $B = 5$. The results are discussed in Section 6.4.3.

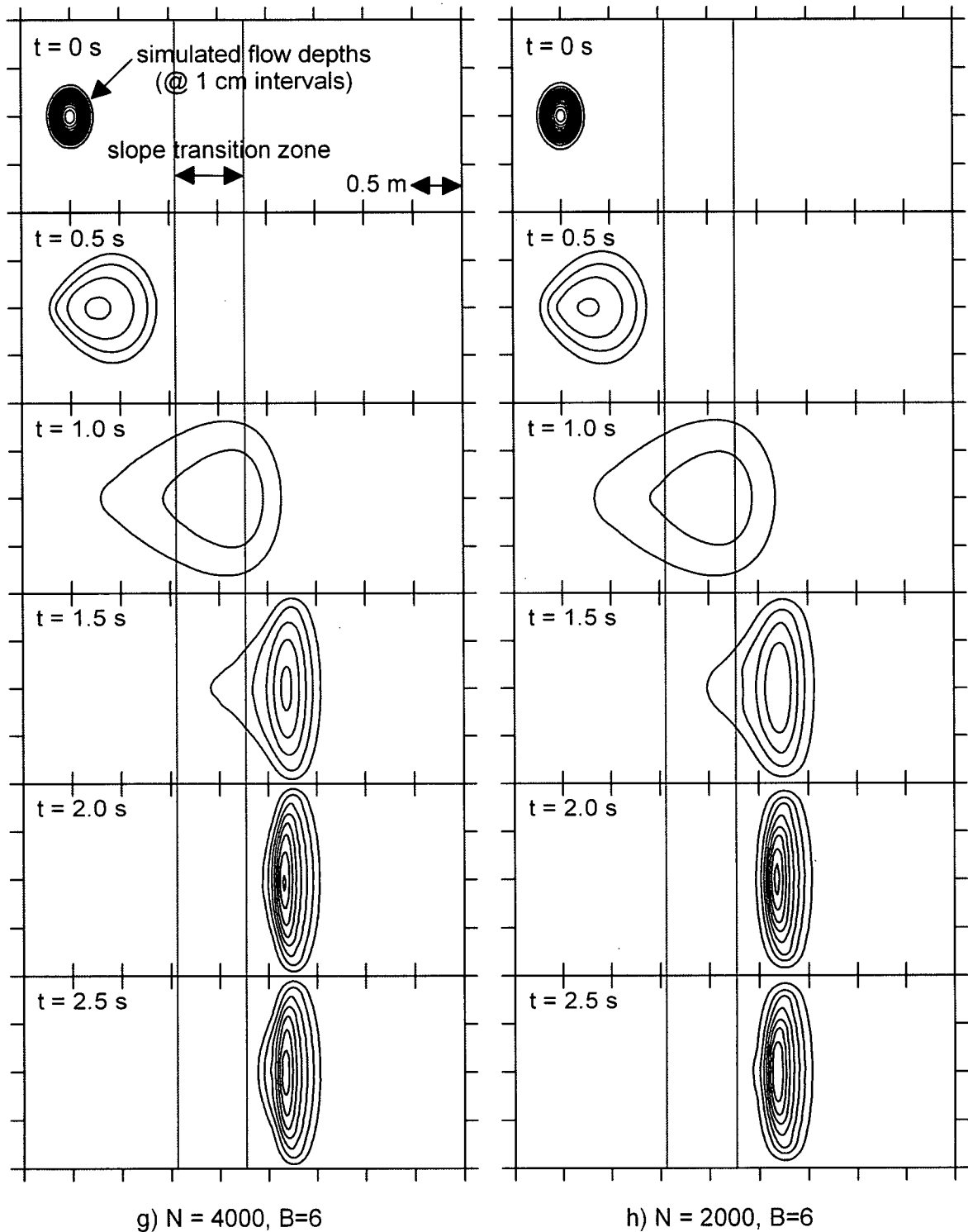


Figure 6.8 (continued). Parametric analyses varying the number of particles and the particle smoothing coefficient. (g) $N = 4000$ and $B = 6$. (h) $N = 2000$ and $B = 6$. The results are discussed in Section 6.4.3.

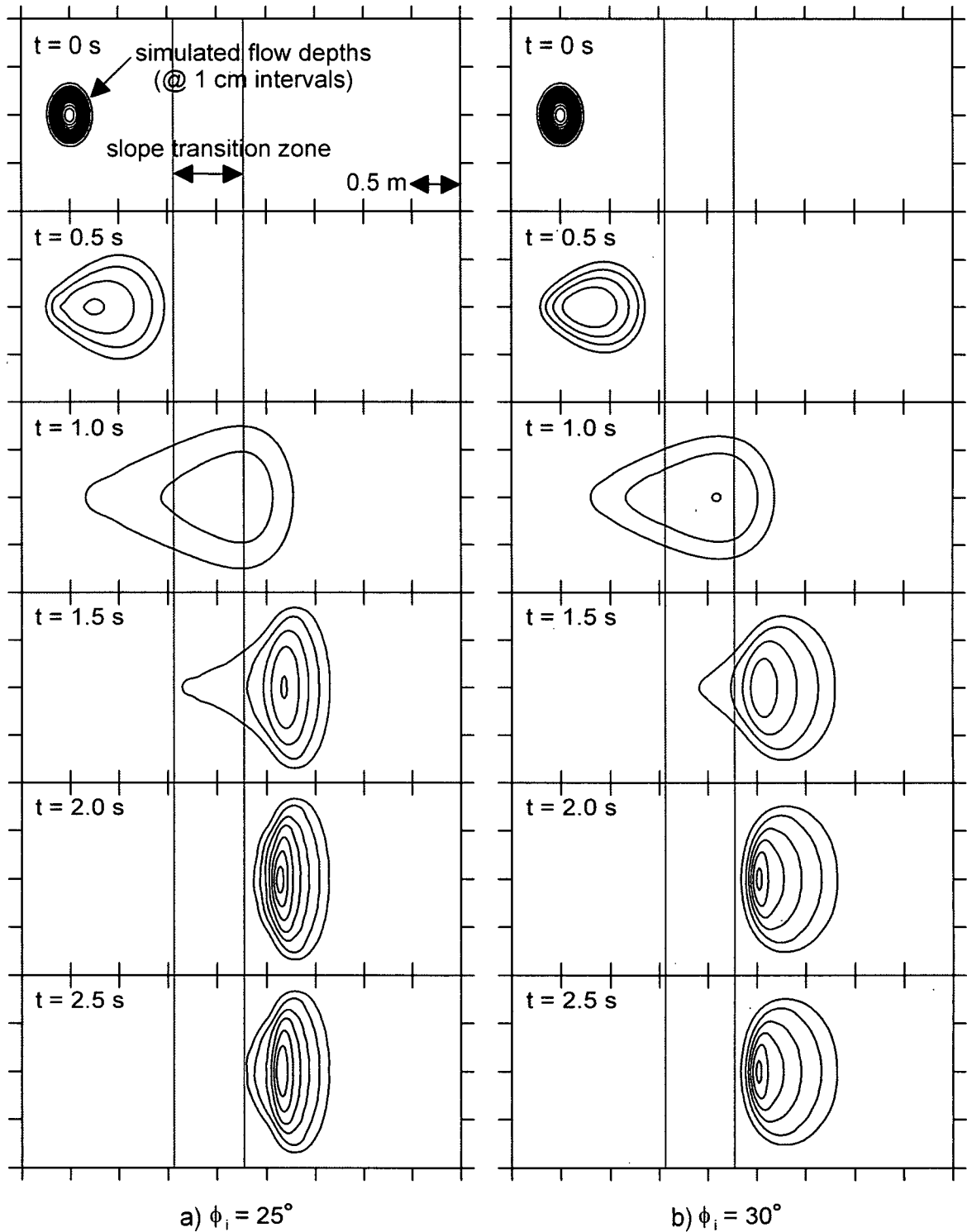


Figure 6.9. Parametric analyses varying the internal friction angle. (a) $\phi_i = 25^\circ$. (b) $\phi_i = 30^\circ$. The results are discussed in Section 6.4.4.

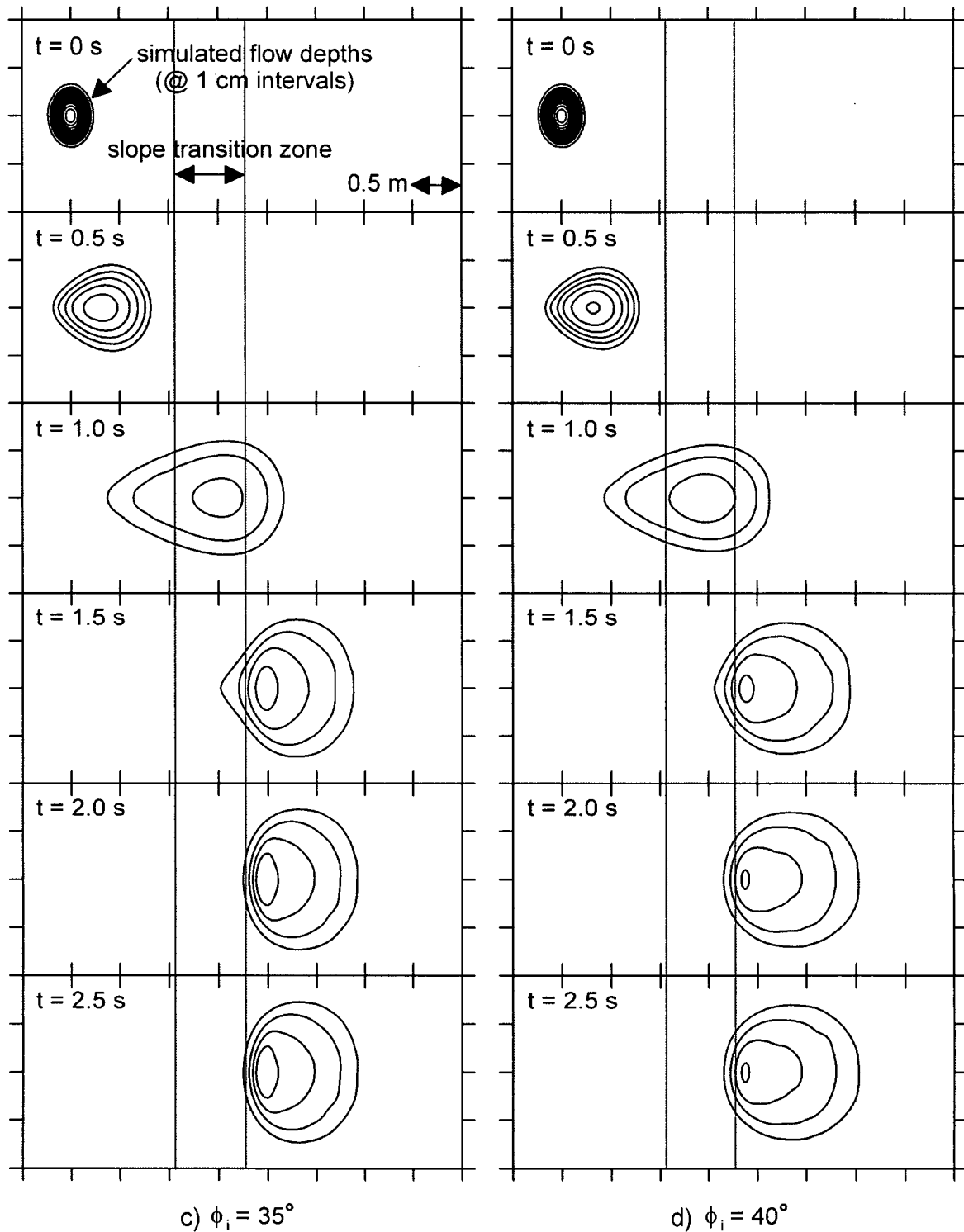


Figure 6.9 (continued). Parametric analyses varying the internal friction angle. (c) $\phi_i = 35^\circ$. (d) $\phi_i = 40^\circ$. The results are discussed in Section 6.4.4.

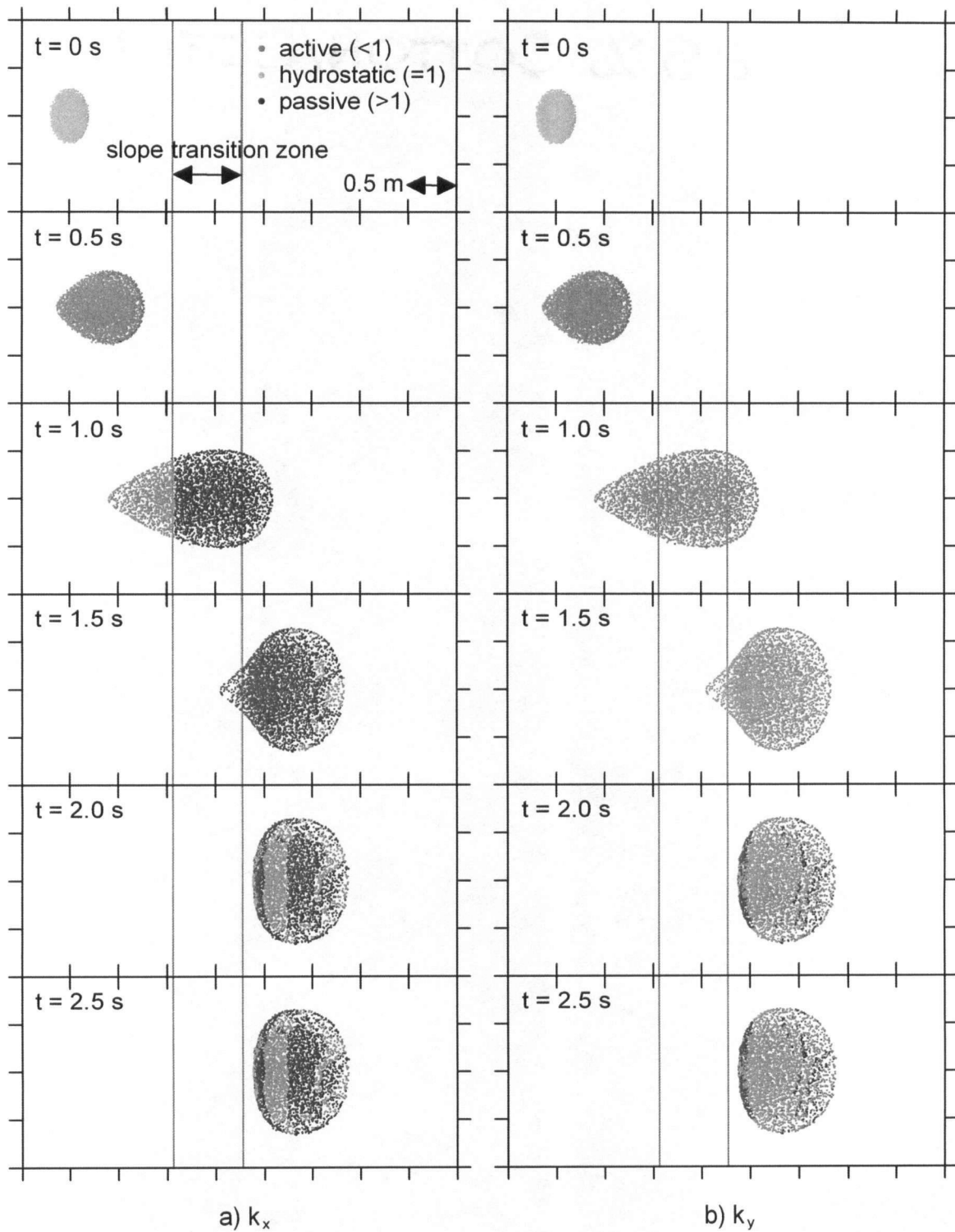


Figure 6.10. Prevailing longitudinal (x direction) and lateral (y direction) stress states recorded at each time interval during run (c) shown in Figure 6.9. The results are discussed in Section 6.4.4.

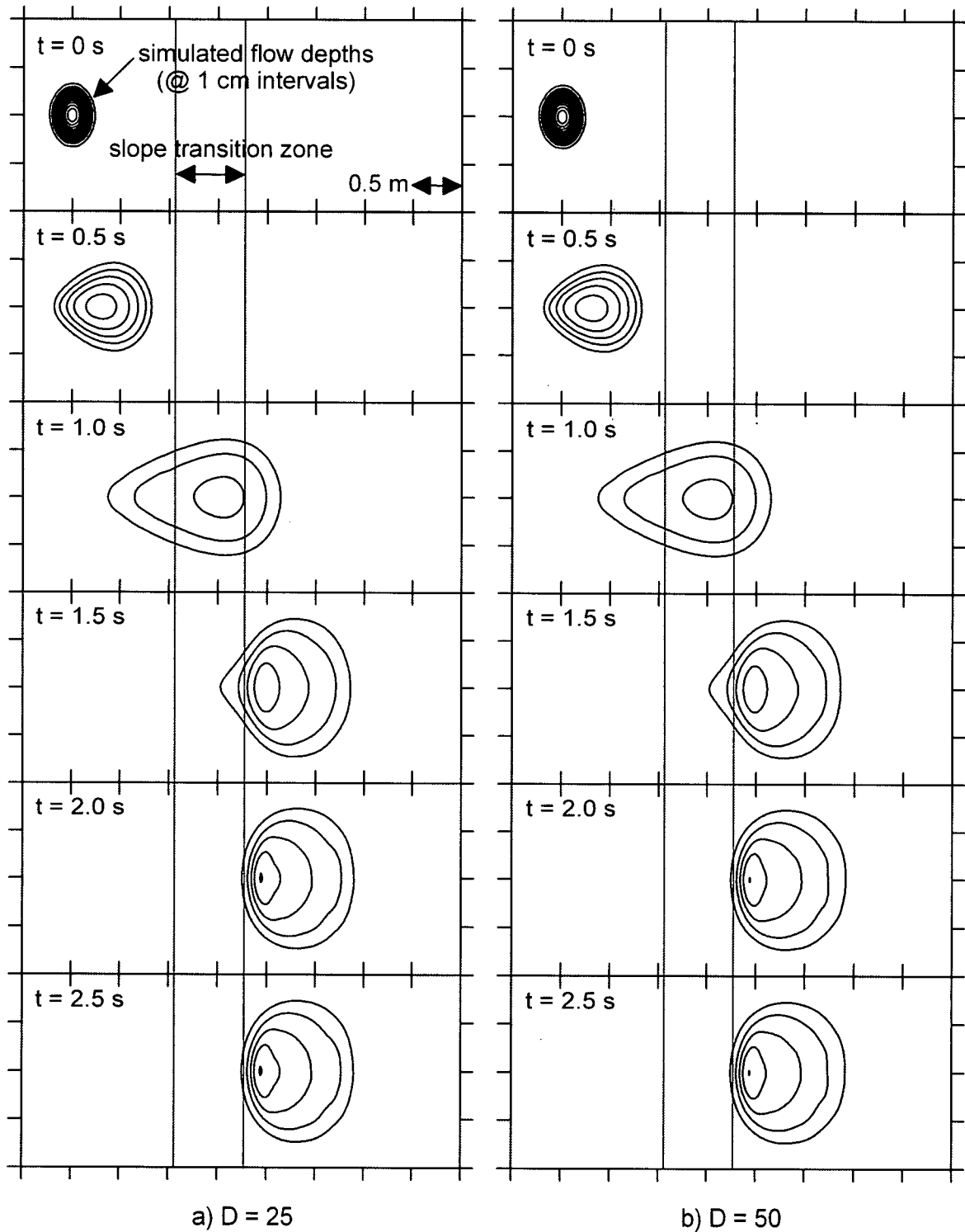


Figure 6.11. Parametric analyses varying the dimensionless stiffness coefficient. (a) $D = 25$. (b) $D = 50$. The results are discussed in Section 6.4.5.

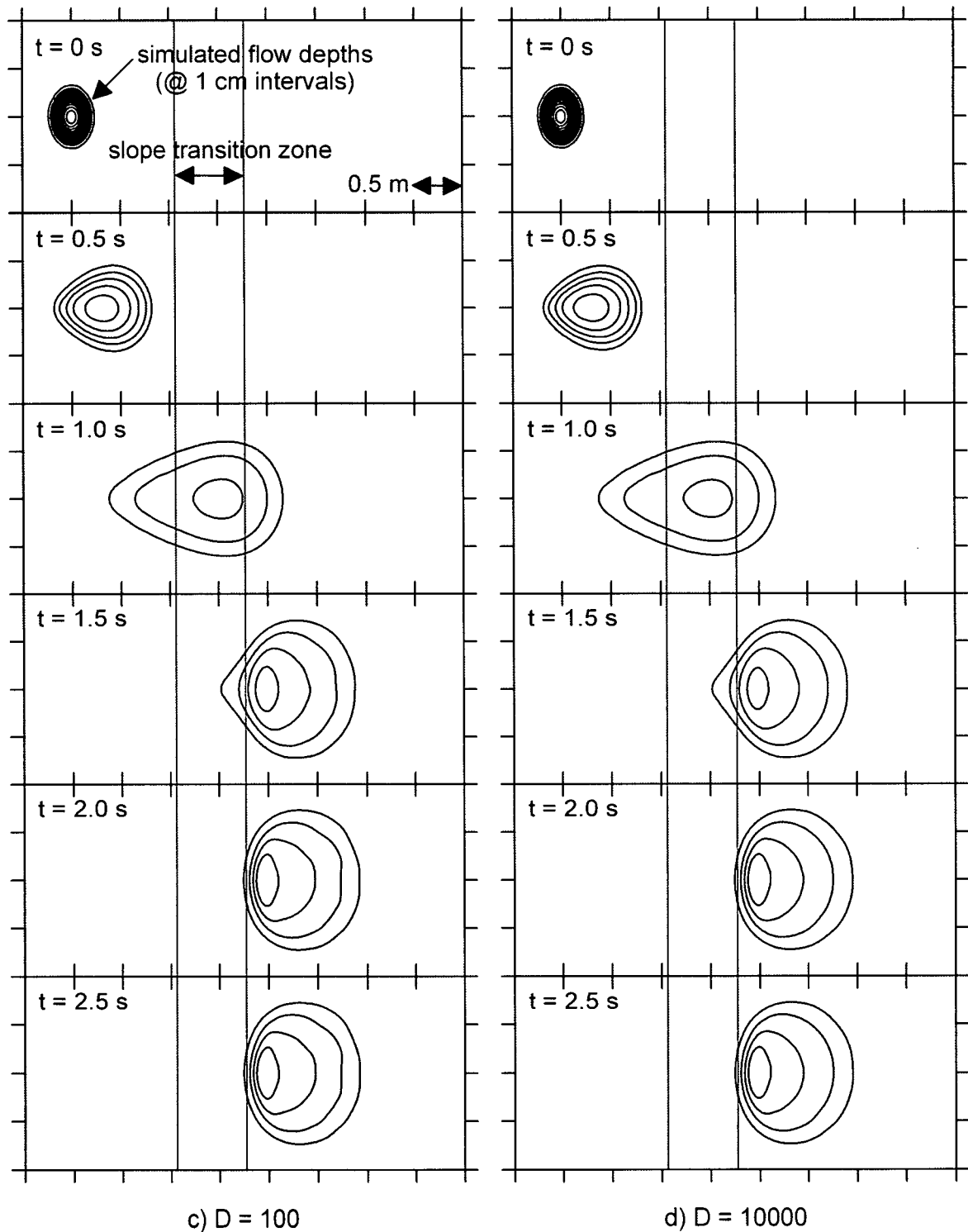


Figure 6.11 (continued). Parametric analyses varying the dimensionless stiffness coefficient. (c) $D = 100$. (d) $D = 10000$ (a pseudo-infinite value). The results are discussed in Section 6.4.5.

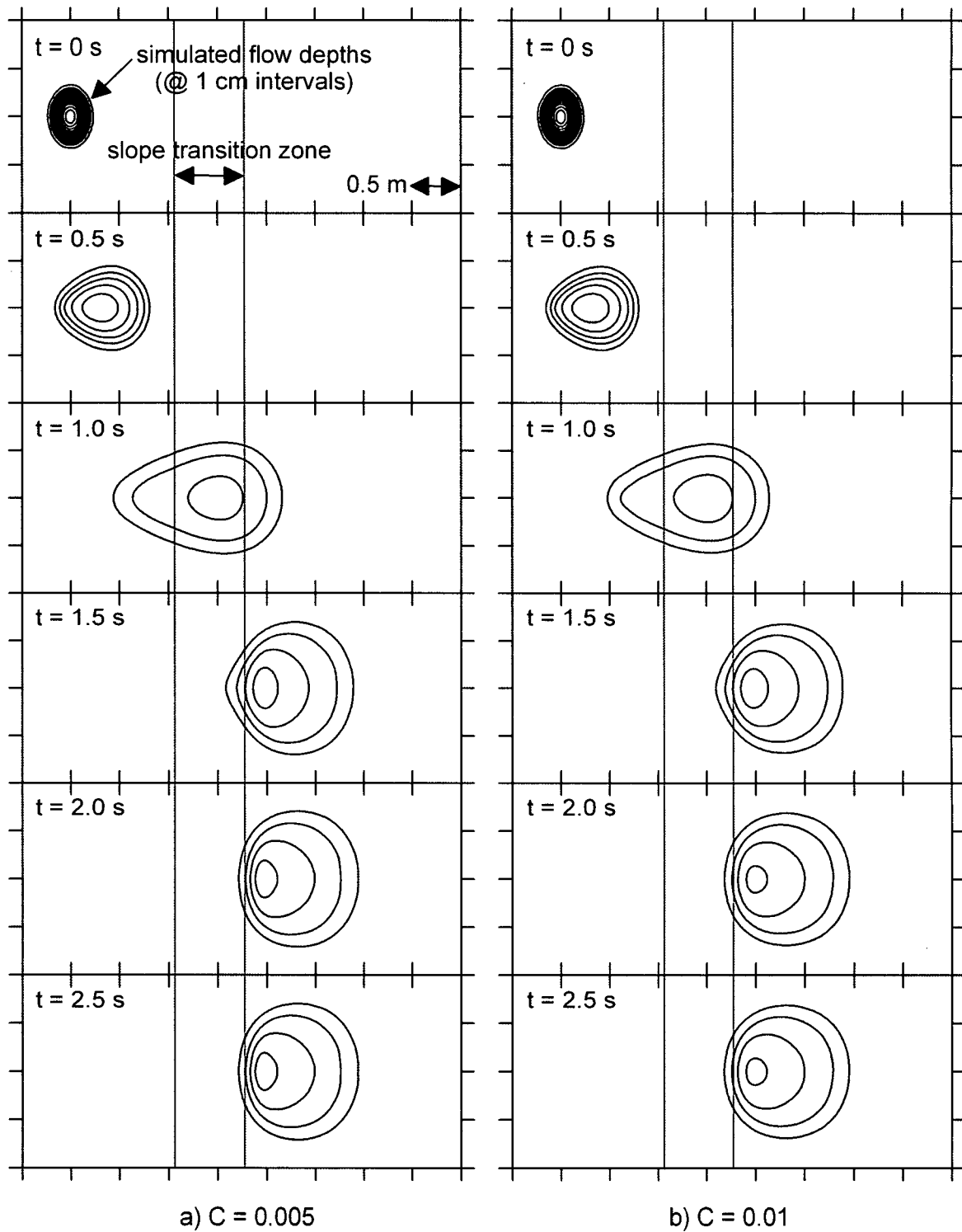


Figure 6.12. Parametric analyses varying the velocity smoothing coefficient. (a) $C = 0.005$. (b) $C = 0.01$. The results are discussed in Section 6.4.6.

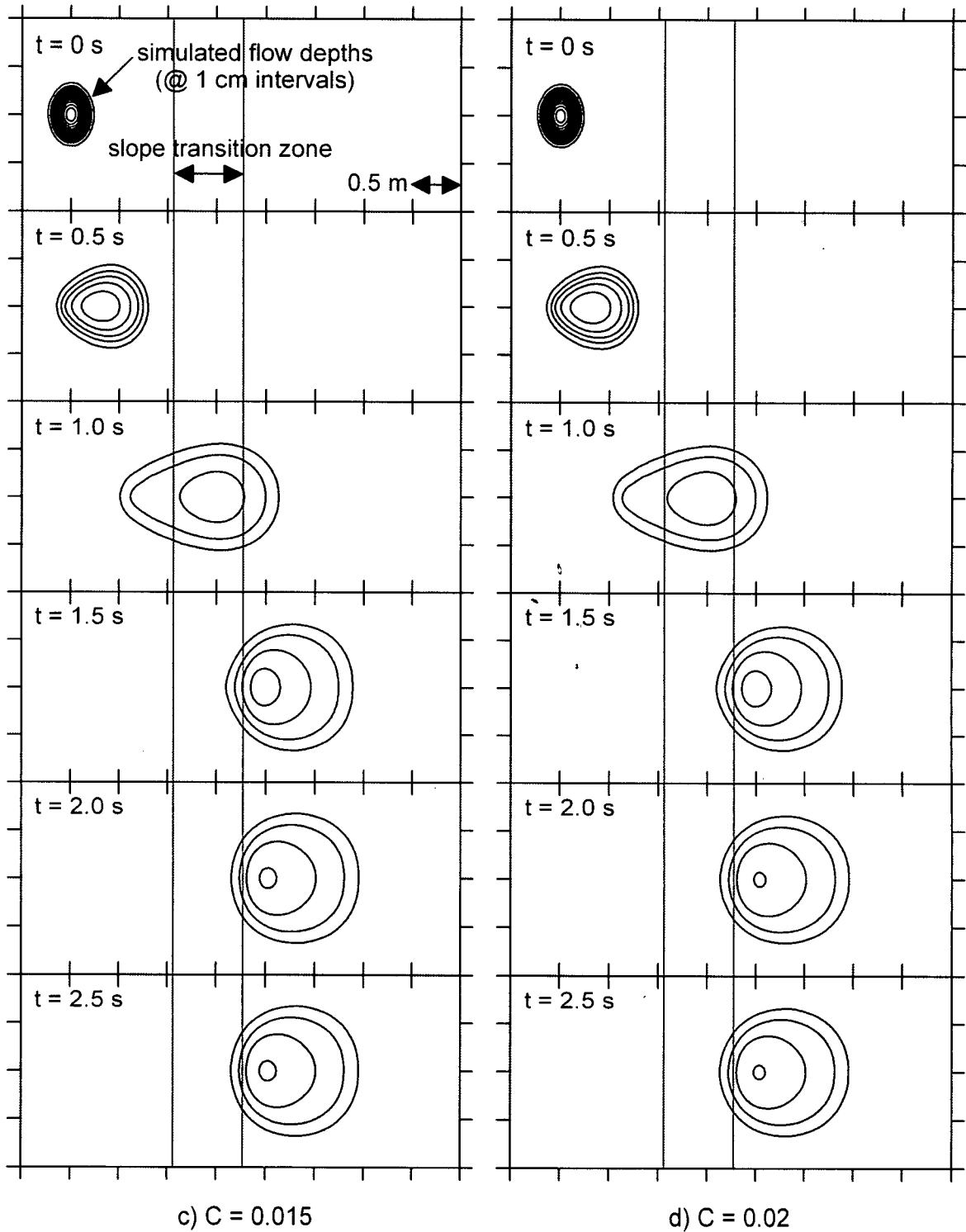


Figure 6.12 (continued). Parametric analyses varying the velocity smoothing coefficient. (c) $C = 0.015$. (d) $C = 0.02$. The results are discussed in Section 6.4.6.

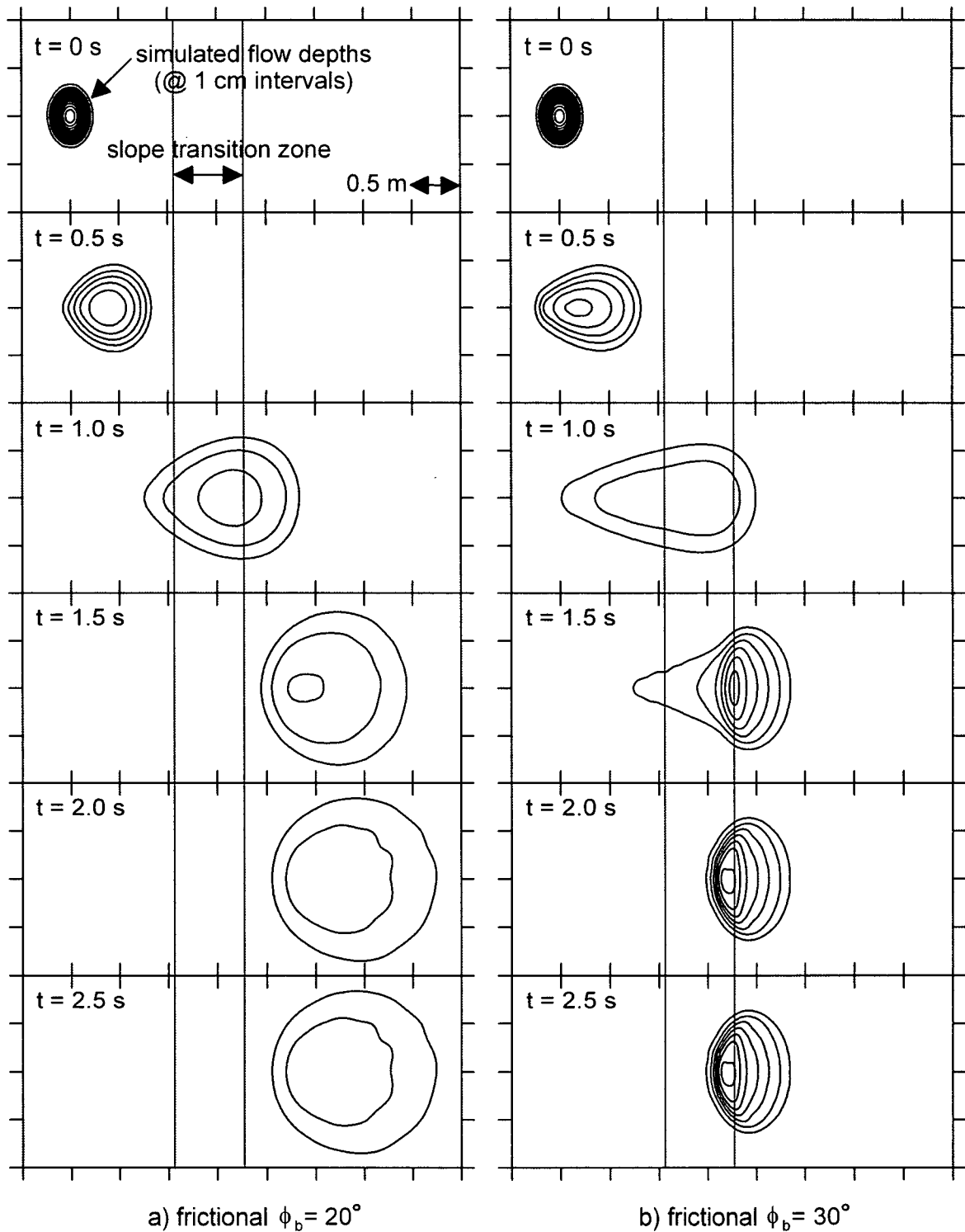


Figure 6.13. Parametric analyses varying the basal rheology and its parameters. A frictional rheology was implemented in these two analyses. (a) $\phi_b = 20^\circ$. (b) $\phi_b = 30^\circ$. The results are discussed in Section 6.4.7.

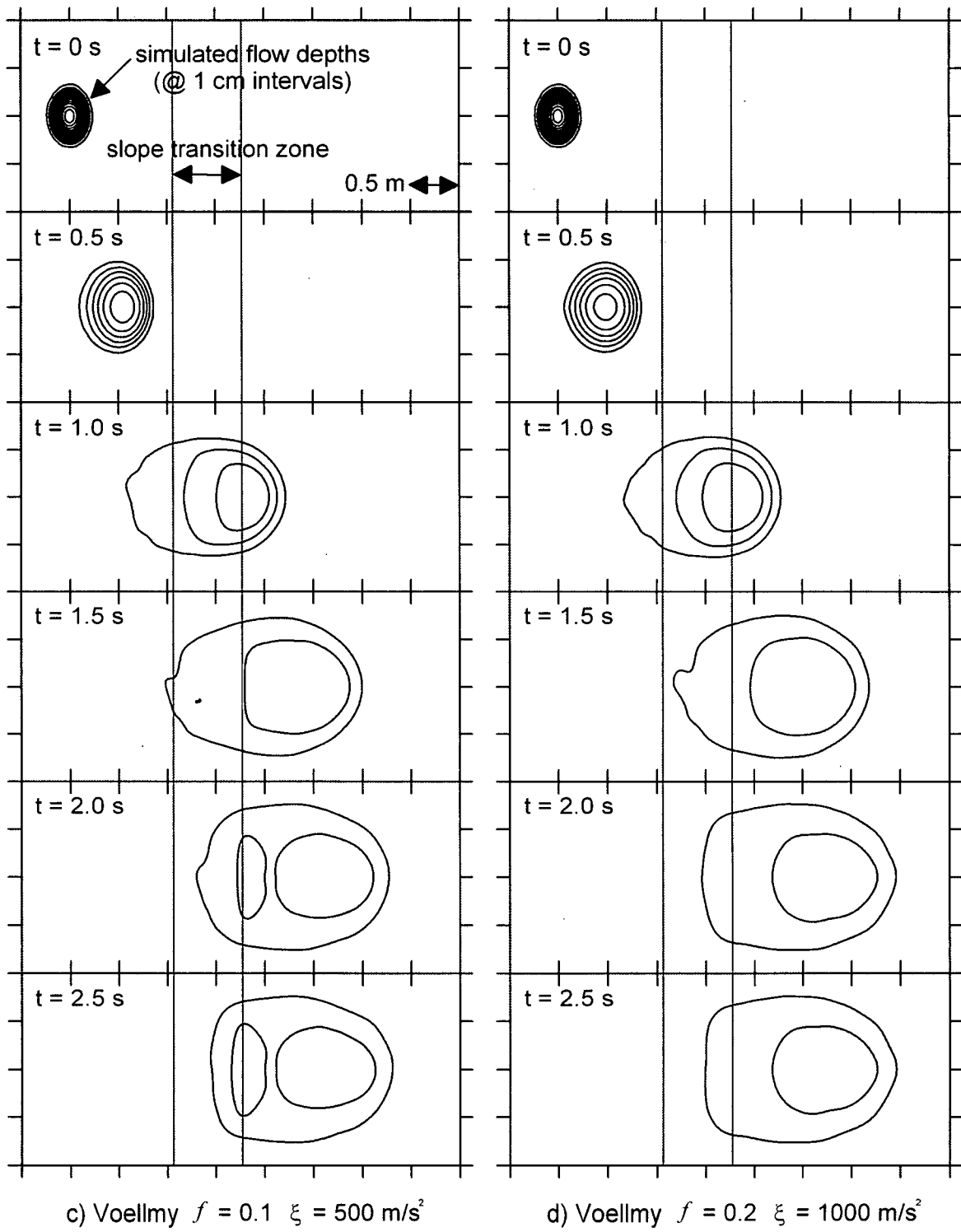


Figure 6.13 (continued). Parametric analyses varying the basal rheology and its parameters. The Voellmy rheology was implemented in these two analyses. (c) $f = 0.1$ and $\xi = 500 \text{ m/s}^2$. (d) $f = 0.2$ and $\xi = 1000 \text{ m/s}^2$. The results are discussed in Section 6.4.7.

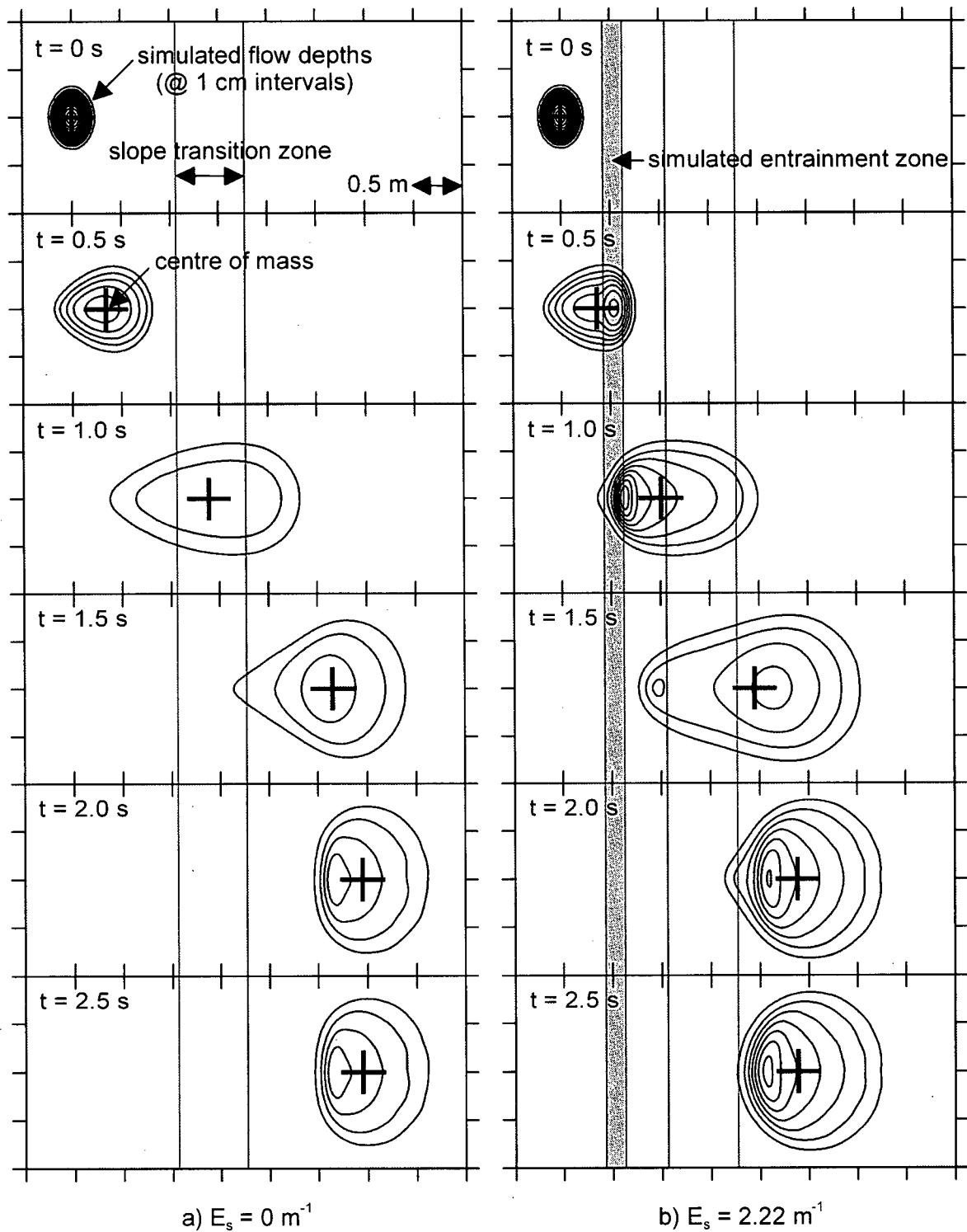


Figure 6.14. Parametric analyses neglecting centripetal acceleration and varying the entrainment growth rate. (a) $E_s = 0$. (b) $E_s = 2.22 \text{ m}^{-1}$. The results are discussed in Section 6.4.8.

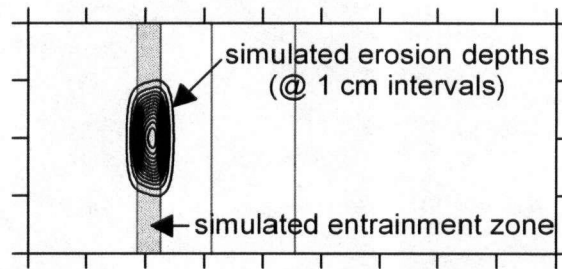


Figure 6.15. Erosion map corresponding to run (b) shown in Figure 6.14b. The results are discussed in Section 6.4.8.

6.5 Channelization

6.5.1 Description

Preliminary simulations of real landslides using DAN3D showed that there is a tendency for particles to line up in the downstream direction in highly channelized reaches. In such cases, the model essentially reverts to 2D and is unable to properly account for lateral momentum balance (cross-stream gravity driving stresses are still accounted for but internal pressure gradients are not). This could be a problem, particularly in channel bends, where superelevation and potential avulsion may not be accurately simulated. Resolution is thought to be the main issue. As the particles stretch out in the downstream direction, gaps form between them. Since the particles are constantly drawn to the thalweg of the channel by gravity, when they find a gap they simply fall in line. Increasing the number of particles (i.e., increasing the resolution) decreases the gap spacing. Velocity smoothing may also help by forcing the particles to move together downstream, rather than individually towards the channel thalweg. These hypothetical experiments demonstrate the influence of the number of particles and velocity smoothing on the behaviour of the model in channels.

6.5.2 Methodology

A hypothetical straight channel 350 m long by 50 m wide (in plan dimensions) was used in this test. The channel was inclined at 20° in the downstream (global X) direction and its parabolic cross-section was defined by:

$$[6-6] \quad \Delta Z = 0.04Y^2$$

where ΔZ is the vertical elevation difference between the thalweg at $Y = 0$ and the sliding surface at cross-stream location Y . The centre of the source, 20 m long by 20 m wide (in plan dimensions), was located at global coordinates $(X = 0, Y = 0)$ and its depth was specified to give zero initial depth gradients in both the downstream and cross-stream directions, producing initial conditions similar to a dam-break. The resulting source volume was approximately 1120 m^3 . The chute configuration and initial particle positions are shown in Figure 6.16.

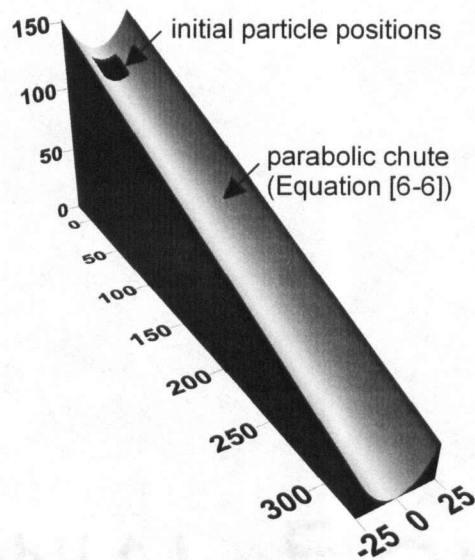


Figure 6.16. Initial configuration of the hypothetical particle channelization tests. The parabolic chute was inclined at 20° .

A frictional basal rheology (Equation [4-41]) with a bulk basal friction angle of $\phi_b = 19^\circ$ was implemented (to permit moderate acceleration on a slope angle of 20°) and the internal friction angle was set to $\phi_i = 0^\circ$ (to simulate hydrostatic conditions). The particle smoothing coefficient was fixed at $B = 4$. The number of particles, N , and the velocity smoothing coefficient, C , were varied and the following three cases were considered: a) $N = 2000$ and $C = 0$; b) $N = 4000$ and $C = 0$; and c) $N = 4000$ and $C = 0.01$.

6.5.3 Results and discussion

The particle positions at time $t = 30$ s are shown in Figure 6.17. Particle alignment was evident in run (a), as the particles had formed a single file line by this time. In contrast, the increased resolution in run (b) allowed the stream to remain up 4 or 5 particles wide. The velocity smoothing in run (c) also appeared to help maintain streamlining and the general order of the flow. Of course, with a sufficiently long channel and continued downstream acceleration and spreading, the particles would eventually align regardless of resolution, but these improvements may be enough to prevent alignment in most practical situations, in which the length and uniformity of channelized reaches are limited. Similar improvements have been observed in simulations of full-scale events. Further sensitivity analyses, possibly using a supercomputer, may be beneficial.

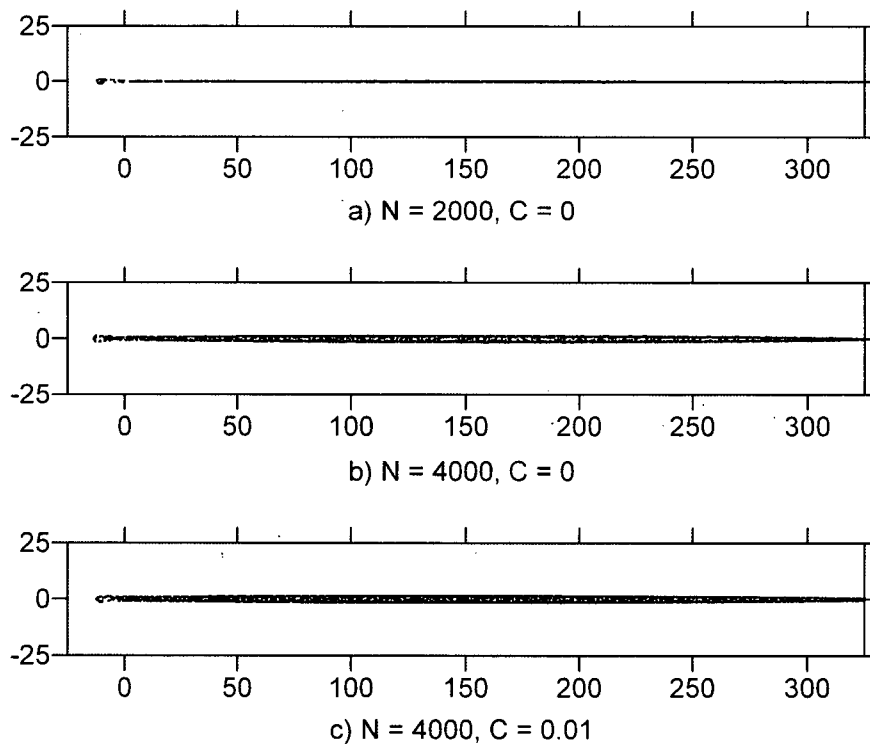


Figure 6.17. Particle positions in channel at time $t = 30$ s. (a) $N = 2000$ and $C = 0$. (b) $N = 4000$ and $C = 0$. (c) $N = 4000$ and $C = 0.01$. The particle alignment problem improved with increased resolution and velocity smoothing.

6.6 Chute experiments

6.6.1 Description

Gray et al. (1999) presented the results of small-scale laboratory experiments similar to the hypothetical experiments of Section 6.4. Dry quartz chips were released from rest on a 40° chute with parabolic cross-section, which was joined to a level runout surface by a smooth transition zone. The entire sliding surface was painted for an even finish. A series of companion experiments using different materials was presented by Wieland et al. (1999). These controlled experiments provide a simple test for the full DAN3D algorithm.

6.6.2 Methodology

DAN3D was used to simulate the experiment involving dry quartz chips (Gray et al. 1999). Detailed descriptions of the experimental setup, presented by Wieland et al. (1999), were used to configure the model. The centre of the source, with a volume of approximately 21.6 litres, was located at global coordinates ($X = 0, Y = 0$). The initial conditions are shown in Figure 6.18.

A frictional basal rheology (Equation [4-41]) was implemented and the bulk basal friction angle was calibrated so that the simulated final position of the front approximately matched that of the experiment. Experimental trimlines presented by Gray et al. (1999) were digitized to facilitate comparison. The internal friction angle was set to $\phi_i = 40^\circ$ to match the value measured by Gray et al. (1999) using independent tests. The following control parameters were used: $N = 4000$ particles, particle smoothing coefficient $B = 6$, velocity smoothing coefficient $C = 0.01$ and stiffness coefficient $D = 200$.

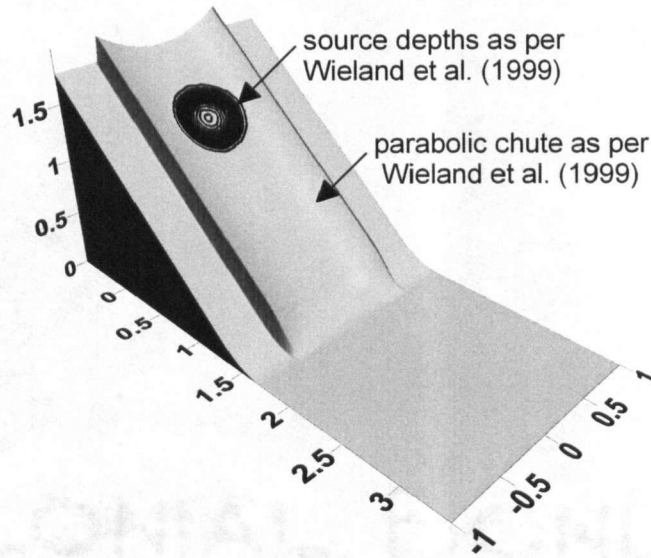


Figure 6.18. Initial configuration of the tests based on experiments presented by Gray et al. (1999) and Wieland et al. (1999). The parabolic chute was inclined at 40° and connected to the horizontal plane by a smooth transition zone. The source depths are shown at 1 cm intervals.

6.6.3 Results and discussion

A comparison of the simulated and measured results is shown in Figure 6.19. A calibrated bulk basal friction angle of $\phi_b = 28^\circ$, close to the laboratory-measured value of $\phi_b = 30^\circ$ reported by Gray et al. (1999), produced the best results (use of the laboratory-measured value produced slightly less runout). The difference between the calibrated and measured values is within the likely measurement error discussed by Wieland et al. (1999). However, it was necessary to offset the simulated results by + 0.1 s to synchronize them with the experiment. It is possible that the model, which assumes hydrostatic initial conditions, was inaccurate at startup, but experimental measurement error could have also contributed to this discrepancy. In the experiment, the material was initially contained under a perspex cap, which was raised “rapidly” (Gray et al. 1999) at time $t = 0$ s. But it is not clear exactly how rapidly the cap was raised, whether it might have remained in contact with the material for a split second after the timer had started, or whether it might have actually pushed the material downslope. The possibility of experimental error seems to be supported by the simulation results presented by Gray et al. (1999), which exhibited a similar time lag. Such time lags

are not important in hazard assessment, as long as the distribution of intensity can be accurately simulated.

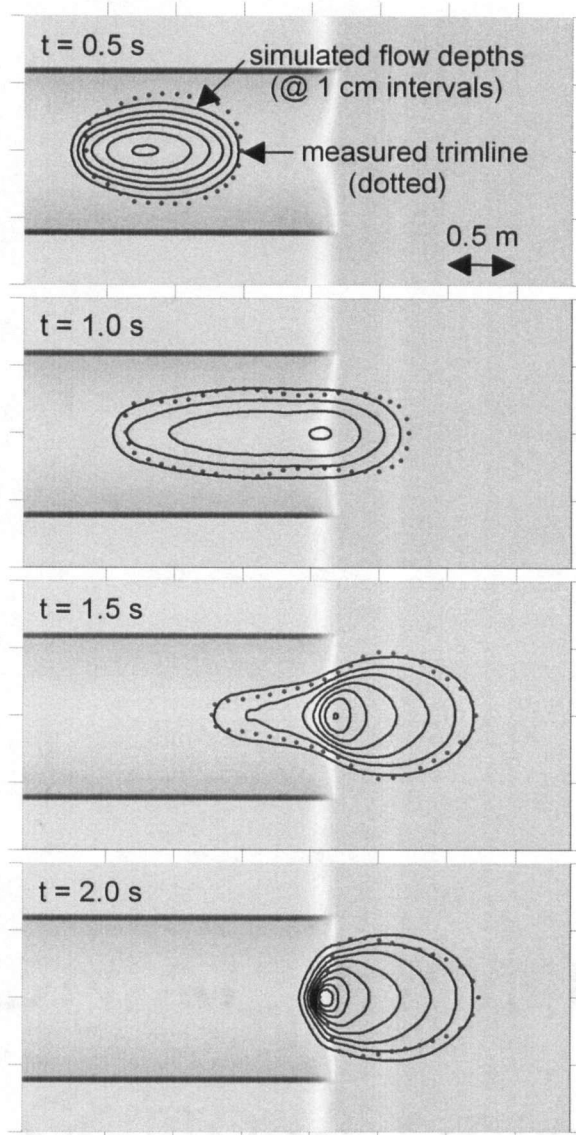


Figure 6.19. Simulation of the straight runout chute experiment presented by Gray et al. (1999). The dots represent the measured experimental trimline (digitized from Gray et al. 1999). Note that the simulation has been offset + 0.1 s for synchronicity with the experiment (i.e., $t = 0.5$ s as shown corresponds with $t = 0.6$ s in the simulation).

Once synchronized, the model accurately simulated the general shape of the flow during motion. The predicted distribution of the final deposit was reasonably accurate, with the

model predicting slightly thicker proximal deposits starting closer to the toe of the chute and more radial spreading in the distal runout zone. The proximal discrepancies may be attributable to the shock (hydraulic jump) that developed in the experiment as the tail flowed into the main deposit, as discussed in Section 6.4. The velocity smoothing that was imposed in this case may have smoothed out the shock and reduced particle penetration, but the complex process of deposition near the tail, including intense transverse shearing and accompanying lateral spreading, was not accurately simulated. In the experiment, it is also possible that material deposited initially at the toe of the chute helped to smooth the slope change through the transition zone, reducing local centripetal acceleration and resistance and allowing the material to travel farther. Similar “self ramping” has been observed in granular runup experiments (e.g., Chu et al. 1995). The lower-than-measured calibrated bulk basal friction angle seems to support this notion, as a lower value may have been required to offset the influence of higher centripetal acceleration and resistance through the transition zone.

Nevertheless, the generally close correspondence between the simulation and the experiment demonstrates the ability of the model to simulate real flows using tightly-constrained rheological parameters. Again, the bulk basal friction angle was the only parameter that was adjusted in this case.

6.7 Deflection experiments

6.7.1 Description

Similar small-scale experiments, but involving flow deflection, were conducted at the University of British Columbia. These tests demonstrate the ability of the model to simulate strongly curved flow and to provide accurate first-order predictions following calibration.

Dry, rounded, well-graded polystyrene beads were used in the experiments. Approximately 20 litres of material was released from a storage box onto a chute with variable slope, which allowed control of the approach width and velocity. The material flowed from the chute onto a 20° approach slope and was then deflected by an inclined plane oriented obliquely to the

approach direction. The deflection angle, δ (the plan angle between the approach direction and the intersection of the deflection and approach planes), and the deflection plane true dip angle, α_d , were adjusted by rotating the deflection plane about a fixed pivot point. Both planes were made of plywood sheets covered with smooth sheet metal, which was marked with a 10 cm square grid. A photograph of the experimental apparatus is shown in Figure 6.20. Four different experimental configurations were used, as shown in Table 6.4. Each configuration was repeated to verify precision. The experiments were photographed at 30 frames per second using a mounted high-speed video camera. The positions of the flow margins relative to the reference grid were recorded at each interval. Velocities were calculated from the positions of the flow front in successive frames.

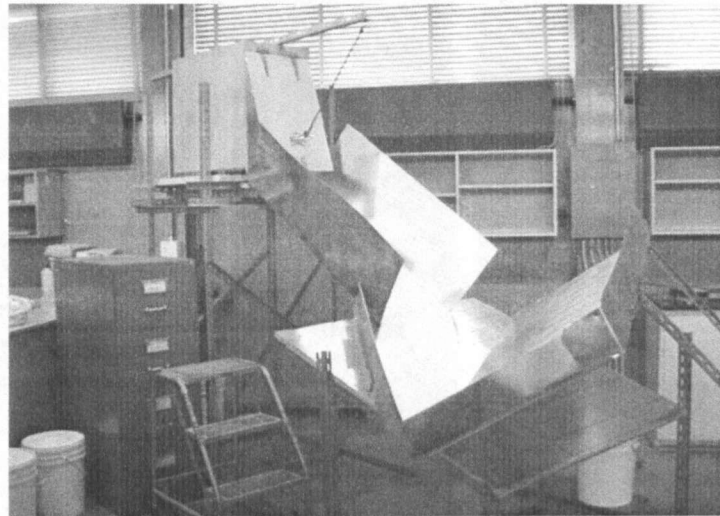


Figure 6.20. Photograph of the experimental apparatus.

Experiment	δ ($^{\circ}$)	α_d ($^{\circ}$)
1 and 2	60	33
3 and 4	45	33
5 and 6	45	45
7 and 8	60	45

Table 6.4. Configurations used in the deflected flow experiments. δ is the deflection angle and α_d is the deflection plane true dip angle.

6.7.2 Methodology

Experiment 1 was arbitrarily chosen to be the prototype for calibration of the numerical model. The box used to contain and release the material at start-up could not be replicated by the digital sliding surface, due to its infinitely sloping sidewalls. As a result, a virtual release chute and initial distribution of material were used by the model (initial conditions similar to those described in Section 6.6). By trial-and-error adjustment of the virtual chute angle, the position, width and velocity of the simulated flow front were synchronized with the experiment at the start of the 20° approach slope. The observed approach velocity was approximately 4.5 m/s in all of the experiments.

A frictional basal rheology (Equation [4-41]) was implemented and both the bulk basal and internal friction angles were systematically adjusted until the simulated maximum runup distance matched that of the prototype experiment. The calibrated model was then applied to prediction under the other three experimental configurations.

6.7.3 Results and discussion

The calibrated simulation of Experiment 1 is shown in Figure 6.21. The model was calibrated to match the observed maximum runup distance of approximately 56 cm (within the measurement error of +/- 2 cm) using a bulk basal friction angle of $\phi_b = 20^\circ$ and an internal friction angle of $\phi_i = 25^\circ$. These friction angles are within a small range of values that were measured in independent tilting table tests, which suggests that the model may not require significant calibration/tuning when the rheology is simple and the material properties can be measured independently. The position of the flow margins and the general trajectory of the flow along the deflection plane were accurately reproduced. The ability of the model to produce an accurate simulation in this case further verifies the global reference grid-independence of the solution method.

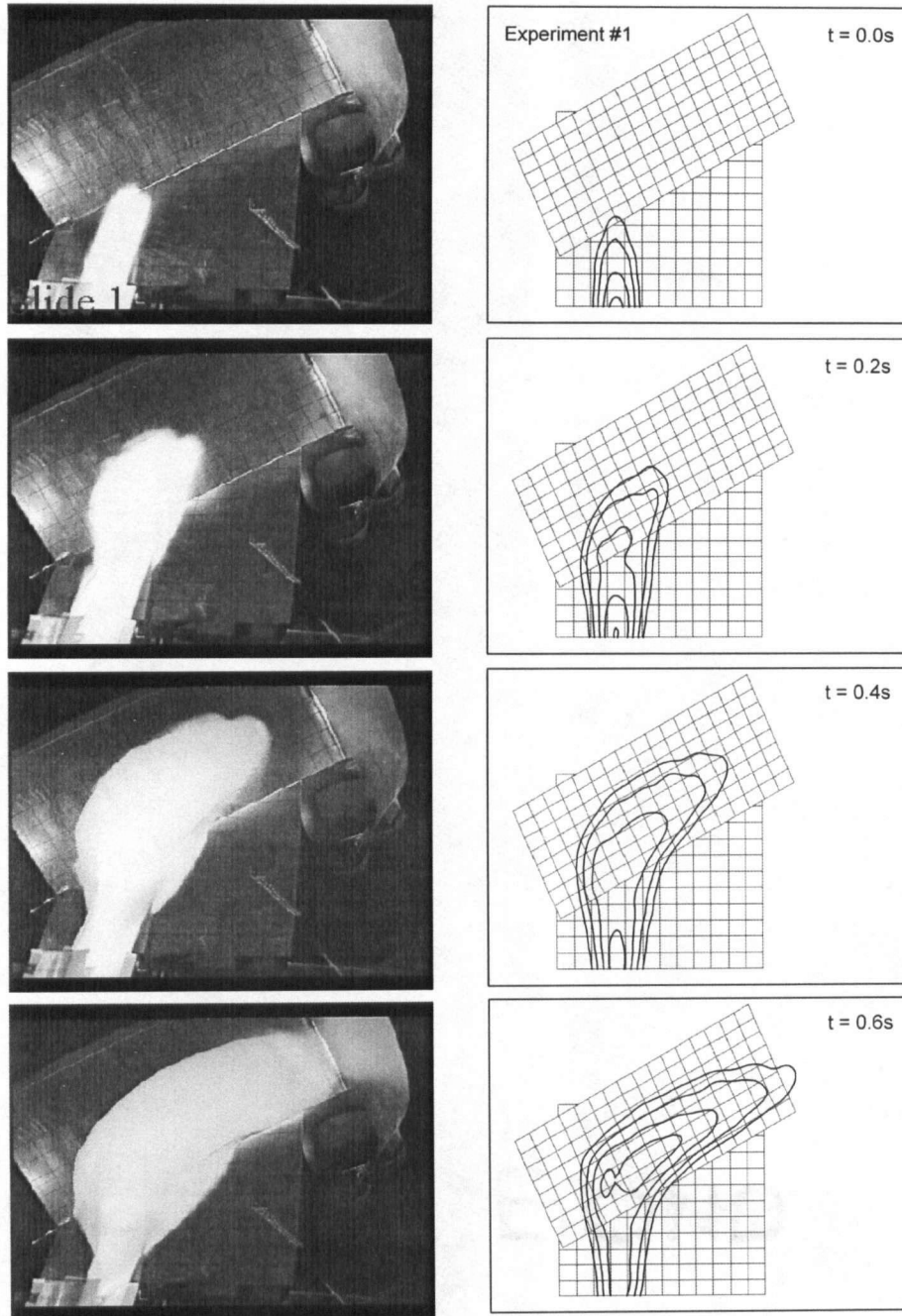


Figure 6.21. Calibrated simulation of Experiment 1 ($\delta = 60^\circ$ and $\alpha_d = 33^\circ$). The experimental and simulated flow positions are shown at 0.2 s intervals. The flow depth contours are shown at 1 cm intervals. The planes are marked with a 10 cm square grid.

The calibrated rheological parameters $\phi_b = 20^\circ$ and $\phi_i = 25^\circ$ were used in predictive runs under the other three experimental configurations. Comparisons of the observed and predicted flow positions at the point of maximum runup for Experiments 3, 5 and 7 are

shown in Figure 6.22. The corresponding observed and predicted runup distances are shown in Table 6.5. In each case, the calibrated model produced accurate predictions (within approximately 5%) of maximum runup distance. At the same time, the velocities and trajectories of the experimental flows were also accurately predicted.

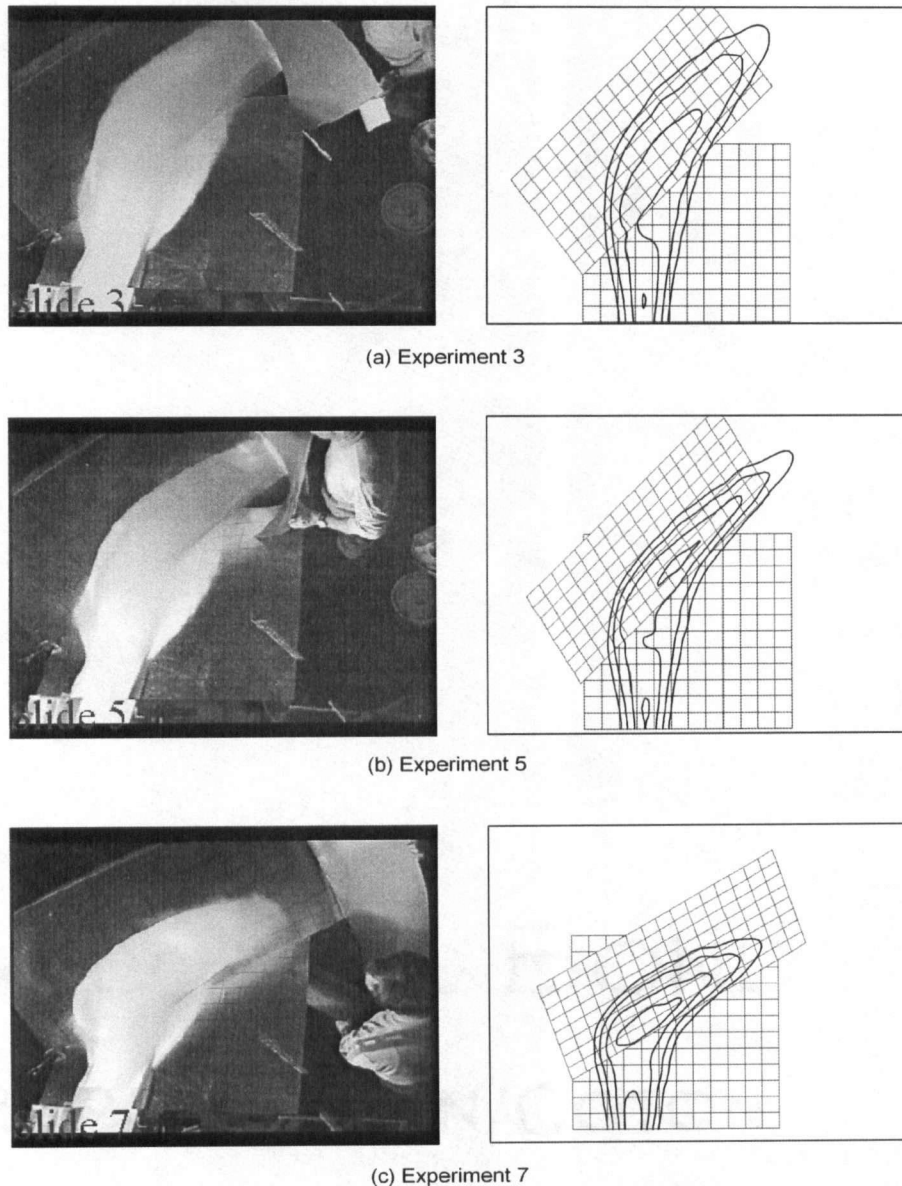


Figure 6.22. Comparisons of observed and predicted maximum runup distances. (a) Experiment 3 ($\delta = 45^\circ$ and $\alpha_d = 33^\circ$). (b) Experiment 5 ($\delta = 45^\circ$ and $\alpha_d = 45^\circ$). (c) Experiment 7 ($\delta = 60^\circ$ and $\alpha_d = 45^\circ$). The experimental and predicted flow positions are shown at the point of maximum runup. The flow depth contours are shown at 1 cm intervals. The planes are marked with a 10 cm square grid.

Experiment	Observed Runup (cm)	Predicted Runup (cm)
3	51	54
5	38	40
7	42	43

Table 6.5. Observed vs. predicted runup distances for Experiments 3, 5 and 7 (measurement error of +/- 2 cm).

These results demonstrate the ability of the calibrated model to make accurate first-order runout predictions, even when the geometry differs from that of the prototype. They also suggest that dynamic modelling may be a practical alternative to analytical methods of predicting superelevation and runup of debris flows against deflection berms, and therefore could be used to design such structures.

6.8 Discussion

Five key aspects of the model have been demonstrated in this chapter:

- 1) The accuracy of the numerical solution method was demonstrated using established analytical methods. Limitations were also identified and possible solutions were proposed.
- 2) The grid-dependency of the model was evaluated using a simple test. The model did not introduce grid-dependence beyond the grid-dependent initial particle distribution (which likely has a negligible influence in most practical cases), but the influence of the assumed orientation of the principal axes has yet to be properly evaluated.
- 3) The general behaviour of the model was demonstrated using a series of parametric analyses. Internal strength, mass and momentum transfer during entrainment and basal resistance all had strong influences on the results, and preliminary appropriate ranges for the input control parameters were suggested.

- 4) The ability of the model to produce accurate simulations was demonstrated using controlled laboratory experiments involving both straight and strongly deflected flow. In both cases, the calibrated input rheological parameters corresponded closely with independently measured values.
- 5) The calibration-prediction methodology and the ability of the calibrated model to produce accurate predictions were demonstrated using controlled laboratory experiments involving various geometries. The results suggest that the same methodology can be applied at full-scale.

It must be acknowledged that, of the methods listed above, only the dam-break comparisons strictly qualify as validation tests as defined, for example, by Iverson (2003). In these cases, the input rheological parameters were identical in both the analytical and numerical models. It must also be acknowledged that these tests are not capable of validating the full 3D model, but rather only a simplified 2D variation.

As with previous 3D models, simple hypothetical and laboratory experiments have been used to evaluate the complete algorithm. In the latter case, the input rheological parameters were adjusted to produce good simulations. However, the calibrated values were very close to the measured material properties, with the differences likely within the associated measurement error. Regardless, such experiments do not strictly qualify as validation tests, as the implicit assumption of purely frictional behaviour may not actually be valid. In this sense, these types of simulations test the validity of the rheological assumptions as much as the accuracy of the model itself.

6.9 Conclusion

The applicability of the DAN3D governing equations and the effectiveness of the numerical solution method have been demonstrated using both analytical and experimental methods. In every case, the input rheological parameters were tightly-constrained and objective criteria were used to define accurate simulation. Parametric analyses have also been used to

demonstrate general model behaviour and constrain the input control parameters for interim practical use, although further work is recommended. Finally, a small-scale example of the calibration-prediction methodology has been presented. But the full capabilities of the model, including its ability to handle complex 3D terrain and account for rheology variations, can only be evaluated using full-scale examples. Back-analysis of real landslides is the subject of the next chapter.

7 CASE STUDIES

7.1 Introduction

The ability of DAN3D to accurately solve the governing equations and the applicability of these equations to the simulation of fluid and granular flows were demonstrated in Chapter 6 using both analytical and experimental methods. Additional features of the model were also demonstrated using simple hypothetical examples. While these types of analyses are important for model validation, they are only one component. The full capabilities of a model that is intended for practical application, not just for the description of idealized flow dynamics or the simulation of controlled experiments, must be evaluated using full-scale case histories. The application of the model to real events also provides opportunities to identify practical limitations and in turn possible future improvements, and is therefore a crucial step in model evolution. But even without significant refinements, simple dynamic models can aid in the qualitative analysis and description of real events, and full-scale application should not be delayed for the sake of exhaustive laboratory testing.

This chapter is a compilation of real cases that have been analyzed using DAN3D. Some of these cases have been studied independently for the purposes of model validation and event description and analysis, while others have been studied in the process of actual landslide hazard and risk assessments. Details have been omitted when necessary for confidentiality. The examples that are included span a wide range of rapid landslide types, from large rock avalanches to relatively small debris avalanches that involve substantial entrainment.

7.2 Frank

7.2.1 Description

On April 29, 1903, approximately 30 million m³ of rock descended the east side of Turtle Mountain into the Crowsnest River valley, partially burying the town of Frank, Alberta and

killing about 70 people. It was Canada's worst landslide disaster (Evans 2001). An oblique aerial view of the landslide area is shown in Figure 7.1.

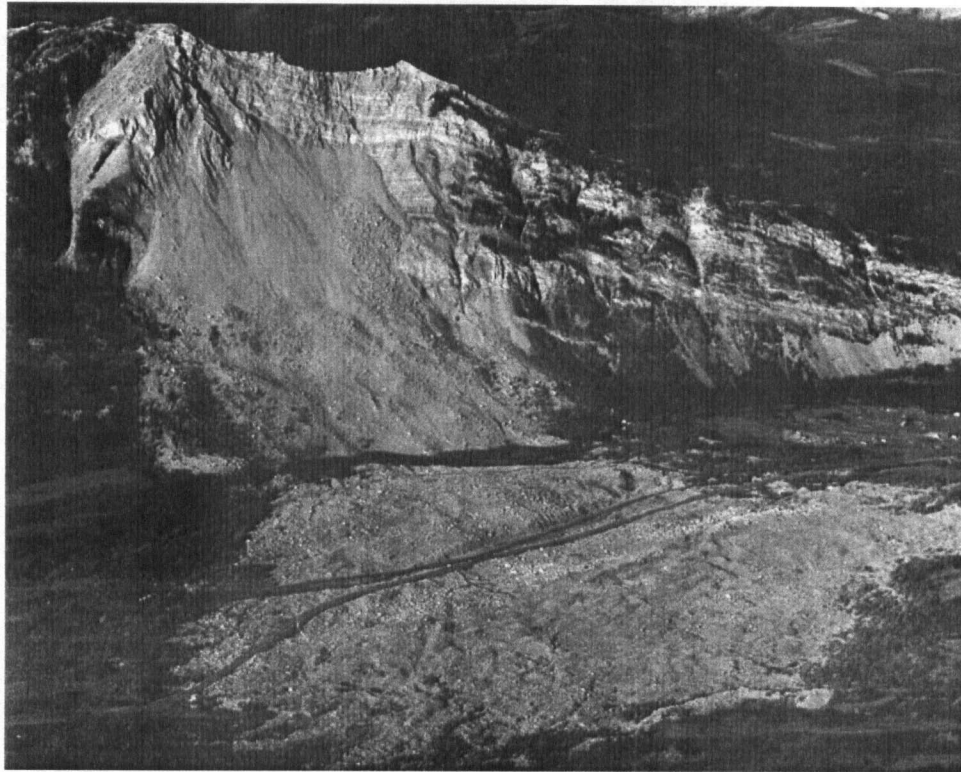


Figure 7.1. Oblique aerial view of the Frank Slide. (Photograph courtesy of Prof. Dave Cruden, University of Alberta, Edmonton, Canada)

The event initiated as a slide along easterly-dipping (approximately slope-parallel) bedding in Palaeozoic limestone, which formed the eastern limb of the Turtle Mountain Anticline (Cruden and Krahn 1973). The toe of the rupture surface corresponded with a minor thrust fault near elevation 1600 m (Cruden and Krahn 1973), while the crown of the head scarp is at approximately elevation 2100 m. Jaboyedoff et al. (2004) suggested that the failure was regressive, propagating upslope from the toe along bedding and then through pre-existing discontinuities in the hinge of the anticline. A number of possible factors contributing to the failure have been suggested, including the adverse geological structure, slope deformation due to coal mining near the base of the mountain, above-average precipitation in the months leading up to the event, ice and water accumulation in cracks near the peak, natural and blast-

induced seismicity, thermal cycles and karst formation (BGC Engineering 2000; Read et al. 2005), but a definitive trigger has never been identified.

The rock debris overrode and probably entrained surficial material below the failure zone, which likely included colluvium and till as well as alluvium from terraces near the toe of the slope. Then, as McConnell and Brock (1904) described, “The great mass, urged forward by the momentum acquired in its descent, and broken into innumerable fragments, ploughed through the bed of Old Man river [the Crowsnest River], and carrying both water and underlying sediments along with it, crossed the valley and hurled itself against and up the opposite terraced slopes to a height of 400 feet.” An eyewitness reported watching a part of the flow front reverse direction as it climbed a high terrace and returned to deposit on a lower one (McConnell and Brock 1904). This response to local topographic details contributed to the “bay and promontory” (McConnell and Brock 1904) morphology of the outer deposit margins, composed mainly of path material (predominantly alluvium from the river bed) that was displaced by the main mass (Cruden and Hungr 1986). A similarly “digitate” inner deposit margin was created by the coarser rock debris, which formed the main deposit with an average thickness of about 14 m (Cruden and Hungr 1986).

The overridden, entrained and displaced path material probably contributed to the mobility of this event, both by decreasing the resistance at the base of the main mass, in part due to rapid undrained loading (e.g., Sassa 1985), and by producing the “splash” zones that extended up to several hundred metres from the edge of the coarser deposits (Cruden and Hungr 1986). Similar secondary, relatively fine-grained margins have been observed in other rock avalanche deposits (e.g., Orwin et al. 2004) and were probably formed by the same mechanism, with important implications for hazard assessment. In the case of the Frank Slide, it was the laterally-displaced alluvium that caused most of the damage in the town itself (Cruden and Hungr 1986), which was situated north of the main path of the landslide. In fact, so much alluvium was displaced that the river bed was lowered by several feet (McConnell and Brock 1904).

Despite the large number of eyewitnesses, the duration of the event is not very well-constrained. Eyewitnesses reported durations ranging between 20 s and 2 minutes, but McConnell and Brock (1904) suggested a maximum duration of about 100 s.

The Frank Slide is an important case study, both because of its historical significance and because it is an excellent example of a large dip slope type failure resulting in long-runout behaviour. A number of similar prehistoric events have occurred in the Canadian Rocky Mountains (Cruden 1976), particularly in the Front Ranges, where dip slopes are ubiquitous. Lessons learned at Frank can potentially be applied to landslide hazard assessment across the region and in similar mountainous areas around the world. A detailed runout analysis for the current South Peak of Turtle Mountain, which overlies a portion of the eastern limb of the Turtle Mountain Anticline that did not fail in 1903 and is considered marginally stable, is currently in progress and will include a detailed back-analysis of the 1903 event. The back-analysis presented in this thesis is only preliminary; it was originally undertaken simply to demonstrate the potential ability of DAN3D to simulate real landslides.

7.2.2 Methodology

A detailed digital elevation model (DEM) of the present-day topography was provided by Dr. Réjean Couture of the Geological Survey of Canada. Detailed records of the pre-event topography do not exist. Therefore, with reference to historical photographs (some taken before 1903), maps and a 1:9600 scale model, the topography of the deposition zone was modified to approximate the pre-slide conditions by removing approximately 30 million m³ from the area according to estimated deposit depths. The starting position of the 30 million m³ (bulking included) slide mass was similarly estimated. These modifications were subjective and loss of some topographic detail resulted, but this did not significantly affect the performance of the model in this case because of the reasonably simple path; the mean slope of the sliding surface was not changed significantly. Obviously, the localized response to topographic details at the flow margins could not be reproduced with these modifications, but the overall motion of the bulk of the mass was not significantly affected.

For this preliminary analysis, a constant frictional basal rheology was used (Equation [4-41]). With this methodology, any changes in resistance that may have occurred during motion are accounted for implicitly in the constant bulk basal friction angle, which was calibrated in this case so that the simulated extent of the deposit on the valley floor approximately matched that of the real event. The bulk internal friction angle was set to $\phi_i = 40^\circ$, which is considered appropriate for dry broken rock, and the following control parameters were used: $N = 2000$ particles, particle smoothing coefficient $B = 4$, velocity smoothing coefficient $C = 0$ and stiffness coefficient $D = 200$ (this analysis was performed when $N = 2000$ particles was the upper limit and before a velocity smoothing algorithm was incorporated).

7.2.3 Results and discussion

The results are shown in Figure 7.2. The model provided a good match of the general extent and distribution of the final deposit using a constant bulk basal friction angle of $\phi_b = 14^\circ$. This low value (relative to that expected of dry broken rock) implies the presence of pore water pressure near the base of the flow, probably following the onset of entrainment downslope of the source area and almost certainly during impact on the floodplain deposits (in fact, liquefaction of the path material may have occurred at this point, resulting in complete loss of frictional resistance). As such, it represents an average value. The calibrated value of ϕ_b is in close agreement with the DAN analysis of the Frank Slide reported by Hungr and Evans (1996), who used a value of $\phi_b = 16^\circ$.

The results of the preliminary analysis resembled the real event in a number of ways. The simulated flow spread thinly across the opposite side of the valley and banked slightly right. The bulk of the flow was deposited proximally, on the opposite side of the Crowsnest River, while the distal flow margin was influenced by the terraced valley topography, running up and back down the slopes and depositing on the terraces, in agreement with the eyewitness account mentioned previously. The average simulated deposit depth was close to the 14 m estimate derived from field investigations (Cruden and Hungr 1986). Finally, the flow came to rest after about 60 s, within the 100 s duration estimated by McConnell and Brock (1904).

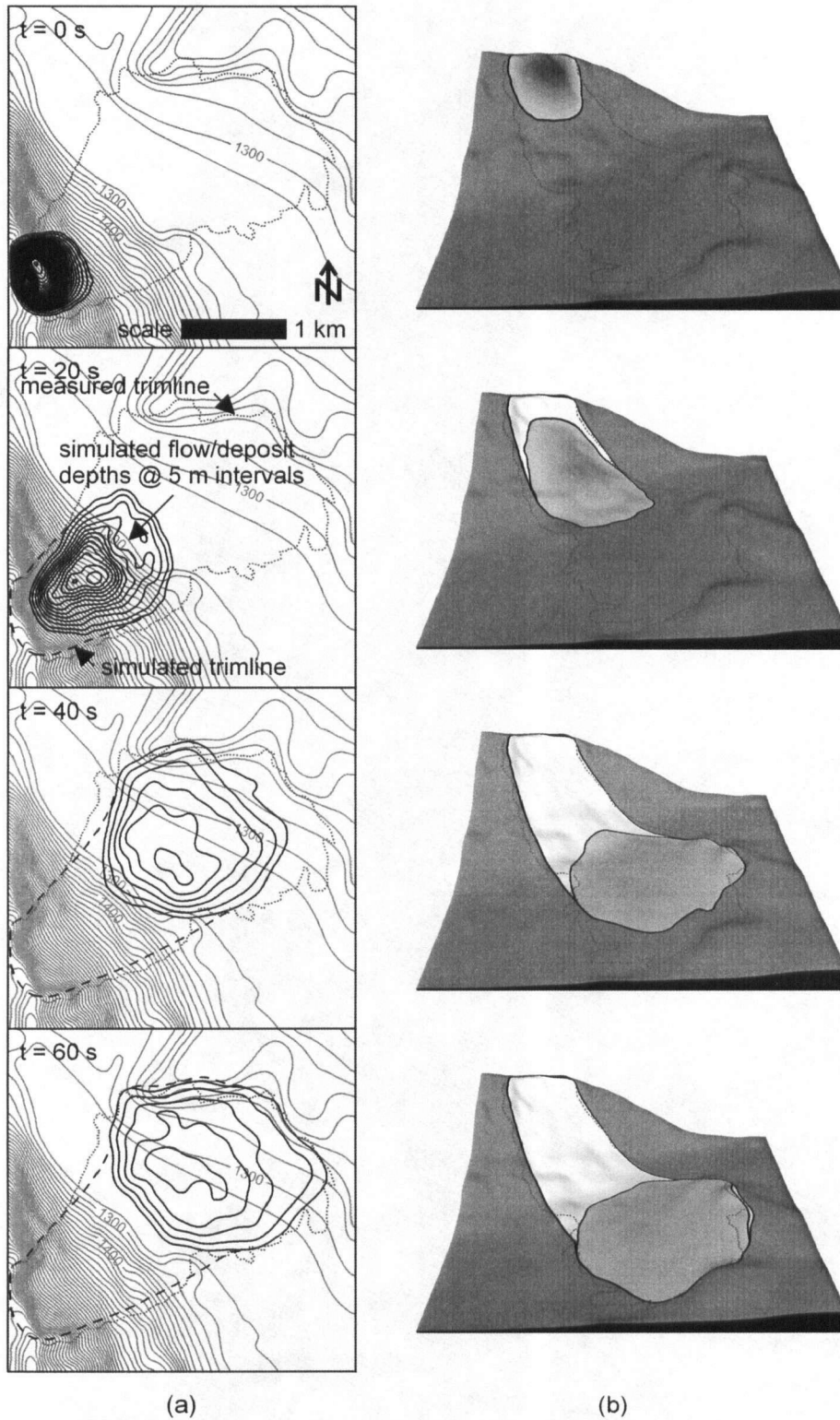


Figure 7.2. Calibrated simulation of the Frank Slide at 20 s intervals in (a) plan and (b) oblique views. The flow/deposit depth contours are at 5 m intervals and the elevation contours are at 20 m intervals. The blue line indicates the extent of the real event (digitized from Canada Department of Mines 1917).

More detailed evaluation of these results and further calibration of the model, including tests with different rheologies that may vary along the path, could probably yield even better correspondence with the prototype, particularly with respect to event duration. As mentioned, this will be undertaken as part of the detailed runout analysis for South Peak. Nevertheless, the preliminary results demonstrate the potential applicability of the model at full-scale.

7.3 Val Pola

7.3.1 Description

On July 28, 1987, a rock avalanche involving between 40 and 50 Mm³ of material occurred in the Valtellina in the central Italian Alps. The event initiated as a wedge failure in highly fractured and jointed gneiss intruded by diorite and gabbro within a prehistoric landslide scar on the eastern slope of Mount Zandila (Costa 1991). The failure was likely related to heavy rainfall during the week of July 15-22, which triggered debris flows in adjacent Val Pola (Pola Creek) and other tributaries of the Adda River (Govi 1989). On July 25, a 600 m long fissure was detected near elevation 2200 m and rockfalls began occurring with increasing frequency, leading up to the catastrophic failure (Govi 1989).

Confined by the plane forming the southern flank of the source area, the rock slide first moved north-east towards Val Pola before turning downslope towards the Adda River, entraining glacial and colluvial surficial material on its way (Crosta et al. 2004). The landslide then impacted the narrow valley floor and continued up the steep opposite slope to a height of approximately 300 m, while deflecting both downstream and upstream around the steep bedrock escarpment known as Plaz. The downstream portion reached Ponte del Diavolo, about 1.5 km from the Val Pola fan, while the upstream portion impacted a lake that had been impounded by debris flow activity on the fan just nine days earlier (Govi 1989; Erismann and Abele 2001). Seven workers who were attempting to drain the lake at the time were killed (Costa 1991). The impact generated a large displacement wave that travelled upstream over 2 km to reach the village of Aquilone, where another 20 people were killed.

The bulk of the landslide material deposited on the valley floor near the toe of the source slope, creating a natural dam that impounded another lake, which eventually extended beyond Aquilone. To mitigate flooding and the possible failure of the landslide dam, the lake was pumped while two diversion tunnels and a spillway were constructed (Govi 1989).

An oblique aerial view looking upstream at the main part of the deposit is shown in Figure 7.3. The substantial runup against the opposite valley wall is evident on the right side of the photograph and the impounded lake is visible at the top.



Figure 7.3. Oblique aerial view of the Val Pola landslide deposit. The source area is outside of the image at the upper left.

7.3.2 Methodology

The input sliding surface and source thickness files were created using pre- and post-event DEMs that were provided by Prof. Giovanni Crosta of the University of Milan. The source thicknesses were approximated by subtracting the post- from the pre-event DEM and

isolating the source area. Based on these manipulations, it appears that approximately 50 Mm³ of material (bulking not included) was mobilized from a combination of two sources: 1) the main failure zone (about 45 Mm³) and 2) the section of the Val Pola channel immediately adjacent (about 5 Mm³). The former corresponds closely with the 43.7 Mm³ source volume that was estimated by Crosta et al. (2004) by neglecting the contribution from the Val Pola channel, which failed prior to the main event as the source of the preceding debris flows; lateral debulking of the main source area because of this may have contributed to the catastrophic failure (Crosta et al. 2004). The presence of this material on the Val Pola fan at the time of the main failure was neglected in the DAN3D simulation. Govi (1989) estimated a smaller total landslide volume of 40 Mm³. Crosta et al. (2004) also estimated that between about 5 and 8 Mm³ of additional material was entrained during movement down the source slope, but this was neglected in their back-analysis of the event using the model developed by Chen and Lee (2000). Bulking due to fragmentation of the source material was also neglected in their analysis, perhaps a reasonable assumption given the highly fractured nature of the source rock prior to failure. In the DAN3D simulation that follows, the approximately 45 Mm³ main failure was bulked by 10%, for a bulked source volume of approximately 50 Mm³. Similar to Crosta et al. (2004), entrainment was neglected.

As in the preceding Frank Slide back-analysis, a constant frictional basal rheology (Equation [4-41]) was used in this case, which again represents a preliminary analysis. The bulk basal friction angle was systematically adjusted until the observed 300 m runup against the opposite valley wall was reproduced and the extent of the main deposit approximately matched that of the real event. Sketches of the observed impact area and deposit distribution, presented in Figure 2.30 of Erismann and Abele (2001) and Figure 4 of Crosta et al. (2004), were used for comparison. The bulk internal friction angle was set to $\phi_i = 35^\circ$, again within the range of values considered appropriate for dry broken rock, and the following control parameters were used: $N = 4000$, $B = 6$, $C = 0.01$ and $D = 200$.

7.3.3 Results and discussion

The results are shown in Figure 7.4. The best simulation (based on the 300 m runup calibration criterion) was achieved using a constant bulk basal friction angle of $\phi_b = 16^\circ$, the same value used by Hungr and Evans (1996) in their DAN analysis of the event. Similar to the Frank Slide back-analysis, this relatively low value implies the presence of pore pressure and/or weaker material near the base of the flow. The calibrated model simulated the runup against the opposite slope and simultaneous division into downstream and upstream lobes around the steep escarpment of Plaz. The model produced slightly too much runup at this particular location, which can be attributed to smoothing of this and other prominent topographic features during pre-processing of the input files. The extent of the deposit, approximately 2.5 km long by 1 km wide, extending downstream to Ponte del Diavolo and upstream past the location of the first impounded lake, matches the observations shown in Figure 4 of Crosta et al. (2004). The formation of the landslide dam was also simulated, although the maximum simulated deposit depth of approximately 120 m was higher than the 90 m maximum local deposit thickness estimated by Govi (1989).

A plot of the maximum simulated flow velocities recorded along the path is shown in Figure 7.5. This plot is a form of hazard intensity map that has been produced using Equation [5-54]. Such maps can be output during forward-analyses to help estimate the vulnerability of elements at risk, $V(L:T)$, as described in Chapter 1. The maximum simulated flow velocity of 99 m/s (356 km/hr), recorded at the leading margin near the toe of the source slope, corresponds with the range of 275-390 km/hr estimated by Costa (1991) on the basis of energy conversion during runup against the opposite slope (relatively high simulated velocities are a well-known characteristic of the frictional model). The simulated duration also matched estimates based on seismograph records described by Crosta et al. (2003); the bulk of the material came to rest within about 70 s, while smaller trailing movements continued to occur, perhaps corresponding to the minor tremors that were recorded by the seismographs up to 120 s after the initial signal.

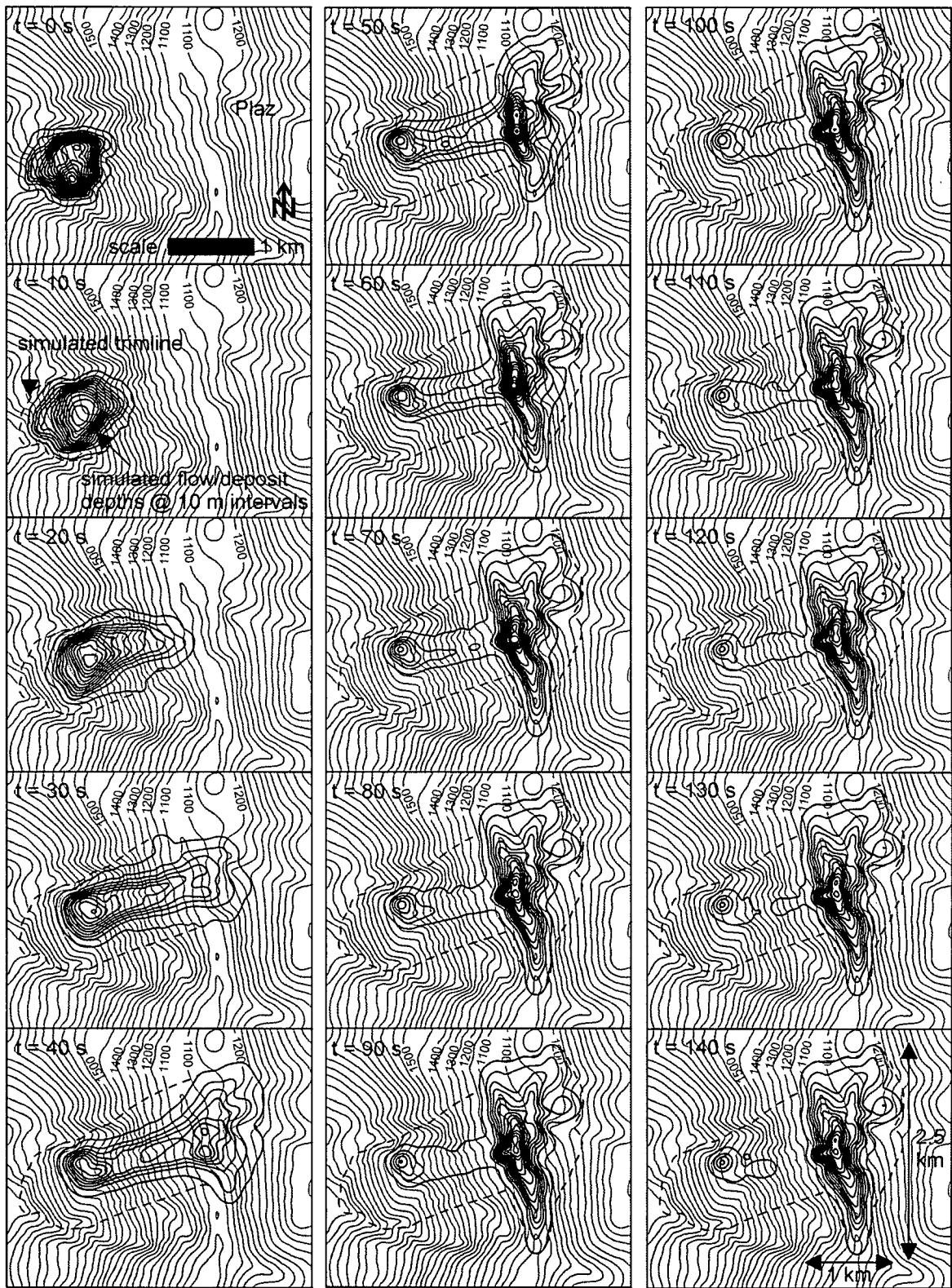


Figure 7.4. Calibrated simulation of the Val Pola landslide at 10 s intervals. The flow/deposit depth contours are at 10 m intervals and the elevation contours are at 50 m intervals.

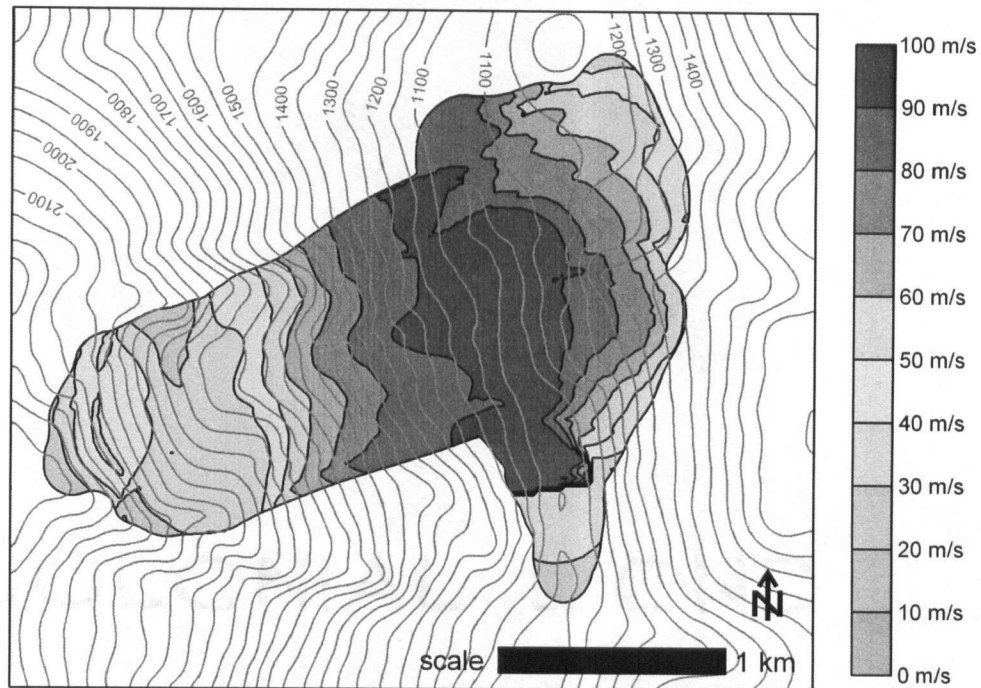


Figure 7.5. Plot of the maximum simulated flow velocities recorded along the path, a form of landslide hazard intensity map (cf., Chapter 1). The maximum velocity contours are at 10 m/s intervals and the elevation contours are at 50 m intervals.

Crosta et al. (2004) presented a dynamic analysis of this event using a constant Voellmy basal rheology (Equation [4-42]) with a friction coefficient of $f = 0.1$ (analogous to a bulk basal friction angle of $\phi_b = 5.7^\circ$) and a turbulence parameter of $\xi = 200 \text{ m/s}^2$. Use of the Voellmy model with these parameters reduces the slope angle on which the material can deposit, reduces the maximum simulated velocity (which may be justified, given the relatively high velocities produced by the frictional model) and increases the simulated duration. However, a comparative simulation using DAN3D and these input parameters did not produce a satisfactory result; the 300 m runup was not reproduced and the downstream lobe travelled well past Ponte del Diavolo, as the mean channel slope in this area was higher than 5.7° .

As in the Frank Slide analysis, the DAN3D simulation presented here could probably be improved by accounting explicitly for entrainment on the source slope as well as possible changes in resistance along the path, most likely corresponding with the onset of entrainment and the impact on the valley floor. However, the qualitative accuracy of this preliminary

analysis is encouraging. Of particular significance is the exact correspondence between the DAN (Hungr and Evans 1996) and DAN3D calibrated bulk basal friction angles. The correspondence between the two models suggests that the existing database of DAN calibrated input parameters (e.g., Hungr and Evans 1996; Ayotte and Hungr 2000; Revellino et al. 2004) can be used with DAN3D, and this idea has been exploited in the analyses that follow. It is also significant that the considerable secondary effects of this event, the landslide-generated displacement wave and the landslide dam, are implied by the simulation. Finally, the substantial deformation of the slide mass caused by the complex topography was easily handled by the model.

7.4 Cervinara

7.4.1 Description

In December 1999, prolonged heavy rainfall triggered a number of landslides near the village of Cervinara in the Campania region of Italy (Revellino et al. 2004). The largest event reached the village, causing six deaths. It originated as a shallow failure in an artificial cut but transformed quickly into a debris avalanche, stripping a mantle of airfall pyroclastic deposits (up to about 2m thick) from its path and increasing significantly in volume (Figure 7.6). At the toe of the source slope the landslide split into two lobes. One lobe, comprising most of the material, turned left into a gully and continued toward the village as a debris flow. The other lobe flowed straight, up and over a small ridge and into an adjacent gully.

7.4.2 Methodology

The input sliding surface data was provided by Dr. Paola Revellino of the University of Sannio. The initial failure was modelled as a 3600 m^3 slide of approximately uniform 2 m depth. The basal resistance in the source zone was modelled using a frictional rheology (Equation [4-41]) with a bulk basal friction angle of $\phi_b = 30^\circ$.

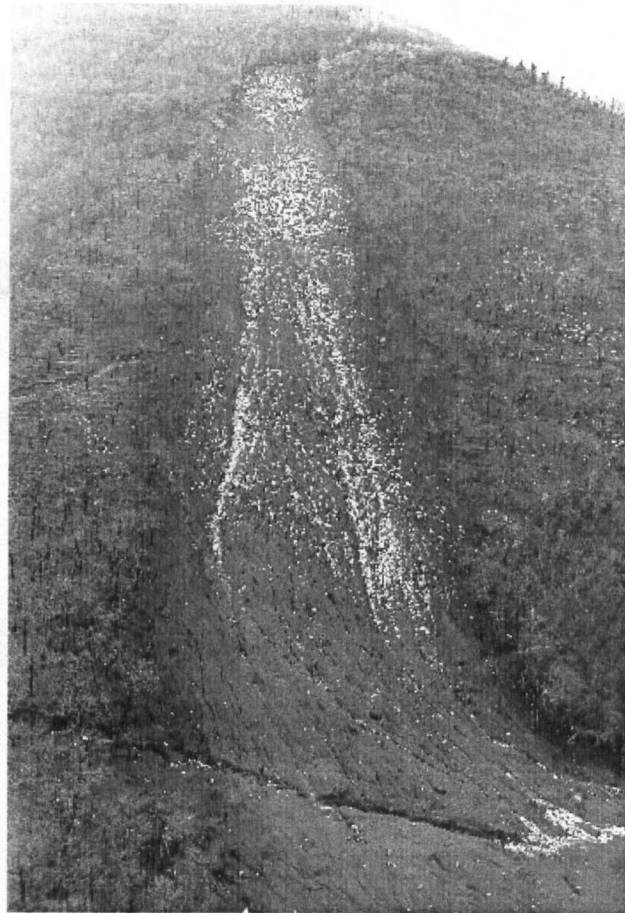


Figure 7.6. View of the source slope of the Cervinara landslide, showing extensive erosion of surficial deposits. (Photograph courtesy of Prof. Francesco M. Guadagno, University of Sannio, Benevento, Italy)

Immediately downslope of the source zone the slide mass impacted and/or overrode additional saturated pyroclastic material in its path and the frictional resistance may have decreased due to rapid undrained loading of the wet substrate. At the same time, rapid shearing of the saturated, dense grain dispersion (e.g., Bagnold 1954), among other possible effects, may have produced a velocity-dependent component of resistance. To account for this change in flow character, the basal rheology was changed to the Voellmy resistance model (Equation [4-42]), which contains a velocity-dependent term. Using DAN in a systematic back-analysis of 17 events in the Campania region (including this particular event), Revellino et al. (2004) found that the Voellmy rheology produced good simulations of travel distance, flow velocity and the distribution of deposits using a friction coefficient of $f = 0.07$ and a turbulence parameter of $\xi = 200 \text{ m/s}^2$. These calibrated values were therefore

used in the DAN3D simulation. The internal friction angle was set to $\phi_i = 35^\circ$, also consistent with Revellino et al.'s (2004) methodology, and the following control parameters were used: $N = 2000$, $B = 4$, $C = 0$ and $D = 200$.

On the source slope, erosion and entrainment of the pyroclastic substrate proceeded at a specified growth rate of $E_s = 0.01 \text{ m}^{-1}$, up to a maximum specified erosion depth of 2 m. It was assumed that significant entrainment did not occur beyond the toe of the slope. This process was critical to the successful simulation of this event, as the simulated flow volume increased approximately 20 fold within the entrainment zone and spread over a much larger area than possible for the relatively small initial slide mass.

7.4.3 Results and discussion

The results of the simulation are shown in Figure 7.7. Like the real event, the simulated flow split at the toe of the source slope, in approximately the same proportion, with the smaller lobe running up and over the small ridge. This runup was aided by an increase in internal pressure in the direction of motion due to convergence of the material at the base of the slope; the specified internal friction angle of $\phi_i = 35^\circ$ produces higher than hydrostatic tangential stresses in directions of compressional strain, corresponding with the passive failure condition (cf., Chapter 2). A trial comparative run using only hydrostatic stress conditions did not produce the same results, although similar runup could be achieved by lowering the basal resistance.

Similar to Revellino et al.'s (2004) DAN analysis, the maximum simulated flow velocities recorded along the path also corresponded with independent velocity estimates. In the final frame of Figure 7.7, the simulated flow front reached the village and was still travelling at over 6 m/s. The simulation was stopped at this point because the DEM did not include details within the village (i.e., streets, buildings, etc.) that strongly influenced the real event.

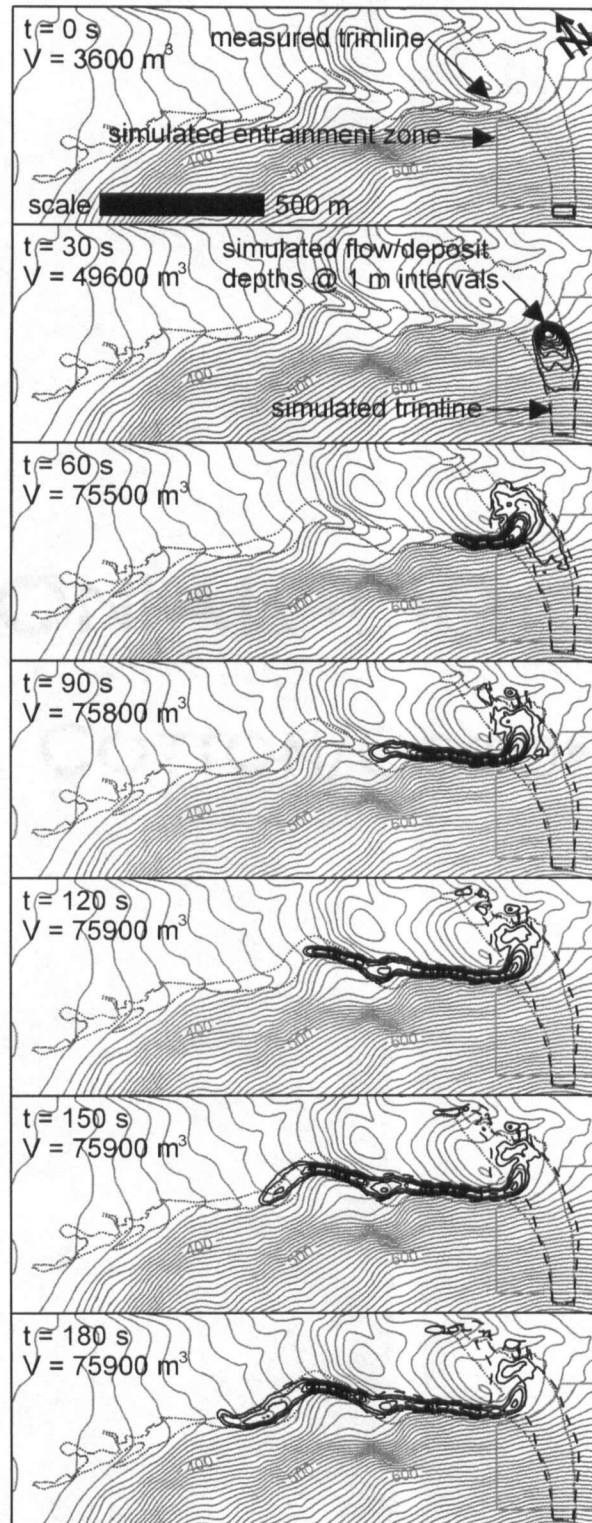


Figure 7.7. Simulation of the Cervinara landslide using calibrated input parameters determined by Revellino et al. (2004). The flow/deposit depth contours are at 1 m intervals and the elevation contours are at 10 m intervals. The simulated flow front reached the village in the last frame, when it was still moving at over 6 m/s.

It must be stressed that this analysis included only a few changeable input parameters, and so the faithful simulation of the external dimensions of the flow did not result from arbitrary adjustments of multiple parameters. Furthermore, the parameters used were the same ones determined by Revellino et al. (2004) on the basis of DAN analyses of multiple events of similar descriptions, and the results again demonstrate good correspondence between the two models. The use of previously calibrated input parameters makes these results equivalent to a first-order prediction.

7.5 Quindici

7.5.1 Description

A similar series of landslides occurred in the Campania region the previous year, in May 1998, causing a total of 161 deaths (Revellino et al. 2004). They were also triggered by prolonged rainfall and involved substantial entrainment of surficial pyroclastic deposits (cf., Figure 2.1 in Chapter 2 for a photograph of events in the area of Sarno, near Quindici). Many of these events were characterized by multiple surges caused by separate failures that were funnelled into the same creek channel. The subject of this analysis is a single surge from one of these events, which jumped out of its channel near the fan apex and impacted the south-eastern part of the village of Quindici.

7.5.2 Methodology

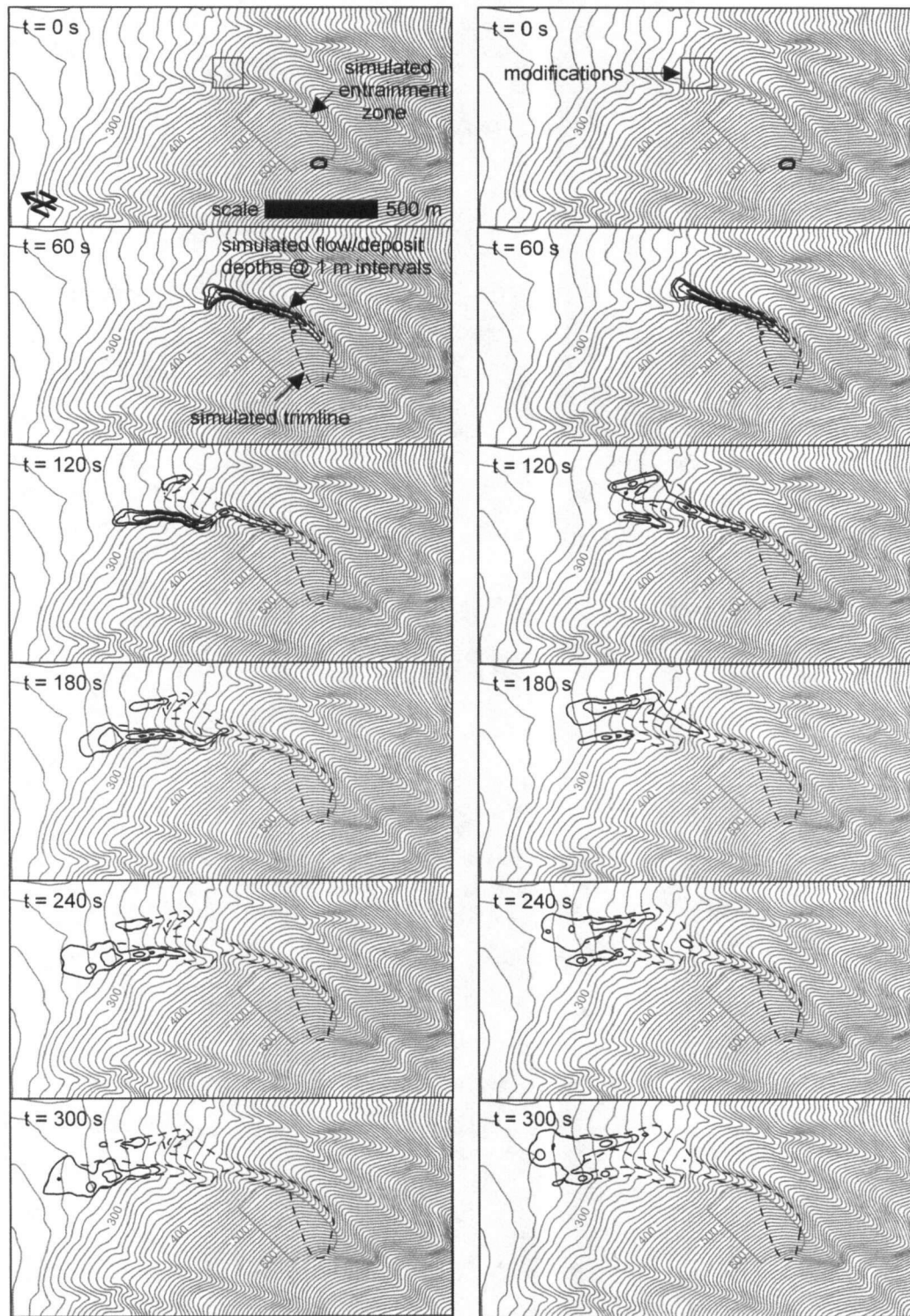
Two cases were considered to demonstrate the sensitivity of the model to complex topography: one using input sliding surface data that was digitized from a contour map, and another with slight modifications to this data near the fan apex. As shown in the next section, these modifications were necessary to reproduce the observed channel avulsion. The initial failure was modelled as a 4200 m^3 slide of approximately uniform 2 m depth. Similar to the preceding Cervinara analysis, the basal resistance in the source zone was modelled using a frictional rheology (Equation [4-41]) with a bulk basal friction angle of $\phi_b = 30^\circ$. Entrainment was enabled downslope of the source area, but not within the creek channel, and

proceeded at a specified rate of $E_s = 0.01 \text{ m}^{-1}$, up to a maximum erosion depth of 2 m. Following the start of entrainment, the basal rheology was changed to the Voellmy model (Equation [4-42]) with the same parameter values that were calibrated by Revellino et al. (2004) using DAN: a friction coefficient of $f = 0.07$ and a turbulence parameter of $\xi = 200 \text{ m/s}^2$. Also again, the internal friction angle was set to $\phi_i = 35^\circ$ and the following control parameters were used: $N = 2000$, $B = 4$, $C = 0$ and $D = 200$.

7.5.3 Results and discussion

The results of both analyses are shown in Figures 7.8. In the first case, most of the simulated flow turned left at the fan apex and remained in the creek channel. This did not match the field observations. A cross-check using the Forced Vortex Equation for superlevation of flows around channel bends (e.g., Hungr et al. 1984) supported the plausibility of this result, given the simulated velocity and the input topography at this location. In the second case, the small changes to the topography near the fan apex were sufficient to produce a significantly different result: most of the simulated flow jumped the channel at this location and spread out across the fan, as in the real event.

Such changes to the local topography could have been caused by antecedent landslide deposits in the channel at the time (several surges apparently occurred in this creek and could have preceded the surge in question), or it is possible that the contour map used to create the original input data was simply not accurate, at least at this particular location. Figure 7.9 is a view of the fan apex (looking upstream from the fan). The deep creek channel on the (downstream) left side of the fan that appears in the original DEM is not evident (although the photograph was taken after the event, which may have altered the local topography). It is also possible that the surge that overtopped the bend had a larger volume and/or higher velocity than simulated, and may not have originated from the location that was assumed in the simulation.



(a) original topography

(b) modified topography

Figure 7.8. Two simulations of the Quindici landslide using calibrated input parameters determined by Revellino et al. (2004). The flow/deposit depth contours are at 1 m intervals and the elevation contours are at 10 m intervals. The modified topography used in (b) was necessary to reproduce the observed channel avulsion at the fan apex.



Figure 7.9. View of the fan apex of the Quindici landslide (looking upstream from the fan). The channel on the right side of the photograph does not appear to be as deep as in the original DEM. (Photograph taken after the events of May 1998, courtesy of Dr. Paola Revellino, University of Sannio, Benevento, Italy)

In any case, the significant differences between the two results demonstrate the sensitivity of the model to complex topography and the importance of accurate input. They also highlight the general difficulty in applying dynamic modelling to processes on fans, which can be very dynamic landforms. When there is uncertainty about whether or not a channelized flow will leave its channel, dynamic modelling may not be sufficiently accurate and a more subjective analysis may be necessary. The Forced Vortex Equation provides a useful cross-check in these situations and should be used to supplement the model results.

7.6 Nomash River

7.6.1 Description

In April 1999, during spring snowmelt, a rock slide – debris avalanche occurred in the headwaters of the Nomash River on western Vancouver Island, British Columbia, Canada

(Guthrie et al. 2003; Hungr and Evans 2004a). Oblique aerial views of the landslide are shown in Figure 7.10. It began as a collapse (cf., Hungr and Evans 2004b) of approximately 300,000 m³ of crystalline limestone, with the head scarp located about 430 m above the river on the western side of the narrow, U-shaped glacial valley. A dry, granular avalanche of this magnitude would be expected to form a steep talus-like deposit at the foot of the source slope. In this case, however, the landslide impacted and mobilized an additional 360,000 m³ of saturated colluvium and till before reaching the valley floor. It then crossed the floodplain, ran up the opposite slope approximately 40 m while making a sharp left turn and continued down the valley for more than one kilometre. Assuming 25% bulking of the source failure, for an initial volume of 375,000 m³, the entrainment ratio was 0.96 (Hungr and Evans 2004a).



Figure 7.10. Oblique aerial views of the Nomash River rock slide –debris avalanche. North is towards the top in the photograph on the left. (Photographs courtesy of Dana Ayotte)

7.6.2 Methodology

Hungr and Evans (2004a) presented a DAN analysis of this event in which they used different pre- and post-entrainment basal shear stress laws to simulate a change in mobility

following incorporation of saturated path material. In their analysis, the initial rock slide was modelled using a frictional law (Equation [4-41]) and at the start of entrainment, immediately below the source area, the basal rheology was changed to the Voellmy model (Equation [4-42]). By systematic back-analysis, Hungr and Evans (2004a) determined that the following parameter values provided a reasonable simulation of the estimated flow velocities, flow depths and deposit depths: $\phi_b = 30^\circ$ before entrainment and $f = 0.05$ and $\xi = 400 \text{ m/s}^2$ after entrainment.

A corresponding simulation was performed using DAN3D and these calibrated basal resistance parameters. A growth rate of $E_s = 1.9 \times 10^{-3} \text{ m}^{-1}$ was specified in the entrainment zone (based on Equation [5-51] assuming $V_f = 735,000 \text{ m}^3$, $V_0 = 375,000 \text{ m}^3$ and $\bar{S} = 350 \text{ m}$). The internal friction angle was set to $\phi_b = 35^\circ$ and the following control parameters were used: $N = 2000$, $B = 4$, $C = 0$ and $D = 200$.

The pre-event sliding surface was modified from a post-event DEM by adding approximately $360,000 \text{ m}^3$ of material to the entrainment zone and subtracting approximately $735,000 \text{ m}^3$ from the deposit area. This redistribution of material was based on the same field estimates of erosion and deposit depths used by Hungr and Evans (2004a). The balance of $375,000 \text{ m}^3$ was redistributed in the source area so that, when superimposed, the sliding surface elevations and unbulked source depths produced a realistic pre-event topography.

As in the Frank Slide analysis presented at the beginning of this chapter, data manipulations such as these, which are based on subjective and uncertain field observations and often inaccurate topographic data, are themselves inherently subjective. At the scale of this example, errors in the estimated pre-event bed elevations on the order of $\pm 10 \text{ m}$ are possible and topographic details on this order, which can have an important influence on the results, may be lost. Similarly, errors in the measured trimline and deposit extent up to several metres in plan distance are possible. With limited data, these uncertainties are unavoidable and need to be considered during interpretation of the results. On the other hand, the assumed distribution of source material does not appear to have a significant influence in

such long-runout cases, as the initial internal pressure gradients cause a rapid redistribution of material upon failure. In the Nomash River case, several trial comparative simulations using strongly skewed source depths all produced comparable results.

7.6.3 Results and discussion

Time lapsed results of the simulation are shown in Figure 7.11. The simulated deposit distribution, with an average depth of approximately 3.7 m and a maximum depth of approximately 7.2 m, agrees with field observations that the landslide covered the floodplain but spread too thinly to dam the river (Hungr and Evans 2004a).

Figure 7.12 compares the measured and simulated trimlines, which coincide within the likely measurement error except in two important locations. First, the simulated flow spread faster than the real event, a result of the inherent assumption (shared by all hydrodynamics-based models) that the rock mass fluidizes instantaneously at failure (location A in Figure 7.12). In reality, fragmentation in rock slides and avalanches occurs progressively, limiting initial spreading. It is also possible that self-channelization due to erosion played a role in providing additional confinement in this case, but topography changes due to erosion were not accounted for in this simulation. Second, the model overestimated the extent of impact at the base of the source slope on the right side of the first turn (location B in Figure 7.12). In the real event, the deep creek channel at this location, which was neglected in the reproduction of the pre-event topography, may have deflected the flow. This discrepancy again emphasizes the sensitivity of landslide motion to 3D topography. As a step in more detailed, iterative back-analysis, the creek channel could be incorporated by further modification of the pre-event topography.

The simulated initial runup against the opposite slope and return runup against the source slope matched the measured trimline within the likely measurement error, which suggests that the flow velocities were very closely simulated. Runup and superelevation measurements were used by Hungr and Evans (2004a) to constrain the flow velocities in their analysis of this event.

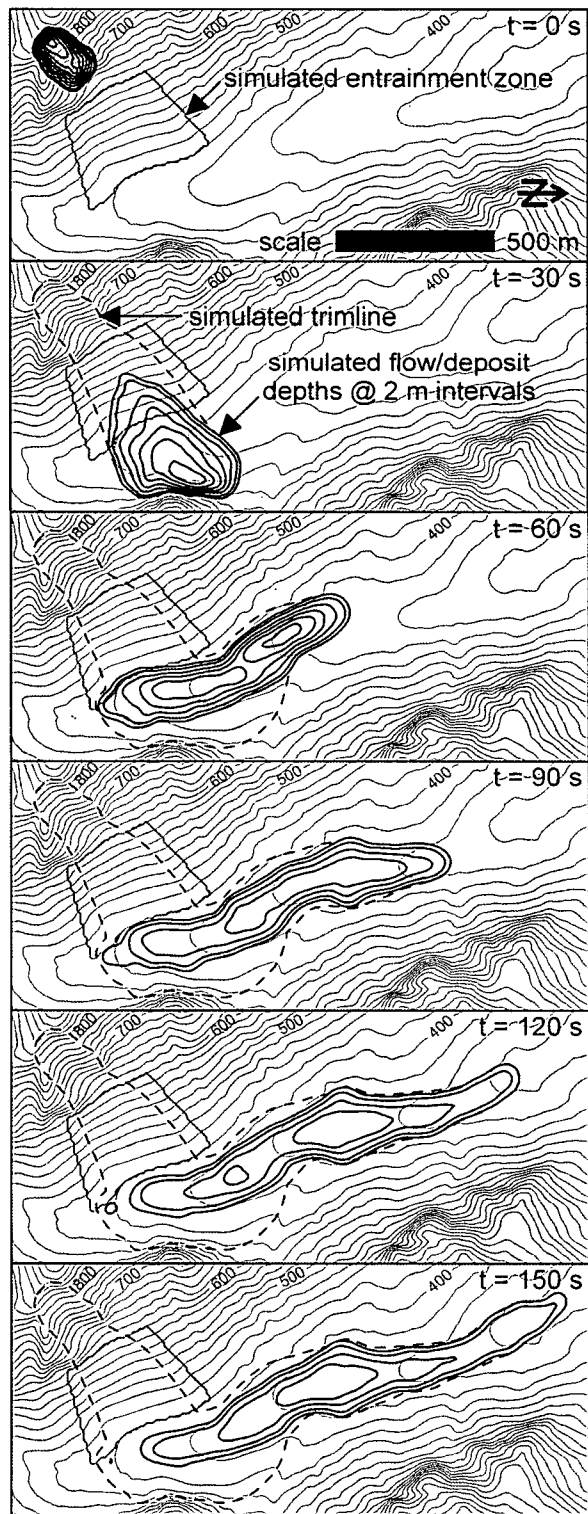


Figure 7.11. Simulation of the Nomash River landslide accounting for entrainment of material from the source slope and using calibrated input parameters determined by Hungr and Evans (2004a). The flow/deposit depth contours are at 2 m intervals and the elevation contours are at 20 m intervals.

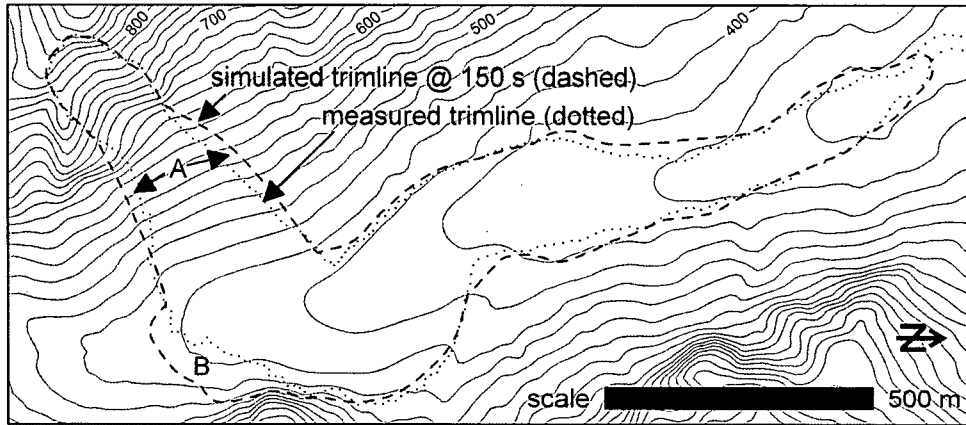


Figure 7.12. Comparison of simulated and measured trimlines showing discrepancies at locations A and B. The elevation contours are at 20 m intervals.

Finally, the simulated distribution of erosion (Figure 7.13) resembles the real case (Figure 7.14). Relatively deeper erosion occurred on the left side toward the base of the source slope and the prominent left side scarp was reproduced. The simulated maximum erosion depth of approximately 8.1 m (a maximum erosion depth was not specified in this simulation) corresponds with the field estimate of 8 m (Hung and Evans 2004a). Note that Figure 7.13 is another form of hazard intensity map (cf., Chapter 1).

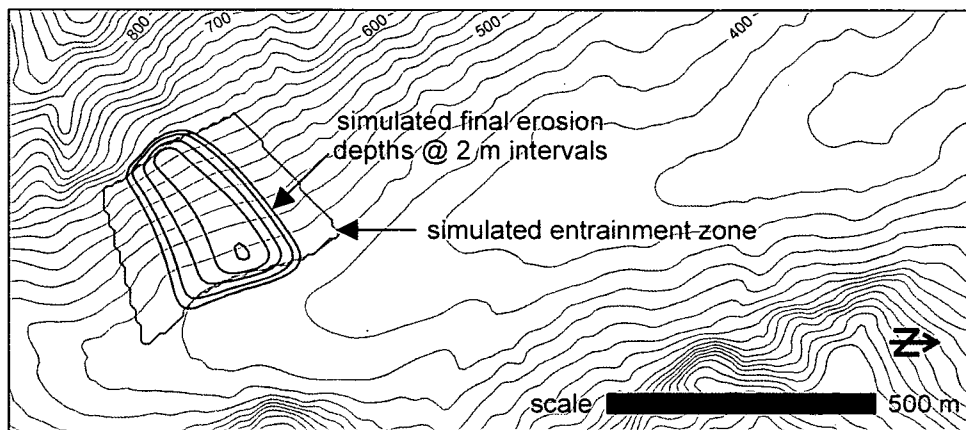


Figure 7.13. Erosion map corresponding to the simulation shown in Figure 7.11, a form of landslide hazard intensity map (cf., Chapter 1). The simulated maximum erosion depth of approximately 8 m matches field observations. The elevation contours are at 20 m intervals.



Figure 7.14. View of the source slope of the Nomash River landslide. The prominent side scarps are evidence of significant erosion. Compare with Figure 7.12.

It must be emphasized that in this case the only parameter adjusted to produce these results was the growth rate, E_s . The resistance parameters were not modified from the DAN analysis of Hungr and Evans (2004a). Again, this suggests that the original DAN model, which is more computationally efficient, is a useful tool for preliminary calibration of DAN3D. In practice, the two models could be used iteratively, with the new model providing estimates of the path profile and width, required by DAN, and DAN in turn providing rapid constraint of the resistance parameters.

A comparison simulation using a constant landslide volume and a frictional rheology with a constant value of $\phi_b = 30^\circ$ is shown in Figure 7.15. As expected, the model predicted that a relatively deeper deposit, with an average depth of approximately 7.5 m and a maximum depth of approximately 17 m, would form at the foot of the source slope. The runout distance was underestimated by more than one kilometre. Clearly, volume and rheology change capabilities are essential to the successful simulation of this event.

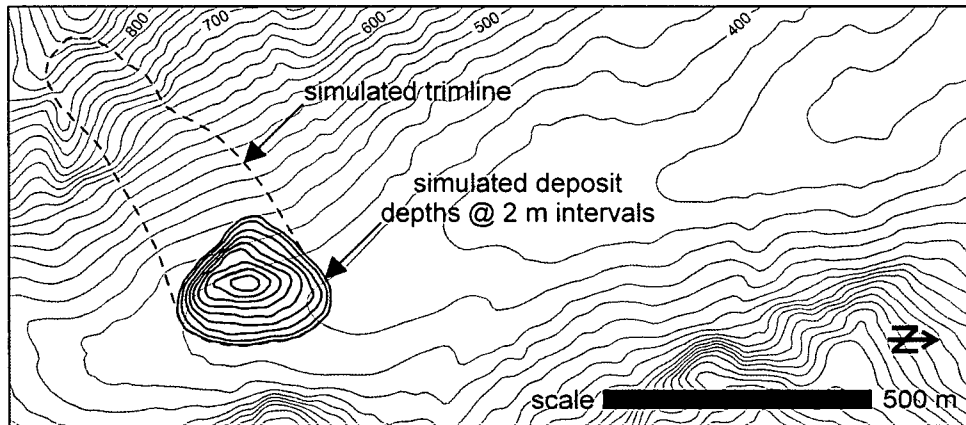


Figure 7.15. Simulation of the Nomash River landslide neglecting entrainment and the associated change in resistance. Instead, a frictional basal rheology was used for the duration of motion. This simulation did not match the observed behaviour of the real event. The deposit depth contours are at 2 m intervals and the elevation contours are at 20 m intervals.

7.7 Zymoetz River

The following analysis was undertaken with the help of Nichole Boulbee, Doug Stead and Jim Schwab.

7.7.1 Description

At approximately 1:30 am PDT on June 8, 2002, a large debris flow severed the Pacific Northern Gas pipeline at the mouth of Glen Falls Creek in the Zymoetz River valley, 18 km east of the city of Terrace in northern British Columbia, Canada (Figure 7.16). The landslide originated more than 4 km from the pipeline, initiating as a slide in volcanic bedrock. The fragmenting rock mass overrode and entrained snow and saturated surficial material on the source slope and in the cirque basin at its toe, before continuing as a debris flow that travelled more than 3 km down a sinuous, confined valley. An aerial view of the landslide path is shown in Figure 7.17.

On the source slope and in the upper part of the cirque basin the landslide deposited a thick, talus-like apron of fragmented rock, with material coming to rest on slopes exceeding 30°. In the valley downslope of the cirque basin, the landslide exhibited much higher fluidity, with

sweeping superelevations and motion persisting on slopes lower than 6° . Debris was deposited in lobes along Glen Falls Creek and in a large fan that extended across and dammed the Zymoetz River.

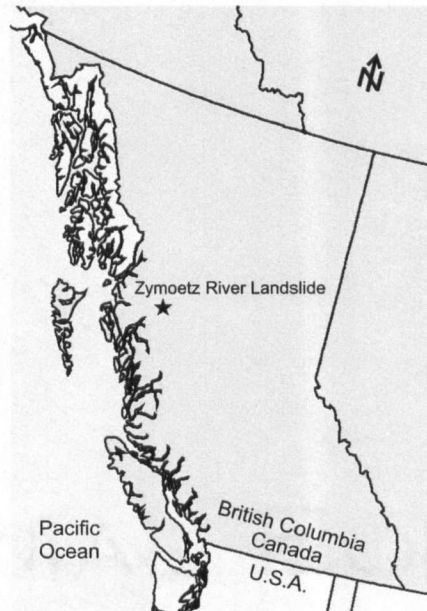


Figure 7.16. Location of the June 8, 2002 Zymoetz River rock slide – debris flow, northern British Columbia, Canada.

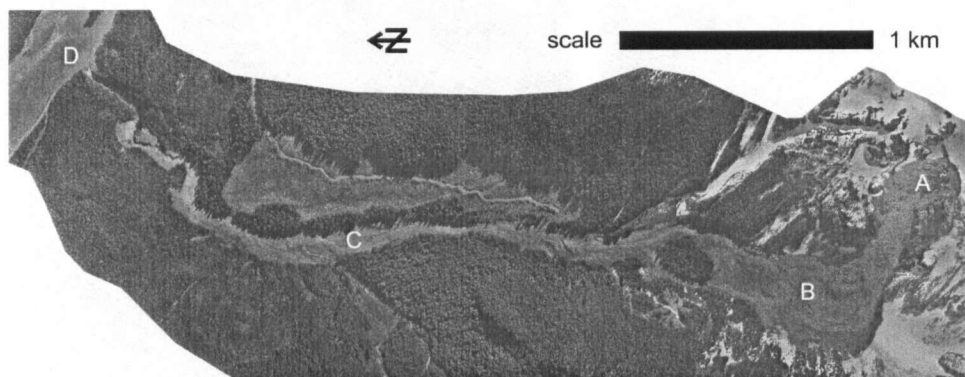


Figure 7.17. Aerial view of the Zymoetz River rock slide – debris flow. (A) source; (B) cirque basin; (C) Glen Falls Creek; (D) Zymoetz River. (Aerial photograph taken June 12, 2002, courtesy of Jim Schwab, Northern Interior Forest Region, Ministry of Forests, Province of British Columbia. Copyright © 2005 Province of British Columbia. All rights reserved. Reprinted with permission of the Province of British Columbia.)

The total economic losses associated with the landslide exceeded CDN \$30 million, including the direct costs of repairing the pipeline as well as lost timber and forestry access time (Schwab et al. 2003). Most of the damage occurred downslope of the cirque basin and can be attributed to the high mobility of the event. With a total volume of approximately $1.4 \times 10^6 \text{ m}^3$ and a *fahrböschung* less than 17° , the event plots well below the mean empirical relationships proposed for catastrophic landslides by Scheidegger (1973) and Li (1983), suggesting exceptional mobility for its size (Figure 7.18). However, the Zymoetz River rock slide – debris flow is only one of several recent events of this type and magnitude in British Columbia (e.g., Schwab et al. 2003; Hungr and Evans 2004a).

Descriptions of the Zymoetz River landslide were presented by Schwab et al. (2003), Boulton (2005) and Boulton et al. (2006). The following description concentrates on aspects of the mobility of the landslide.

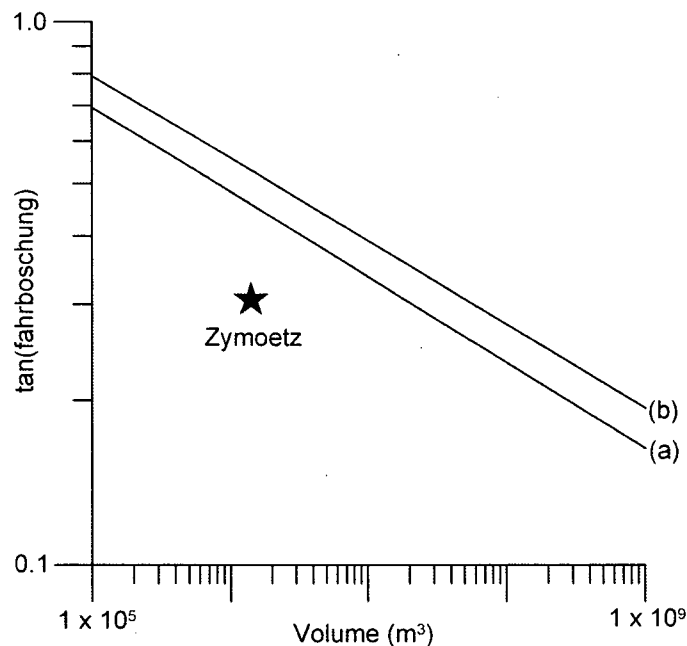


Figure 7.18. Plot of landslide volume vs. the tangent of the *fahrböschung* (angle of the line connecting the crown of the source to the toe of the deposit, as measured along the curving path). The Zymoetz River event (volume = $1.4 \times 10^6 \text{ m}^3$, $\tan(\text{fahrböschung}) = 0.31$) plots below the empirical relationships proposed by (a) Scheidegger (1973) and (b) Li (1983).

An enlarged aerial view of the proximal part of the path is shown in Figure 7.19. The rock slide initiated in heavily jointed volcaniclastic rock mid-slope on the east wall of a cirque (location A on Figure 7.19). A prominent joint set dipping downslope at about 45° formed the main sliding surface, while a sub-vertical backscarp extended up to the crown at elevation 1390 m (Boulton 2005). Regional precipitation and temperatures were above and below normal seasonal levels, respectively, in the months prior to failure, as reflected in a 200% above normal snowpack (Schwab et al. 2003), but no significant coinciding climatic trigger was recorded. Tectonic deformation, alteration, glacial over-steepening, frost action and pore pressure changes have all been suggested as possible factors contributing to the apparent long-term, progressive degradation of the rock mass, leading ultimately to failure (Schwab et al. 2003; Boulton et al. 2006). There is evidence of at least one previous rock slide immediately adjacent to the present source scar (Schwab et al. 2003), which may have created an apron of coarse talus at the toe of the source slope.

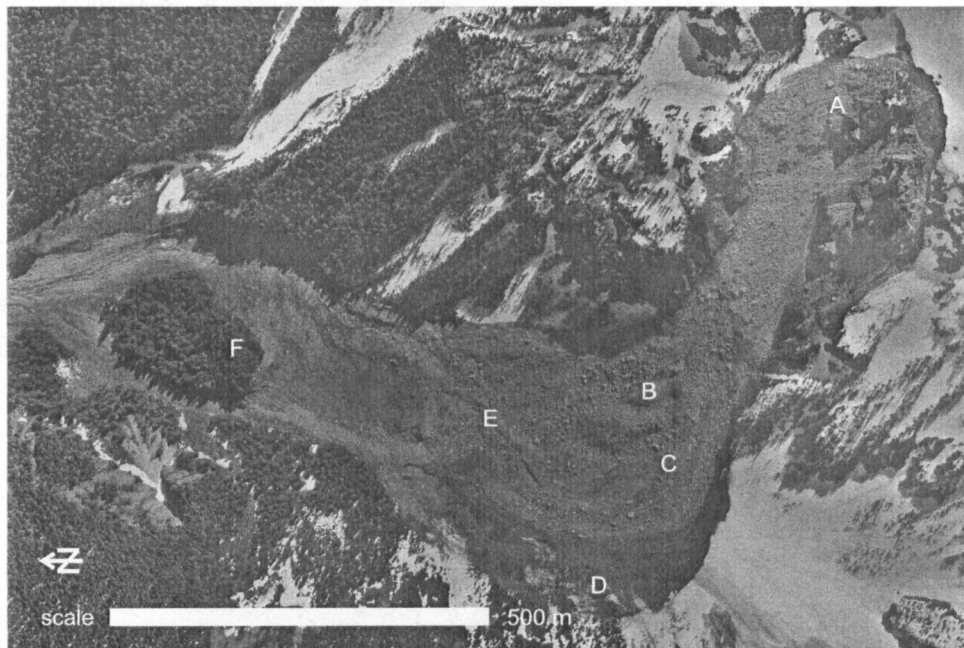


Figure 7.19. Enlarged aerial view of the proximal part of the path. (A) source; (B) exposed till; (C) thick deposits over snow; (D) thin deposits over snow in bend; (E) location of end moraine near elevation 880 m; (F) forested bedrock knob. (Aerial photograph taken June 12, 2002, courtesy of Jim Schwab, Northern Interior Forest Region, Ministry of Forests, Province of British Columbia. Copyright © 2005 Province of British Columbia. All rights reserved. Reprinted with permission of the Province of British Columbia.)

Based on calculations using pre- and post-event digital elevation models (DEMs), which are described in more detail in the next section, approximately 720,000 m³ of rock was displaced from the source area during the initial slide. Accounting for an estimated 25% bulking of the failure due to fragmentation (e.g., Sherard et al. 1963) gives a source volume of approximately 900,000 m³.

The first phase of motion was over snow, colluvium (talus and old rock slide debris) and bare rock. The snowpack was up to 5 m deep in the cirque basin at the time of the event (Schwab et al. 2003). A snow-covered area of about 200,000 m² was traversed by the landslide within the cirque basin between the source zone and the location of the snowline, near a prominent end moraine located at approximately elevation 880 m.

Some rock debris slid across the surface of the snow while some plowed into it and pushed it forward or became embedded. At the same time, snow was also entrained, as evidenced by exposed substrate at some locations. Figure 7.20 is a view up the source slope several months after the event. A ridge of till (a lateral moraine), which was covered with snow prior to the event, is exposed in the centre of the image (location B on Figure 7.19). Striations in the till that were carved by the passing rock suggest that it was stripped of surficial material, including snow and likely loose colluvium. On either side of the till ridge and further upslope are talus-like deposits of coarse rock avalanche debris (rockfall or secondary failures following the main event contributed to the amount of this material to an unknown degree). Approximately 100,000 m³ of coarse rock debris was spread over the source slope, which averaged more than 30°. Based on field measurements, another approximately 500,000 m³ of coarse rock debris, averaging about 3 m thick, came to rest in the upper part of the cirque basin immediately below the source area (Boulton et al. 2006), some of it on top of snow (Figure 7.21 and location C on Figure 7.19). Plowed snow was deposited along the margins of this rock debris.



Figure 7.20. View from toe of source slope toward source area (at top of photograph). The till exposed in the centre (location B on Figure 7.19) is surrounded by coarse rock avalanche deposits. (Photograph courtesy of Nichole Boulton)



Figure 7.21. Rock avalanche deposits on top of snow in the upper part of the cirque basin (location C on Figure 7.19). (Photograph courtesy of Nichole Boulton)

Contrasting with the coarse debris is a curving segment adjacent to its left margin on the outside of the first major curve of the path (location D on Figure 7.19). Here, the original snow cover remained in place, but was marked by strongly-defined curving striations, evidently caused by debris having travelled in an extremely rapid arching motion over the snow. The high point of the arch is almost 60 m above the valley thalweg. Using the Forced Vortex Equation for superelevation (e.g., Hungr et al. 1984), the flow velocity of the debris sliding over snow in this curve was estimated to be approximately 26 m/s (Boulton et al. 2006). Little or no debris was deposited in this segment. The thicker rock avalanche deposits overlap its proximal and distal margins, suggesting that they arrived only when the curving motion over the snow had been completed.

While evidently highly mobile, it is unlikely that this part of the landslide was responsible on its own for triggering the massive entrainment and motion of material into the distal segment of the path. The reason for this is that only a relatively small quantity of the landslide material was evidently involved, which slid over the snowpack but was unable to entrain much of it. The increase in mobility was probably caused by rapid, undrained loading of wet surficial material (e.g., Hutchinson and Bhandari 1971; Sassa 1985) by the leading edge of the more massive main flow. Such liquefaction of path material has long been invoked as a mechanism of long-runout (e.g., Buss and Heim 1881, Sassa 1988, Voight and Sousa 1994, Abele 1997). A very similar mechanism and sequence of transition between a rock slide and debris avalanche at Eagle Pass, British Columbia was described by Hungr and Evans (2004a). It is possible that an end moraine, which appears to demarcate the two main phases of motion (location E on Figure 7.19), affected local drainage of spring meltwater below the snowline, causing saturation of loose material accumulated in the path. At the same time, the thalweg upstream of the end moraine was probably filled with loose, fine-grained soil and organics.

After crossing the end moraine, the landslide dropped out of the basin and continued downstream in a second, more fluid phase of motion (Figure 7.22). The flow divided around a forested bedrock knob near elevation 830 m (location F on Figure 7.19), with most of the material branching to the east. It rejoined near elevation 690 m and followed Glen Falls

Creek the remaining 2.6 km to the Zymoetz River. An enlarged aerial view of the distal part of the path is shown in Figure 7.23.



Figure 7.22. Oblique aerial view of the cirque basin showing the change in deposit composition and morphology near the end moraine. (A) location of end moraine near elevation 880 m; (B) forested bedrock knob. (Photograph taken on June 8, 2002, courtesy of Jim Schwab, Ministry of Forests, Province of British Columbia)

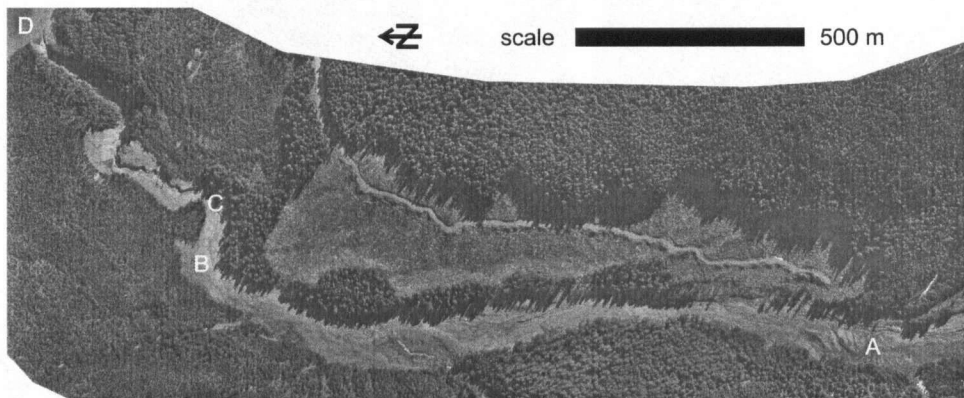


Figure 7.23. Enlarged aerial view of the distal part of the path. (A) channel widening due to entrainment at the lateral margins; (B) superelevation around bend; (C) upper end of gorge; (D) fan. (Aerial photograph taken June 12, 2002, courtesy of Jim Schwab, Northern Interior Forest Region, Ministry of Forests, Province of British Columbia. Copyright © 2005 Province of British Columbia. All rights reserved. Reprinted with permission of the Province of British Columbia.)

The extremely rapid motion along Glen Falls Creek is evidenced by superelevations up to 40 m above the base of the creek channel. Velocities back-calculated from superelevation data in this segment ranged between 14 and 26 m/s (Boulton et al. 2006). These high velocities continued far into the distal part of the path. For example, the velocity at location B on Figure 7.23 was estimated to be between 16 and 18 m/s (Boulton et al. 2006). The high mobility of the debris flow was evidently aided by a significant amount of water, as mud splashes high above the creek channel were observed on trees next to the path (Boulton 2005).

The creek channel itself was widened substantially, by up to about 80 m in some locations, as colluvium, topsoil and vegetation were entrained along the margins of the flow (e.g., location A on Figure 7.23). Material was simultaneously deposited in discontinuous lobes up to 4 m thick (Boulton 2005). Based on field measurements, approximately 200,000 m³ of material was deposited along Glen Falls Creek (Boulton et al. 2006), the majority of which stopped just upstream of a narrow bedrock gorge (location C on Figure 7.23). These deposits were finer than the material deposited in the cirque basin and included volcanic source material as well as additional volcanics, limestone, till and some organics derived from the basin, the channel banks and existing channel deposits (Boulton 2005).

The debris flow deposits can be seen in Figure 7.24, which is a view up the channel towards the cirque basin. Incorporation of finer material and additional water is evident in the character (gradation, lithology and water content) of deposits left in the channel downstream of the end moraine and in the distal fan deposit. It is likely that this change in the character of the flowing material increased the mobility of the landslide and allowed motion to continue beyond the cirque basin.



Figure 7.24. Oblique aerial view up the channel towards the source area (at top of photograph). The debris flow superelevated around numerous bends and left discontinuous deposits. (A) The flow overtopped a 20 m high ridge near the confluence with a tributary creek (Photograph taken on June 13, 2002, courtesy of Jim Schwab, Ministry of Forests, Province of British Columbia)

The Pacific Northern Gas pipeline was severed near the mouth of the creek, igniting an intense fire. Approximately $600,000 \text{ m}^3$ of material reached the Zymoetz River and formed a large fan/dam that blocked the river for about 30 minutes (location D on Figure 7.23) (Schwab et al. 2003). A view of the fan is shown in Figure 7.25. The fine materials blanketing the fan were deposited during a second, smaller debris flow that was witnessed at 10:15 am PDT. This secondary event likely resulted from sidewall destabilization due to erosion by the main event. It appears to have originated from a debris slide that entered the channel below the cirque basin and may have remobilized fresh deposits in its path (Jim Schwab, personal communication).

An estimated total volume of $1.4 \times 10^6 \text{ m}^3$ was mobilized during the event, about $500,000 \text{ m}^3$ of which was entrained along the path.

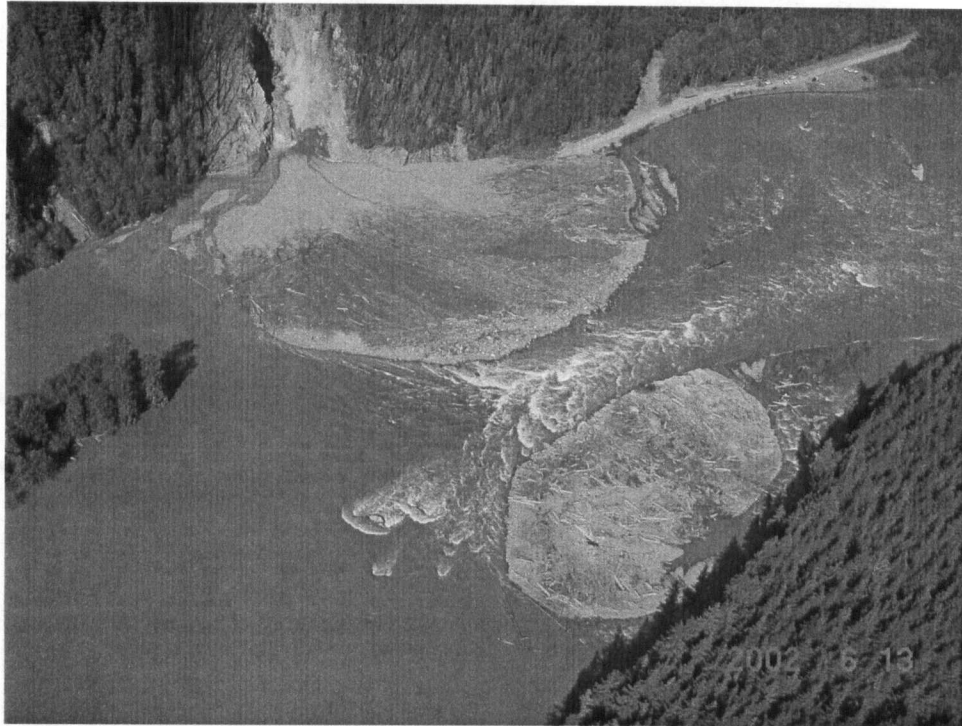


Figure 7.25. Oblique aerial view of the large fan created by the landslide, which temporary dammed the Zymoetz River. (Photograph taken on June 13, 2002, courtesy of Marten Geertsema, Ministry of Forests, Province of British Columbia)

7.7.2 Methodology

Initial back-analyses using DAN (Hungry 1995) suggested that a more realistic simulation of the event could be achieved by accounting explicitly for the complex 3D geometry (Boulton 2005).

Pre- and post-event DEMs at 2 m resolution were provided. The source depths were approximated by subtracting the post- from the pre-event DEM and isolating the probable main failure zone. Data outside of this zone were filtered, leaving a displaced volume of approximately $720,000 \text{ m}^3$. The isolated source depths were then subtracted from the pre-event DEM to approximate the initial sliding surface elevations. The failure was bulked approximately 25% at the source, for an initial volume of $900,000 \text{ m}^3$. The data spacing was increased to 10 m for input into the model.

The two main phases of motion were simulated as one continuous event, starting as frictional motion of broken rock and transforming into debris flow at the point where significant entrainment of saturated material from the path began (estimated to be near location E on Figure 7.19). Above elevation 880 m, the approximate location of the snowline and the moraine, the basal resistance was governed by a frictional model (Equation [4-41]). The bulk basal friction angle was calibrated to produce a reasonable simulation of the distribution of coarse deposits in the proximal path. Entrainment was neglected during this phase.

The first surge passing through the proximal area, which apparently slid over snow, could well have been analyzed as a separate event, even though it may have occurred only seconds before the main detachment. An alternative method was used: a lower bulk basal friction angle was imposed on a relatively small volume of material at the flow front to simulate the influence of snow on the mobility of the leading edge of the rock slide and reproduce the superelevation against the opposite wall of the cirque basin (location D on Figure 7.19). A value of $\phi_b = 18^\circ$ (based on a separate DAN3D back-analysis using a smaller detachment volume, which was performed by Suzanne Chalindar) was assigned to the first 10% of the material ($90,000 \text{ m}^3$) to reach elevation 980 m, approximately where the real landslide began to spread out over the deep snowpack in the upper part of the cirque basin. This volume was chosen to represent the apparently small volume of material near the flow front, which ran over but did not entrain the snow. Trial runs showed that the model was not very sensitive to the selected flow front volume, within a reasonable range; a much smaller volume would not cover the observed impact area, while a much larger volume would likely produce large enough flow depths to cause entrainment of the snow. The relatively low value of ϕ_b used to model this part of the event implies inherently lower dynamic friction between the rock and the snow, which may have also been mediated by pore fluid, possibly supplied by wet or rapidly melting snow incorporated into the flow. This methodology is consistent with the hypothesis that the relatively less mobile but more massive main body of the landslide was responsible for initiating the entrainment and change in behaviour in the cirque basin.

Based on the estimated presence of loose, saturated soils in the path upstream of the end moraine, as described in the previous section, entrainment was enabled below elevation 880

m, and the Voellmy basal resistance model (Equation [4-42]) was implemented. The two Voellmy resistance parameters were adjusted by trial-and-error to achieve the best simulation of the second main phase of motion in terms of the estimated flow velocities, observed flow trimlines and observed distribution of deposits. To simulate entrainment during this phase, a volume growth rate of $E_s = 3.3 \times 10^{-4} \text{ m}^{-1}$ was specified below elevation 880 m (based on Equation [5-51] assuming $V_f = 800,000 \text{ m}^3$ and $V_0 = 300,000 \text{ m}^3$, based on the aforementioned volume balance estimates for the real event, and $\bar{S} = 3000 \text{ m}$).

The internal friction angle was set to $\phi_i = 35^\circ$ and the following control parameters were used for the duration of motion: $N = 4000$, $B = 4$, $C = 0.01$ and $D = 200$.

7.7.3 Results and discussion

The results are shown in Figure 7.26 (Figure 7.26a shows the first 60 s of motion at 10 s intervals, while Figure 7.26b shows 600 s of motion at 100 s intervals). The best simulation of the main proximal phase of motion, based mainly on the distribution of deposits near the toe of the source slope, was achieved using $\phi_b = 31^\circ$. This value corresponds closely to the “expected” coefficient of sliding friction ($\tan \phi_b$) of 0.6 proposed for rock avalanches by Hsu (1975). It approximates the dynamic friction angle of dry, broken rock, which suggests that pore fluid pressures had a minimal influence on the dynamics during this phase of motion. The distribution and talus-like morphology of the dry rock avalanche deposits were reproduced, including the exposure of the lateral moraine near the centreline (compare location A on Figure 7.26b with location B on Figure 7.19).

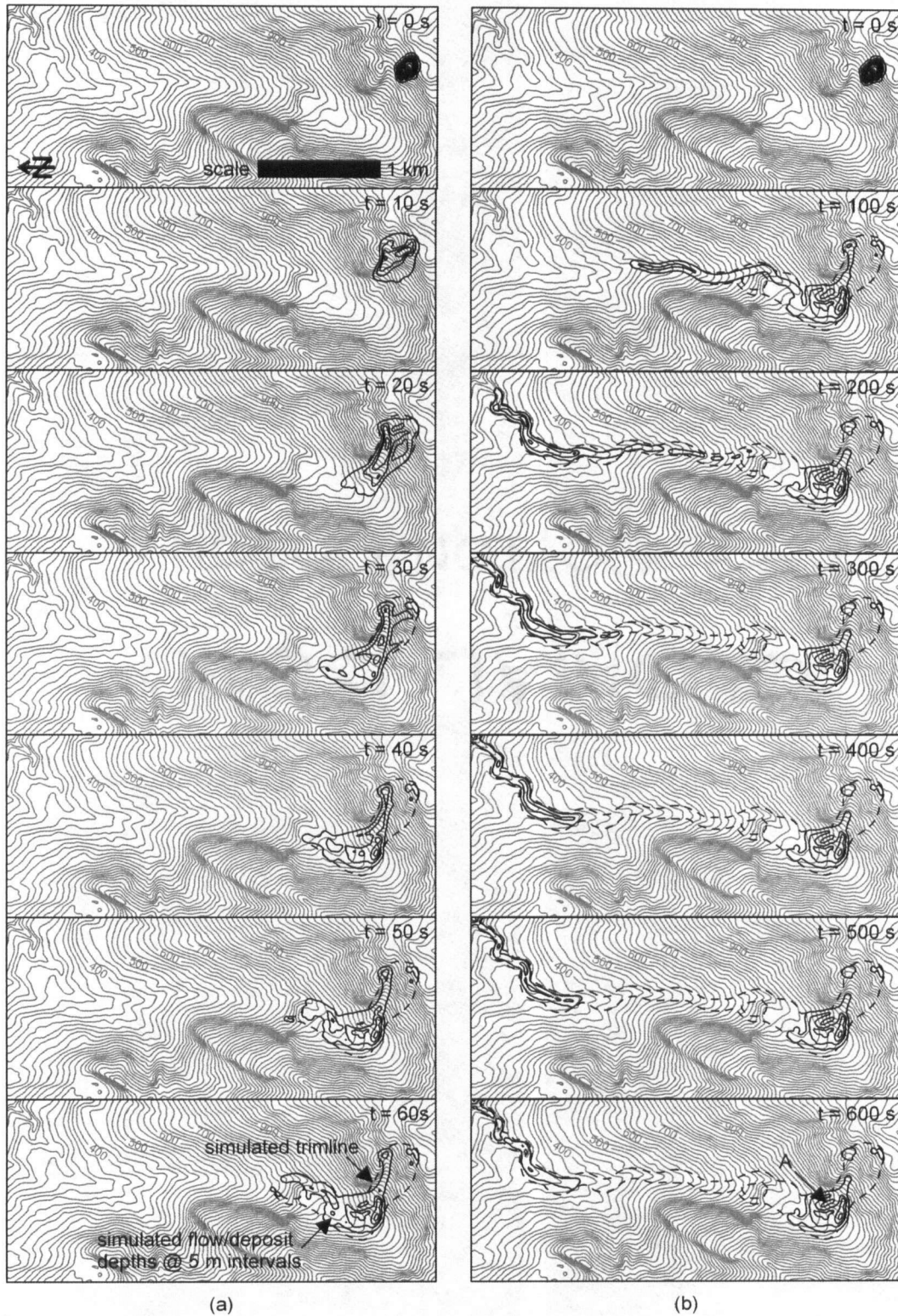


Figure 7.26. Calibrated simulation of the Zymoetz River landslide at (a) 10 s intervals and (b) 100 s intervals. The flow/deposit depth contours are at 5 m intervals and the elevation contours are at 20 m intervals. (A) exposed till.

Values of $f = 0.1$ and $\xi = 1000 \text{ m/s}^2$, which correspond to a set of parameters calibrated in previous back-analyses of similar events (cf., Hungr and Evans 1996), produced the best simulation of the distal phase of motion. In this case, the friction coefficient of 0.1 approximates the slope of the channel just upstream of the gorge, which allowed some material to deposit in that area, as in the real event. The relatively low friction coefficient simulates a low component of frictional resistance due to persistent, high pore fluid pressures within the bulk of the flow. The turbulence parameter of 1000 m/s^2 was calibrated so that the simulated flow velocities in the distal path approximately matched the velocities estimated using superelevation data. For example, the calibrated model produced velocities just over 16 m/s in the bend at location B on Figure 7.23, which corresponds with the 16 to 18 m/s range that was estimated by Boulton et al. (2006) using the Forced Vortex Equation.

A plot of the maximum simulated flow velocities recorded along the path is shown in Figure 7.27. The locations and values of superelevation-based estimates are superimposed on the figure. The highest velocities, up to about 45 m/s, were recorded in the upper part of the cirque basin, where entrainment is believed to have initiated. While there is no information available regarding the total duration of the real event, the correspondence between the simulated and back-calculated flow velocities suggests that the duration was well-constrained by the model. The model was stopped manually after 600 s, by which time most of the material had come to rest.

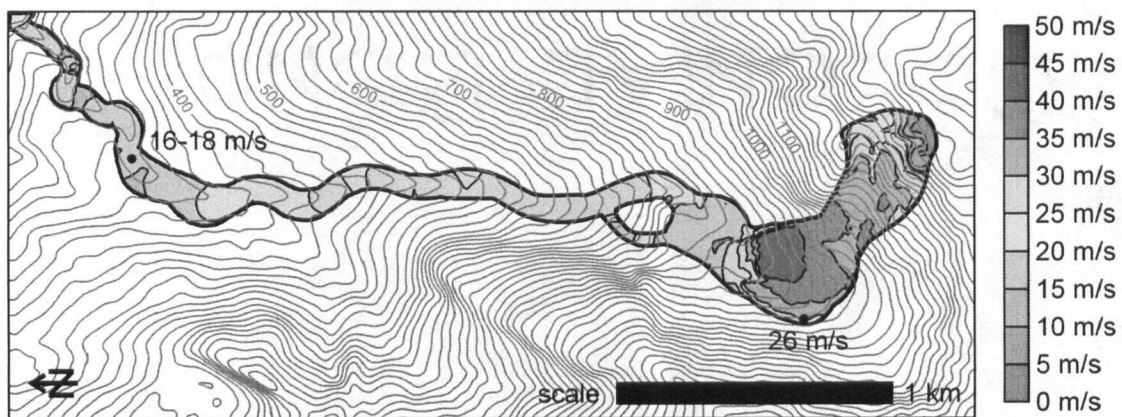


Figure 7.27. Plot of the maximum simulated flow velocities recorded along the path. Velocities back-calculated using superelevation data are superimposed. The maximum velocity contours are at 10 m/s intervals and the elevation contours are at 20 m intervals.

The simulated trimline and distribution of material after 600 s are superimposed on the aerial photograph in Figure 7.28. Note that the shadows of the trees obscure the trimline on the east side. The model produced a reasonable simulation of the actual trimline, reproducing the division of flow around the forested bedrock knob and the superelevations in the basin and distal part of the channel. An exception is noted at location A on Figure 7.28; the model did not reproduce the overtopping of a 20 m high ridge near the junction with a tributary creek (shown in Figure 7.24), but instead deflected around it, producing a series of superelevations immediately downstream. This discrepancy may be because the simulated flow was not deep enough or was not travelling fast enough when it encountered the ridge. It is possible, as McClung (2001) has suggested in a detailed review of the Forced Vortex Equation, that the velocities may have been underestimated in the downstream bend. In the future, it would perhaps be more appropriate to adjust the model itself to match the observed superelevations, rather than to match back-calculated velocities. It is also possible that the DEM was inaccurate. For example, the right channel bank may not have been steep enough to confine the flow, as observed in the real case, or the ridge itself may have been slightly exaggerated, preventing overtopping. In any case, this discrepancy again highlights the sensitivity of landslide motion to complex topography.

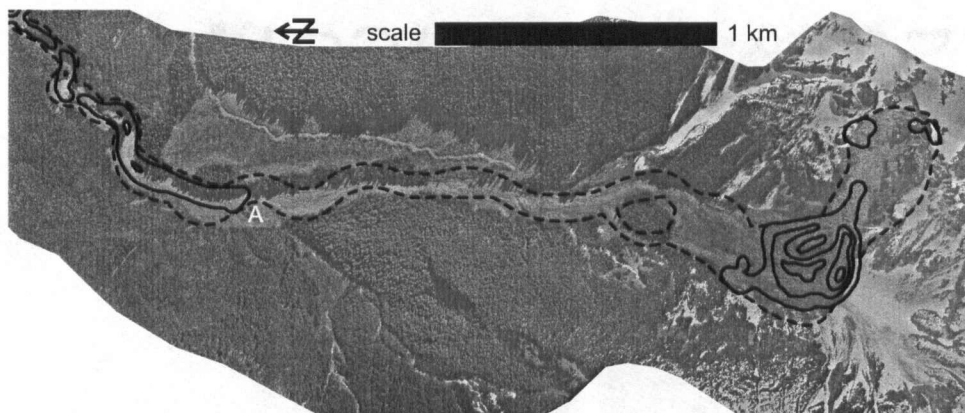


Figure 7.28. Simulated trimline and distribution of material after 600 s, superimposed on the aerial photograph. The trimline on the east side is obscured by shadows. (A) 20 m high ridge near creek junction. (Aerial photograph taken June 12, 2002, courtesy of Jim Schwab, Northern Interior Forest Region, Ministry of Forests, Province of British Columbia. Copyright © 2005 Province of British Columbia. All rights reserved. Reprinted with permission of the Province of British Columbia.)

The overall distribution of deposits was reasonably simulated. Thick, talus-like deposits were formed near the toe of the source slope and material was deposited in the channel, mostly upstream of the gorge. The balance of the material reached the Zymoetz River (note that the DEM did not extend far enough to allow simulation of the fan formation).

The model was able to capture the most important features of this complex event, including the key influences of snow and saturated surficial material in the cirque basin and the channel. To do so, it was necessary to divide the case into two main phases, each to be modelled differently. In this particular case, a third, different set of parameters was imposed on a small part of the landslide, in order to reproduce a minor feature of the event. These input parameters were not adjusted arbitrarily, but were based on observed and/or estimated factual information. The morphology of the path and the deposits were taken into account in the selection of appropriate rheologies and independent estimates of flow velocities and deposit volumes were used. The presence of specific materials in the path prior to the event that could have influenced its mobility was also considered. For example, the end moraine in the cirque basin was identified during field work as an important location demarcating the two main phases of motion, which appears to be corroborated by the modelling results. This physical evidence was combined with previous experience analyzing similar events to converge on appropriate values for the resistance parameters.

It is interesting to consider the possible seasonal influence in this case, as snow and associated meltwater appear to have been important factors. A key question could be: If the same rock slope had failed during the late summer dry season, would the landslide have travelled so far? Such seasonal effects on mobility may be important to consider in risk studies.

This back-analysis further demonstrates the concept of modelling rock slide – debris avalanches/flows using two phases: a frictional phase in the proximal path, where little entrainment occurs, and a Voellmy (or other rheology representing reduced frictional resistance) phase in the distal path, where relatively fine-grained, saturated material can be entrained (Hungr and Evans 2004a). As in the preceding Nomash River analysis, successful

simulation would not have been possible using constant, dry, frictional parameters. This result supports the notion that long runout of many rock and debris avalanches can be connected with the process of material entrainment (e.g., Sassa 1985) and that this process must be included in dynamic modelling.

7.8 McAuley Creek

The following analysis was undertaken with the help of Steve Evans, Réjean Couture, Marc-Andre Brideau and Kevin Turner.

7.8.1 Description

The preceding Zymoetz River landslide was part of an unusual cluster of events across British Columbia in the spring of 2002 (e.g., Schwab et al. 2003; Evans et al. 2003). During the same season, in either late May or early June, a rock avalanche occurred about 30 km east of Vernon in the province's southern Interior Plateau. The event initiated as a slide in gneissic rock exhibiting strong easterly dipping foliation on the west side of McAuley Creek (Evans et al. 2003). This location had been identified previously as a potential landslide source area. Tension cracks near the present head scarp are visible on pre-event aerial photographs and a similar prehistoric landslide is evident immediately upstream. A definitive trigger for the 2002 failure has not been identified, but heavy rainfall may have been a factor (Evans et al. 2003). Based on calculations using pre- and post-event DEMs, which are described in the next section, an approximate total of 7.4 Mm^3 (bulked) of material was involved.

An aerial view of the McAuley Creek landslide is shown in Figure 7.29 and an oblique aerial view is shown in Figure 2.15 in Chapter 2. The event exhibited two-phase behaviour similar to the Zymoetz River landslide. Most of the material came to rest near the toe of the source slope and formed a deep deposit that dammed McAuley Creek for a short time, until it was able to drain through the predominantly coarse debris. In contrast to this low-mobility proximal phase, about 1 Mm^3 of the material from the downstream flow margin spread out

along the floor of the narrow valley and formed a relatively thin, 1.6 km long distal deposit. The two phases appear to have been contiguous, with no overlapping of flow margins to suggest the occurrence of distinct movement episodes.

The mobility of the distal phase may have been caused by rapid loading of wet and possibly saturated glaciolacustrine deposits located along the channel, which were identified during post-event fieldwork. It is also possible that entrainment of surficial material from the left side of the source slope (which was also evident), rather than loading of valley-bottom deposits, was responsible for the increased mobility, but the lack of significant runup/superelevation against the opposite valley wall suggests that this influence was minimal.

The McAuley Creek landslide is the subject of an ongoing detailed analysis. A first-attempt back-analysis of the event is presented here to demonstrate how “off the shelf” input parameters, based on previous modelling experience, can produce good preliminary results. This has important implications for the potential for true landslide runout prediction using DAN3D.

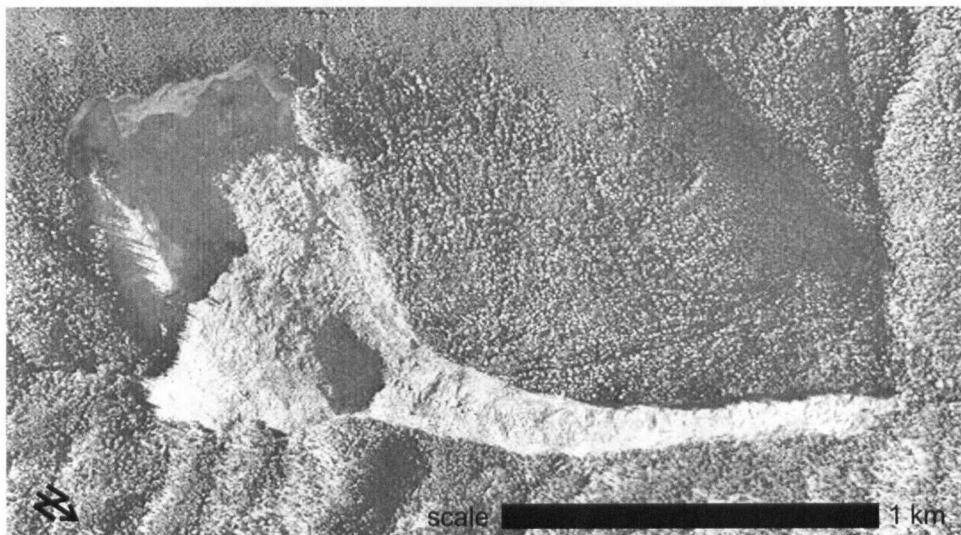


Figure 7.29. Aerial view of the McAuley Creek landslide showing the deep proximal and shallow distal deposits. (Aerial photograph courtesy of Steve Evans, University of Waterloo, Canada)

7.8.2 Methodology

Pre- and post-event spot elevations derived from photogrammetry were provided by the Geological Survey of Canada. Digital elevation models at 10 m grid node spacing were created from this data using Surfer (Golden Software Inc.). A uniform 10 m vertical thickness was subtracted from the pre-event DEM to filter out the influence of tree cover on the pre-event ground surface elevation data. Accounting for 20% bulking of the source failure, this filtering produced a pre- versus post-event volume balance of material within the landslide impact area. The assumed 10 m average vertical error also corresponds somewhat with the British Columbia Ministry of Forests' local tree height estimates of between 20 and 37 m, when combined with local crown closure estimates of between 46 and 75% (Kevin Turner, personal communication).

The source depths were approximated by subtracting the post- from the modified pre-event DEM and isolating the probable main failure zone. Because the proximal deposits overlapped the failure surface, manual adjustments to the resulting source depths (based on estimated local failure surface elevations) were necessary above elevation 1150 m, the assumed toe of the failure surface. The resulting displaced volume was approximately 6.2 Mm³. The source depths were then subtracted from the modified pre-event DEM to approximate the sliding surface elevations. The failure was bulked 20%, for a total initial volume of 7.4 Mm³.

As in the Zymoetz River case, the two phases of motion were modelled using a frictional basal rheology (Equation [4-41]) in the proximal path and a Voellmy basal rheology (Equation [4-42]) in the distal path. "Off the shelf" rheological input parameters were selected for this preliminary analysis. The bulk basal friction angle in the proximal path was set to $\phi_b = 30^\circ$. Again, this value corresponds closely to Hsu's (1975) "expected" value for sliding rock, and it has been used in several of the preceding cases. In this case, it is also slightly lower than the average slope angle of the failure surface, and so its use approximates limiting equilibrium conditions at initiation.

The rheology change was implemented below elevation 1060 m, approximately where the more mobile lobe extended from the main deposit, and the Voellmy friction coefficient and turbulence parameter were set to $f = 0.1$ and $\xi = 500 \text{ m/s}^2$, respectively. These values were recommended by Hungr and Evans (1996) based on back-analyses of 23 rock avalanches using DAN. Similar calibrated values were determined by Hungr et al. (1998), Ayotte and Hungr (2000), Revellino et al. (2004) and Pirulli (2005). In this case, the friction coefficient approximates the average slope of the creek channel downstream of the main deposit, which allows the distal flow to spread out and deposit there. At the same time, the finite turbulence parameter, which is within the range of values used in the preceding cases, limits the flow velocities along the channel.

Although entrainment did occur during the real event, volume change was neglected in this analysis, as the amount of surficial material available along the path was small relative to the source volume. As in previous cases, the internal friction angle was set to $\phi_i = 35^\circ$ and the following control parameters were used: $N = 4000$, $B = 4$, $C = 0.01$ and $D = 200$.

7.8.3 Results and discussion

The results are shown in Figure 7.30. A good simulation of the extent of the impact area and the distribution of deposits was achieved using the preliminary input parameter values. The relatively deep proximal and thin distal deposits were reproduced, with the distal lobe comprising approximately 1 Mm^3 of material, as estimated in the real event. Similar to several of the preceding cases, comparative analyses have shown that the observed distribution of deposits cannot be simulated using constant rheology assumptions.

The lack of significant runup and superelevation in the real event means that velocity estimates are not available for comparison. However, this feature was also reproduced by the model, suggesting that the simulated velocities were reasonable. The simulated velocity along the distal channel ranged up to about 25 m/s, which is within reason for a debris flow of this magnitude. A lower/higher simulated value could be achieved by reducing/increasing the value of the Voellmy turbulence parameter.

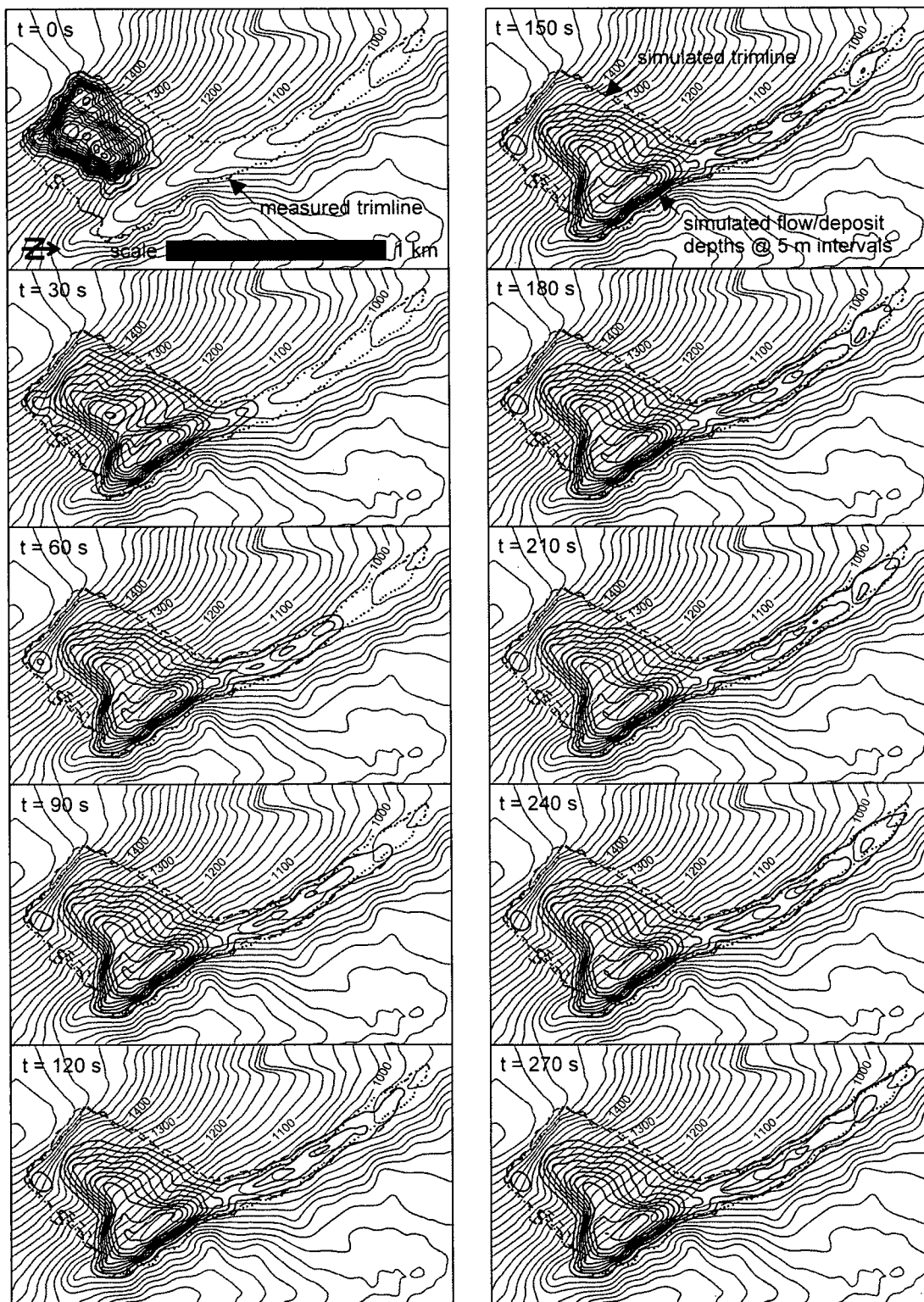


Figure 7.30. Simulation of the McAuley Creek landslide using “off the shelf” input parameters. The flow/deposit depth contours are at 5 m intervals and the elevation contours are at 20 m intervals.

These good preliminary results suggest that true prediction, involving objective input parameter selection from a database of back-analyses, may eventually be possible. In this case, the most subjective decision was where to implement the change from frictional to Voellmy behaviour. This decision would have been difficult to make without the post-event field evidence. In reality, there was probably no noticeable difference between the surficial deposits upstream and downstream of this location prior to the event. Any surficial deposits that may have contributed to the high mobility of the distal phase could also extend upstream beneath the present main deposit, which remained there perhaps because it was simply deep enough to bridge them. More experience analyzing this type of event may help reduce this subjectivity.

7.9 Kolka

The following analysis was undertaken with the help of Olga Tutubalina, Sergey Chernomorets, Dmitry Petrakov, Valeriy Drobyshev and Steve Evans.

7.9.1 Description

On September 20, 2002, a large ice/rock avalanche – debris flow occurred in the Caucasus Mountains in North Ossetia, Russia. The event involved the failure of Kolka Glacier at the head of the Genaldon River valley. It impacted a large area over a width of up to 500 m and a total distance of about 36 km, comprising an 18 km long proximal ice/rock avalanche phase, which stopped upstream of the Karmadon Gates (a narrow pass in the Skalistyy Range), and an 18 km long distal debris flow phase. Velocities up to 250 km/hr along the proximal path have been estimated based on flow cross-sections and seismic data (Drobyshev 2003b and 2005). The main deposit formed an ice and debris dam in the Karmadon depression that caused extensive flooding and damage to property upstream, as shown in Figure 1.2 in Chapter 1. Another view of the main deposit area is shown in Figure 7.31. An estimated 125 people were killed in the disaster.



Figure 7.31. View of the main deposit of the Kolka Glacier event, looking downstream from the right side of the Genaldon valley towards the Karmadon Gates. (Photograph taken on September 22, 2002, two days after the event, courtesy of Mr. Igor Galushkin, Ministry of Natural Resources, North Ossetia, Russia)

The exact trigger for the event is still in dispute. Ice and rock falls onto Kolka Glacier from the northern face of Mt. Dzhimarai-khokh occurred in the two months leading up to the disaster, and a relatively large event of this type was originally thought to have triggered the catastrophic failure (Huggel et al. 2005). However, recently-discovered satellite images taken less than 9 hours prior to the event suggest that a large triggering slope failure did not occur, but that a surge of the rear part of Kolka Glacier was underway (Tutubalina et al. 2005). This suggests the possibility of a “standing start” (Olga Tutubalina, Sergey Chernomorets and Steve Evans, personal communication), with catastrophic failure and rapid acceleration perhaps caused by a combination of brittle failure of the ice and rapid loading of water and/or saturated material at its base or immediately downstream. Not disputed is the poor condition of Kolka Glacier at the time, and the possible involvement of a significant amount of meltwater.

The following back-analysis was undertaken to produce a simulation of the proximal movement phase in order to aid in the description and detailed analysis of the event. This work is ongoing. A simple two-parameter calibration method is demonstrated.

7.9.2 Methodology

A DEM of the sliding surface at 50 m resolution was created using large-scale topographic maps. An outline of the Kolka Glacier source area was digitized from a detailed post-event geomorphic map (Figure 3b in Petrakov et al. 2004a). In accordance with the “standing start” scenario described above, a total bulked volume of 130 Mm^3 , representing Kolka Glacier and the antecedent accumulation of ice and rock fall debris on its surface, was assumed to start from rest within this area (a uniform vertical source thickness of approximately 85 m was used). This volume is within the range of total volume estimates presented by Drobyshev (2003a), Petrakov et al. (2004b) and Huggel et al. (2005). The estimated volumes of material entrained and deposited along the path were approximately equal and were small relative to the source volume; entrainment was therefore neglected.

A Voellmy resistance model (Equation [4-42]) with constant parameters was used for the following three reasons:

- 1) There was no evidence of a significant change in behaviour along the path (upstream of the Karmadon Gates) that would justify a user-imposed change in rheology or rheological parameters in the simulation.
- 2) The event initiated, travelled and deposited on very low slope angles, implying a persistently low frictional component of resistance. This behaviour can be simulated with the Voellmy model using a suitably low friction coefficient.
- 3) The turbulence component of the Voellmy model can be used to limit the simulated flow velocities, which (considering the above requirement for low frictional resistance) would otherwise be too high.

The Voellmy friction coefficient, f , and turbulence parameter, ξ , were systematically adjusted, as shown in the next section, to produce good simulations of the estimated velocities along the path, the estimated time of arrival of the flow front at the Karmadon Gates and the final distribution of deposits upstream (only a relatively small volume squeezed through the Gates to generate the distal debris flow). The internal friction angle was set to $\phi_i = 20^\circ$, considered appropriate for a mass composed predominantly of flowing ice, and the following control parameters were used: $N = 4000$, $B = 4$, $C = 0.01$ and $D = 200$.

7.9.3 Results and discussion

The results of a model run using $f = 0.05$ and $\xi = 1000 \text{ m/s}^2$ are shown in Figure 7.32. This combination of parameter values produced the best simulation of the estimated flow velocities along the Genaldon valley and the arrival time of the front at the Karmadon Gates (approximately 6 minutes). A 2D matrix (for various f and ξ) of maximum simulated velocity plots, which was used to help make this judgment, is shown in Figure 7.33. All of these model runs reproduced the sinuous motion of the ice/rock avalanche along the Genaldon valley and the main deposit that dammed the valley in the Karmadon depression. As such, the independent velocity estimates provided a crucial secondary constraint.

A comparison of estimated and simulated arrival times along the path is shown in Figure 7.34. A different reference starting point was used in each case, so the DAN3D results have been offset by + 45 s to filter out this discrepancy and facilitate comparison. The Drobyshev (2003b and 2005) curve is slightly steeper, reflecting slightly higher velocities. Similarly higher velocities were recorded by the model in the deeper part of the flow immediately behind the front. This is a characteristic of the Voellmy rheology; the turbulence term produces relatively higher resistance in shallower parts of the flow, including near the front. This depth-dependence results in surging behaviour, with the flow front constantly being overtaken and/or pushed forward by the deeper and faster trailing flow. When this behaviour is taken into account, the Drobyshev and DAN3D results are actually in good agreement.

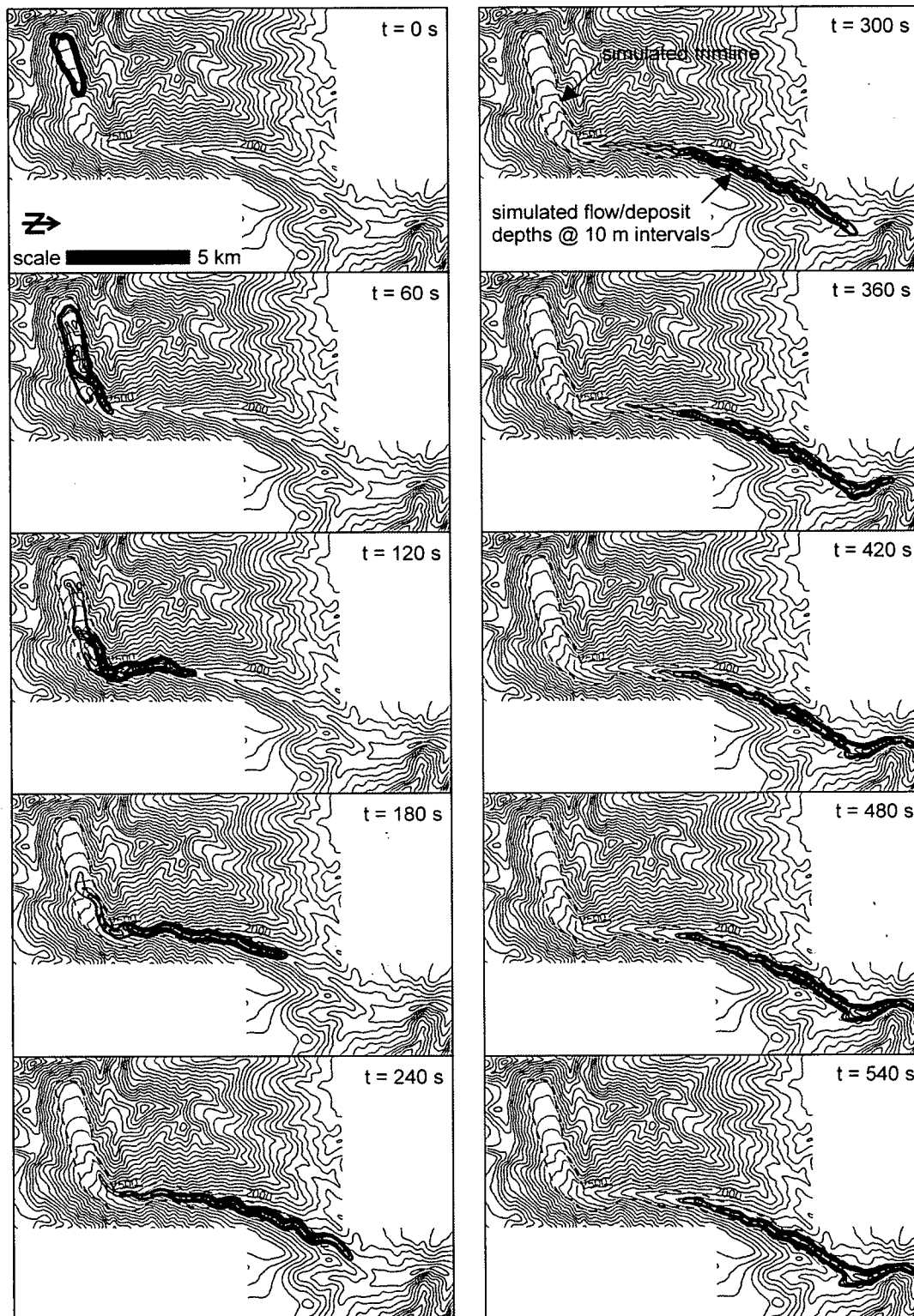


Figure 7.32. Calibrated simulation of the Kolka event at 60 s intervals. The flow/deposit depth contours are at 10 m intervals and the elevation contours are at 100 m intervals. The sinuous motion of the ice/rock avalanche along the Genaldon valley was reproduced.

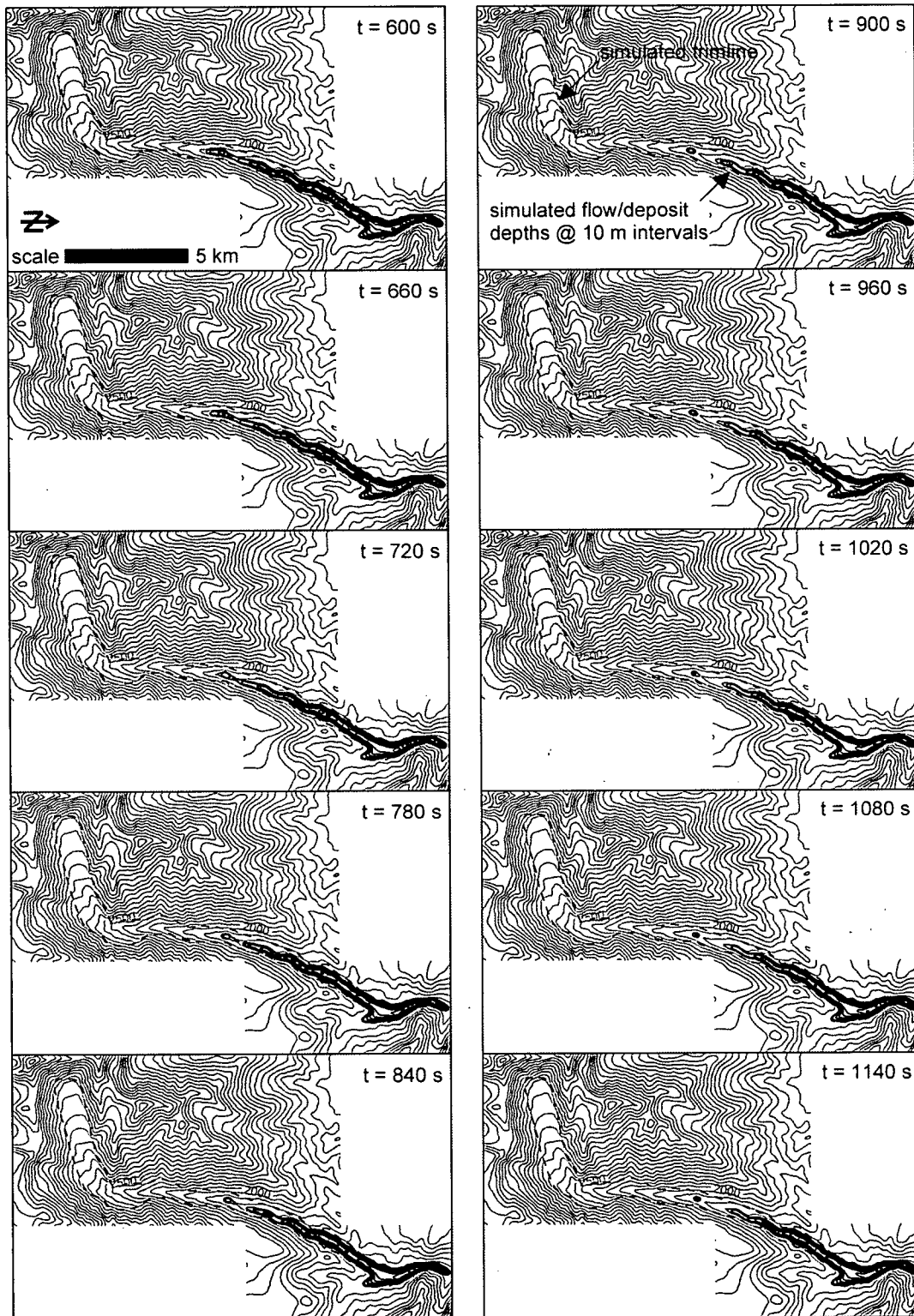


Figure 7.32 (continued). Calibrated simulation of the Kolka event at 60 s intervals. The flow/deposit depth contours are at 10 m intervals and the elevation contours are at 100 m intervals. The ice and debris dam in the Karmadon depression was reproduced.

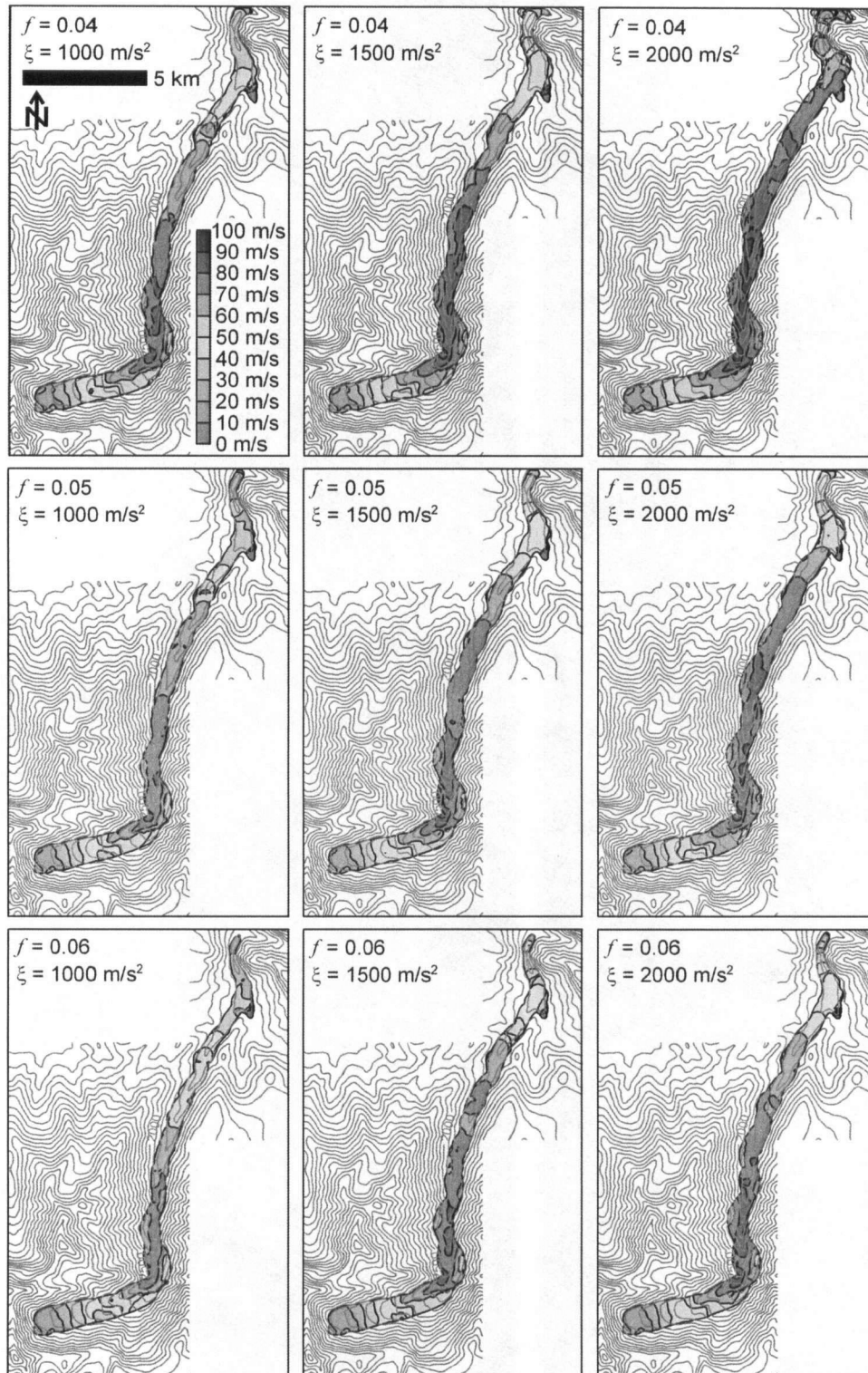


Figure 7.33. Matrix of maximum velocity plots for model runs with various combinations of f and ξ . The velocity contours are at 10 m/s intervals and the elevation contours are at 100 m intervals. The best simulation of the estimated velocities along the path was obtained using $f = 0.05$ and $\xi = 1000 \text{ m/s}^2$ (middle left).

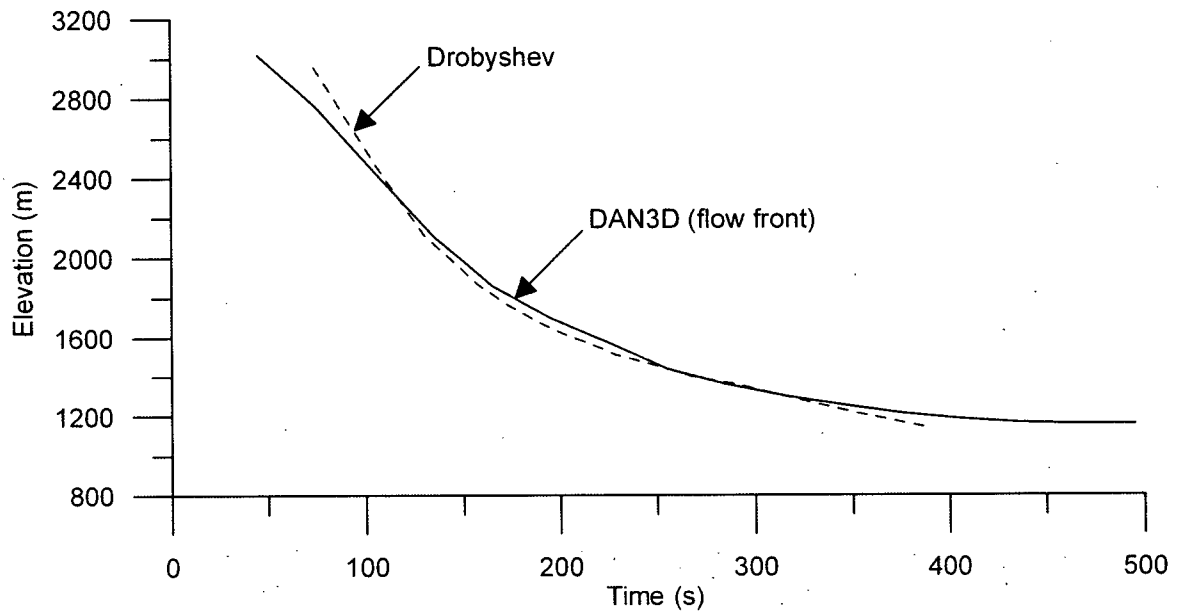


Figure 7.34. Comparison of arrival times along the path estimated by Drobyshev (2003b and 2005, based on estimated maximum velocities) and DAN3D using $f = 0.05$ and $\xi = 1000$ m/s² (based on simulated flow front arrival times). The DAN3D timing has been offset by + 45 s to facilitate comparison, as different reference starting points were used in each case.

A comparative analysis using the same pair of input parameters was performed to examine the triggering scenario postulated by Huggel et al. (2005). An initial downslope velocity of 25 m/s was imposed on the 130 Mm³ source to account for momentum transfer from a large ice or rock avalanche from Mt. Dzhimarai-khokh. This had only a minor influence on the results. The flow accelerated slightly faster but soon reached similar maximum velocities in the Genaldon channel. The mass arrived at the Karmadon Gates sooner but formed an almost identical deposit. Note that this result may simply reflect the character of the Voellmy rheology and does not necessarily discount the possibility of a triggering slope failure.

The Voellmy rheology is largely empirical, and so physical justification for parameter selection is often difficult. This case is no exception. The calibrated friction coefficient $f = 0.05$ is lower than the average slope gradient in the starting zone (approximately 0.1), which allowed the mass to accelerate rapidly from rest without the need to impose an initial velocity. At the same time, it is slightly higher than the average slope gradient in the Karmadon depression, which allowed the mass to deposit there. While justification for the

exact value of f used is still difficult, liquefaction of material at the base of the flow could account for such a low component of frictional resistance, and a continuous supply of water from ice melt during motion could explain its persistence. In contrast, the turbulence parameter is almost purely empirical, and can only be justified on the basis of estimated and simulated flow velocity comparisons.

The matrix method demonstrated in Figure 7.33 is an effective way to perform these types of comparisons when two independent parameters must be calibrated. Similar matrices can be constructed to compare simulated trimlines and deposit distributions. Efficiency can be gained by stepping through the matrix systematically, rather than running every possible combination of parameters. This approach has been used in other back-analyses and sensitivity analyses.

7.10 Other cases

A number of other cases have been analyzed for private consulting assignments and are detailed in various technical reports. A brief description of each case follows:

- 1) A calibration back-analysis of the 1946 Six des Eaux Froides rock avalanche in the Swiss Alps was performed. DAN (Hungr 1995) was used for preliminary calibration, with good correspondence to the subsequent DAN3D results. Various combinations of frictional and Voellmy rheologies were attempted (employing the matrix calibration method outlined in the previous section). The best simulation of the event, in terms of the observed extent of the impact area and distribution of deposits, was achieved using a constant Voellmy rheology with parameters $f = 0.13$ and $\xi = 450 \text{ m/s}^2$, close to Hungr and Evans' (1996) recommended values of $f = 0.1$ and $\xi = 500 \text{ m/s}^2$.
- 2) A back-analysis of a small rock avalanche near Preonzo, Switzerland in 2002 and a forward-analysis of a potential similar failure nearby were performed using input parameters derived from an independent DAN analysis. The results were used to

cross-check the DAN results and to help assess the risk to facilities and the effectiveness of protective measures located near the base of the slope. A frictional rheology was implemented and ϕ_b was varied between 30° and 35°. The results were very sensitive to the value of the bulk basal friction angle in a range close to the mean slope angle.

- 3) A calibration back-analysis of the 1915 Jane Camp landslide in British Columbia was performed and the results were used to guide a forward-analysis of a potential failure nearby. Similar to the preceding case, a parametric approach was adopted during the predictive phase. Various combinations of frictional and Voellmy rheologies were used with a range of parameter values, and a number of possible entrainment scenarios were examined.
- 4) A forward-analysis of a potential mine waste dump failure was performed to help assess the risk to expensive equipment located downslope. Different assumed source volumes and locations were analyzed. Simulated flow velocities and depths along a possible protective fence line were output for use in impact pressure and energy calculations.
- 5) A similar forward-analysis of a potential colluvium failure at another mine site was performed. In this case, a parametric approach was used to assess the sensitivity of the results to the assumed soil conditions. A subsequent analysis was performed to help assess the effectiveness of a berm in the distal path.
- 6) A calibration back-analysis of the January 2005 landslide in North Vancouver, British Columbia was performed and the results were used to guide a forward-analysis of a potential failure nearby. Forward-analyses using various assumed source volumes originating from within the 2005 scar were also analyzed to help assess the effectiveness of a berm/basin at the toe of the slope. The results were cross-checked using an established analytical method for predicting runup against adverse slopes

(e.g., Hungr et al. 1984). Hazard intensity maps of simulated flow velocities and depths were output for use in vulnerability estimation.

As an important step in model development and distribution, DAN3D has also been used by other workers, and their input has led to several improvements. Alex Strouth (University of British Columbia) used the model to back-analyze the 2003 Afternoon Creek rock avalanche in Washington State. Suzanne Chalindar (École Polytechnique Fédérale de Lausanne) used the model to back-analyze the Mystery Creek rock avalanche in British Columbia and the 1970 Huascarán debris avalanche in Peru, and continues to use it to analyze several cases in the Swiss Alps. Tyler Trudel (University of British Columbia) used the model to perform a detailed parametric analysis of the 1970 Huascarán event. Alexandra Campbell, Graham Janson and Heather Taylor (Queen's University, Kingston) used the model as part of an undergraduate design project to assess outburst flood risks at Ruapehu Volcano in New Zealand.

7.11 Discussion

The back-analyses presented in this chapter demonstrate the applicability of DAN3D at full-scale to a wide variety of landslide types. The results are summarized in Table 7.1. The importance of each of the features outlined in Chapter 2 has been demonstrated in context. In particular, the analysis of rock slide – debris avalanche type events (Hungr and Evans 2004a) requires the full suite of model capabilities.

In each case, the model has been calibrated in some way (either directly or by using DAN as a preliminary tool) to produce a satisfactory simulation of the real event, but it is important to note that this process is not arbitrary. In general, the frictional basal resistance model appears to produce good simulations of dry granular behaviour, while the Voellmy model produces good results when a significant amount of water is apparently involved. As such, the appropriateness of each model for a given case can usually be objectively determined. Although the associated input parameters are not considered real material properties, they are still (often tightly) constrained by the observed and/or estimated behaviour of the real event,

as defined by objective calibration criteria. At the same time, the parameters can often be related to both the initial and final limiting equilibrium conditions. There should never be a need to introduce any input that is not supported by field observations or in conflict with previous modelling experience.

Case Study	Landslide Type	N	B	C	D	ϕ_i (°)	Basal Rheology and Parameters		E_s (m ⁻¹)
							Before Entrainment	After Entrainment	
Frank	rock avalanche	2000	4	0	200	40	frictional $\phi_b = 14^\circ$	no change	0
Val Pola	rock avalanche	4000	6	0.01	200	35	frictional $\phi_b = 16^\circ$	no change	0
Cervinara	debris avalanche/ flow	2000	4	0	200	35	frictional $\phi_b = 30^\circ$	Voellmy $f = 0.07$ $\xi = 200 \text{ m/s}^2$	0.01
Quindici	debris avalanche/ flow	2000	4	0	200	35	frictional $\phi_b = 30^\circ$	Voellmy $f = 0.07$ $\xi = 200 \text{ m/s}^2$	0.01
Nomash River	rock slide – debris avalanche	2000	4	0	200	35	frictional $\phi_b = 30^\circ$	Voellmy $f = 0.05$ $\xi = 400 \text{ m/s}^2$	1.9×10^{-3}
Zymoetz River	rock slide – debris flow	4000	4	0.01	200	35	frictional $\phi_b = 31^\circ$	Voellmy $f = 0.1$ $\xi = 1000 \text{ m/s}^2$	3.3×10^{-4}
McAuley Creek	rock avalanche	4000	4	0.01	200	35	frictional $\phi_b = 30^\circ$	Voellmy $f = 0.1$ $\xi = 500 \text{ m/s}^2$	0
Kolka	ice/rock avalanche	4000	4	0.01	200	20	Voellmy $f = 0.05$ $\xi = 1000 \text{ m/s}^2$	no change	0

Table 7.1. Parameter values used in each case study. N is the number of particles, B is the particle smoothing coefficient, C is the velocity smoothing coefficient, D is the stiffness coefficient, ϕ_i is the internal friction angle, ϕ_b is the bulk basal friction angle (for frictional basal resistance), f is the basal friction coefficient (for Voellmy basal resistance), ξ is the turbulence parameter (for Voellmy basal resistance) and E_s is the entrainment growth rate within a specified entrainment zone.

For this reason, the repeatedly good correspondence between the DAN and DAN3D results is encouraging, and suggests that the already extensive database of DAN-calibrated cases will continue to be a useful reference. At the same time, significant efficiency can be gained by using the two models in a complementary manner.

Still, a high level of uncertainty remains when it comes to parameter selection, making accurate deterministic runout prediction difficult. As a result, a parametric approach to forward-analysis has been adopted. Quantifying this uncertainty is the next step, but the database will have to grow substantially before probabilistic parameter selection will be possible. More experience with the model by a larger community of users may accelerate this process and lead to the development of a standardized analysis methodology that may also help reduce subjectivity.

7.12 Conclusion

A variety of real landslides have been back-analyzed using DAN3D. The results have further validated the model and in turn provided insight that has aided in event description and analysis. They have also served to expand the existing database of calibrated cases. This experience has been translated into forward-analyses that have been used in practice to help assess landslide risks and provide guidance for the design of protective measures, within the established framework outlined in Chapter 1. A move towards probabilistic runout prediction is desirable but will require a considerable expansion of the database. As such, continued back-analysis of real case studies remains a priority.

8 CONCLUSIONS

8.1 Introduction

As described in Chapter 1, this thesis has been an effort to advance the state-of-the-art in dynamic modelling for the practical purposes of landslide risk assessment and the design of protective measures. To do so, specific objectives were defined and a new continuum dynamic model that satisfies these objectives, DAN3D, has been developed. The new model is based on a number of existing continuum dynamic models, most significantly DAN (Hungar 1995), but includes several innovations, incorporated into a unique system of governing equations and a unique numerical solution method, that make it substantially original. It has been validated using analytical and experimental methods and its applicability at full-scale has been demonstrated using back-analyses of real case studies. This work has been extended in practice to parametric forward-analyses of potential events.

The purpose of this final chapter is to summarize these innovations and the main results of this research to date. Recommendations are also presented to guide future work with the model by others.

8.2 Summary of work completed

Highlights of the work presented in Chapters 1 to 7 follow:

- 1) The need for effective methods of performing landslide runout analysis and the potential for continuum dynamic modelling to address this need were identified. Inherent limitations of the 2D model DAN, which has been used extensively, were also identified and a 3D extension of the model was therefore proposed.
- 2) The following five key objectives for model development were defined: a model intended for practical landslide runout analysis should be able to simulate motion across complex 3D terrain, simulate strain-dependent, non-hydrostatic, anisotropic

internal stresses, simulate mass and momentum transfer due to entrainment, simulate variations in rheology along the path and within the landslide and, at the same time, operate in an efficient manner.

- 3) A comprehensive review of existing continuum dynamic models in the context of these objectives was presented.
- 4) The depth-averaged governing equations of motion for an “equivalent fluid” (Hungar 1995) were formally derived. The resulting equations incorporate aspects of each of the five objectives for model development.
- 5) Smoothed Particle Hydrodynamics (SPH) was adapted for incompressible, depth-averaged flow across an irregular 3D surface. The method permits discretization of the governing equations within a Lagrangian framework and satisfies mass balance without the need for a computational mesh.
- 6) A strain interpolation method based on strain gauge rosette theory was developed. The method takes advantage of the particle-tracking nature of SPH and provides estimates of strain magnitude in addition to orientation. A simplified version of the original rigorous method is currently implemented in the model.
- 7) A corresponding stress redistribution method was developed, which increments the internal stresses in proportion to the estimated strain to account for finite material stiffness. The updated internal stresses are coupled to the basal shear stress (a generic function in the equivalent fluid framework) and limited by a frictional yield criterion, which permits non-hydrostatic, anisotropic stress states in accordance with classical Rankine earth pressure theory.
- 8) A simple entrainment algorithm based on the concept of natural exponential volume growth was developed. The rates of mass and momentum transfer are controlled by a user-specified growth rate and the availability of material is limited by a user-

specified, spatially-variable bed-depth. Both parameters can be constrained by actual field evidence. Rheology changes associated with entrainment can also be implemented.

- 9) An intensity parameter interpolation method was developed to eliminate the need for separate post-processing of particle-centred data. This feature provides output in the form of hazard intensity maps that can be used directly in risk studies to estimate vulnerability, design protection and characterize potential secondary effects.
- 10) Established analytical solutions of the 1D dam-break problem were used to test the accuracy of the basic numerical solution method, with satisfactory results.
- 11) A hypothetical experiment analogous to a 2D dam-break was used to evaluate the grid-dependency of the numerical solution method. The model did not introduce any grid-dependence beyond the grid-dependent initial particle distribution.
- 12) Additional hypothetical experiments were used to demonstrate the general behaviour of the model and evaluate its sensitivity to the various input parameters. Interim values for the input control parameters were recommended.
- 13) Controlled experiments were used to evaluate the ability of the model to produce accurate simulations of real granular flows. Satisfactory results were achieved with appropriate calibration of the input rheological parameters, although the calibrated values were very close to the measured material properties.
- 14) Additional controlled experiments involving deflected flow (performed at the University of British Columbia) were used to demonstrate the calibration-prediction methodology and the ability of the calibrated model to produce accurate first-order predictions, even when the geometry differs from that of the prototype.

- 15) A variety of full-scale landslide case studies were used to evaluate the full capabilities of the model and the importance of each of the five objectives for model development was demonstrated in context.
- 16) As in the case of the small-scale experiments, the calibrated model produced accurate simulations at full-scale and, in the process, proved to be a useful tool for event description and analysis. Various systematic and objective calibration methods were demonstrated. In general, independent observations and/or estimates of both the extent and velocity/duration of the real event are required to provide reasonable constraint. Both the initial and final limiting equilibrium conditions can provide further constraint.
- 17) In general, the frictional basal resistance model appears to be appropriate for simulating dry granular flows, while the Voellmy model appears to be more appropriate for simulating wet or saturated flows. The concept of modelling rock slide – debris avalanches/flows using a frictional proximal phase and a Voellmy distal phase (e.g., Hungr and Evans 2004a) was further demonstrated.
- 18) Good correspondence between DAN and DAN3D results was repeatedly observed, suggesting that DAN is a useful tool for efficient preliminary calibration of the new model and that the existing database of DAN-calibrated parameters is a useful reference.
- 19) Sensitivity to complex terrain was observed in several cases, highlighting the importance of accurate topographic input.
- 20) The seasonal influences of snow and associated meltwater on mobility were noted, which may be important to consider in risk studies.

8.3 Recommendations for future work

Although the model is considered fit for interim use and has already been applied in practice, several limitations have been identified and further research is warranted. A number of recommendations follow:

- 1) Limited spatial resolution is an issue, as shown in the dam-break and channelization cases in Chapter 6. Resolution is sacrificed near flow margins and there is a tendency for particles to align in the downstream direction in highly channelized reaches of a path. An increase in the number of particles the model can use and the introduction of a velocity smoothing method has improved the situation, but more work can still be done. Optimization of the code and coinciding advances in computational capacity may permit a further increase in the maximum number of particles, which would be the simplest way to increase resolution. Tests using a supercomputer with a parallelized version of the code may be beneficial. Implementation of a spatially-variable smoothing length (e.g., Wang and Shen 1999) is another option, which has only been investigated briefly to date. In the meantime, these limitations need to be taken into account when determining the appropriateness of the model in a given case and when interpreting the results.
- 2) The model is not explicitly shock-capturing. Velocity smoothing smoothes out strong shocks but does not replicate actual energy losses. Explicit shock-capturing capabilities may be a good addition to the model, or at least provide a way to investigate the influence of neglecting such energy losses.
- 3) Validation testing should continue as more analytical methods and experimental results become available.
- 4) Comprehensive parametric analyses should be performed to expand on the preliminary study presented in Chapter 6. In particular, the influence of internal stiffness, as controlled by the dimensionless stiffness coefficient, D , requires further

investigation. Carefully controlled laboratory experiments and/or well-described full-scale case studies would make good prototypes for this type of work, which Suzanne Chalindar and Tyler Trudel have already initiated. Eventually, appropriate values for the control input parameters should be built into the model, reducing the number of user-adjustable parameters.

- 5) A more thorough look at the influence of different smoothing kernels may be beneficial. For example, the cubic kernel is very similar to the default Gaussian kernel (cf., Chapter 5), but may increase computational efficiency and does not require a cutoff depth to be specified at the flow margins.
- 6) The rigorous strain interpolation method described in Chapter 5 can be implemented once more realistic/justifiable stress redistribution assumptions can be made.
- 7) In general, more research into actual entrainment mechanisms and processes is needed. For example, laboratory experiments could be designed to isolate the main controlling factors. Eventually, more complex entrainment relationships based on this type of work and additional field observations can be implemented in the model, with the current assumption of natural exponential volume growth serving as a baseline. The possible influence of self-channelization due to erosion on the spreading behaviour of real events could also be investigated.
- 8) The influence of rheology changes caused by surficial material in the path of large rock avalanches and their relationship to the plowing mechanism of entrainment could be investigated in more detail. For example, the Frank and Val Pola analyses presented in Chapter 7, which used constant rheology assumptions, could be revisited. The Hope and Cheam rock avalanches near Vancouver, British Columbia are other potential case studies that exhibited this behaviour (e.g., Orwin et al. 2004).
- 9) The influence of flow heterogeneity requires more research. Rheology variations within the landslide can be implemented in DAN3D, but to date this feature has only

- been used to a limited extent. The original SPH method can also handle spatial density variations, and this capability could be useful for investigating the effects of density variations caused by entrainment, dilation, comminution, fragmentation and general pore pressure and material property differences.
- 10) A method that accounts explicitly for airborne/freefall conditions and the associated momentum and energy changes on impact could be implemented.
 - 11) A method that accounts for the initial cohesion of a landslide mass (e.g., prior to significant fragmentation of a rock slide) could be implemented. A progressively-decreasing velocity smoothing coefficient, C , could be used for this purpose, although a progressively-decreasing internal cohesion (additional to the assumed internal friction) may be a more elegant method.
 - 12) A commercial Windows-based version of the model is currently at an advanced stage of development (by others), but will require considerable debugging and testing before it can be distributed. In the meantime, distribution of the original DOS-based version should continue, in order to expand the community of users.
 - 13) The back-analyses presented in Chapter 7 form the basis for a collection of DAN3D-calibrated cases, but significantly more work is required. Continued back-analysis of real events in parallel with the other recommendations on this list is essential.
 - 14) A probabilistic approach to input parameter selection should be investigated once the database of calibrated parameters has reached a sufficiently large size. In the meantime, a parametric approach to forward-analysis is recommended.
 - 15) The application of DAN3D to the analysis of snow avalanche motion could be investigated.

8.4 Discussion

Clearly, many more improvements can be made, but it is important to avoid getting mired in the process. With ongoing development in mountainous areas, the need for practical landslide risk assessment tools is immediate, and perpetual testing of continuum dynamic models does not serve this need very well. At the same time, it must be acknowledged that landslides are extremely complex phenomena, and computer models cannot be expected to account for all of this complexity. In the end, all models, no matter how complex, are subject to errors and uncertainty. Arguably, more headway can be gained by trying to quantify this uncertainty than by trying to perfect the governing equations or numerical solution methods.

In keeping with the approach formalized by Hungr (1995), this thesis has been influenced to a large extent by two key concepts: 1) the idea that continuum dynamic models should be able to account for the most important characteristics of real landslides, while remaining as simple as possible; and 2) the idea that full-scale application is an essential component of the development process. Although there is significant room for improvement, which will inevitably result in increased complexity, I hope that future work with the model will remain faithful to this basic approach.

8.5 Conclusion

The continuum dynamic model proposed in this thesis satisfies the overall objective of this work. A 3D extension of the existing 2D model DAN has been developed for the purposes of practical landslide runout analysis. The new model addresses the inherent limitations of the original model but retains all of its key features, which are essential for the simulation of real landslides. In the process, several innovations have been made. The model is based on a new system of governing equations, which are discretized and solved using a new and efficient numerical method. It has been validated at both laboratory and field-scale and its utility has been demonstrated in practice. With continued work, including ongoing back-analysis of real landslide case studies, the new model has the potential for true predictive capability.

REFERENCES

- Abele, G. 1997. Rockslide movement supported by the mobilization of groundwater-saturated valley floor sediments. *Zeitschrift fur Geomorphologie*, 41: 1-20.
- Amsden, A.A. and Harlow, F.H. 1970. The SMAC method: a numerical technique for calculating incompressible fluid flows. Los Alamos National Laboratory Report LA-4370.
- Ayotte, D. and Hungr, O. 2000. Calibration of a runout prediction model for debris-flows and avalanches. *In Proceedings of the Second International Conference on Debris-Flow Hazards Mitigation, Taipei. Edited by G.F. Wieczorek and N.D. Naeser. A.A. Balkema, Rotterdam. pp. 505-514.*
- Bagnold, R.A. 1954. Experiments on a gravity-free dispersion of large solid spheres in a Newtonian fluid under shear. *Proceedings of the Royal Society of London, A*, 225: 49-63.
- Benz, W. 1990. Smooth particle hydrodynamics: a review. *In The numerical modelling of nonlinear stellar pulsations. Edited by J.R. Buchler. Kluwer Academic, Dordrecht. pp. 269-288.*
- BGC Engineering Inc. 2000. Geotechnical Hazard Assessment – South Flank of Frank Slide, Hillcrest, Alberta. Report to Alberta Environment.
- Boultbee, N. 2005. Characterization of the Zymoetz River Rock Avalanche. M.Sc. Thesis, Simon Fraser University, Vancouver.
- Boultbee, N., Stead, D., Schwab, J., Geertsema, M. 2006. The Zymoetz River rock avalanche, June 2002, British Columbia, Canada. *Engineering Geology*, 83(1): 76-93.
- Brufau, P., Garcia-Navarro, P., Ghilardi, P., Natale, L. and Savi, F. 2000. 1D mathematical modelling of debris flow. *Journal of Hydraulic Research*, 38(6): 435-446.
- Bursik, M., Martínez-Hackert, B., Delgado, H. and Gonzalez-Huesca, A. 2003. A smoothed-particle hydrodynamic automaton of landform degradation by overland flow. *Geomorphology*, 53: 25-44.
- Buss, E. and Heim, A. 1881. *Der Bergsturz von Elm. Worster, Zurich. (in German)*
- Calvetti, F., Crosta, G. and Tartarella, M. 2000. Numerical simulation of dry granular flows: from the reproduction of small-scale experiments to the prediction of rock avalanches. *Rivista Italiana di Geotecnico*, 34(2): 21-38.
- Canada Department of Mines. 1917. Frank, Alberta, Map 57A. Canada Department of Mines, Ottawa.

- Cannon, S.H. 1993. An empirical model for the volume-change behavior of debris flows. *In Proceedings of Hydraulic Engineering '93, San Francisco. Edited by H.W. Shen, S.T. Su and F. Wen. American Society of Civil Engineers, New York, Vol. 2, pp. 1768-1773.*
- Cannon, S.H. and Savage, W.Z. 1988. A mass-change model for the estimation of debris-flow runout. *Journal of Geology, 96: 221-227.*
- Cannon, S.H. and Savage, W.Z. 1990. A mass-change model for the estimation of debris-flow runout: a discussion. *Journal of Geology, 99: 792-794.*
- Carson, M.A. and Kirkby, M.J. 1972. *Hillslope form and process. Cambridge University Press, London.*
- Chen, H. and Lee, C.F. 2000. Numerical simulation of debris flows. *Canadian Geotechnical Journal, 37: 146-160.*
- Chen, H. and Lee, C.F. 2002. Runout analysis of slurry flows with Bingham model. *Journal of Geotechnical and Geoenvironmental Engineering, December, pp. 1032-1042.*
- Chen, H. and Lee, C.F. 2003. A dynamic model for rainfall-induced landslides on natural slopes. *Geomorphology, 51: 269-288.*
- Chiou, M.C., Wang, Y. and Hutter, K. 2005. Influence of obstacles on rapid granular flows. *Acta Mechanica, 175: 105-122.*
- Chow, V.T. 1959. *Open-channel Hydraulics. McGraw-Hill, New York. 680 pp.*
- Chu, T., Hill, G., McClung, D.M., Ngun, R. and Sherkat, R. 1995. Experiments on granular flows to predict avalanche runup. *Canadian Geotechnical Journal, 32: 285-295.*
- Cleary, P.W. and Prakash, M. 2004. Discrete-element modelling and smoothed particle hydrodynamics: potential in the environmental sciences. *Philosophical Transactions of the Royal Society of London, A, 362: 2003-2030.*
- Corominas, J. 1996. The angle of reach as a obility index for small and large landslides. *Canadian Geotechnical Journal, 33: 260-271.*
- Costa, J.E. 1991. Nature, mechanics, and mitigation of the Val Pola Landslide, Valtellina, Italy, 1987-1988. *Zeitschrift fur Geomorphologie, 35(1): 15-38.*
- Coussot, P. 1994. Steady, laminar flow of concentrated mud suspensions in open channel. *Journal of Hydraulic Research, 32(4): 535-559.*
- Crosta, G.B., Chen, H. and Lee, C.F. 2004. Replay of the 1987 Val Pola Landslide, Italian Alps. *Geomorphology, 60(11): 127-146.*

Cruden, D.M. 1976. Major rock slides in the Rockies. *Canadian Geotechnical Journal*, 13: 8-20.

Cruden, D.M. and Krahn, J. 1973. A re-examination of the geology of the Frank Slide. *Canadian Geotechnical Journal*, 10: 581-591.

Cruden, D.M. and Hungr, O. 1986. The debris of the Frank Slide and theories of rockslide-avalanche mobility. *Canadian Journal of Earth Sciences*, 23: 425-432.

Cruden, D.M. and Varnes, D.J. 1996. Landslide types and processes. *In* Landslides: investigation and mitigation, Transportation Research Board Special Report 247, United States National Research Council. *Edited by* A.K. Turner and R.L. Schuster. National Academy Press. pp. 36-75.

Cundall, P.A. and Strack, O.D.L. 1979. A discrete numerical method for granular assemblies. *Geotechnique*, 29(1): 47-65.

Davies, T.R. 1982. Spreading of rockslide debris by mechanical fluidization. *Rock Mechanics*, 15: 9-24.

Davies, T.R., McSaveney, M.J. and Hodgson, K.A. 1999. A fragmentation-spreading model for long-runout rock avalanches. *Canadian Geotechnical Journal*, 36: 1096-1110.

Davies, T.R. and McSaveney, M.J. 2002. Dynamic simulation of the motion of fragmenting rock avalanches. *Canadian Geotechnical Journal*, 39: 789-798.

Denlinger, R.P. and Iverson, R.M. 2001. Flow of variably fluidized granular masses across three-dimensional terrain, 2. Numerical predictions and experimental tests. *Journal of Geophysical Research*, 106(B1): 553-566.

Denlinger, R.P. and Iverson, R.M. 2004. Granular avalanches across irregular three-dimensional terrain: 1. Theory and computation. *Journal of Geophysical Research*, 109: F01014.

Dent, J.D. and Lang, T.E. 1980. Modeling of snow flow. *Journal of Glaciology*, 26(94): 131-140.

Dent, J.D. and Lang, T.E. 1983. A biviscous modified Bingham model of snow avalanche motion. *Annals of Glaciology*, 4: 42-46.

Drobyshev, V.N. 2003a. Glacial disaster in North Ossetia on 20 September 2002. Vladikavkaz, unpublished manuscript. (in Russian)

Drobyshev, V.N. 2003b. Estimation of the velocity for the ice collapse movement along the Genaldon gorge. Vladikavkaz, unpublished manuscript. (in Russian)

Drobyshev, V.N. 2005. Analysis and interpretation of the process of Kolka glacier collapse in the Genaldon gorge on 20 September 2002 on the basis of records from Tsey and Fiagdon seismic stations. Vladikavkaz, unpublished manuscript. (in Russian)

Egashira, S. and Ashida, K. 1997. Sediment transport in steep slope flumes. *In Proceedings of the Roc Japan Joint Seminar on Water Resources.*

Egashira, S., Honda, N. and Itoh, T. 2001. Experimental study on the entrainment of bed material into debris flow. *Physics and Chemistry of the Earth (C)*, 26(9): 645-650.

Erismann, T.H. and Abele, G. 2001. *Dynamics of Rockslides and Rockfalls.* Springer-Verlag, Berlin.

Erlichson, H. 1991. A mass-change model for the estimation of debris-flow runout: a second discussion: conditions for the application of the rocket equation. *Journal of Geology*, 99: 633-634.

Evans, M.W. and Harlow, F.H. 1957. The Particle-in-Cell method for hydrodynamic calculations. Los Alamos National Laboratory Report LA-2139. 76 pp.

Evans, S.G. 2001. Landslides. *In A synthesis of geological hazards in Canada. Edited by G.R. Brooks.* Geological Survey of Canada, Bulletin 548, pp. 43-79.

Evans, S.G., Hungr, O. and Clague, J.J. 2001. Dynamics of the 1984 rock avalanche and associated distal debris flow on Mount Cayley, British Columbia, Canada; implications for landslide hazard assessment on dissected volcanoes. *Engineering Geology*, 61: 29-51.

Evans, S.G., Couture, R., Turner, K. and Fuller, T. 2003. The 2002 rock avalanche at McAuley Creek, near Vernon, British Columbia; implications for regional landslide hazard assessment. *In Proceedings of the 3rd Canadian Conference on Geotechnique and Natural Hazards*, Edmonton. p. 299.

Fannin, R.J. and Wise, M.P. 2001. An empirical-statistical model for debris flow travel distance. *Canadian Geotechnical Journal*, 38: 982-994.

Fell, R., Ho, K.K.S., Lacasse, S. and Leroi, E. 2005. A framework for landslide risk assessment and management. *In Proceedings of the International Conference on Landslide Risk Management*, Vancouver. *Edited by O. Hungr, R. Fell, R. Couture and E. Eberhardt.* A.A. Balkema, London. pp. 3-25.

García, R., López, J.L., Noya, M., Bello, M.E., Bello, M.T., González, N., Paredes, G., Vivas, M.I. and O'Brien, J.S. 2003. Hazard mapping for debris-flow events in the alluvial fans of northern Venezuela. *In Proceedings of the 3rd International Conference on Debris-flow Hazards Mitigation: Mechanics, Prediction and Assessment*, Davos. *Edited by D. Rickenmann and C.L. Chen.* Millpress, Rotterdam. pp. 589-599.

Gauer, P. and Issler, D. 2004. Possible erosion mechanisms in snow avalanches. *Annals of Glaciology*, 38: 384-392.

Ghilardi, P., Natale, L. and Savi, F. 2001. Modeling of debris flow propagation and deposition. *Physics and Chemistry of the Earth*, 26(9): 651-656.

Gingold, R.A. and Monaghan, J.J. 1977. Smoothed Particle Hydrodynamics: theory and application to non-spherical stars. *Monthly Notices of the Royal Astronomical Society*, 181: 375-389.

González, E., Herreros, M.I., Pastor, M., Quecedo, M. and Fernández Merodo, J.A. 2003. Discrete and continuum approaches for fast landslide modelling. *In Proceedings of the 1st International PFC Symposium, Gelsenkirchen. Edited by H. Konietzky. Swets and Zeitlinger, Lisse. pp. 307-313.*

Govi, M. 1989. The 1987 Landslide on Mount Zandila in the Valtellina, Northern Italy. *Landslide News*, 3: 1-3.

Gray, J.M.N.T. and Tai, Y.C. 1998. On the inclusion of a velocity-dependent basal drag in avalanche models. *Annals of Glaciology*, 26: 277-280.

Gray, J.M.N.T., Wieland, M. and Hutter, K. 1999. Gravity-driven free surface flow of granular avalanches over complex basal topography. *Proceedings of the Royal Society of London, A*, 455: 1841-1874.

Gray, J.M.N.T., Tai, Y.C. and Noelle, S. 2003. Shock waves, dead zones and particle-free regions in rapid granular free-surface flows. *Journal of Fluid Mechanics*, 491: 161-181.

Greve, R. and Hutter, K. 1993. Motion of a granular avalanche in a convex and concave curved chute: experiments and theoretical predictions. *Philosophical Transactions of the Royal Society of London, Physical Sciences and Engineering*, 342(1666): 573-600.

Greve, R., Koch, T. and Hutter, K. 1994. Unconfined flow of granular avalanches along a partly curved surface, Part 1: Theory. *Proceedings of the Royal Society of London, A*, 445: 399-413.

Guthrie, R.H., Evans, S.G. and Hungr, O. 2003. A rock slide – debris avalanche of May 1999, Nomash River, Vancouver Island. *In Proceedings of the 3rd Canadian Conference on Geotechnique and Natural Hazards, Edmonton. p. 289.*

Harlow, F.H. 1957. Hydrodynamic problems involving large fluid distortions. *Journal of the Association for Computing Machinery*, 4(2): 137-142.

Harlow, F.H. and Welch, J.E. 1965. Numerical calculation of time-dependent viscous incompressible flow of fluid with free surface. *Physics of Fluids*, 8(12): 2182-2189.

Heim, A. 1932. *Bergsturz und Menschenleben (Landslides and Human Lives)*. Translated by N. Skermer. Bitech Press, Vancouver, 1989.

Heinrich, Ph., Boudon, G., Komorowski, J.C., Sparks, R.S.J., Herd, R. and Voight, B. 2001. Numerical simulation of the December 1997 debris avalanche in Montserrat, Lesser Antilles. *Geophysical Research Letters*, 28(13): 2529-2532.

Hsu, K.J. 1975. Catastrophic debris streams (sturzstroms) generated by rockfalls. *Geological Society of America Bulletin*, 86: 129-140.

Huber, A. 1980. Schwallwellen in Seen als Folge von Felsstürzen. Mitteilung No. 47 der Versuchsanstalt für Wasserbau, Hydrologie und Glaziologie an der ETH Zurich. pp. 1-122. (in German)

Hübl, J. and Steinwendtner, H. 2001. Two-dimensional simulation of two viscous debris flows in Austria. *Physics and Chemistry of the Earth*, 26(9): 639-644.

Huggel, C., Zraggen-Oswald, S., Haerberli, W., Kääh, A., Polkvoj, A., Galushkin, I. and Evans, S.G. 2005. The 2002 rock/ice avalanche at Kolka/Karmadon, Russian Caucasus: assessment of extraordinary avalanche formation and mobility, and application of QuickBird satellite imagery. *Natural Hazards and Earth System Sciences*, 5: 173-187.

Hungr, O. 1981. Dynamics of rock avalanches and other types of slope movements. Ph.D. thesis, The University of Alberta, 506 pp.

Hungr, O. 1990. A mass-change model for the estimation of debris-flow runout: a reply. *Journal of Geology*, 98: 791-792.

Hungr, O. 1995. A model for the runout analysis of rapid flow slides, debris flows, and avalanches. *Canadian Geotechnical Journal*, 32: 610-623.

Hungr, O. 1997. Some methods of landslide hazard intensity mapping. *In Proceedings of the Landslide Risk Workshop, Honolulu*. Edited by D.M. Cruden and R. Fell. A.A. Balkema, Rotterdam. pp. 215-226.

Hungr, O., Sun, H.W. and Ho, K.K.S. 1998. Mobility of selected landslides in Hong Kong - Pilot back-analysis using a numerical model. Report of the Geotechnical Engineering Office, Hong Kong SAR Government.

Hungr, O. 2000. Analysis of debris flow surges using the theory of uniformly progressive flow. *Earth Surface Processes and Landforms*, 25: 1-13.

Hungr, O. 2002. Analytical models for slides and flows. *In Proceedings of the UNESCO/IGCP International Symposium on Landslide Mitigation and Protection of Cultural and Natural Heritage, Kyoto*. Edited by K. Sassa. Disaster Prevention Research Institute, Kyoto University. pp. 559-586.

Hungr, O. 2004. Landslide hazards in BC: achieving balance in risk assessment. *Innovation, Journal of the Association of Professional Engineers and Geoscientists of BC*, 8(3): 12-15.

Hungr, O., Morgan, G.C. and Kellerhals, R. 1984. Quantitative analysis of debris torrent hazards for design of remedial measures. *Canadian Geotechnical Journal*, 21: 663-677.

Hungr, O. and McClung, D.M. 1987. An equation for calculating snow avalanche run-up against barriers. *In Proceedings of the Symposium on Avalanche Formation, Movement and Effects, Davos. International Association of Hydrological Sciences, Publication 162*, pp. 605-612.

Hungr, O. and Evans, S.G. 1996. Rock avalanche runout prediction using a dynamic model. *In Proceedings of the 7th International Symposium on Landslides, Trondheim. Edited by K. Senneset. A.A. Balkema, Rotterdam*. pp. 233-238.

Hungr, O., Evans, S.G., Bovis, M. and Hutchinson, J.N. 2001. A review of the classification of landslides of the flow type. *Environmental and Engineering Geoscience*, 7(3): 1-18.

Hungr, O., Dawson, R., Kent, A., Campbell, D. and Morgenstern, N.R. 2002. Rapid flow slides of coal mine waste in British Columbia, Canada. *In Catastrophic landslides: effects, occurrence and mechanisms. Edited by S.G. Evans and J.V. DeGraff. Geological Society of America, Reviews in Engineering Geology 15*. pp. 191-208.

Hungr, O. and Evans, S.G. 2004a. Entrainment of debris in rock avalanches; an analysis of a long run-out mechanism. *Geological Society of America Bulletin*, 116(9/10): 1240-1252.

Hungr, O. and Evans, S.G. 2004b. The occurrence and classification of massive rock slope failure. *Felsbau, Rock and Soil Engineering, Journal for Engineering Geology, Geomechanics and Tunnelling*, 2: 16-23.

Hürlimann, M., Corominas, J., Moya, J. and Copons, R. 2003. Debris-flow events in the eastern Pyrenees: preliminary study on initiation and propagation. *In Proceedings of the 3rd International Conference on Debris-flow Hazards Mitigation: Mechanics, Prediction and Assessment, Davos. Edited by D. Rickenmann and C.L. Chen. Millpress, Rotterdam*. pp. 115-126.

Hutchinson, J.N. and Bhandari, R.K. 1971. Undrained loading, a fundamental mechanism of mudflow and other mass movements. *Géotechnique*, 21: 353-358.

Hutter, K. and Savage, S.B. 1988. Avalanche dynamics: The motion of a finite mass of gravel down a mountain side. *In Proceedings of the 5th International Symposium on Landslides, Lausanne. Edited by C. Bonnard. A.A. Balkema, Rotterdam*. pp. 691-697.

Hutter, K. and Koch, T. 1991. Motion of a granular avalanche in an exponentially curved chute: experiments and theoretical predictions. *Philosophical Transactions of the Royal Society of London A*, 334: 93-138.

- Hutter, K., Siegel, M., Savage, S.B. and Nohguchi, Y. 1993. Two-dimensional spreading of a granular avalanche down an inclined plane, Part 1: Theory. *Acta Mechanica*, 100: 37-68.
- Iverson, R.M. 1997. The physics of debris flows. *Reviews of Geophysics*, 35(3): 245-296.
- Iverson, R.M. 2003. How should mathematical models of geomorphic processes be judged? *In Prediction in Geomorphology, Geophysical Monograph Series, Vol. 135. Edited by P.R. Wilcock and R.M. Iverson. American Geophysical Union, Washington. pp. 83-94.*
- Iverson, R.M., Schilling, S.P. and Vallance, J.W. 1998. Objective delineation of lahar inundation zones. *Geological Society of America Bulletin*, 110: 972-984.
- Iverson, R.M. and Denlinger, R.P. 2001. Flow of variably fluidized granular masses across three-dimensional terrain, 1. Coulomb mixture theory. *Journal of Geophysical Research*, 106(B1): 537-552.
- Iverson, R.M., Logan, M. and Denlinger, R.P. 2004. Granular avalanches across irregular three-dimensional terrain: 2. Experimental tests. *Journal of Geophysical Research*, 109: F01015.
- Jaboyedoff, M., Couture, R. and Locat, P. 2004. Structural analysis of Turtle Mountain (Alberta) using digital elevation model (DEM). *In Proceedings of the 57th Canadian Geotechnical Conference, Québec City. Section 1C, pp. 7-13.*
- Jakob, M. 2005. Debris-flow hazard analysis. *In Debris-flow Hazards and Related Phenomena. Edited by M. Jakob and O. Hungr. Praxis-Springer Publishers, Heidelberg. pp. 411-443.*
- Jakob, M., Anderson, D., Fuller, T., Hungr, O. and Ayotte, D. 2000. An unusually large debris flow at Hummingbird Creek, Mara Lake, British Columbia. *Canadian Geotechnical Journal*, 37: 1109-1125.
- Jaky, J. 1944. The coefficient of earth pressure at rest. *Journal of the Society of Hungarian Architects and Engineers*, October, pp. 355-358.
- Jeyapalan, J.K. 1981. Analyses of flow failures of mine tailings impoundments. Ph.D. thesis, University of California, Berkeley.
- Jeyapalan, J.K., Duncan, J.M. and Seed, H.B. 1983a. Analyses of flow failures of mine tailings dams. *Journal of Geotechnical Engineering*, 109(2): 150-171.
- Jeyapalan, J.K., Duncan, J.M. and Seed, H.B. 1983b. Investigation of flow failures of tailings dams. *Journal of Geotechnical Engineering*, 109(2): 172-189.
- Johnson, A.M. 1970. *Physical Processes in Geology*. Freeman, Cooper and Company, San Francisco. 577 pp.

Johnson, N.L. 1996. The legacy and future of CFD at Los Alamos. *In* Proceedings of the 1996 Canadian CFD Conference, Ottawa.

King, J. 1996. Tsing Shan debris flow. Geotechnical Engineering Office, Hong Kong Government, Special Project Report SPR 6/96. Kowloon, Hong Kong. 100 pp.

Kobayashi, Y. and Kagawa, T. 1987. The prediction of hazards from debris avalanches and rockfalls with the aid of computer simulations. *In* Proceedings of the International Symposium on Engineering Geological Environment in Mountainous Areas, Beijing, Vol. 1, pp. 567-572.

Koch, T., Greve, R. and Hutter, K. 1994. Unconfined flow of granular avalanches along a partly curved surface, Part 2: Experiments and numerical computations. *Proceedings of the Royal Society of London, A*, 445: 415-435.

Körner, H.J. 1976. Reichweite und Geschwindigkeit von Bergstürzen und Fließschneelawinen. *Rock Mechanics*, 8: 225-256.

Laigle, D. and Coussot, P. 1997. Numerical modeling of mudflows. *Journal of Hydraulic Engineering*, 123(7): 617-623.

Lang, T.E., Dawson, K.L. and Martinelli Jr., M. 1979. Application of numerical transient fluid dynamics to snow avalanche flow, Part 1: Development of computer program AVALNCH. *Journal of Glaciology*, 22(86): 107-115.

Lang, T.E. and Martinelli Jr., M. 1979. Application of numerical transient fluid dynamics to snow avalanche flow, Part 2: Avalanche modeling and parameter error evaluation. *Journal of Glaciology*, 22(86): 117-126.

Li, J. and Yuan, J. 1983. The main features of the mudflow in Jiang-Jia Ravine. *Zeitschrift für Geomorphologie*, 27: 325-341.

Li, T. 1983. A mathematical model for predicting the extent of a major rockfall. *Zeitschrift für Geomorphologie*, 27: 473-482.

Lied, K. and Bakkehoi, S. 1980. Empirical calculations of snow-avalanche runout distance based on topographic parameters. *Journal of Glaciology*, 26(94): 165-177.

Liu, K.F. and Mei, C.C. 1989. Slow spreading of a sheet of Bingham fluid on an inclined plane. *Journal of Fluid Mechanics*, 207: 505-529.

Lucy, L.B. 1977. A numerical approach to the testing of the fission hypothesis. *Astrophysical Journal*, 82(12): 1013-1024.

- MacArthur, R.C. and Schamber, D.R. 1986. Numerical methods for simulating mudflows. In Proceedings of the 3rd International Symposium on River Sedimentation, Mississippi. pp. 1615-1623.
- Major, J.J. and Iverson, R.M. 1999. Debris-flow deposition: Effects of pore-fluid pressure and friction concentrated at flow margins. Geological Society of America Bulletin, 111:1424-1434.
- Mangeny, A., Heirich, P. and Roche, R. 2000. Analytical solution for testing debris avalanche numerical models. Pure and Applied Geophysics, 157: 1081-1096.
- Mangeny-Castelnau, A., Vilotte, J.P., Bristeau, O., Perthame, B., Bouchut, F., Simeoni, C. and Yerneni, S. 2003. Numerical modeling of avalanches based on Saint Venant equations using a kinetic scheme. Journal of Geophysical Research, 108(B11): 2527.
- McClung, D.M. 2000. Extreme avalanche runout in space and time. Canadian Geotechnical Journal, 37: 161-170.
- McClung, D.M. 2001. Superelevation of flowing avalanches around curved channel bends. Journal of Geophysical Research, 106(B8): 16,489-16,498.
- McClung, D.M. and Mears, A.I. 1991. Extreme value prediction of snow avalanche runout. Cold Regions Science and Technology, 19: 163-175.
- McClung, D.M. and Mears, A.I. 1995. Dry-flowing avalanche run-up and runout. Journal of Glaciology, 41: 359-372.
- McConnell, R.G. and Brock, R.W. 1904. Report on the great landslide at Frank, Alberta, 1903. In Part VIII, Annual Report 1903, Department of the Interior, Dominion of Canada.
- McEwen, A.S. and Malin, M.C. 1989. Dynamics of Mount St. Helens' 1980 pyroclastic flows, rockslide-avalanche, lahars, and blast. Journal of Volcanology and Geothermal Research, 37: 205-231.
- McLellan, P.J. and Kaiser, P.K. 1984. Application of a two-parameter model to rock avalanches of the Mackenzie Mountains. In Proceedings of the 4th International Symposium on Landslides, Toronto. Vol. 1, pp. 135-140.
- Mears, A.I. 1981. Design criteria for avalanche control structures in the runout zone. United States Department of Agriculture, Forest Service, Rocky Mountain Forest and Range Experimental Station, General Technical Report RM-84, 28 pp.
- Monaghan, J.J. 1989. On the problem of penetration in particle methods. Journal of Computational Physics, 82: 1-15.

Monaghan, J.J. 1992. Smoothed Particle Hydrodynamics. *Annual Reviews in Astronomy and Astrophysics*, 30: 543-574.

Morgenstern, N.R. and Sangrey 1978. Methods of slope stability analysis. *In Landslides, Analysis and Control. Transportation Research Board Special Report 176, United States National Academy of Sciences. Edited by R.J. Schuster and R.J. Krizek. National Academy Press. pp. 155-171.*

Naaïm, M., Faug, T. and Naaïm-Bouvet, F. 2003. Dry granular flow modelling including erosion and deposition. *Surveys in Geophysics*, 24: 569-585.

Nagasawa, M. and Kuwahara, K. 1993. Smoothed particle simulations of the pyroclastic flow. *International Journal of Modern Physics, B*, 7(9/10): 1979-1995.

Nicoletti, P.G. and Sorriso-Valvo, M. 1991. Geomorphic controls of the shape and mobility of rock avalanches. *Geological Society of America Bulletin*, 103: 1365-1373.

O'Brien, J.S. 2003. Reasonable assumptions in routing a dam break mudflow. *In Proceedings of the 3rd International Conference on Debris-flow Hazards Mitigation: Mechanics, Prediction and Assessment, Davos. Edited by D. Rickenmann and C.L. Chen. Millpress, Rotterdam. pp. 683-693.*

O'Brien, J.S., Julien, P.Y. and Fullerton, W.T. 1993. Two-dimensional water flood and mudflow simulation. *Journal of Hydraulic Engineering*, 119(2): 244-261.

Orwin, J.F., Clague, J.J. and Gerath, R.F. 2004. The Cheam rock avalanche, Fraser Valley, British Columbia, Canada. *Landslides*, 1: 289-298.

Pariseau, W.G. 1980. A simple mechanical model for rockslides and avalanches. *Engineering Geology*, 16: 111-123.

Patra, A.K., Bauer, A.C., Nichita, C.C., Pitman, E.B., Sheridan, M.F., Bursik, M., Rupp, B., Webber, A., Stinton, A.J., Namikawa, L.M. and Renschler, C.S. 2005. Parallel adaptive numerical simulation of dry avalanches over natural terrain. *Journal of Volcanology and Geothermal Research*, 139: 1-21.

Perla, R., Cheng, T.T. and McClung, D.M. 1980. A two-parameter model of snow-avalanche motion. *Journal of Glaciology*, 26(94): 197-207.

Petley, D.N., Dunning, S.A. and Rosser, N.J. 2005. The analysis of global landslide risk through the creation of a database of worldwide landslide fatalities. *In Proceedings of the International Conference on Landslide Risk Management, Vancouver. Edited by O. Hungr, R. Fell, R. Couture and E. Eberhardt. A.A. Balkema, London. pp. 367-373.*

Petrakov, D.A., Tutubalina, O.V. and Chernomorets, S.S. 2004a. Changes of glacial features and terrain after the 2002 Genaldon Disaster: assessment and forecast. *In Proceedings of the Conference on High Mountain Hazard Prevention, Vladikavkaz and Moscow.*

Petrakov, D.A., Tutubalina, O.V. and Chernomorets, S.S. 2004b. The 2002 Genaldon glacial catastrophe: one year later. *Kriosfera Zemli, VIII(1): 29-39. (in Russian)*

Pierson, T.C. 1986. Flow behaviour of channelized debris flows, Mount St. Helens, Washington. *In Hillslope Processes. Edited by A.D. Abrahams. Allen and Unwin, Boston. pp. 269-296.*

Pirulli, M. 2005. Numerical modelling of landslide runout: A continuum mechanics approach. Ph.D. thesis, Politecnico di Torino, Italy. 204 pp.

Pirulli, M., Preh, A., Roth, W., Scavia, C. and Poisel, R. 2003. Rock avalanche run out prediction: combined application of two numerical methods. *In Proceedings of the International Symposium on Rock Mechanics, South African Institute of Mining and Metallurgy, Johannesburg, pp. 903-908.*

Pirulli, M., Scavia, C. and Hungr, O. 2004. Determination of rock avalanche run-out parameters through back analyses. *In Proceedings of the 9th International Symposium on Landslides, Rio de Janeiro. Edited by W.A. Lacerda, M. Ehrlich, S.A.B. Fontoura and A.S.F. Sayão. A.A. Balkema, London, pp. 1361-1366.*

Pitman, E.B., Nichita, C.C., Patra, A., Bauer, A., Sheridan, M. and Bursik, M. 2003a. Computing granular avalanches and landslides. *Physics of Fluids, 15(12): 3638-3646.*

Pitman, E.B., Nichita, C.C., Patra, A.K., Bauer, A.C., Bursik, M. and Webb, A. 2003b. A model of granular flows over an erodible surface. *Discrete and Continuous Dynamical Systems, Series B, 3(4): 589-599.*

Pouliquen, O. 1999. Scaling laws in granular flows down rough inclined planes. *Physics of Fluids, 11(3): 542-548.*

Press, W.H., Teukolsky, S.A., Vetterling, W.T. and Flannery, B.P. 2002. Numerical recipes in C++, the art of scientific computing. Cambridge University Press, Cambridge.

Pudasaini, S.P. and Hutter, K. 2003. Rapid shear flows of dry granular masses down curved and twisted channels. *Journal of Fluid Mechanics, 495: 193-208.*

Pudasaini, S.P., Wang, Y. and Hutter, K. 2005. Rapid motions of free-surface avalanches down curved and twisted channels and their numerical simulation. *Philosophical Transactions of the Royal Society of London, A, 363: 1551-1571.*

Rankine, W.J.M. 1857. On the stability of loose earth. *Philosophical Transactions of the Royal Society of London, 147.*

Read, R.S., Langenburg, W., Cruden, D.M., Field, M., Stewart, R., Bland, H., Chen, Z., Froese, C.R., Cavers, D.S., Bidwell, A.K., Murray, C., Anderson, W.S., Jones, A., Chen, J., McIntyre, D., Kenway, D., Bingham, D.K., Weir-Jones, I., Seraphim, J., Freeman, J., Spratt, D., Lamb, M., Herd, E., Martin, D., McLellan, P. and Pana, D. 2005. Frank Slide a century later: the Turtle Mountain monitoring project. *In Proceedings of the International Conference on Landslide Risk Management, Vancouver. Edited by O. Hungr, R. Fell, R. Couture and E. Eberhardt. A.A. Balkema, London. pp. 713-723.*

Revellino, P., Hungr, O., Guadagno, F.M., Evans, S.G. 2004. Velocity and runout simulation of destructive debris flows and debris avalanches in pyroclastic deposits, Campania region, Italy. *Environmental Geology, 45: 295-311.*

Rickenmann, D. 1999. Empirical relationships for debris flows. *Natural Hazards 19(1): 47-77.*

Rickenmann, D. and Koch, T. 1997. Comparison of debris flow modelling approaches. *In Proceedings of the 1st International Conference on Debris-flow Hazards Mitigation: Mechanics, Prediction and Assessment. Edited by C.L. Chen. ASCE, New York. pp. 576-585.*

Rickenmann, D., Weber, D. and Stepanov, B. 2003. Erosion by debris flows in field and laboratory experiments. *In Proceedings of the 3rd International Conference on Debris-flow Hazards Mitigation: Mechanics, Prediction and Assessment, Davos. Edited by D. Rickenmann and C.L. Chen. Millpress, Rotterdam. pp. 883-893.*

Sailer, R., Rammer, L. and Sampl, P. 2002. Recalculation of an artificially released avalanche with SAMOS and validation with measurements from a pulsed Doppler radar. *Natural Hazards and Earth System Sciences, 2: 211-216.*

Salm, B. 1966. Contribution to avalanche dynamics. *In Proceedings of the Symposium on Scientific Aspects of Snow and Ice Avalanches, Davos. International Association of Scientific Hydrology Publication 69. pp. 19-29.*

Salm, B., Burkard, A. and Gubler, H. 1990. Berechnung von Fliesslawinen eine Anleitung für Praktiker mit Beispielen. *Mitteilungen des Eidgenössischen Institut für Schnee- und Lawinenforschung, No. 47, 37 pp.*

Sampl, P. 1993. Current status of the AVL avalanche simulation model - Numerical simulation of dry snow avalanches. *In Proceedings of the Pierre Beghin International Workshop on Rapid Gravitational Mass Movements, Grenoble. Edited by L. Buisson and G. Brugnot. pp. 269-276.*

Sassa, K. 1985. The mechanism of debris flows. *In Proceedings of the 11th International Conference on Soil Mechanics and Foundation Engineering, San Francisco. Vol. 1, pp. 1173-1176.*

Sassa, K. 1988. Geotechnical model for the motion of landslides. *In Proceedings of the 5th International Symposium on Landslides, Lausanne. Edited by C. Bonnard. A.A. Balkema, Rotterdam. pp. 37-56.*

Sassa, K. 2002. Mechanism of rapid and long travelling flow phenomena in granular soils. *In Proceedings of the UNESCO/IGCP International Symposium on Landslide Mitigation and Protection of Cultural and Natural Heritage, Kyoto. Edited by K. Sassa. Disaster Prevention Research Institute, Kyoto University. pp. 11-30.*

Savage S.B. and Hutter, K. 1989. The motion of a finite mass of granular material down a rough incline. *Journal of Fluid Mechanics, 199: 177-215.*

Savage S.B. and Hutter, K. 1991. The dynamics of avalanches of granular materials from initiation to runout, Part 1: Analysis. *Acta Mechanica, 86: 201-223.*

Schamber, D.R. and MacArthur, R.C. 1985. One-dimensional model for mud flows. *In Proceedings of the ASCE Specialty Conference on Hydraulics and Hydrology in the Small Computer Age. American Society of Civil Engineers, New York. Vol. 2, pp. 1334-1339.*

Scheidegger, A.E. 1973. On the prediction of the reach and velocity of catastrophic landslides. *Rock Mechanics, 5: 231-236.*

Schwab, J.W., Geertsema, M. and Evans, S.G. 2003. Catastrophic rock avalanches, west-central British Columbia. *In Proceedings of the 3rd Canadian Conference on Geotechnique and Natural Hazards, Edmonton. pp. 291-299.*

Selby, M.J. 1985. *Earth's changing surface.* Oxford University Press, Oxford.

Sherard, J.L., Woodward, R.J., Gizienski, S.F. and Clevenger, W.A. 1963. *Earth and earth-rock dams.* John Wiley and Sons, New York, 722 pp.

Sheridan, M.F. and Patra, A.K. 2005. Modeling and simulation of geophysical mass flows. *Journal of Volcanology and Geothermal Research, 139: vii.*

Sheridan, M.F., Stinton, A.J., Patra, A., Pitman, E.B., Bauer, A. and Nichita, C.C. 2005. Evaluating Titan2D mass-flow model using the 1963 Little Tahoma Peak avalanches, Mount Rainier, Washington. *Journal of Volcanology and Geothermal Research, 139: 89-102.*

Sousa, J. and Voight, B. 1991. Continuum simulation of flow failures. *Géotechnique, 41(4): 515-538.*

Sovilla, B. and Bartelt, P. 2002. Observations and modelling of snow avalanche entrainment. *Natural Hazards and Earth System Sciences, 2: 169-179.*

Stadler, R. 1986. Stationäres, schnelles Fließen von dicht gepackten trockenen und feuchten Schüttgütern. Dr. Ing. Dissertation, University of Karlsruhe.

- Stoker, J.J. 1957. *Water Waves*. Interscience, New York.
- Tai, Y.C. and Gray, J.M.N.T. 1998. Limiting stress states in granular avalanches. *Annals of Glaciology*, 26: 272-276.
- Takahashi, T. 1978. Mechanical characteristics of debris flow. *Journal of the Hydraulics Division of the American Society of Civil Engineers*, 104(HY8): 1153-1169.
- Takahashi, T. 1991. *Debris flow*. International Association for Hydraulic Research monograph. A.A. Balkema, Rotterdam.
- Takahashi, T. and Yoshida, H. 1979. Study on the deposition of debris flows Part 1: Deposition due to abrupt change of bed slope. *Annals of the Disaster Prevention Research Institute, Kyoto University*, 22B-2. (in Japanese)
- Takahashi, T., Nakagawa, H., Harada, T. and Yamashiki, Y. 1992. Routing debris flows with particle segregation. *Journal of Hydraulic Engineering*, 118(11): 1490-1507.
- Terzaghi, K. 1920. Old earth pressure theories and new test results. *Engineering News Record*, 85: 632.
- Terzaghi, K. and Peck, R.B. 1967. *Soil mechanics in engineering practice*. John Wiley and Sons, New York.
- Thurber Engineering Ltd. and Golder Associates Ltd. 1993. Cheekye River terrain hazard study. Unpublished report to the British Columbia Ministry of Environment, Lands and Parks, Victoria.
- Trunk, F.J., Dent, J.D. and Lang, T.E. 1986. Computer modeling of large rock slides. *Journal of Geotechnical Engineering*, 112: 348-360.
- Turnbull, B. and Bartelt, P. 2003. Mass and momentum balance model of a mixed flowing/powder snow avalanche. *Surveys in Geophysics*, 24: 465-477.
- Tutubalina, O.V., Chernomorets, S.S. and Petrakov, D.A. 2005. Kolka Glacier before the 2002 collapse: new data. *Kriosfera Zemli*, IX(4): 62-71. (in Russian)
- VanDine, D.F. 1985. Debris flows and debris torrents in the southern Canadian Cordillera. *Canadian Geotechnical Journal*, 22: 44-68.
- Voellmy, A. 1955. Über die Zerstörungskraft von Lawinen. *Schweizerische Bauzeitung*, 73: 212-285.
- Voight, B. and Pariseau, W.G. 1978. *Rockslides and Avalanches: An Introduction*. In *Rockslides and Avalanches*. Edited by B. Voight. Elsevier, New York. Vol. 1, pp. 1-67.

Voight, B. and Sousa, J. 1994. Lessons from Ontake-san: a comparative analysis of debris avalanche dynamics. *Engineering Geology*, 38: 261-297.

Voight, B., Komorowski, J.C., Norton, G.E., Belousov, A.B., Belousova, M., Boudon, G., Francis, P.W., Franz, W., Heinrich, P., Sparks, R.S.J. and Young, S.R. 2002. The 26 December (Boxing Day) 1997 sector collapse and debris avalanche at Soufriere Hills Volcano, Montserrat. *In* The Eruption of Soufriere Hills Volcano, Montserrat from 1995 to 1999. *Edited by* T.H. Druitt and B.P. Kokelaar. Geological Society of London Memoir, 21: 363-407.

Wang, Z. and Shen, H.T. 1999. Lagrangian simulation of one-dimensional dam-break flow. *Journal of Hydraulic Engineering*, 125(11): 1217-1220.

Wang, Y., Hutter, K. and Pudasaini, S.P. 2004. The Savage-Hutter theory: A system of partial differential equations for avalanche flows of snow, debris, and mud. *Zeitschrift fur Angewandte Mathematik und Mechanik*, 84(8): 507-527.

Wieland, M., Gray, J.M.N.T. and Hutter, K. 1999. Channelized free-surface flow of cohesionless granular avalanches in a chute with shallow lateral curvature. *Journal of Fluid Mechanics*, 392: 73-100.

Wise, M.P., Moore, G. and VanDine, D. 2004. Land Management Handbook 56: Landslide Risk Case Studies in Forest Development and Planning Operations. British Columbia Ministry of Forests, Research Branch, Victoria. 124 pp.